Multi-Level Modelling of the Hydrodynamics in Gas Phase Polymerisation Reactors

Samenstelling promotiecommissie:

Prof.dr.ir. G.F. Versteeg, voorzitter	Universiteit Twente
Prof.dr.ir. J.A.M. Kuipers, promotor	Universiteit Twente
Dr.ir. M. van Sint Annaland, assistent-promotor	Universiteit Twente
Prof.dr.-ing. J. Werther	Technische Universität Hamburg-Harburg, Duitsland
Prof.dr. S.T. Johansen	SINTEF Materials and Technology, Zweden
Prof.dr.ir. J. Westerweel	TU Delft
Prof.dr. W.J. Briels	Universiteit Twente
Prof.dr.ir. M.M.C.G. Warmoeskerken	Universiteit Twente
Ir. G.I.V. Bonte	SABIC Euro Petrochemicals bv

The research in this thesis was financially supported by the Dutch Polymer Institute (DPI), the Netherlands

Publisher:
PrintPartners Ipskamp, Postbus 333, 7500 AH Enschede

ISBN 90-365-2211-0

MULTI-LEVEL MODELLING OF THE HYDRODYNAMICS IN GAS PHASE POLYMERISATION REACTORS

PROEFSCHRIFT

ter verkrijging van
de graad van doctor aan de Universiteit Twente,
op gezag van de rector magnificus,
prof.dr. W.H.M. Zijm,
volgens besluit van het College voor Promoties
in het openbaar te verdedigen
op donderdag 30 juni 2005 om 15:00 uur

door

Gijsbertus Albert Bokkers
geboren op 29 juni 1976
te Putten

Dit proefschrift is goedgekeurd door de promotor

Prof.dr.ir. J.A.M. Kuipers

en de assistent-promotor

Dr.ir. M. van Sint Annaland

Je moet dat doen waarvan je denkt dat je het niet kunt.

Eleanor Roosevelt

Aan mijn ouders

Contents

Summary **1**

Samenvatting **5**

1 General Introduction **9**

Abstract 9

1.1 Gas-phase olefin polymerisation reactors 10

1.2 Modelling of gas-phase olefin polymerisation reactors 12

1.3 Multi-level modelling 13

1.4 Objectives of the project 16

1.5 Outline of the thesis 17

2 Development of an experimental technique to measure the granular temperature in a fluidised bed using Particle Image Velocimetry **19**

Abstract 19

2.1 Introduction 20

2.2 Theoretical background 21

2.2.1 Cross-correlation of digital images 22

2.2.2 Relation between the displacement peak and the granular temperature 25

2.2.3 Interpolation of the displacement peak 27

2.3 Testing of the proposed method with computer-generated (synthetic) images 28

2.3.1 Image generation software 28

2.3.2 Uniform particle velocity 29
2.3.3 Gaussian velocity profile 32
2.4 Experimental set-up and optimisation of the method 33
2.4.1 Fluidised bed set-up 33
2.4.2 Image recording settings 35
2.4.3 PIV settings 35
2.4.4 Autocorrelation tests with real particles 36
2.4.5 Cross-correlation tests with real particles 39
2.5 Single bubble experiments 40
2.6 Freely bubbling experiment 46
2.7 Conclusions 53

3 Bubble size and bubble induced particle drift by a single bubble in monodisperse gas-solid fluidised beds: Comparison of model predictions with experiments 55

Abstract 55
3.1 Introduction 57
3.2 Discrete Particle Model 58
3.2.1 Soft-sphere collision model 59
3.2.2 Gas-particle drag 60
3.3 Two Fluid Model 64
3.3.1 Frictional viscosity 65
3.4 Numerical solution strategy 67
3.4.1 Verification of the CFD models 68
3.5 Settings of the experiments and the CFD models 70
3.6 Bubble size and induced particle drift 72
3.6.1 Bubble shape and size 74
3.6.2 Particle mixing induced by a single bubble 84
3.7 Conclusions 90

4 Development of a Multi Fluid Model: derivation and numerical implementation **95**

Abstract . . . 95

4.1 Introduction . . . 97

4.2 Kinetic theory of granular flow of multi-component mixtures . . . 98

4.2.1 Definitions . . . 99

4.2.2 Conservation equations . . . 101

4.2.3 Velocity distribution and pair distribution function . . . 103

4.2.4 Radial distribution function and chemical potential . . . 109

4.2.5 Constitutive equations . . . 111

4.3 Numerical solution method . . . 113

4.3.1 Discretisation of the governing equations . . . 114

4.3.2 Solution procedure of the finite difference equations . . . 115

4.3.3 Diffusion force equation . . . 118

4.3.4 Boundary conditions . . . 120

4.4 Conclusions . . . 121

A.1 Diffusion force equation . . . 122

5 Segregation in bi-disperse fluidised beds: comparison of CFD model predictions with experiments **127**

Abstract . . . 127

5.1 Introduction . . . 129

5.2 Minimum fluidisation velocity . . . 131

5.3 Particle segregation rates in a freely bubbling bi-disperse fluidised bed . 134

5.3.1 Settings of the experiments and the CFD models . . . 134

5.3.2 Segregation rates: comparison of DPM results with experiments . 137

5.3.3 Segregation rates: comparison of MFM results with experiments 140

5.3.4 Effect of the superficial gas velocity and the mixture composition 141

5.4 Granular temperature in segregating system . . . 148

5.5 Conclusions . . . 150

6 Modelling of large-scale dense gas-solid fluidised beds using the Discrete Bubble Model **153**

Abstract . . . 153

6.1 Introduction . . . 155

6.2 Discrete Bubble Model . . . 157

6.2.1 Model assumptions . . . 157

6.2.2 Emulsion phase hydrodynamics . . . 157

6.2.3 Bubble dynamics . . . 158

6.2.4 Number of bubbles . . . 159

6.2.5 Bubble coalescence/break-up . . . 159

6.2.6 Constitutive equation for the drag coefficient . . . 160

6.2.7 Boundary conditions . . . 162

6.2.8 Solution method . . . 164

6.3 Model verification . . . 166

6.4 DBM simulation results . . . 166

6.4.1 Effect of coalescence . . . 170

6.4.2 Visible bubble flow . . . 173

6.4.3 Effect of superficial gas velocity . . . 177

6.4.4 Effect of aspect ratio . . . 180

6.4.5 Industrial scale fluidised bed . . . 183

6.5 Outlook . . . 185

6.6 Conclusions . . . 186

A Results presented in Chapters 2, 3 and 5 **189**

Nomenclature **199**

Bibliography **207**

Dankwoord **217**

Levensloop **221**

Summary

The gas-solid fluidised bed process is the most versatile process for the production of polyolefins, because it allows the production of polyolefins with a broad distribution of both the product density and molecular weight. In spite of the excellent heat transfer characteristics of a fluidised bed, the production capacity is still limited by the rate of heat removal and temperature control in the polyolefin production process is a major point of attention. The rate of heat removal is largely determined by the large scale convection patterns prevailing in the gas phase olefin polymerisation reactor, induced by the in situ formed and growing gas bubbles. Moreover, the bubbles play an intricate role in the particle mixing and segregation behaviour of the fluidised bed. To improve the design, operation and scale-up of these gas-fluidised bed processes, a better understanding and a quantitative description of these phenomena is required. Therefore, the main objective of this project was the development of fundamental hydrodynamic models to describe and study the hydrodynamic behaviour of the gas-solid fluidised bed reactor.

In order to model the large scale circulation patterns prevailing in a gas phase olefin polymerisation reactor and, on the other hand, also get more insight into the role of individual bubbles in the particle mixing and segregation behaviour, a multi-level modelling approach has been used with the idea that lower level models can provide closure relations, regarding gas-particle and particle-particle interactions, for the higher level models. In this thesis four different hydrodynamic models are considered. On the lowest level the Lattice Boltzmann Model (LBM) has been employed, where the gas-particle drag on an ensemble of spheres ($< \mathcal{O}(10^2)$) can be computed a priori (van der Hoef et al., 2005). The second model in the hierarchy of multi-level modelling is the

Discrete Particle Model (DPM), used for small scale fluidised beds ($< \mathcal{O}(10^6)$ particles), where every individual particle is tracked using Newton's second law of motion and the particle collisions are evaluated with a detailed collision model. The DPM relies on closure equations for the gas-particle drag. For larger engineering scale systems ($> \mathcal{O}(10^6)$ particles), a Multi Fluid Model (MFM) is required, where the solids phase is computed as a continuum, where closures for the solids phase rheology can be obtained from the Kinetic Theory of Granular Flow (KTGF). To compute the large scale circulation patterns prevailing in an industrial scale fluidised bed, a Discrete Bubble Model (DBM) has been employed, where the gas bubbles are modelled as discrete elements and the emulsion phase is considered as a continuum. Lower level models in addition to experimental data should be used to provide closure information on the bubble behaviour and the emulsion phase rheology.

Experimental validation is a crucial step in the development of fundamental hydrodynamic models. In continuum models based on the kinetic theory of granular flow, the random fluctuating velocity of the particles, i.e. the granular temperature, is a key parameter. Therefore, a whole-field non-intrusive measurement technique, based on Particle Image Velocimetry (PIV), has been developed to measure the local granular temperature profiles in fluidised beds. The new technique has been successfully applied to measure the granular temperature and particle velocity profiles around a single bubble injected into a mono-disperse fluidised bed at incipient fluidisation conditions and in a freely bubbling fluidised bed, where the particles are mixed more vigorously. In principle this technique can be extended to binary mixtures of particles, provided that the particles with different diameters or densities can be separated in the images.

Since bubbles play a crucial role in the hydrodynamics of gas-solid fluidised beds, firstly a simple and idealised case of a single bubble injected into a mono-disperse fluidised bed has been studied in order to analyse the effect of gas-particle and particle-particle interactions. The single bubble case was studied with both the Two Fluid Model based on the KTGF and the Discrete Particle Model and the simulation results

were compared with dedicated experiments. Regarding the gas-particle interaction, it was concluded that the drag models by Ergun (1952) and Wen and Yu (1966) slightly overpredicted the size of the bubble. The implementation of a new drag model obtained by van der Hoef et al. (2005), using Lattice Boltzmann simulations, gave a better agreement of the bubble size compared to the experimental findings. The particle mixing induced by the passage of a single bubble could be very well predicted by the DPM, but was largely overpredicted by the TFM. This is most probable related to the fact that the KTGF does not take into account the effect of friction during long-term and multi-particle contacts, which results in an overprediction of the emulsion phase mobility.

After studying a single bubble rising through a mono-disperse fluidised bed, the next step was to study the particle mixing and segregation behaviour in bi-disperse freely bubbling fluidised beds. Several authors have used a Multi Fluid Model to study mixing and segregation in a binary mixture of particles. However, in these MFMs the particle velocities were assumed to be (nearly) Maxwellian distributed around different mean velocities and with different granular temperatures for all the species involved. This appears to be inconsistent with the first (equilibrium) approximation obtained from the Chapman-Enskog procedure for the situation where many collisions occur between particles of the different species. Therefore, a new set of closures has been derived for the rheologic properties of multi-component mixtures of slightly inelastic spheres using the Chapman-Enskog solution procedure of successive approximations. The model equations were implemented in a numerical code using an efficient new numerical algorithm that directly accounts for the compressibility of the solids phase. Subsequently, the new MFM was used to compute mixing and segregation rates in a bi-disperse freely bubbling fluidised bed. The MFM simulation results, together with Discrete Particle Model simulations, have been compared with Digital Image Analysis experiments obtained by Goldschmidt et al. (2003). The new MFM reasonably describes the segregation rates, but seems to underestimate the segregation rates at longer times, which is in strong contrast to other MFMs reported in the literature that strongly overpredict the segregation rates. This underprediction of the segregation rate is probably

related to the neglect of frictional stresses associated with long-term multiple-particle contacts resulting in an overestimation of the mobility of the emulsion phase. The DPM, however, could very well predict the correct rate of segregation compared to the experiments, provided that a poly-disperse drag relation by van der Hoef et al. (2005) was implemented in the DPM.

In order to describe the macro-scale emulsion phase circulation patterns in industrial scale fluidised bed reactors, a Discrete Bubble Model has been developed. The DBM accounts for the bubble coalescence and break-up and for the very important two-way coupling between the bubbles and the emulsion phase, which enables a direct computation of the emulsion phase velocity profiles. A comparison of the DBM simulation result without bubble coalescence with a DBM simulation where the bubble coalescence was properly accounted for demonstrated the dominating effect of bubble coalescence on the large-scale circulation patterns prevailing in bubbling fluidised beds. The lateral profiles of the visible bubble flow rate computed with the DBM agreed quite well with experimental results reported by Werther (1974). Furthermore, it was demonstrated that the DBM was able to model the hydrodynamics of industrial scale fluidised bed reactors (4 m x 4 m x 8 m) within acceptable calculation times. In general, it can be concluded that the DBM is able to capture the salient features of the hydrodynamics of bubbling fluidised beds. However, further research is required to improve the closure equations for the bubble behaviour and bubble coalescence and break-up to arrive at a quantitative description.

Samenvatting

Het meest veelzijdige productieproces voor polyolefinen is het gas-vast gefluïdiseerd bed proces, omdat hierin polyolefinen gemaakt kunnen worden met zowel een brede product-dichtheidsverdeling als een brede moleculair-gewichtsverdeling. Ondanks de uitstekende warmteoverdrachtseigenschappen van een gefluïdiseerd bed is de productiecapaciteit gelimiteerd door de snelheid waarmee de reactiewarmte kan worden afgevoerd. Daarom is de beheersing van de temperatuur in het polyolefine proces een belangrijk punt van aandacht. De snelheid waarmee de reactiewarmte wordt afgevoerd, wordt hoofdzakelijk bepaald door de grootschalige convectiepatronen. Deze worden geïnduceerd door de spontaan gevormde en groeiende gas bellen, die voorkomen in de gasfase olefine polymerisatie reactor. Verder spelen de gasbellen een gecompliceerde rol in het menging en segregatie gedrag van het gefluïdiseerde bed. Om het ontwerp, de operatie en de opschaling van deze gefluïdiseerde bedden te verbeteren, is meer kennis en een kwantitatieve beschrijving nodig van het meng- en segregatiegedrag van deze gefluïdiseerde bedden. Het doel van dit project was om fundamentele hydrodynamische modellen te ontwikkelen om het hydrodynamisch gedrag van het gas-vast gefluïdiseerde bed te beschrijven en te bestuderen.

Om enerzijds de grootschalige convectie patronen die voorkomen in gasfase olefine polymerisatie reactoren te beschrijven en anderzijds meer inzicht te verwerven in de rol van gasbellen in het menging en segregatie gedrag is een 'multi-level modelling' benadering toegepast. Gedetailleerde modellen zullen sluitingsrelaties aangaande de gas-deeltjes en de deeltjes-deeltjes interacties kunnen leveren aan de minder gedetailleerde modellen. In dit proefschrift worden vier verschillende hydrodynamische modellen beschouwd. Op het laagste niveau wordt het 'Lattice Boltzmann Model' (LBM) gebruikt waar de gas-deeltjes weerstand op een groep deeltjes ($< \mathcal{O}(10^2)$) a priori kan

worden berekend (van der Hoef et al., 2005). Het tweede model in de hiërarchie van 'multi-level' modellering is het 'Discrete Particle Model' (DPM) dat voornamelijk gebruikt wordt voor kleinschalige gefluïdiseerde bedden ($< \mathcal{O}(10^6)$ particles), waarbij elk individueel deeltje wordt gevolgd volgens de tweede wet van Newton en de botsingen tussen de deeltjes worden beschreven met een gedetailleerd botsingsmodel. Het DPM gebruikt sluitingsrelaties voor de gas-deeltjes interactie. Voor nog grotere systemen ($> \mathcal{O}(10^6)$ particles) wordt het 'Multi Fluid Model' (MFM) gebruikt, waarbij de deeltjesfase wordt beschreven als een continuum, waarvoor sluitingsrelaties voor de vaste stof rheologie kunnen worden verkregen met de kinetische theorie voor granulaire stromingen (KTGF). De grootschalige convectie patronen die voorkomen in een gefluïdiseerd bed op industriële schaal worden gemodelleerd met een 'Discrete Bubble Model' (DBM), waar de gasbellen worden gemodelleerd als discrete elementen en de emulsiefase wordt beschouwd als een continuum. Sluitingsrelaties voor het gedrag van de bellen en de rheologie van de emulsiefase kunnen worden afgeleid met behulp van gedetailleerdere modellen in combinatie met experimenten.

Experimentele validatie is cruciaal voor de ontwikkeling van fundamentele hydrodynamische modellen. In continuum modellen die zijn gebaseerd op de KTGF is de fluctuatie snelheid van de deeltjes, i.e. de granulaire temperatuur, een sleutelparameter. Daarvoor is een nieuwe meettechniek ontwikkeld, gebaseerd op Particle Image Velocimetry (PIV), die de lokale granulaire temperatuurprofielen in een gefluïdiseerd bed kan meten. Deze nieuwe techniek is succesvol gebleken bij het meten van de granulaire temperatuur en de deeltjes snelheidsprofielen rondom een geïnjecteerde enkele bel in zowel een monodispers gefluïdiseerd bed op minimum fluidisatiesnelheid als in een bubbelend gefluïdiseerd bed waar de deeltjes heftiger worden gemengd. In principe kan deze techniek worden uitgebreid naar binaire deeltjes mengsels, mits de deeltjes met verschillende dichtheden of diameters kunnen worden onderscheiden in de digitale beelden.

In verband met de cruciale rol die bellen spelen in de hydrodynamica van gas-vast

gefluïdiseerde bedden is eerst een eenvoudige en geïdealiseerde situatie bestudeerd. Hierbij wordt een enkele bel geïnjecteerd in een monodispers gefluïdiseerd bed om het effect van gas-deeltjes en deeltjes-deeltjes interacties te analyseren. De enkele bel situatie is bestudeerd met zowel het 'Two-Fluid Model' (TFM) gebaseerd op de KTGF en het 'Discrete Particle Model' en de simulatieresultaten zijn vergeleken met gedetailleerde experimenten. Betreffende de gas-deeltjes interacties kon worden geconcludeerd dat de weerstandsmodellen van Ergun (1952) en Wen and Yu (1966) de grootte van de bel licht overschatten in zowel het DPM als het TFM. Implementatie van een nieuw weerstandsmodel van van der Hoef et al. (2005), gebaseerd op Lattice Boltzmann simulaties, resulteerde in een betere voorspelling van de belgrootte ten opzichte van de experimentele resultaten. De deeltjesmenging geïnduceerd door het voorbijgaan van een enkele bel werd zeer goed voorspeld door het DPM, maar werd erg overschat door het TFM. Dit heeft waarschijnlijk te maken met het feit dat de KTGF geen rekening houdt met het effect van frictie tijdens langdurig contact tussen enkele en meerdere deeltjes, hetgeen resulteert in een overschatting van de beweeglijkheid van de emulsiefase.

Na het bestuderen van een enkele bel in een monodispers gefluïdiseerd bed is de deeltjesmenging en het segregatiegedrag in bidisperse vrij-bubbelende gefluïdiseerde bedden onderzocht. Verscheidene auteurs hebben een 'Multi Fluid Model' (MFM) gebruikt om de menging en segregatie in binaire mengsels van deeltjes te bestuderen. In deze MFM's wordt echter verondersteld dat de deeltjessnelheden (bijna) Maxwellian verdeeld zijn rondom verschillende gemiddelde snelheden en met verschillende granulaire temperaturen voor al de aanwezige deeltjesfasen. Deze aanname blijkt niet overeenkomstig met de eerste (evenwichts)benadering van de Chapman-Enskog procedure voor de situatie waarbij veel botsingen plaatsvinden tussen deeltjes van verschillende fasen. Daarom is er een nieuwe set vergelijkingen afgeleid voor de rheologische eigenschappen van mengsels van licht inelastische deeltjes bestaande uit meerdere fasen volgens de Chapman-Enskog oplossingsmethode van opeenvolgende benaderingen. De modelvergelijkingen zijn geïmplementeerd in een numerieke code waarbij een nieuw efficient numeriek algorithme is gebruikt die rekening houdt met de compressibiliteit

van de deeltjesfase. Het nieuwe MFM is gebruikt om menging- en segregatiesnelheden in een bidispers vrij-bubbelend gefluïdiseerd bed te berekenen. De MFM simulatieresultaten zijn evenals de DPM simulaties vergeleken met de digitale beeld analyse experimenten van Goldschmidt et al. (2003). Het nieuwe MFM beschrijft de segregatiesnelheden behoorlijk, maar na langere tijd blijkt de MFM de segregatiesnelheid te onderschatten. Dit is opvallend omdat andere MFM's die in de literatuur zijn gepresenteerd de segregatiesnelheden juist sterk overschatten. Het onderschatten van de segregatiesnelheden is waarschijnlijk te wijten aan het negeren van de frictionele spanningen die voortkomen uit de langdurige deeltjes-deeltjes contacten tussen meerdere deeltjes wat resulteert in een overschatting van de mobiliteit van de emulsie fase. Het DPM daarentegen voorspelde de segregatiesnelheden vrij goed vergeleken met de experimenten, mits de polydisperse weerstandsrelatie door van der Hoef et al. (2005) was geïmplementeerd in het DPM.

Om de grootschalige convectiepatronen van de emulsiefase in gefluïdiseerde bedden op industriële schaal te beschrijven is een 'Discrete Bubble Model' ontwikkeld. In het DBM zijn coalescentie en het breken van bellen verdisconteerd en tevens wordt er rekening gehouden met de zeer belangrijke twee-weg koppeling tussen de bellen en de emulsiefase, die een directe berekening van de emulsiefasesnelheid mogelijk maakt. Vergelijking tussen de DBM simulatieresultaten zonder coalescentie en de DBM simulatieresultaten met coalescentie laat zien dat coalescentie van bellen een dominant effect heeft op de grootschalige convectiepatronen in bubbelende gefluïdiseerde bedden. De laterale profielen van de snelheid van de zichtbare bellenstromingen berekend met het DBM kwamen vrij goed overeen met de experimentele resultaten door Werther (1974). Verder is gebleken dat het DBM de hydrodynamica kan beschrijven van een industriële gefluïdiseerd bed reactor (4 m x 4 m x 8 m) binnen acceptabele rekentijd. In het algemeen kan worden geconcludeerd dat het DBM het meest bepalende gedrag van de hydrodynamica in een bubbelend gefluïdiseerd bed kan beschrijven. Echter, er is meer onderzoek nodig om de sluitingsrelaties voor het belgedrag, de coalescentie en het breken van de bellen te verbeteren om tot een meer kwantitatieve beschrijving te komen.

Chapter 1

General Introduction

Abstract

To model the hydrodynamics of industrial scale fluidised bed reactors for gas-phase polymerisation processes, a multi-level model approach is adopted in this work. The basic idea is that fundamental models can be used to study the phenomena prevailing at small scales and that the effects of these phenomena can be captured with closure equations by higher-level models. A short overview is presented of the models that are used at different length scales of dense fluidised suspensions. The goal of the project is discussed and the chapter is concluded with an outline of the thesis.

1.1 Gas-phase olefin polymerisation reactors

The most important polyolefins produced are high density polyethylene (HDPE), low density polyethylene (LDPE), linear low density polyethylene (LLDPE) and polypropylene (PP) with an annual production of 100 million tons around the world (based on production data for 1999 and 2000 (McKenna and Soares, 2001)). Different processes have been developed to produce these polyolefins, where the liquid slurry process, the solution process and the gas phase polymerisation process are the most frequently used. The gas phase polymerisation process is the most recently developed and also the most versatile process.

The liquid slurry process, which is the oldest process for PE production, produces PE covering a broad molecular weight distribution. However, the range of product densities that can be produced with this process is limited. The solution processes can produce PE over a broad range of product densities, but only for a limited range of molecular weights. Gas phase polymerisation processes, however, can produce PE with large ranges of both product densities and molecular weight distributions (Burdett et al., 2001). The gas phase polymerisation processes are based on fluidised bed technology. The fluidised bed process has many distinct advantages compared to the more conventional liquid slurry and solution processes:

- Construction costs and operating costs can be reduced by 30% and 35% respectively, due to the lower operating pressure.
- No involvement of any liquid phase in the reaction zone, so that this process is not constrained by solubility or viscosity;
- Separation of the product from the catalyst or solution is avoided.

One of the main concerns of the fluidised bed process is that the operating temperature must be kept below the melting point of the polymer produced, to avoid sticking of the polymer particles. Since the polymerisation reaction is highly exothermic, temperature control is a major point of attention for the fluidised bed polymerisation reactor.

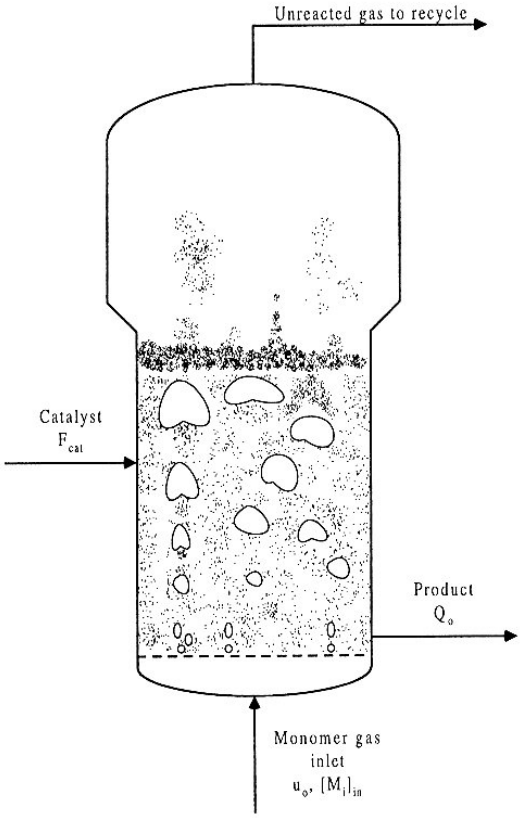

Figure 1.1: UNIPOL process.

One of the fluidised bed gas phase olefin polymerisation reactors operated in industry is the so-called UNIPOL process, originally invented by Union Carbide. In Figure 1.1 a schematic representation is shown of this reactor, which consists of a reaction zone and a disengagement zone. The aspect ratio of this reactor is typically around 7, where the top part is wider to permit entrained particles to fall back into the fluidised bed. Extremely active and selective (50-100 kg polymer per gram of catalyst) Ziegler-Natta or metallocene catalysts are used in this proces, that need not to be retrieved from the produced polymer particles. The monomer gas is fed through the bottom plate of the reactor and fulfils multiple roles in the reactor. First of all, the monomer is used as raw material for the polymerisation reaction. Furthermore, the monomer gas fluidises the particles and removes the heat produced in the reactor. Only 5% of the monomer gas is converted per pass in order to limit the heat production rate and the remaining part of the unreacted gas is cooled, compressed and recycled back into the reactor. Overall, the

monomer conversion will be 100%. Extra cooling capacity is achieved by operating the reactor in 'condensed mode', which means that part of the monomer is fed as a liquid, which is evaporated in situ consuming part of the produced reaction heat. The larger polymer particles (0.3-1.0 mm) tend to reside in the bottom part of the reactor, referred to as particle segregation, where the product particles are withdrawn.
Despite the fact that fluidised beds possess excellent heat transfer characteristics, still the production capacity of this polymerisation process is limited by the rate of heat removal from the reactor. The rate of heat removal is largely determined by the prevailing macroscale circulation patterns in the gas-solid emulsion phase, induced by the in situ created and growing gas bubbles rising through the emulsion phase. On the other hand, bubbles play an intricate role in the particle segregation phenomenon. In this thesis hydrodynamic models are developed to further the understanding on the evolution of circulation patterns in the emulsion phase and the underlying mechanisms and particle segregation dynamics.

1.2 Modelling of gas-phase olefin polymerisation reactors

Since the development of the gas-phase olefin polymerisation process, the modelling of the polymerisation reactor has been a continuous subject of research focussing on different levels of detail. Many models have been developed to describe the different phenomena prevailing in this type of reactors, like polymerisation reactions, heat and mass transfer, gas phase mixing, particle segregation and so forth. All the developed models can roughly be divided into three catagories, i.e. kinetic models, phenomenological models and fundamental hydrodynamic models. Kinetic models are mainly used to describe polymerisation rates and polymer molecular weight distributions. Choi and Ray (1985) were the first to model the dynamic behaviour of a fluidised bed reactor for solid catalysed gas phase olefin polymerisation using a phenomenological model. Hatzantonis et al. (2000) extended this model to account for the effect of varying bubble size on the dynamic and steady state behaviour of these fluidised bed reactors. A generalised steady-state population balance model was developed by Hatzantonis et al. (1998) to

investigate the development of the particle-size distribution in gas phase fluidised bed olefin polymerisation reactors. Kim and Choi (1999) developed a multi-compartment model to model mixing and segregation phenomena in this type of reactors.

With the fast increase of computational power over the past decade it has become possible to develop Computational Fluid Dynamics (CFD) models to study the particle and fluid dynamics occurring in gas phase olefin polymerisation reactors on a much more fundamental footing. McKenna et al. (1998) used a CFD model to investigate the heat transfer characteristics and the influence of particle-particle interactions. Kaneko et al. (1999) incorporated chemical reactions and energy balances in a Discrete Element Model (DEM) to follow the temperature behaviour of the particles and the gas phase in a fluidised bed reactor for polyolefin production in great detail. In DEM all the particles are tracked individually and potential hot spot formation on the mesoscopic scale can be well studied in detail with this model. Detailed CFD modelling of a real industrial scale gas phase olefin polymerisation reactor, incorporating all important phenomena like fluid and particle dynamics, heat and mass transfer, mixing and segregation, is far out of reach with currently available computer power and will remain so for the foreseeable future. Therefore, a multi-level modelling strategy has been adopted to enable the study of the dynamic behaviour of industrial scale reactors using the input from lower-level models. In the next paragraph, the multi-level modelling approach adopted in this project will be elucidated.

1.3 Multi-level modelling

In order to model the hydrodynamic behaviour of an industrial scale olefin polymerisation reactor, a multi-level modelling approach has been developed, which is based on the idea that fundamental detailed models can provide closure equations for the phenomena prevailing at small scales to be used in higher level models. A schematic picture of the multi-level modelling approach is shown in Figure 1.2. In fluidised bed modelling the gas-particle interaction is one of the important closures to be included,

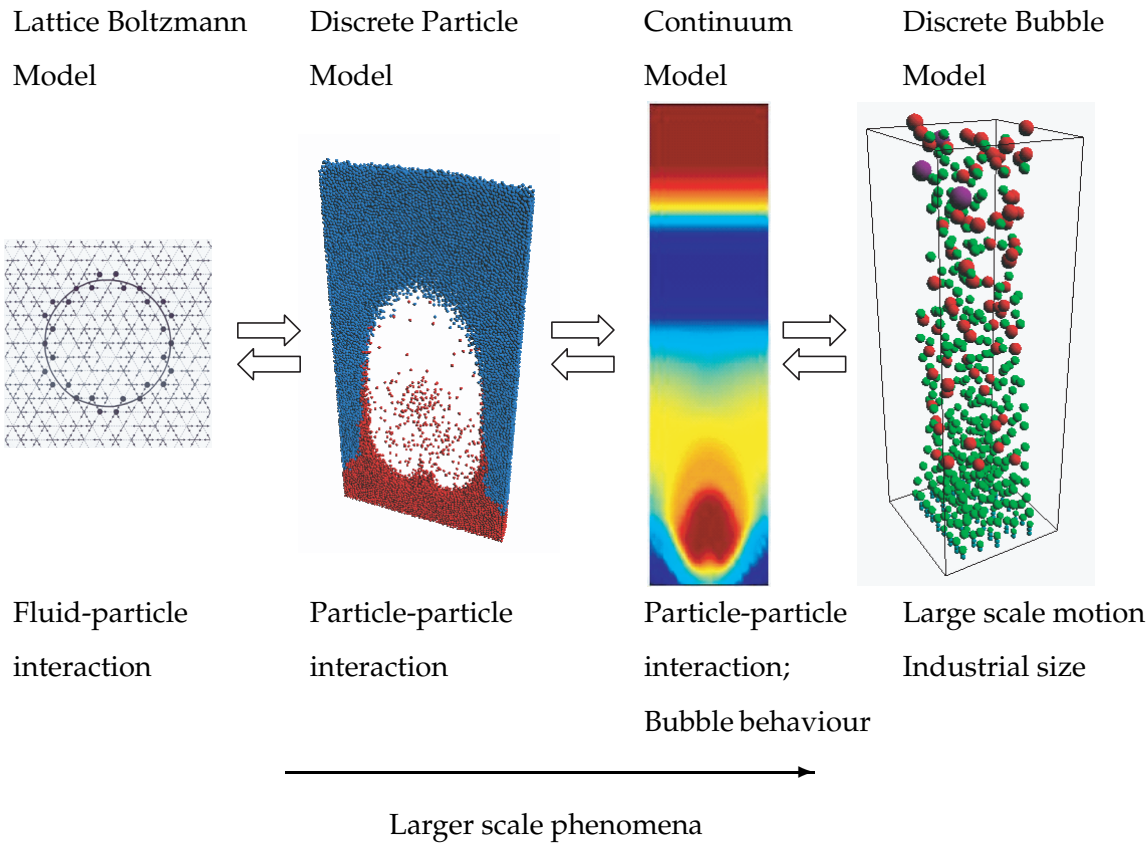

Figure 1.2: Multi-level modelling strategy for dense gas-solid fluidised beds (van der Hoef et al., 2004).

since it determines the minimum fluidisation velocity (and hence also the excess velocity determining the visible bubble flow rate) and the required energy input rate to the system. With the Lattice Boltzmann Model (LBM), which is the most detailed model in the hierarchy of multi-level modelling, the gas-particle interaction can be computed a priori. In view of the required computation times, the LBM is limited to small configurations of mono-disperse or multi-disperse spheres up to $\mathcal{O}(10^2)$. From LBM the effective drag force for particles in a dense assembly can be computed a priori. Therefore, it is essential that the fluid flow is solved on a scale that is at least one order of magnitude smaller than the diameter of the particles, so that the details of the flow can be resolved correctly (van der Hoef et al., 2005). The drag force relation obtained from LBM simulations can be incorporated in higher-level models, which do not resolve the details of the flow around the particles.

The second model is the Discrete Particle Model (DPM) which is very well suited to model fluidised beds at a relatively small scale ($< \mathcal{O}(10^6)$ particles). In the DPM or Euler-Lagrange model every particle is tracked individually where the particle velocities are obtained from Newton's second law of motion, whereas the gas phase flow field is computed from the volume-averaged Navier-Stokes equations. Particle-particle and particle-wall collisions are computed with a detailed collision model taking into account the non-ideality of the particle encounters. An important closure equation for this model is the effective momentum exchange between the particles and the gas phase, which is represented by a drag force relation. In most models for particle-laden flows the well-known combination of Ergun (low porosities) and Wen&Yu drag closure (high porosities) is applied. However, Lattice Boltzmann simulations have revealed large discrepancies with respect to aforementioned drag models, especially for low porosities ($\epsilon < 0.8$) and Re numbers exceeding 50 (Koch and Hill (2001)). The DPM is a valuable research tool to study the effect of different gas-particle drag closures on the fluidisation behaviour. Moreover, the effect of particle-particle collisions on the fluidisation behaviour can be studied in great detail, on the basis of which assumptions required in higher level models, such as the continuum model with the Kinetic Theory of Granular Flow (KTGF), can be validated.

In systems where the number of particles exceeds typically one million, the DPM is not practical anymore, since it consumes too much computational time to compute the motion of all these individual particles. Therefore, a continuum approach is required to model larger scale fluidised beds. The Multi Fluid Model (MFM) is a continuum (Euler-Euler) model where both the particulate phase and the gas phase are modelled as inter-penetrating continua. The solids phase rheology is described with the Kinetic Theory of Granular Flows (KTGF) to obtain closure equations for, among others, the solids phase viscosity and the solids phase pressure as a function of the random fluctuating particle velocity (i.e. the granular temperature). The assumptions made in the KTGF can in principle be validated with the DPM.

In order to model the hydrodynamics of an industrial scale fluidised bed with dimensions that can typically amount 4 m wide and 15 m high, even the MFM requires too much computational resources to resolve the bubbles with sufficient accuracy. Therefore a fourth model in the hierarchy of multi-level modelling, the Discrete Bubble Model (DBM), has been developed for the simulation of industrial scale fluidised beds. The DBM is, like the DPM, an Euler-Lagrange model where the bubbles are tracked individually, whereas the emulsion phase is modelled as a continuum. In this work, the DBM is employed to gain insight in the large circulation patterns that are encountered in industrial scale fluidised beds. This model also needs closures that can be obtained from experimental findings or from lower level models, such as the emulsion phase viscosity and the bubble behaviour, like the initial and maximum bubble size and the terminal rise velocity of bubbles in fluidised beds.

1.4 Objectives of the project

The main objective of this project is the development and its subsequent use of advanced hydrodynamic models to study bubble behaviour, particle mixing and segregation phenomena and macro-scale circulation patterns prevailing in gas phase olefin polymerisation reactors. A multi-level modelling approach has been adopted where the lower level models are used to provide closures for the higher-level models. The hydrodynamic models will be validated on basis of dedicated cold flow experiments.

The Multi Fluid models presented in the literature largely overpredict the rate of segregation in bi-disperse fluidised beds. Therefore, in this work, firstly, an extensive and detailed study is carried out on the effects of gas-particle and particle-particle interactions by studying the shape and size of a single bubble injected into a mono-disperse fluidised bed and the induced particle drift. Thereafter, the dynamic behaviour of a segregating freely bubbling bi-disperse fluidised bed is studied with both the DPM and the MFM. Finally, the large scale circulation patterns in industrial scale fluidised bed

reactors are studied with the Discrete Bubble Model.

1.5 Outline of the thesis

Validation of hydrodynamic models is essential to be able to rely on the results produced with these models. In *Chapter 2* a new non-invasive technique based on Particle Image Velocimetry (PIV) will be presented that is developed to measure granular temperature profiles in pseudo-2D fluidised beds. The granular temperature is a key variable in the Kinetic Theory of Granular Flow, which provides closure equations for the solids phase rheology in continuum models.

In *Chapter 3* the bubble size and shape and the solids mixing induced by a single bubble injected into a mono-disperse fluidised bed at incipient fluidisation conditions is studied with both the DPM and the TFM and compared with experimental data. Both models are subjected to a parameter study regarding the particle-particle and gas-particle interactions and in addition the effect of bed width and particle size will be assessed. A single bubble injected into a fluidised bed is a simple and idealised case to check the gas-particle and particle-particle interactions independently.

In *Chapter 4* a new set of closure relations is presented for a Multi Fluid model based on the kinetic theory of granular flow of multi-component mixtures. Furthermore, a new numerical algorithm was devised to implement the new closures into an efficient 3D computer code. Subsequently, the new MFM is employed to predict segregation rates in binary mixtures of particles. The results are compared with DPM simulations and with Digital Image Analysis experiments performed by Goldschmidt et al. (2003). Particle segregation constitutes a phenomenon which is very sensitive to a variety of influences, such as the superficial gas velocity, volume ratio of the small and large particles, drag model etc., which will be discussed in detail in *Chapter 5*. Compared to Multi Fluid models presented in the literature, the new MFM in this work describes the mechanism of segregation in a much more realistic way.

In *Chapter 6* a new model is developed to describe the large scale circulation patterns prevailing in large gas phase olefin polymerisation reactors. The DBM, normally used in the modelling of gas-liquid bubble columns, is adapted to model the hydrodynamics of fluidised bed reactors where the bubbles are represented in a discrete fashion, whereas the emulsion phase is modelled as a continuum. It is shown that the DBM is able to capture the large scale circulation patterns of bubbling fluidised beds within acceptable computational times.

Chapter 2

Development of an experimental technique to measure the granular temperature in a fluidised bed using Particle Image Velocimetry

Abstract

To describe the hydrodynamics in engineering scale gas-solid fluidised beds, continuum models based on the Kinetic Theory of Granular Flow have been developed, in which the random fluctuating velocity of the particles, i.e. the granular temperature, is a key parameter. In this chapter a whole-field non-intrusive measurement technique, based on Particle Image Velocimetry, will be presented, to measure the local granular temperature in fluidised beds. The technique assumes that the particle velocity distribution and the particle image intensity distribution are Gaussian, which is often satisfied. A detailed description of the novel technique and an extensive testing of the method is presented. Experiments have been carried out in two pseudo-2D fluidised beds with diameters of 15 cm and 30 cm, both filled with 1.5 mm and 2.5 mm glass beads, for which all the properties including the collision parameters, have been measured accurately. Particle velocity and granular temperature profiles have been measured for a single bubble injected into a mono-disperse fluidised bed at minimum fluidisation conditions and for a freely bubbling mono-disperse fluidised bed. With this set of experimental data, fundamental hydrodynamic models can be validated thoroughly.

2.1 Introduction

To study the hydrodynamics in engineering scale fluidised bed reactors, continuum (Euler-Euler) models have been developed. In these models both the gas phase and the particulate phase are described as interpenetrating continua. Closure relations are required to describe the solids phase rheology, for which in most modern continuum models the Kinetic Theory of Granular Flow (KTGF) is employed. Basically, this theory is an extension of the kinetic theory of dense gases (Chapman and Cowling, 1970) to particulate flows. In the KTGF the actual particle velocity is decomposed in a mean solids velocity and a random fluctuating velocity. The extent of fluctuation is defined as the granular temperature, which is the key parameter in the KTGF. To validate continuum models based on the KTGF experimental data is required, particularly the spatial distribution of the granular temperature. By using this information, supported with simulation results with even more detailed CFD-models, such as the Discrete Particle Model (Tsuji et al., 1993; Hoomans et al., 1996; Xu and Yu, 1997) where every particle is tracked individually, the validity of the underlying assumptions in the KTGF can be assessed.

Despite the fact that so many researchers use the continuum approach based on the KTGF to model fluidised beds, there are only a few reports on measurements of the granular temperature. Cody et al. (1996) introduced and validated a novel non-intrusive experimental technique to measure the granular temperature of mono-disperse glass spheres at the wall of a fluidised bed. This technique measures the acoustic shot noise excitation of the surface of the fluid bed vessel by random particle impact. Zhang et al. (1996) measured particle velocities and particle velocity fluctuations (granular temperature) in riser flow of cohesive (group C) particles using a Laser Doppler Anemometer system. More recently, Wildman and Huntley (2000) and Wildman (2002) have used Particle Tracking Velocimetry (PTV) to measure the granular temperature in a vibro-fluidised bed. In this technique the velocity of every individual particle is measured and from these data the velocity distribution and the granular temperature can be cal-

culated. The disadvantage of this technique, however, is that a very high frame rate is required in order to keep track of every single particle. Furthermore, the particle tracking technique demands a very high spatial resolution with a correspondingly very small measurement area in order to obtain precise velocity and granular temperature measurements.

In this chapter a new non-invasive technique to measure the granular temperature profiles in dense fluidised beds is developed based on Particle Image Velocimetry (PIV). In the recent past, PIV has already been used to measure the whole-field instantaneous particle velocity field in a fluidised bed (Bokkers et al., 2004a). In this chapter this method is extended to measure the granular temperature field directly.
Firstly, the theoretical background of PIV is shortly presented and the relation of the displacement peak and the granular temperature is explained. Subsequently, the new technique is validated with computer-generated (synthetic) images. Finally, the measured granular temperature profiles are presented and discussed for a single bubble injected into a mono-disperse fluidised bed at incipient fluidisation conditions and for a freely bubbling fluidised bed.

2.2 Theoretical background

The PIV method was originally developed for flow measurement in single phase, gas or liquid, systems. Tracer particles are injected into the flow and the trajectories of these particles are recorded with a high-speed digital video camera. Two consecutive images are cross-correlated (see Figure 2.1) and one peak ($< R_D(s) >$) stands out from the background noise. The location of this peak relative to the centre is equal to the (ensemble) average movement of the particles between the two images. Of course not the entire image is correlated, but rather the image is divided into small so-called interrogation areas, which makes it possible to capture the whole flow-field with sufficient resolution.

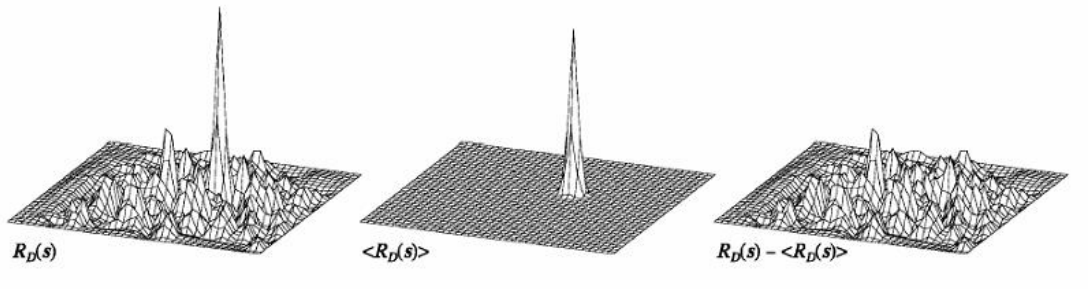

Figure 2.1: Example of the cross-correlation of PIV images; left: total correlation; middle: average velocity peak; right: random correlation (taken from Westerweel (1997)).

2.2.1 Cross-correlation of digital images

The spatial cross-covariance of two images can be separated in an ensemble mean value $\langle C(x,y)\rangle$ and a random fluctuating term $C'(x,y)$:

$$C(x,y) = \langle C(x,y)\rangle + C'(x,y) = R_D(x,y) + R_C(x,y) + R_F(x,y) + C'(x,y) \tag{2.1}$$

In this equation R_D is the displacement correlation peak, R_C is the background correlation and R_F is the correlation between the mean and fluctuating image intensities. These last two terms can be eliminated by subtracting the mean image intensity from the intensity of the two images. The displacement correlation peak, which gives the mean movement of the ensemble of particles, can be calculated via:

$$R_D(x,y) = N_I \cdot F_I(x,y) \cdot F_O \cdot F_T(x,y) \cdot \rho(x,y) \tag{2.2}$$

in which N_I represents the total number of particles in the interrogation area. $F_I(x,y)$ indicates the loss of correlation due to in-plane movement of particles out of the interrogation area. Fast particles are more likely to escape from the field-of-view (see Figure 2.2). F_O represents the loss of correlation due to particles entering or leaving the interrogation area perpendicular to the plane. It is assumed that F_O is not a function of the position, since the time between two images (δt) is typically very small and a pseudo-2D fluidised bed is used. $F_T(x,y)$ is the shape of the peak due to the particle image properties and $\rho(x,y)$ is a function that represents the shape of the peak due to the velocity distribution. According to Westerweel (1997) the spatial cross-covariance

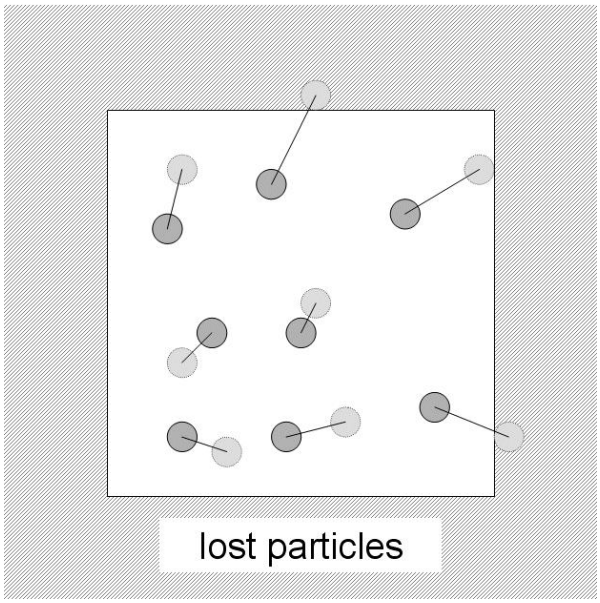

Figure 2.2: Illustration of the in-plane loss of particles: particles with a higher velocity are more likely to have moved out of the interrogation area in the second image.

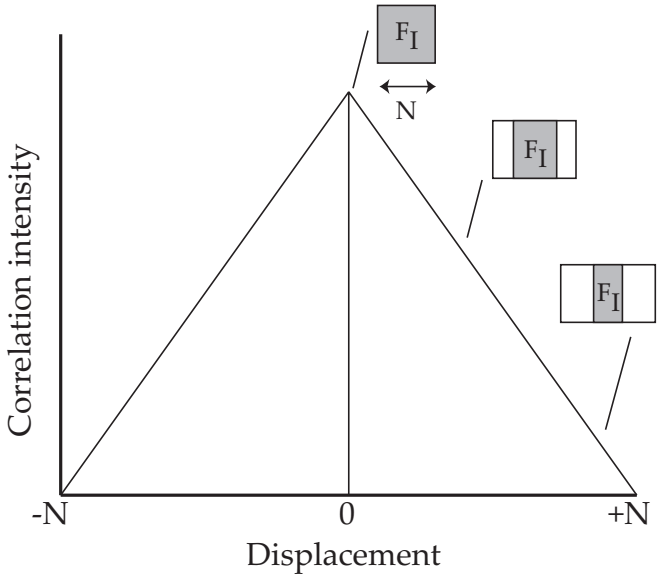

Figure 2.3: Illustration of the velocity bias: when the displacement in the correlation plane increases, the area that can be correlated decreases. This is especially important for very wide peaks.

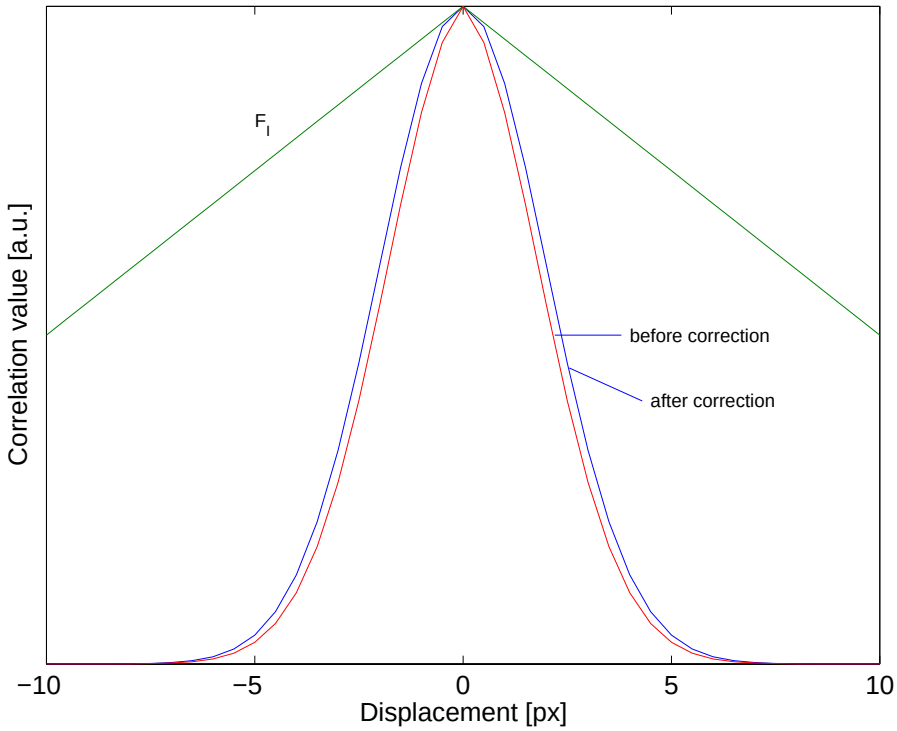

Figure 2.4: Illustration of the velocity bias correction: a linear correction is applied to the correlation which gives the 'true' cross-covariance.

for digital images can be calculated by equation 2.3. Matrices I' and I'' (both $N_x \times N_y$ pixels), contain the pixel intensities of the two frames that are correlated. $\langle I \rangle$ represents the mean image intensity, used to eliminate the terms R_C and R_F from the correlation.

$$\hat{R}[x,y] = \frac{1}{N_x N_y} \sum_{i=1}^{N_x} \sum_{j=1}^{N_y} \left(I'[i,j] - \langle I \rangle\right) \left(I''[i+x, j+y] - \langle I \rangle\right) \tag{2.3}$$

Note that the square bracket notation refers to the discrete form of the equation. At higher displacements (x,y) the image area that is effectively correlated decreases (see Figure 2.3). This means that the effective particle number decreases and the correlation value at that displacement is lower than it should be. Because of this effect the velocity distribution is biased towards lower velocities, hence the name velocity bias. It is important to realise that this effect influences the width of a Gaussian correlation peak even when there is no movement (i.e. autocorrelation). To correct for this, $\hat{R}[x,y]$ is divided by the estimated in-plane particle loss F_I to obtain the 'true' cross-covariance $R[x,y]$ (equations 2.4 and 2.5). This important correction is graphically illustrated in

Figure 2.4.

$$R[x,y] = \frac{\hat{R}[x,y]}{F_I[x,y]} \tag{2.4}$$

$$F_I[x,y] = \left(1 - \frac{(x-x_c)}{N_x}\right)\left(1 - \frac{(y-y_c)}{N_y}\right) \tag{2.5}$$

2.2.2 Relation between the displacement peak and the granular temperature

After the cross-correlation, a Gaussian curve is fitted to the displacement peak (equation 2.6). There are several reasons to select a Gaussian shape: First of all, the in-plane light intensity distribution (z-direction) is assumed to be Gaussian. Secondly, the intensity distribution of a particle (perpendicular to the light plane) is approximately Gaussian. Finally, the particles typically have an approximately Gaussian velocity distribution.

$$R_D(x,y) \sim e^{-\frac{(x-x_c)^2}{2\sigma_{cc,x}^2}} \cdot e^{-\frac{(y-y_c)^2}{2\sigma_{cc,y}^2}} \tag{2.6}$$

Note that x_c and y_c represent the average displacement in the x- and y-direction respectively. The width of the displacement peak can be expressed in the standard deviations $\sigma_{cc,x}$ and $\sigma_{cc,y}$, which can be determined from the fitted Gaussian curve. First of all, the width of the displacement peak is related to the particle diameter, because larger particles give rise to a higher correlation. Secondly, the width is related to the velocity profile, from which the granular temperature can be calculated.
In order to determine the granular temperature from the width of the displacement peak the contribution of the particle size F_T needs to be eliminated. This standard deviation in the average displacement peak caused by the particle size can be determined via autocorrelation of the images:

$$F_T[x,y] \sim e^{-\frac{(x-x_c)^2}{2\sigma_{ac,x}^2}} \cdot e^{-\frac{(y-y_c)^2}{2\sigma_{ac,y}^2}} \tag{2.7}$$

It is important to note that the correlation of a Gaussian particle image gives a Gaussian curve that is $\sqrt{2}$ times as wide:

$$F_T[x,y] \sim e^{-\frac{(x-x_c)^2}{4\sigma_p^2}} \cdot e^{-\frac{(y-y_c)^2}{4\sigma_p^2}} \tag{2.8}$$

where σ_p is the particle image standard deviation. Westerweel (2000) also gives a formula to correlate F_T with the particle image diameter d_t:

$$F_T[x,y] = \frac{4}{\pi d_t^2} \cdot e^{-4\frac{(x-x_c)^2}{d_t^2}} \cdot e^{-4\frac{(y-y_c)^2}{d_t^2}} \tag{2.9}$$

Combination of equations 2.7, 2.8 and 2.9 relates the particle image diameter d_t to the different standard deviations:

$$d_t = 4\sigma_p = 2\sqrt{2}\sigma_{ac} \tag{2.10}$$

Since the velocity profile is also assumed to be Gaussian:

$$\rho[x,y] \propto \frac{1}{\sqrt{2\pi}\sigma_{d,x}} \cdot e^{-\frac{(x-x_c)^2}{2\sigma_{d,x}^2}} \cdot \frac{1}{\sqrt{2\pi}\sigma_{d,y}} e^{-\frac{(y-y_c)^2}{2\sigma_{d,y}^2}} \tag{2.11}$$

equations 2.6, 2.7 and 2.11 can be combined yielding the following relations for the displacement standard deviation:

$$\sigma_{d,x}^2 = \sigma_{cc,x}^2 - \sigma_{ac,x}^2 \tag{2.12}$$

$$\sigma_{d,y}^2 = \sigma_{cc,y}^2 - \sigma_{ac,y}^2 \tag{2.13}$$

The definition of the granular temperature, rewritten in terms of displacement is given by equations 2.14 and 2.15.

$$\theta_x = m_n\langle(v_x - \langle v_x\rangle)^2\rangle = \frac{m_n}{\Delta t^2}\langle(x-x_c)^2\rangle = \frac{m_n}{\Delta t^2}\int_{-\infty}^{\infty} f_n\,(x-x_c)^2\,dx \tag{2.14}$$

$$\theta_y = m_n\langle\big(v_y - \langle v_y\rangle\big)^2\rangle = \frac{m_n}{\Delta t^2}\langle(y-y_c)^2\rangle = \frac{m_n}{\Delta t^2}\int_{-\infty}^{\infty} f_n\,(y-y_c)^2\,dy \tag{2.15}$$

Substitution of the Gaussian velocity profile (equation 2.9) relates the granular temperature to the standard deviation of the displacement peak (equation 2.16 and 2.17).

$$\theta_x = \frac{m_n}{M\Delta t^2}\sigma_{d,x}^2 \tag{2.16}$$

$$\theta_y = \frac{m_n}{M\Delta t^2}\sigma_{d,y}^2 \tag{2.17}$$

where M is the camera magnification. Finally, the overall granular temperature is averaged in 2 dimensions assuming an isotropic velocity distribution function.

$$\theta = \frac{\theta_x + \theta_y}{2} \tag{2.18}$$

2.2.3 Interpolation of the displacement peak

In order to calculate the standard deviation of the correlation peak, the correlation peak is fitted to a Gaussian curve. PIV-software commonly uses a 3-point Gaussian fit to find the displacement with sub-pixel accuracy:

$$\hat{\epsilon}_x = x_c - x_m = \frac{C - A}{2(2B - A - C)} \qquad [-0.5..0.5] \tag{2.19}$$

$$\hat{\epsilon}_y = y_c - y_m = \frac{E - D}{2(2B - D - E)} \qquad [-0.5..0.5] \tag{2.20}$$

$$A = \ln R[x_m - 1, y_m] \tag{2.21}$$

$$B = \ln R[x_m, y_m] \tag{2.22}$$

$$C = \ln R[x_m + 1, y_m] \tag{2.23}$$

$$D = \ln R[x_m, y_m - 1] \tag{2.24}$$

$$E = \ln R[x_m, y_m + 1] \tag{2.25}$$

Here x_m and y_m represent the integer location of the peak. The standard deviation of the peak in the x- and y-direction can be calculated via:

$$\sigma_x^2 = \frac{1}{2B - A - C} \tag{2.26}$$

$$\sigma_y^2 = \frac{1}{2B - D - E} \tag{2.27}$$

When using PIV with small (tracer) particles, the correlation peak will probably be in the order of three pixels wide. However, with the particles that are used in gas-solid fluidised beds, it can easily be 10 pixels wide. In this case, the interpolation should be extended to include more than 3 points to enhance the attainable measurement accuracy of the granular temperature.

First, the points which are used for the interpolation have to be selected. Only points higher than 50% of the main peak height are included, to exclude random correlation and secondary peaks. This is especially important for measurements in dense granular systems. Then, the natural logarithm of the selected data is used, reducing the

Gaussian peak to a parabola (equation 2.28).

$$\ln R[x, y_m] = \ln(c_0) - \frac{(x - x_c)^2}{2\sigma_x^2} = c_1 + c_2 x + c_3 x^2 \tag{2.28}$$

$$c_1 = \ln(c_0) - \frac{x_c^2}{2\sigma - x^2} \qquad c_2 = \frac{x_c}{\sigma_x^2} \qquad c_3 = -\frac{1}{2\sigma_x^2}$$

Finally, equation 2.28 can be interpolated using a least square approximation (Press and Vetterling, 1992). The solution to this problem can readily be calculated using equation 2.29.

$$A^T A \cdot c = A^T \cdot b \tag{2.29}$$

$$A = \begin{bmatrix} 1 & x_1 & x_1^2 \\ .. & .. & .. \\ 1 & x_n & x_n^2 \end{bmatrix} \quad A^T = \begin{bmatrix} 1 & .. & 1 \\ x_1 & .. & x_n \\ x_1^2 & .. & x_n^2 \end{bmatrix} \quad b = \begin{bmatrix} R'(x_1) \\ .. \\ R'(x_n) \end{bmatrix} \quad c = \begin{bmatrix} c_1 \\ c_2 \\ c_3 \end{bmatrix}$$

Once the constants c_1, c_2 and c_3 have been computed, the average displacement and the standard deviation can be easily calculated.

2.3 Testing of the proposed method with computer-generated (synthetic) images

The original PIV-software by Westerweel (1993) was modified to calculate and output the standard deviation of the correlation peak, as described in the previous paragraph. A least square approximation was added, so that the large displacement peaks obtained for granular systems can be accurately interpolated. The first step before using this software to analyse pictures of a fluidised bed, is to test and validate the program with artificially created images with pre-selected average velocities and granular temperatures. With these tests the influence of different parameters, such as the particle diameter and the particle number density, is investigated.

2.3.1 Image generation software

For testing purposes an image generation program was written. With this program pairs of synthetic images can be made, where the particle size and number density can

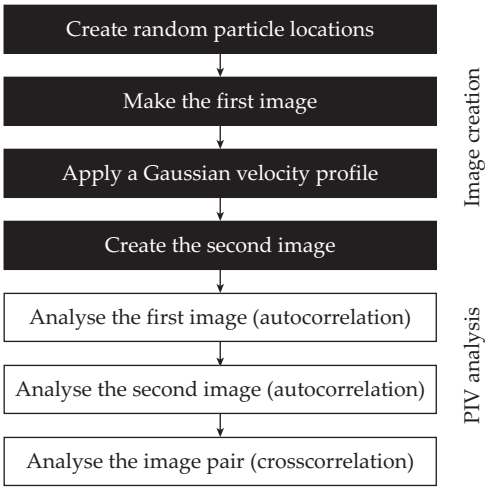

Figure 2.5: Order of operation when testing the PIV software.

be pre-specified. Using the positions of the particles on the first image, the ensemble of particles can be moved assuming a Gaussian velocity distribution function and a second image can be created (see Figure 2.5). In the first image the particles are placed at completely random positions, while assuring that the particles do not overlap. This can be accomplished by introducing the particles, each at a time, check for overlap and try a new position if the particle overlaps with other particles. This method will work for systems that are not too densely packed.

2.3.2 Uniform particle velocity

First of all the new least-squares interpolation method was tested using a uniform velocity in the x- and y-direction. The different simulated cases are given in Table 2.1.

Table 2.1: Test settings for the displacement error.

Variable	Tested range	Step size
Particle image diameter	2-20 px	2 px
Particle number density	5-75	5
x-displacement	0-0.5 px	0.05 px
y-displacement	0-0.5 px	0.05 px

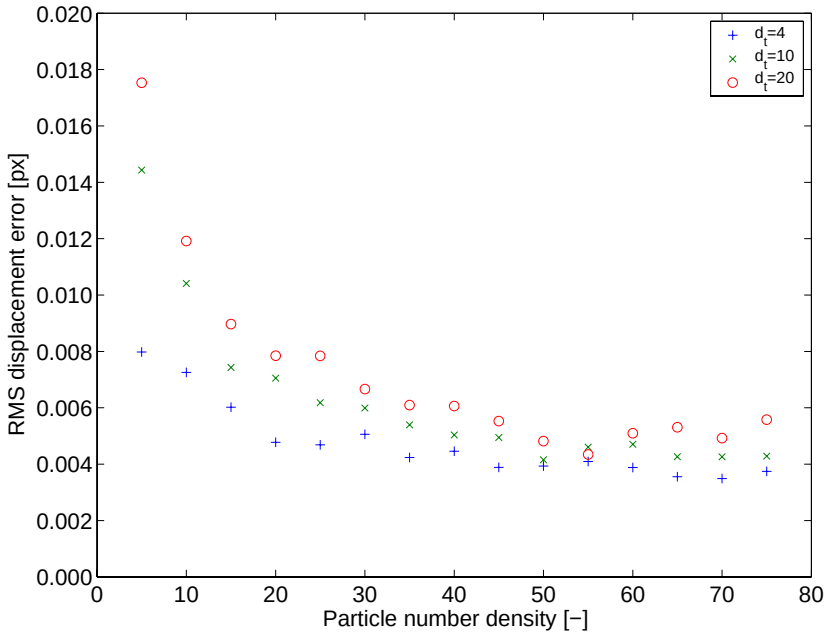

Figure 2.6: Influence of the particle number density on the RMS displacement error for a uniform particle displacement.

In Figure 2.6 the results for different particle number densities are compared for three different particle sizes using the new least-squares method. It can be seen that the displacement error decreases asymptotically with higher number densities. At lower particle number densities, the velocity is systematically overestimated, because the velocity bias correction only works properly for a statistically sound number of particles. At higher particle number densities the RMS displacement error is hardly dependent on the particle number density, as expected from theory because of the uniform displacement (Westerweel, 1997). The results for the RMS displacement error as a function of different particle sizes at a number density of 50 particles are given in Figure 2.7. A comparison between both interpolation methods shows that the least squares method produces much better results for large particle images. The minimum number of points for the least-squares method is three points, for which it reduces to an exact three-point fit. This is confirmed by the results, because the error is the same when using particles of 2 pixels wide. Also the autocorrelation has been analysed for different particle velocities. Figure 2.8 shows the measured standard deviation as a function of

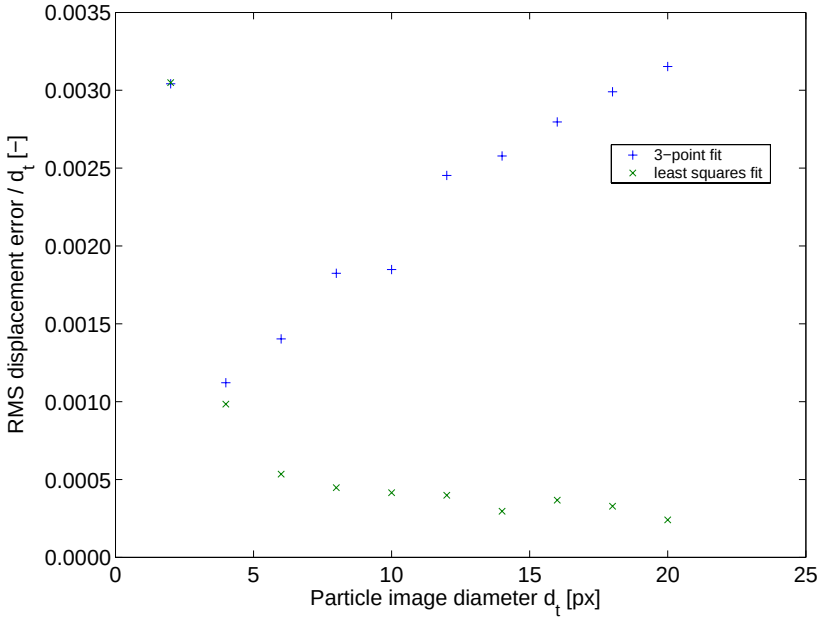

Figure 2.7: Influence of the particle image diameter on the RMS displacement error, using perfectly Gaussian test images and a uniform particle velocity.

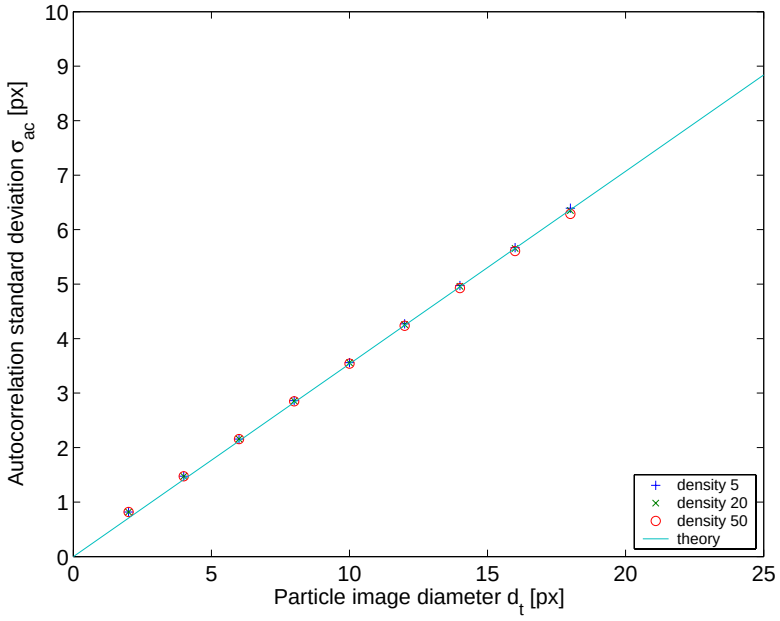

Figure 2.8: Measured particle standard deviation versus theoretical value for different particle number densities.

the particle image size. For each combination of particle number density and particle size, the x- and y-velocity are varied as indicated in Table 2.1. It can be concluded that the measurements follow the theoretical relation very well.

2.3.3 Gaussian velocity profile

As a second test a Gaussian velocity profile was applied to the test particles with a specified standard deviation in the x- and y-direction. This way, it can be verified whether the software reproduces the granular temperature as specified in the generation of the test images. The relative error in the measured granular temperature for various combinations of standard deviations in the x- and y-directions is shown in Figure 2.9(a) for different particle numbers. It is shown that the relative error made in the measured granular temperature is not a function of the number of particles used in the test images. It should be noted that the particle velocity distribution in the generated test images was always perfectly Gaussian. The bottom right corner in Figure 2.9(a) is empty, since only a limited number of standard deviations was tested.
The points in the bottom left corner of the figure represent the situation of a low standard deviation in the x-direction and a higher value for the y-direction or vice versa, showing a small relative error in the granular temperature measurement. However, in the situation that both the standard deviation in the x direction and in the y direction are high, the relative error increases, as can be seen in the upper right corner of Figure 2.9(a). From this can be concluded that the granular temperature can be measured with a small relative error for systems where the particles move mainly in one direction. This is also demonstrated in Figure 2.9(b).
The maximum granular temperature encountered in the set-up used in this work resembles a standard deviation of 20 px^2. From Figure 2.9(a) it can be concluded that for this value of the squared standard deviation the maximum relative error is approximately 50%. However, in general this error will be smaller, since in the fluidised bed experiments investigated in this work most of the particles will move locally in one main flow direction.

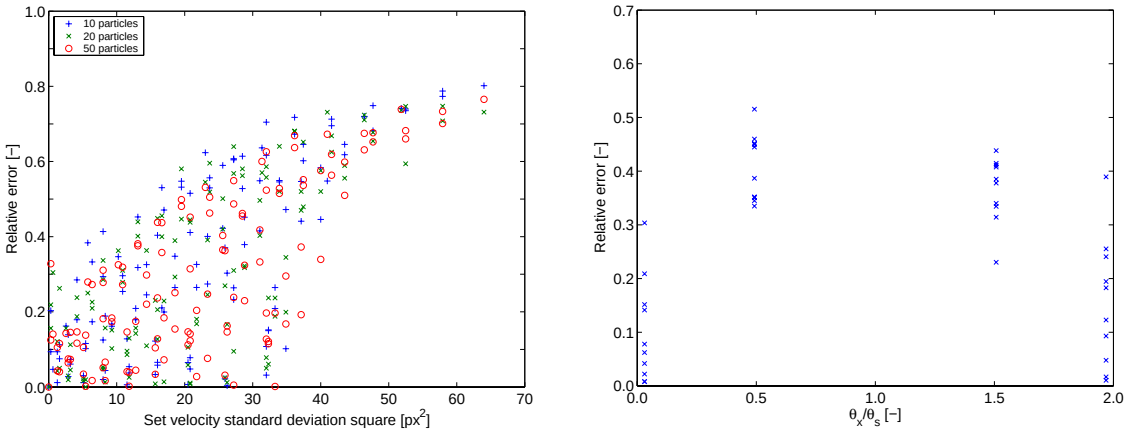

Figure 2.9: Relative error in the granular temperature measurement from the computer-generated images as a function of the number of particles.

2.4 Experimental set-up and optimisation of the method

2.4.1 Fluidised bed set-up

The developed method has been applied to measure the local granular temperature in a fluidised bed. A schematic drawing of the experimental set-up is given in Figure 2.10. Two different fluidised beds have been used. The first bed has internal dimensions of 15 cm wide, 1.5 cm deep and about 1 m high and the other bed is 30 cm wide, 1.5 cm deep and about 1 m high. The front plate of the small bed is made of glass and the back plate of polycarbonate (Lexan). The large bed has a front and a back plate made of glass. All the side walls are made of aluminium and the bottom consists of a sintered porous plate. In both beds gas can be injected into the fluidised bed with a central jet. The jet in the small bed is 1.0 cm wide by 1.5 cm deep and the jet in the larger bed is 1.5 x 1.5 cm. The remaining part of the bottom surface delivers the gas for the background fluidisation. In all the experiments air was used to fluidise spherical glass beads of 1.5 or 2.5 mm diameter.

Four different mass-flow controllers were used, which made it possible to perform single bubble experiments, i.e. an experiment where a single bubble is injected via the jet into a bed at minimum fluidisation conditions, as well as freely bubbling experiments. For a single bubble experiment the background velocity was set to min-

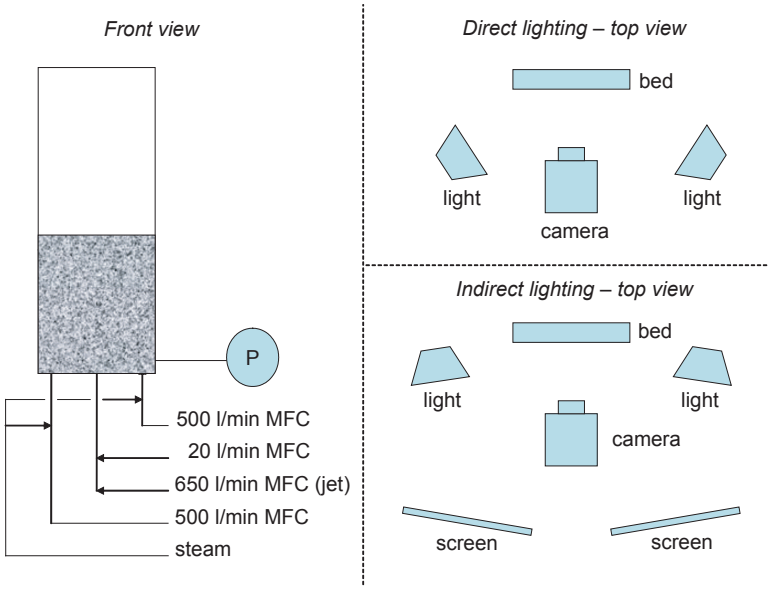

Figure 2.10: Experimental set-up. Left: the arrangement of the mass flow controllers; Right: the position of the lights and camera.

imum fluidisation using the two 500 l/min and the 20 l/min mass-flow controllers. The bubble was then generated by a jet, which was controlled by a 650 l/min mass-flow controller. Steam was added to get a humidity of about 60% to avoid problems with static electricity.

Before the measurements were carried out, the mass-flow controllers were calibrated and for each particle size the minimum fluidisation velocity was measured (Table 2.2). This was done by measuring and plotting the pressure at the bottom of the bed as

Table 2.2: Measured and theoretical minimum fluidisation velocities.

Particle size (mm)	U_{mf} theory (m/s)	U_{mf} measured (m/s)
1.5	0.83	0.87
2.5	1.23	1.31

a function of the superficial gas velocity. The velocity where the slope of the curve changes is the minimum fluidisation velocity. Compared to the theoretical values (Kunii and Levenspiel, 1991) the measured values are slightly higher.

Table 2.3: Digital camera and recording settings.

Setting	Small set-up	Large set-up
Effective resolution [px^2]	923 x 664	984 x 1109
Pixel clockrate [MHz]	66	66
Read-out time [ms]	1.836	1.955
Exposure time [ms]	0.500	0.500
Delay [ms]	0.000	0.000
Frame rate [Hz]	545	511

2.4.2 Image recording settings

The camera (LaVision ImagerPro HS, with 2GB internal memory) makes non-interlaced pictures of 1280 (h) by 1024 (v) pixels at a frame rate of 625 Hz. To reduce noise, the pixel clockrate was decreased. The area of the sensor was chosen such, that only the fluidised bed was recorded, enabling longer recording times and higher frame rates. The exposure time was set at 0.5 ms, which effectively eliminates motion blur, without increasing the noise level. All the settings for the camera are summarised in Table 2.3. The illumination of the particles in the fluidised bed is very important for the quality of the correlation. Direct lighting has the advantage of a higher contrast and therefore the particles can be differentiated more easily. This improves the separation of the correlation peak from the random correlation. Indirect lighting has been tried, which resulted in a more pronounced Gaussian peak of the particle intensity distribution, but it greatly reduces the contrast (Figure 2.11). Hence, direct lighting was used in all the experiments.

2.4.3 PIV settings

For the two fluidised beds (15 cm and 30 cm wide) and the two particle sizes, the size of the interrogation areas has to be determined. This has a profound impact on the range of granular temperatures that can be detected. In general, with larger interrogation areas larger ranges in granular temperatures can be measured, since there are

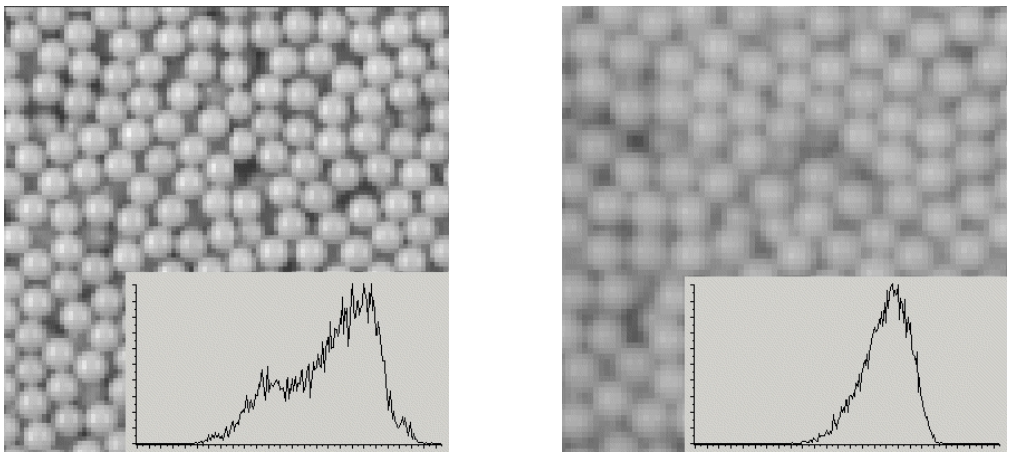

Figure 2.11: Example of direct (left) and indirect (right) lighting of the particles and the corresponding intensity distribution.

more particles in each interrogation area. However, too large interrogation areas may deteriorate the Gaussian velocity distribution, so an optimum has to be found.
In Table 2.4 the interrogation area settings are given for the different particle sizes and fluidised beds used in this investigation. Tests showed that the accuracy of the granular temperature measured is dominated by the quality of the velocity distribution. Therefore, a particle number density of about 100 was chosen, to assure sufficient accuracy also in less dense areas of the fluidised bed.

Table 2.4: Digital camera and recording settings.

Fluid bed width [mm]/[px]	Particle diameter [mm]/[px]	Interrogation area size [px^2]
150/664	1.5/6.6	72 x 72
150/664	2.5/11.1	120 x 120
300/1109	1.5/5.5	60 x 60
300/1109	2.5/9.2	90 x 90

2.4.4 Autocorrelation tests with real particles

First, the correlation of a single particle is checked (Figure 2.12). It can be seen that the shape of the correlation is nicely Gaussian and it is surrounded by a correlation of zero

value.

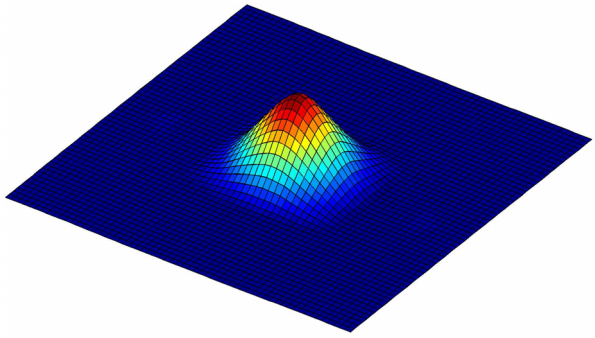

Figure 2.12: Correlation for a single real particle.

The second step is to correlate a dense region of particles (Figure 2.13). The shape of the correlation peak is again nicely Gaussian, however the peak is much narrower than for the single particle. This is caused by the normalization of the mean image intensity in the correlation (equation 2.3). For the single particle the mean image intensity is almost zero (black), while for the dense system it is approximately the mean intensity of the particle itself (grey). This effectively reduces the peak width and height, but fortunately does not impair the shape of the correlation.

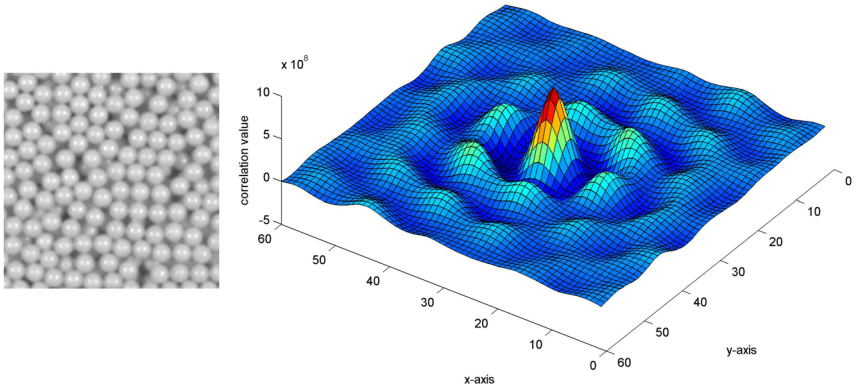

Figure 2.13: Picture of a dense particle region (left) and its correlation (right).

When particles are arranged in a structured packing, the secondary correlation peaks may become dominant (Figure 2.14, left). This is caused by the periodic nature of the Fast Fourier Transformation (FFT) used to calculate the correlation. In principle the exact correlation can be calculated according to the definition of the cross-correlation,

but this is very slow in comparison. To fix the periodic issues associated with a FFT zero-padding is used (Westerweel, 1993), which places a black border with a width of 50% of the interrogation area around the picture. It is important to do this after normalising the intensity, to avoid that the black border will give a correlation of itself. The result is given in Figure 2.14 (right) and it can be observed that the detectability of the main peak has improved significantly.

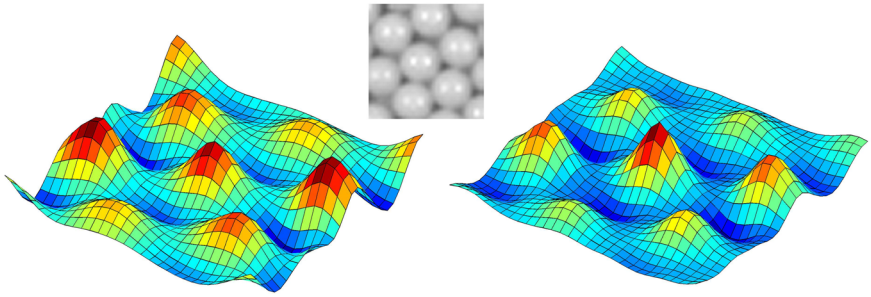

Figure 2.14: Correlation of a structured particle packing without (left) and with zero-padding (right).

Another problem arises when we look at the interface of the particles to an empty region, for instance at the top of the fluidised bed or at the bubble interface. Because the image is normalised using the average image intensity, the black background will correlate with itself just as strongly as the particles. The resulting correlation therefore has a wide ridge on top of which the desired Gaussian peak is located (Figure 2.15, middle). Apparently a homogeneous particle distribution is required for the image normalisation to work properly. However, this is often not the case when granular systems are

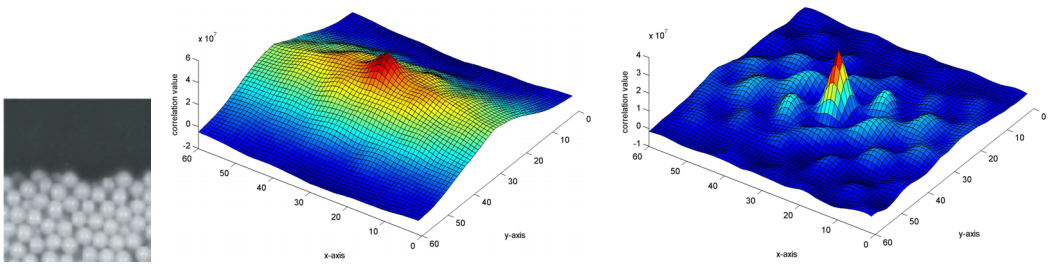

Figure 2.15: Image (left) and the correlation of an inhomogeneous interrogation area before correction (middle) and after correction (right).

concerned. Therefore a modification was devised to cancel the correlation of the background with itself. First of all, the background intensity is subtracted from the image, so that all of the background is really black. Secondly, the pixels with an intensity larger than zero are not normalised in this procedure. They give rise to a correlation of zero, effectively acting as zero-padding and not interfering with the correlation. The improvement of the correlation peak for the same inhomogeneous region is clear from Figure 2.15 (right).

2.4.5 Cross-correlation tests with real particles

First of all some experiments were done to test the performance of the extended PIV method with real glass particles at different locations in the small fluidised bed (Figure 2.16). From these results it can be seen that all the cross-correlation peaks are indeed Gaussian, as assumed, even for these non-ideal particles. It can also be seen that the extended interpolation routine based on more than three points is an important improvement.

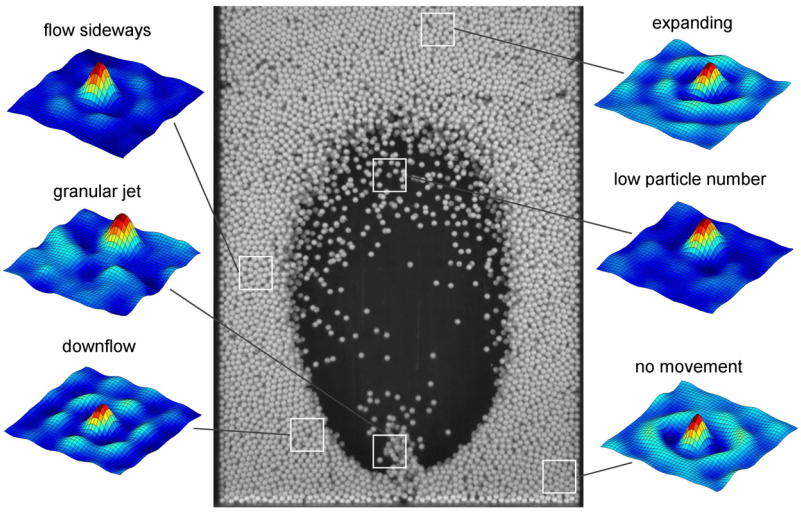

Figure 2.16: Image cross-correlation at different locations in a single bubble experiment, using 2.5 mm particles in the 15 cm fluidised bed set-up.

Now that the developed method has been verified and optimised, it is used to measure the particle velocity field and the granular temperature profiles inside fluidised beds.

Firstly, the idealised case where a single bubble is injected into a fluidised bed at incipient fluidisation conditions is studied. In section 2.6 a freely bubbling bed is studied, where the bubbles are formed in situ.

2.5 Single bubble experiments

The single bubble experiments have been carried out in a small fluidised bed (15 cm wide) and a larger fluidised bed (30 cm wide). It was found that the shape of the single bubble in the small fluidised bed is influenced by the side walls. Therefore, also experiments in a larger fluidised bed have been performed to reduce the disturbance of the side walls. Both fluidised beds were filled with glass beads with different diameters to study the effect of the particle diameter on the granular temperature profiles. The settings for the experimental set-up are listed in Table 2.5.
In Figures 2.17 and 2.18 the snapshots are shown of the single bubble injected into the small fluidised bed at incipient fluidisation conditions filled with 2.5 mm particles. From the first snapshot, showing the bed without fluidisation, a small uniform granular temperature in the order of $10^{-8} - 10^{-9}$kg m^2/s^2 was found. This background (noise) granular temperature should have been zero, since the particles do not move at all. This background granular temperature is caused by random correlation and the 50 Hz frequency of the lights. In the subsequent snapshots, as the bubble rises in the fluidised bed, the highest granular temperatures (orders of magnitude higher than the background granular temperature) are found in the vicinity of the bubble. In the second snapshot the particles above the injected bubble expand uniformly as can be seen in the particle velocity profile and results therefore in a low granular temperature. Also, when the bubble has passed, the granular temperature immediately drops down to the initial granular temperature, as is shown in the last snapshot.
In Figures 2.19 and 2.20 the results are depicted of the same experiment, but now with 1.5 mm particles. Because of the smaller diameter of the particles the size of the interrogation area could be decreased, resulting in a higher resolution of the granular temperature field. The background granular temperature is the same as for the 2.5 mm

Table 2.5: Experimental settings for the single bubble experiments.

Bed:	*small*	*large*
width	0.15 m	0.30 m
depth	0.015 m	0.015 m
height	1.0 m	1.0 m
initial bed height	0.18 m	0.22 m
front plate	glass	glass
back plate	polycarbonate (″Lexan″)	glass
left and right wall	aluminium	aluminium
porous plate average pore size	10 μm	10 μm
porous plate thickness	1.5 mm	1.5 mm
jet width	0.01 m	0.015 m
Particle properties:	*small*	*large*
material	glass	glass
diameter	1.5 mm	2.5 mm
density	2526 kg/m^3	2526 kg/m^3
minimum fluidisation velocity (experimentally)	0.87 m/s	1.31 m/s
collision parameters:	*particle-particle collisions*	*particle-wall collisions*
normal restitution	0.97$\pm$0.01	0.97$\pm$0.01
friction	0.10$\pm$0.01	0.09$\pm$0.01
tangential restitution	0.33$\pm$0.05	0.33$\pm$0.05

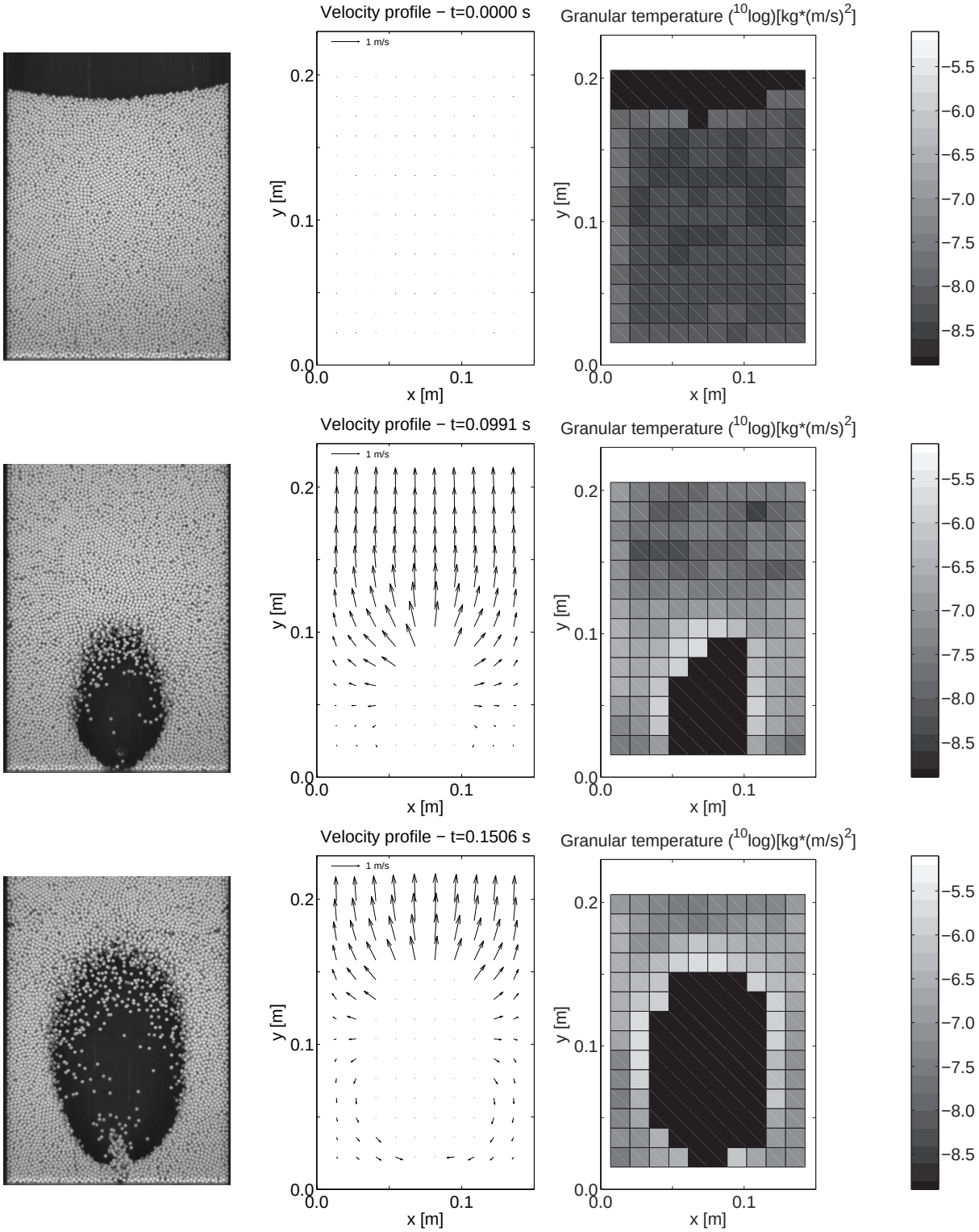

Figure 2.17: Single bubble experiment in the 15 cm set-up using 2.5 mm glass beads (for color figures see Figure A.1).

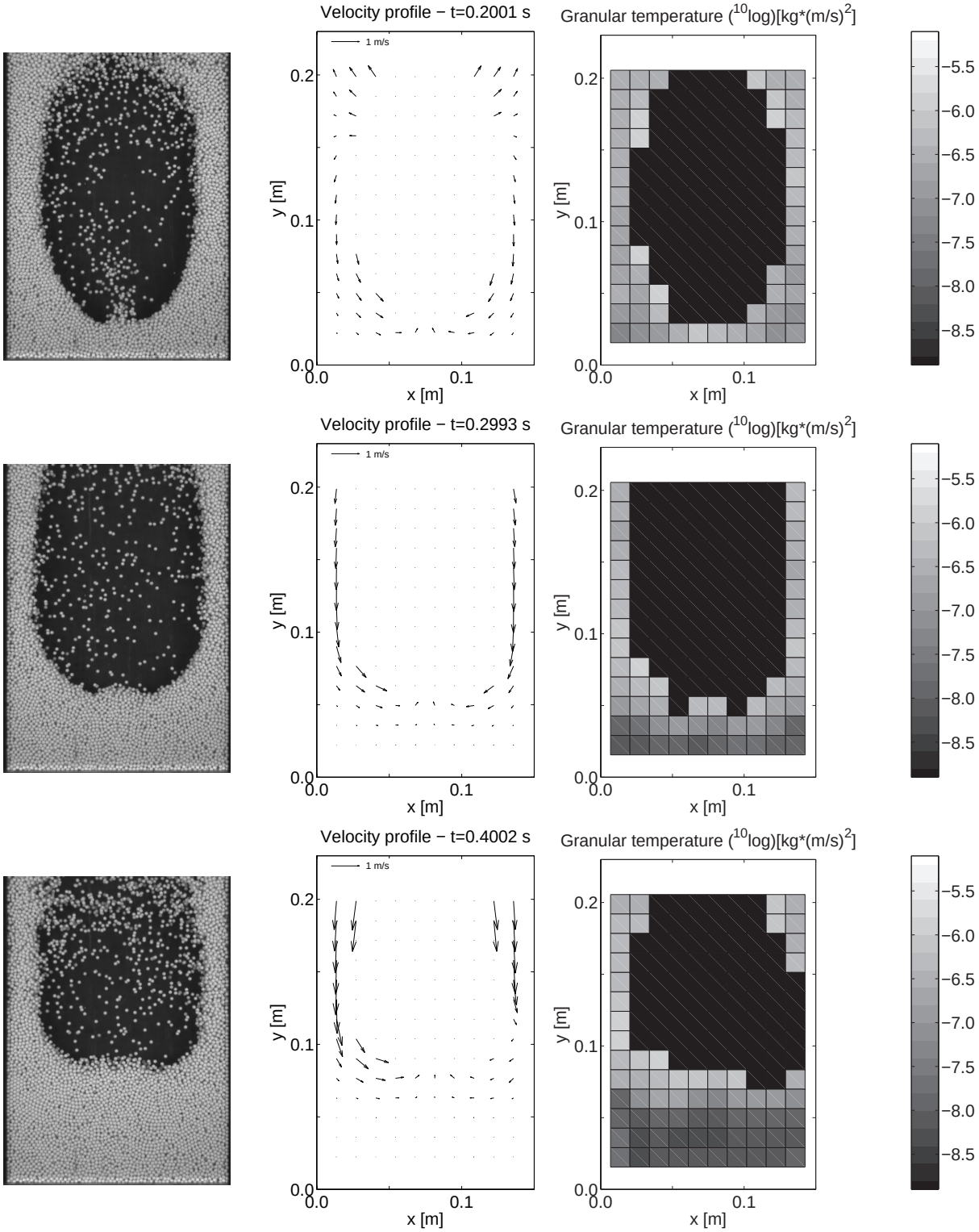

Figure 2.18: Single bubble experiment in the 15 cm set-up using 2.5 mm glass beads (for color figures see Figure A.2).

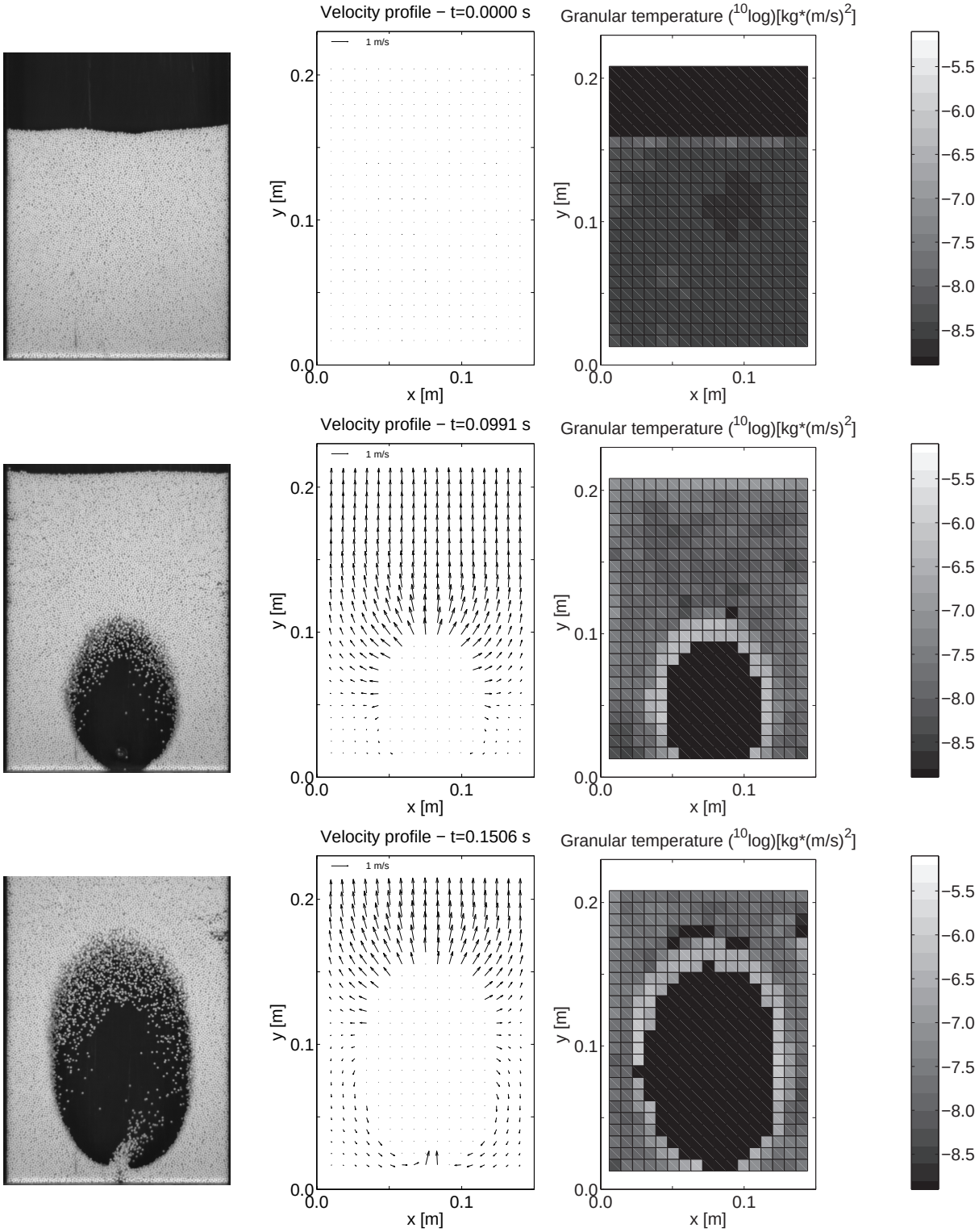

Figure 2.19: Single bubble experiment in the 15 cm set-up using 1.5 mm glass beads (for color figures see Figure A.3).

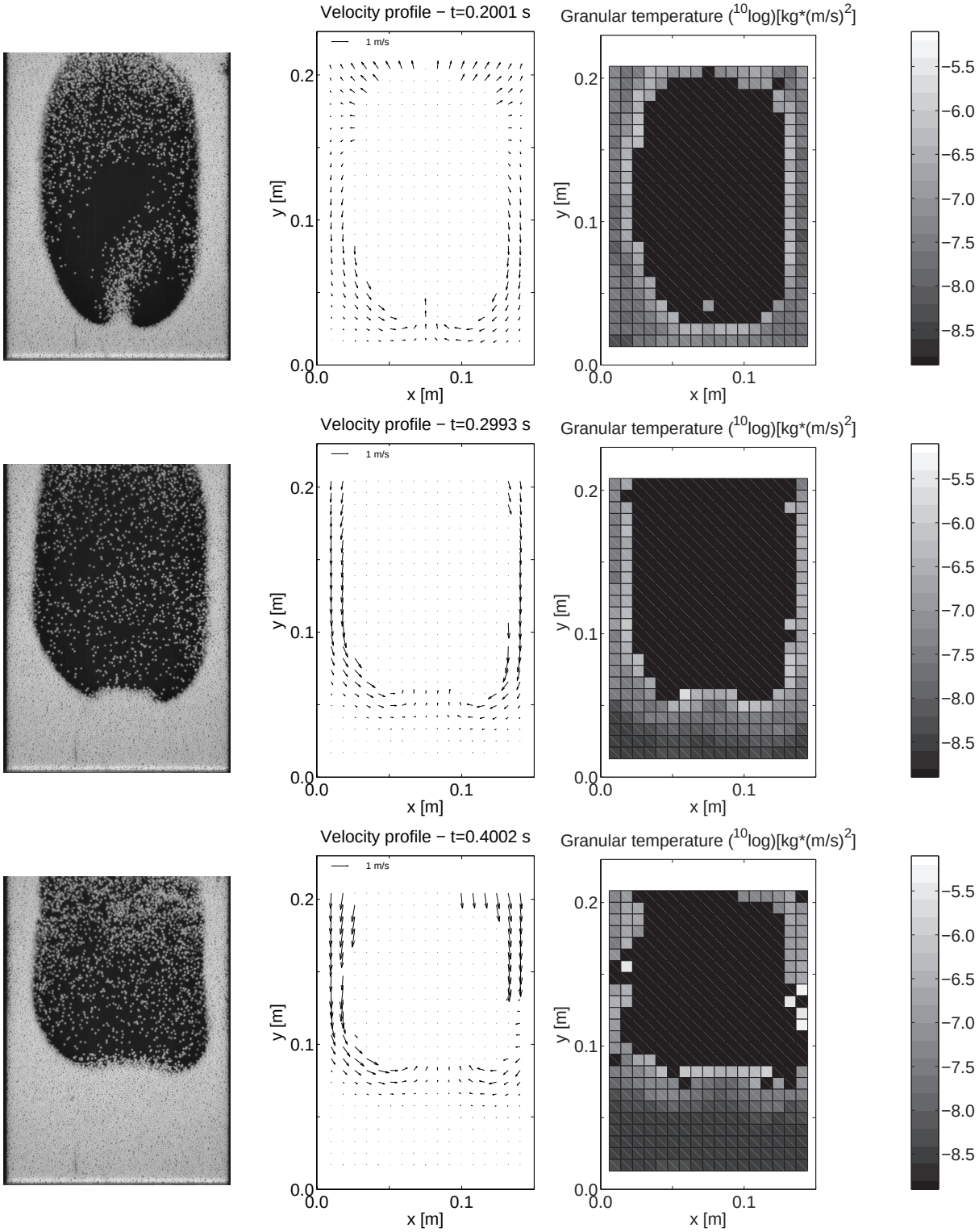

Figure 2.20: Single bubble experiment in the 15 cm set-up using 1.5 mm glass beads (for color figures see Figure A.4).

particles. Again it is clearly demonstrated that the highest granular temperatures are found very close to the bubble. When the bubble is fully injected into the fluidised bed and rises to the top an even higher granular temperature is found in the wake of the bubble as is demonstrated in the last two snapshots. Compared to the experiment with 2.5 mm particles the granular temperature is somewhat lower because of the lower mass of the 1.5 mm particles.
The bubble injected in the fluidised bed of 30 cm wide has a rounder shape, since the bubble is not influenced by the presence of side walls (see Figures 2.21-2.24). Like in the small fluidised bed, the highest granular temperatures are found in a small area around the bubble. The level of the granular temperature in the vicinity of the bubble is higher for the 2.5 mm particles. Furthermore, the area around the bubble with increased granular temperature is much larger.

2.6 Freely bubbling experiment

To investigate whether the method is capable of analysing systems where there is more vigorous mixing, a freely bubbling experiment was conducted for 1.5 mm particles in the small fluidised bed with a superficial gas velocity of 1.5 m/s. The results are shown in Figures 2.25 and 2.26.
From the freely bubbling experiments it can be discerned that, like in the single bubble experiments, the highest granular temperatures are found in the vicinity of the bubbles, even around the very small bubbles. The level of the granular temperature around the bubbles is quite comparable with the levels encountered in the single bubble experiment with 1.5 mm particles. The larger bubbles in the freely bubbling fluidised bed show an even higher granular temperature in the wake. The granular temperature gradient from the bubble surface to the dense phase is again quite high.

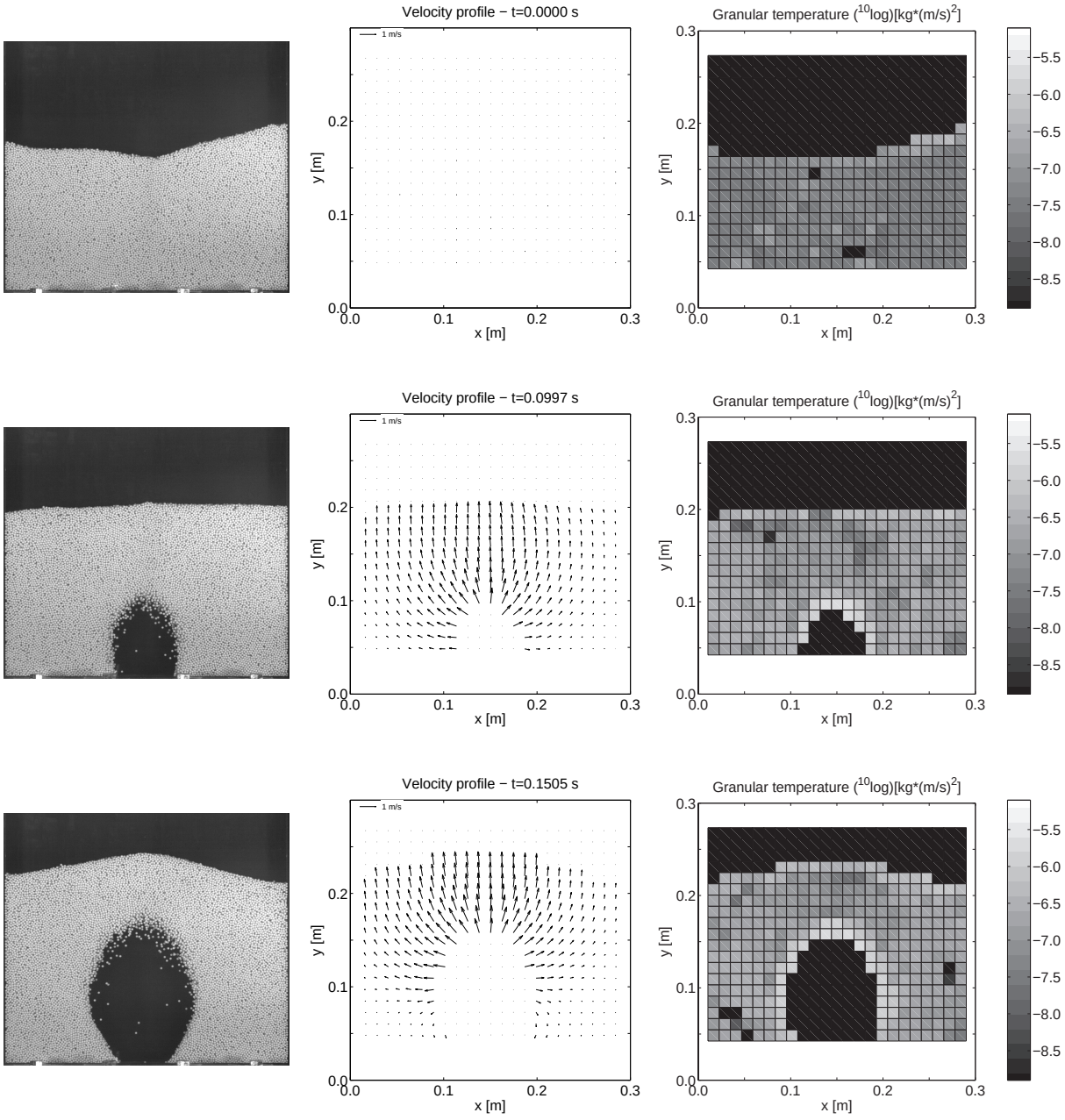

Figure 2.21: Single bubble experiment in the 30 cm set-up using 2.5 mm glass beads (for color figures see Figure A.5).

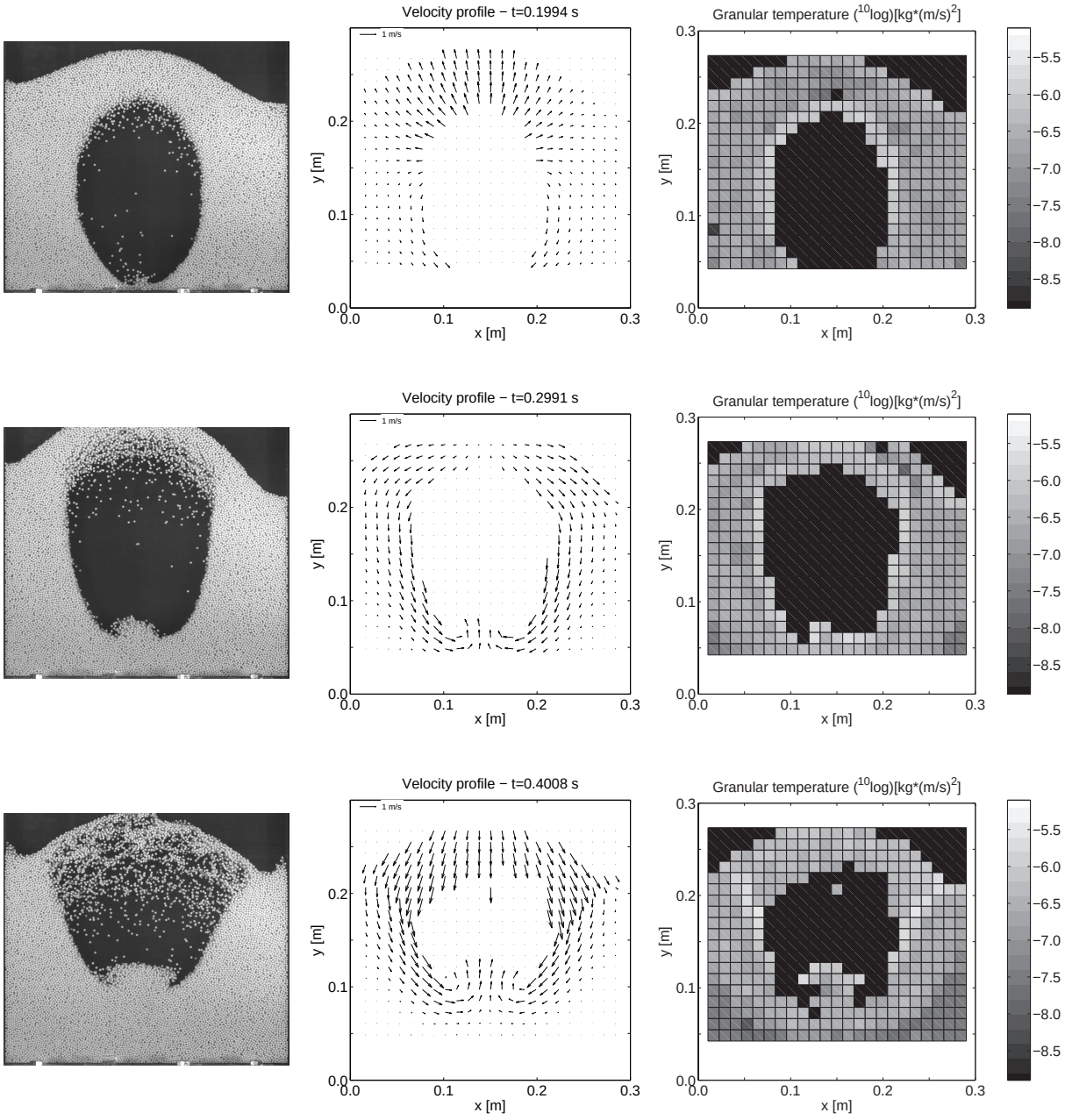

Figure 2.22: Single bubble experiment in the 30 cm set-up using 2.5 mm glass beads (for color figures see Figure A.6).

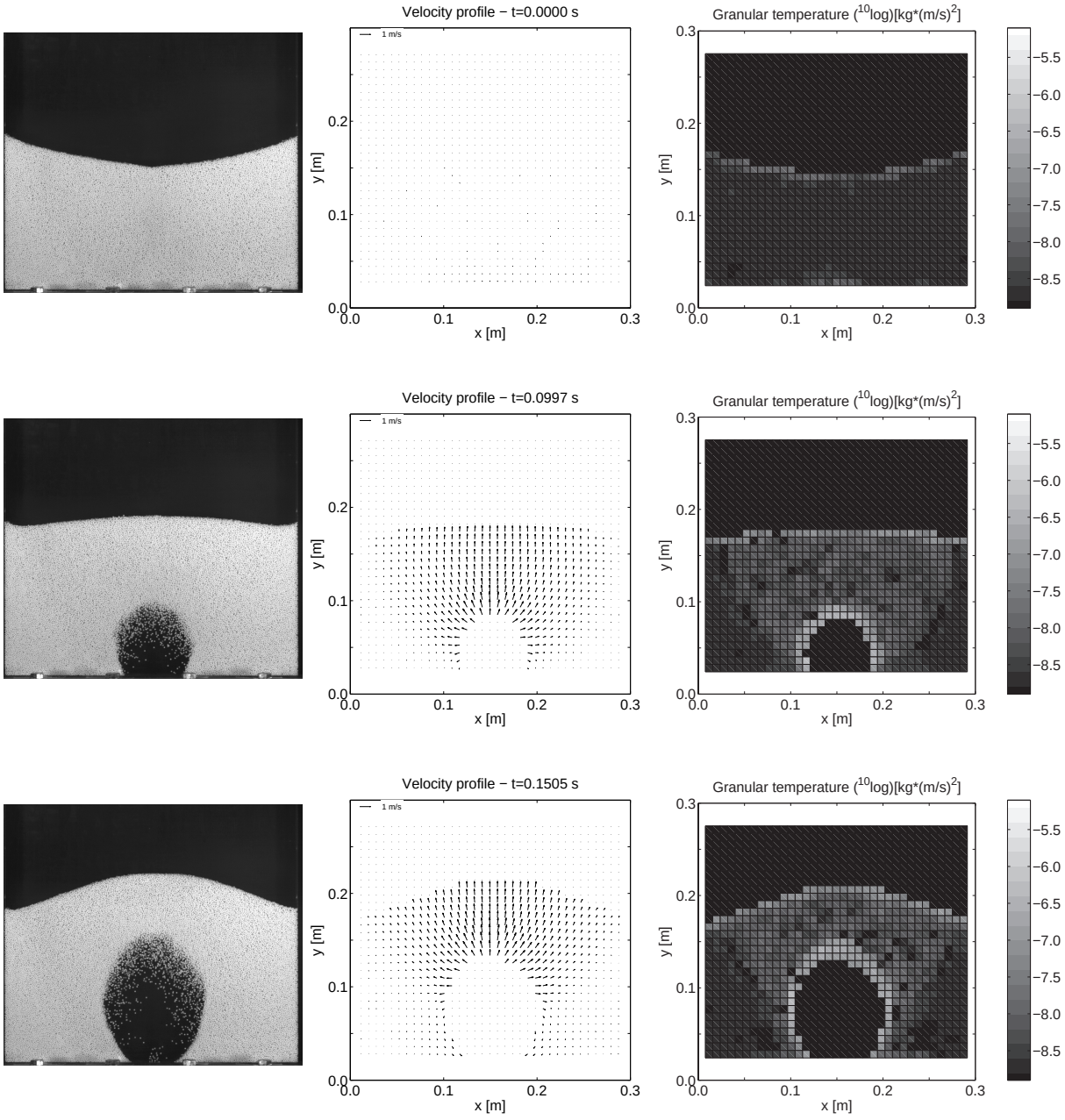

Figure 2.23: Single bubble experiment in the 30 cm set-up using 1.5 mm glass beads (for color figures see Figure A.7).

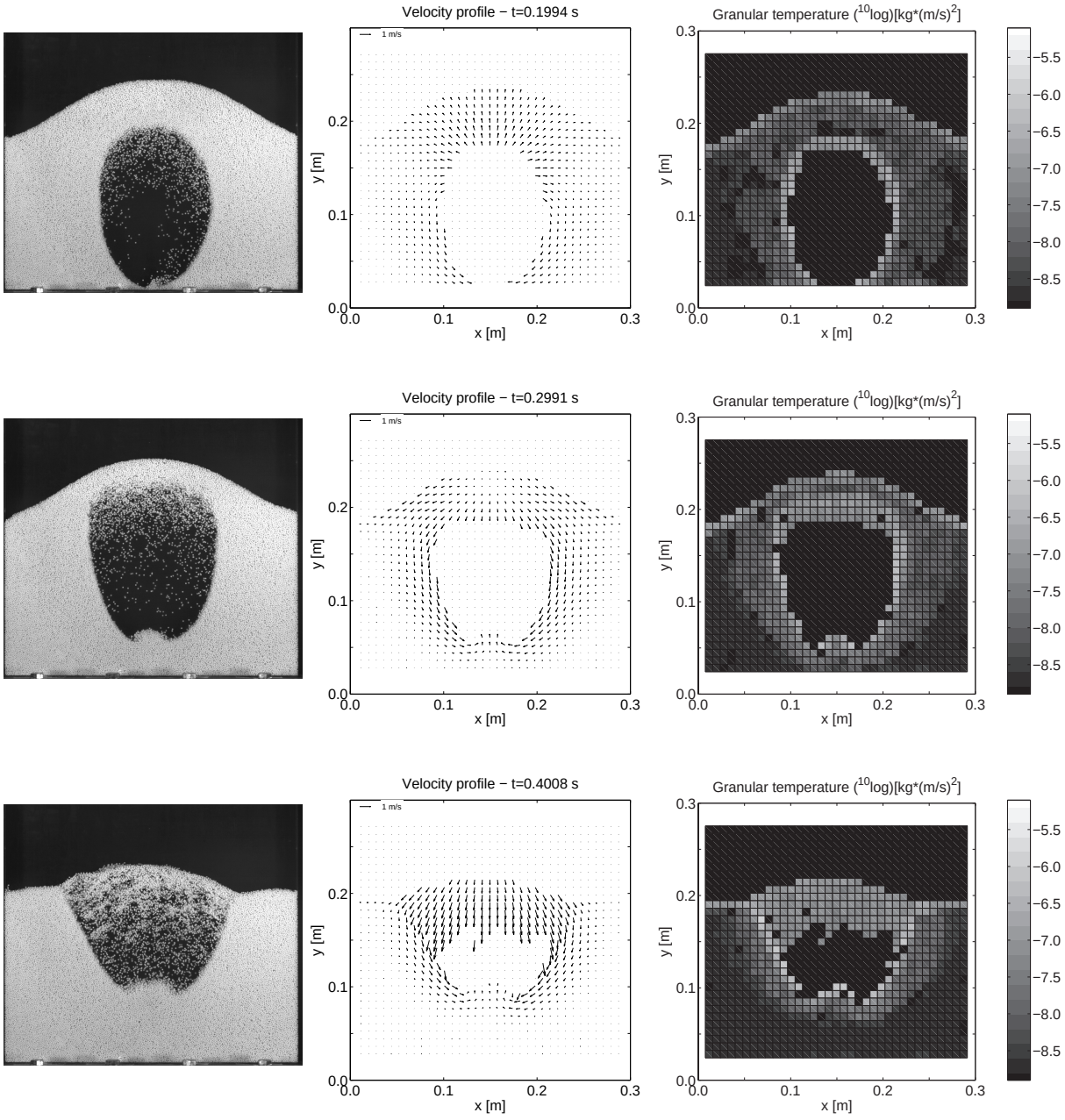

Figure 2.24: Single bubble experiment in the 30 cm set-up using 1.5 mm glass beads (for color figures see Figure A.8).

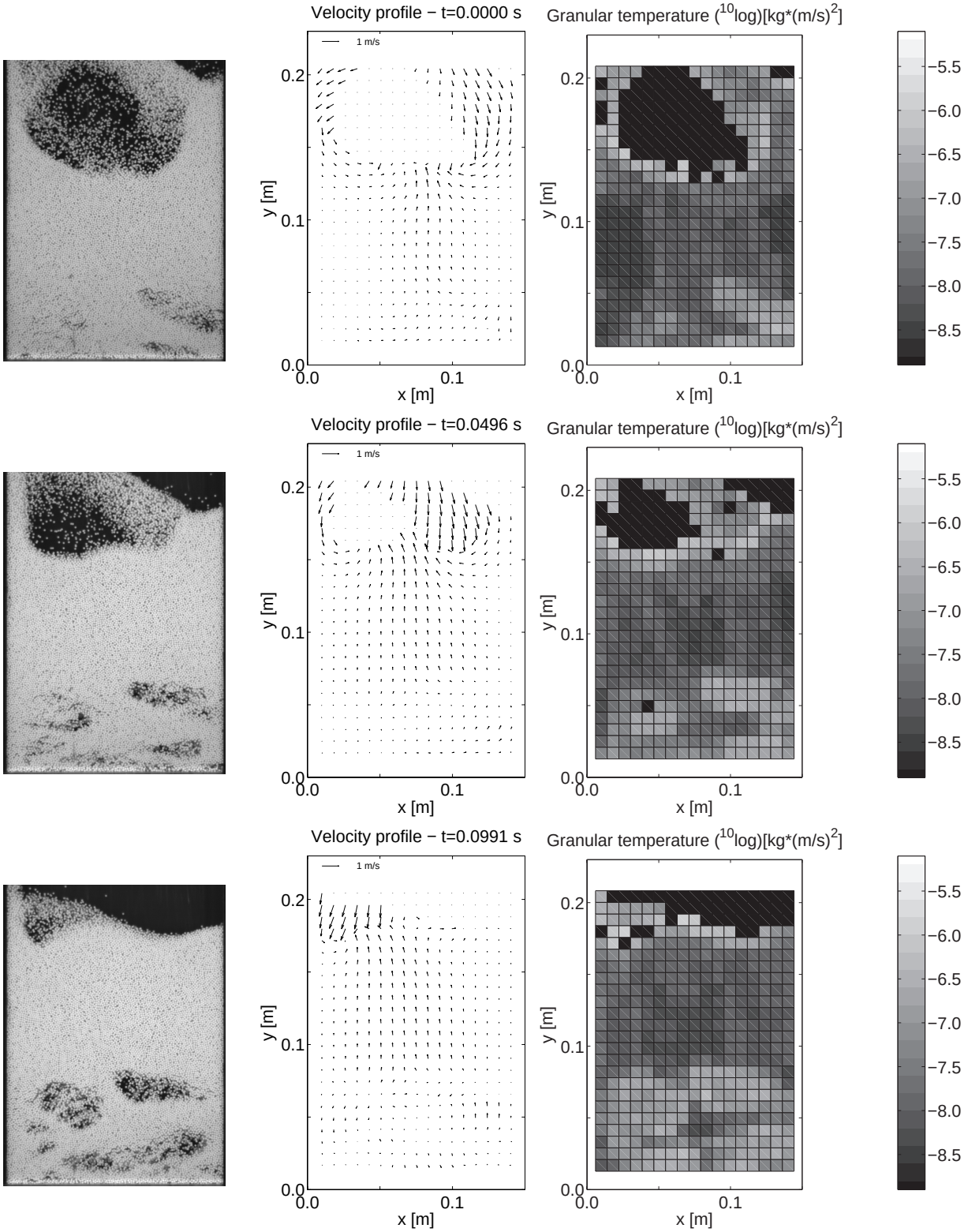

Figure 2.25: Freely bubbling experiment in the 15 cm set-up using 1.5 mm glass beads (for color figures see Figure A.9).

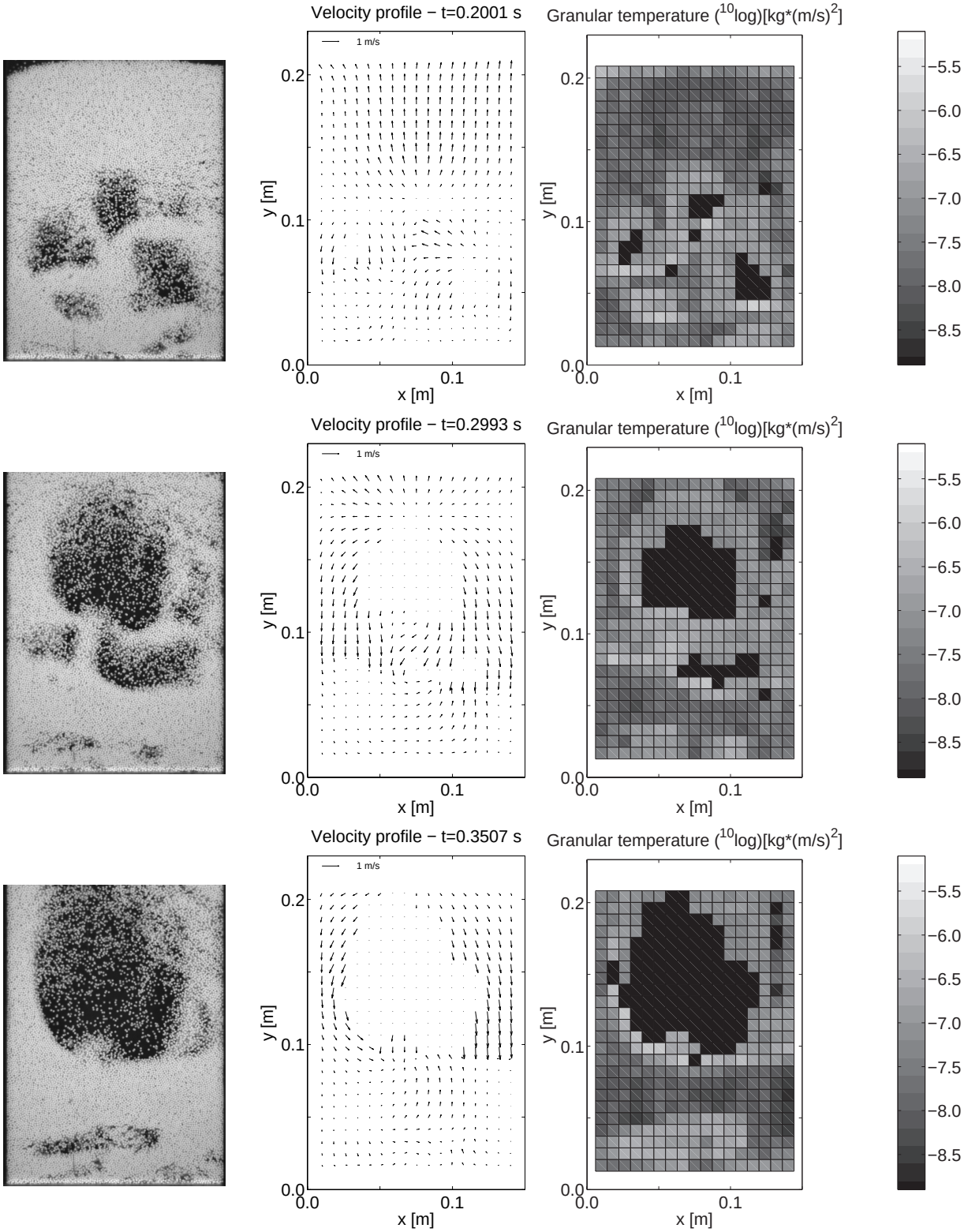

Figure 2.26: Freely bubbling experiment in the 15 cm set-up using 1.5 mm glass beads (for color figures see Figure A.10).

2.7 Conclusions

A new non-invasive whole-field technique has been developed to measure the local granular temperature instantaneously in a pseudo-2D fluidised bed. The classical PIV analysis, widely used in the field of gas-liquid flow measurement, has been extended to granular media. An important assumption in this new method is that the particle velocity distribution, the light intensity distribution and the particle image intensity distribution are Gaussian. The granular temperature can be computed from the standard deviation of the Gaussian fit to the displacement peak, once the contribution of the particle diameter to the width of the displacement peak has been eliminated.

The new method was tested with artificially generated pictures to investigate the effects of the particle size and the particle number density. From these tests it could be concluded that the error in the displacement peak decreases with a higher particle number density. The original 3-point Gaussian fit of the displacement peak has been replaced by a least squares fit to obtain a better fit for particle diameters larger than 3 pixels, resulting in a decrease of the displacement error as a function of the particle image diameter.

In the experimental set-up direct lighting of the fluidised bed has been applied, although the light intensity distribution was less Gaussian. Direct lighting however results in a higher contrast and therefore the particles can be differentiated more easily. Auto-correlation of a single real particle and a dense particle region in the fluidised bed both resulted in a nice Gaussian peak. To improve the detectability of the displacement peak, especially around the bubble interface, zero-padding has been applied (Westerweel, 1993).

Experiments were carried out in a pseudo-2D fluidised bed with a diameter of 15 cm and 30 cm filled with 1.5 mm and 2.5 mm particles. For these particles all the properties including the collision parameters were accurately measured. The images were taken with a high speed and high resolution camera. Particle velocity and granular temperature profiles have been succesfully measured in a mono-disperse fluidised bed where a single bubble was injected via a central jet and in a freely bubbling fluidised

bed. From the single bubble experiments it could be concluded that the highest granular temperature levels were found in close vicinity of the bubble interface and that the experiments with particles of 1.5 mm give a somewhat smaller granular temperature level because of the lower mass. Also, the granular temperature profiles have successfully been measured in a freely bubbling fluidised bed where the particles were mixed much more vigorously. Again, only in a small region around the bubble interface increased granular temperature levels were measured.

It has been demonstrated that the PIV technique has successfully been extended to be able to measure instantaneous granular temperature fields in pseudo-2D fluidised beds, which can be used to validate continuum models based on the KTGF. This technique is not only limited to mono-disperse systems, but can in principle easily be applied to bi-disperse systems, provided that the particles with different size can be separated in the images.

Chapter 3

Bubble size and bubble induced particle drift by a single bubble in mono-disperse gas-solid fluidised beds: Comparison of model predictions with experiments

Abstract

In many industrial multi-disperse gas-solid fluidised bed applications, particle mixing and segregation phenomena play a very important role. The extent of segregation and particle mixing is strongly influenced by the bubble dynamics. To describe the bubble dynamics and particle mixing and segregation in dense gas-solid fluidised beds, fundamental hydrodynamic models are required. In this work a single bubble injected into a mono-disperse fluidised bed at incipient fluidisation conditions has been studied with both the Two-Fluid Model based on the Kinetic Theory of Granular Flow and a Discrete Particle Model and the simulation results have been compared with dedicated experiments.

The drag model by Ergun (1952) and Wen and Yu (1966), originally implemented in both CFD models, overpredicted the size of the injected bubble. Implementation of a new drag relation by van der Hoef et al. (2005), based on Lattice Boltzmann simulations, gave a better agreement with the experimental findings. The particle mixing

induced by a single bubble could be very well predicted by the DPM, contrary to the TFM. The TFM largely overpredicts the induced particle mixing most probably because the TFM does not take into account the effect of friction during long-term and multi-particle contacts. Artificially increasing the shear viscosity by means of a shear viscosity model did not improve the TFM results. Although the induced particle drift by a single injected bubble was somewhat decreased, the bubble shape and behaviour no longer agreed with the experimental observations. However, extra dissipation of granular energy by using an effective coefficient of normal restitution improved the TFM simulation results considerably, regarding the granular temperature profile and the bubble shape, but did not decrease the induced particle mixing.

3.1 Introduction

In many industrial gas-solid fluidised bed applications, for example in gas-phase polymerisation reactors or in granulation processes, the particle size distribution and the particle residence time distribution - and hence the particle properties - are largely determined by both the rate of particle segregation and the rate of particle mixing induced by the movement of the bubbles. Therefore, a fundamental understanding of the influence of the bubble characteristics and bubble dynamics is necessary in order to quantitatively describe the particle mixing. With fundamental hydrodynamic models the mixing and segregation behaviour of these types of gas-solid contactors can be studied in great detail.

To describe the hydrodynamics of dense gas-solid fluidised beds, Discrete Particle Models (DPM) and Two-Fluid continuum models (TFM) have been developed. In the DPM (Euler-Lagrange model) the gas phase is treated as a continuum and every particle is tracked individually using a detailed collision model to account for non-ideal particle-particle or particle-wall interactions. However, the maximum number of particles that can be modelled with the DPM is less than typically $10^5 - 10^6$, whereas the number of particles that are present in an engineering scale fluidised bed is orders of magnitude higher. Therefore, continuum models (Euler-Euler models), where the gas phase and the solid phase are considered as fully interpenetrating fluida, have been developed to model engineering scale fluidised beds. The most modern continuum models use closures derived by the Kinetic Theory of Granular Flow (KTGF) to describe the solids phase rheology. Although the continuum models have been studied extensively in the literature (e.g Gidaspow, 1994; Simonin, 1996; Kuipers and van Swaaij, 1998), these models still lack the capability of describing quantitatively particle mixing and segregation rates in multi-disperse fluidised beds. To understand the shortcomings of the continuum models, the DPM can be used as a research-tool to validate the underlying assumptions in the TFM. As a first step in better understanding the mixing and segregation behaviour of multi-disperse fluidised beds, in this chapter the single bubble formation and the particle mixing induced by a single bubble injected in

a mono-disperse fluidised bed at incipient fluidisation conditions is studied. Experiments were carried out in two pseudo-2D fluidised beds with a width of 15 cm and 30 cm containing a mono-disperse mixture of spherical glass beads (1.5 or 2.5 mm), whose collisional properties were experimentally determined. With a high speed CCD camera images of the fluidised bed were recorded from which the bubble size, particle velocity and granular temperature fields were determined using the extended PIV technique developed in Chapter 2. To visualise the extent of particle mixing, glass beads differing only in colour were used.

The experimental results on the bubble formation and the extent of particle mixing in the fluidised bed will be compared with model predictions by the DPM and the TFM to validate the sub-grid scale models for the gas-particle drag and the particle-particle interactions. First the model equations, numerical implementation and numerical verification of the DPM and TFM are described.

3.2 Discrete Particle Model

In the Discrete Particle Model (DPM) the gas phase hydrodynamics are described by the continuity and the volume-averaged Navier-Stokes equations:

$$\frac{\partial(\epsilon\rho_g)}{\partial t} + \nabla \cdot \epsilon\rho_g\vec{u} = 0 \tag{3.1}$$

$$\frac{\partial(\epsilon\rho_g\vec{u})}{\partial t} + \nabla \cdot \epsilon\rho_g\vec{u}\vec{u} = -\epsilon\nabla P_g - \nabla \cdot \epsilon\vec{\tau}_g - \vec{S}_p + \epsilon\rho_g\vec{g} \tag{3.2}$$

The source term $\vec{S}_p$ accounts for the momentum exchange between the gas phase and the particles:

$$\vec{S}_p = \frac{1}{V}\int \sum_{k=0}^{N_p} \frac{V_{p,k}\beta}{1-\epsilon}(\vec{u} - \vec{v}_{p,k})\delta(\vec{r} - \vec{r}_{p,k})\mathrm{d}V \tag{3.3}$$

where the δ-function ensures that the reaction force acts as a point force at the positions of the particles in the system. Every particle is tracked individually using Newton's second law of motion:

$$m_p\frac{d\vec{v}_p}{dt} = \vec{F}_{contact} + \vec{F}_{external} \tag{3.4}$$

Collisions between the particles (and the walls) are evaluated with a detailed collision model. Two approaches can be distinguished regarding the collision model used in the DPM, namely the hard-sphere and the soft-sphere approach. In the hard-sphere DPM only instantaneous binary collisions are considered, whereas in the soft-sphere DPM the particles may overlap (to a very small extent) and are displaced simultaneously, allowing for multiple particle collisions. The soft-sphere approach is especially suited for dense fluidised beds where the particles have a very high collision frequency. Hence in this work the soft-sphere approach has been used. In paragraph 3.2.1 the soft-sphere collision model will be explained in further detail and a relation is derived for the contact force $\vec{F}_{contact}$ and in paragraph 3.2.2 relations are presented for the external force $\vec{F}_{external}$. For more details about the hard-sphere collision model used the interested reader is referred to Hoomans et al. (1996).

3.2.1 Soft-sphere collision model

The soft-sphere collision model used here describes a collision with the linear spring/ dash-pot model by Cundall and Strack (1979), which is the most popular contact force model used in the modelling of granular dynamics. Besides the equation of motion presented in equation 3.4, the equation of rotational motion is solved:

$$I\frac{d\vec{\omega}}{dt} = \vec{T} \tag{3.5}$$

where $\vec{T}$ is the torque acting on the particle and where I represents the moment of inertia, given by:

$$I = \frac{2}{5}m_p R_p^2 \tag{3.6}$$

The contact forces are calculated from the amount of overlap between the particles and their relative velocities. Two particles have overlap if the distance between their centres is smaller than the sum of their radii. The contact forces are divided into a normal (F_n) and a tangential component (F_t). Summation of the forces with respect to the other particles results in the following relations for the contact force and the torque:

$$\vec{F}_{contact,a} = \sum_b \left(\vec{F}_{n,ab} + \vec{F}_{t,ab}\right) \tag{3.7}$$

$$\vec{T}_a = \sum_b \left(R_a \vec{n}_{ab} \times \vec{F}_{t,ab} \right) \tag{3.8}$$

The equations to compute the contact forces between two colliding particles are listed in Table 3.1. The three collision parameters, the coefficient of normal restitution (e), the coefficient of tangential restitution (β_0) and the coefficient of friction (μ) can be obtained from accurate impact measurements. A detailed description of this measurement technique is presented by Kharaz et al. (1999).

3.2.2 Gas-particle drag

The second force in Newton's second law of motion is the external force which is described by the following relation:

$$\vec{F}_{external} = m_p \vec{g} - V_p \nabla P_g + \frac{V_p \beta}{1-\epsilon} (\vec{u} - \vec{v}_p) \tag{3.9}$$

where the first term is the force due to gravity and the second term is due to the pressure gradient in the continuous phase. The third term is the drag force exerted on the particles by the fluid, where β is the so-called momentum exchange coefficient. The most popular equation used for β is the well-known Ergun equation (Ergun, 1952), which is based on experimental data for the pressure drop over fixed, dense beds of spheres. For the regions where the porosity exceeds 0.8 the equation by Wen and Yu (1966) is applied, derived from experimental data for the terminal velocity of sedimenting spheres at different porosities. Both equations are listed in Table 3.2. Although these drag relations still find widespread application in gas fluidised bed modelling, Lattice Boltzmann simulations (LBM) recently revealed large differences compared to the Ergun/Wen&Yu equations especially for low porosities (below 0.8) at high Reynolds numbers ($\mathrm{Re} > 50$). With LBM the interaction between a particle and the surrounding fluid can be calculated from first principles.

In literature the definition of the drag forces derived from LBM are presented in a different form compared to the drag force relations implemented in the DPM. Therefore a short description is given on the relation between the momentum exchange coefficient β and the dimensionless drag force F.

Table 3.1: Equations for the contact force according to the soft-sphere collision model.

Normal unit vector

$$\vec{n}_{ab} = \frac{\vec{r}_b - \vec{r}_a}{\mid \vec{r}_b - \vec{r}_a \mid}$$

Relative velocity between particles a and b:

$$\vec{v}_{ab} = (\vec{v}_a - \vec{v}_b) + (R_a\vec{\omega}_a + R_b\vec{\omega}_b) \times \vec{n}_{ab}$$

Normal component of relative velocity:

$$\vec{v}_{n,ab} = (\vec{v}_{ab} \cdot \vec{n}_{ab})$$

Tangential component of relative velocity:

$$\vec{v}_{t,ab} = \vec{v}_{ab} - \vec{v}_{n,ab}$$

Tangential unit vector:

$$\vec{t}_{ab} = \frac{\vec{v}_{t,ab}}{\mid \vec{v}_{t,ab} \mid}$$

Normal displacement:

$$\xi_n = (R_a + R_b) - \mid \vec{r}_a - \vec{r}_b \mid$$

Tangential displacement:

$$\xi_t(t) = \int_{t_0}^{t} \vec{v}_{t,ab} dt$$

Normal and tangential contact forces:

$$\vec{F}_{contact,n,ab} = -k_n\xi_n\vec{n}_{ab} - \eta_n\vec{v}_{n,ab}$$

if $\mid \vec{F}_{contact,t,ab} \mid \leq \mu \mid \vec{F}_{contact,n,ab} \mid$

$$\vec{F}_{contact,t,ab} = -k_t\xi_t - \eta_t\vec{v}_{t,ab} \qquad \text{(sticking)}$$

if $\mid \vec{F}_{contact,t,ab} \mid > \mu \mid \vec{F}_{contact,n,ab} \mid$

$$\vec{F}_{contact,t,ab} = -\mu \mid \vec{F}_{n,ab} \mid \vec{t}_{ab} \qquad \text{(sliding)}$$

Model parameters:

Tangential spring stiffness:

$$k_t = \frac{2}{7}\left(\frac{\pi^2 + (\ln \beta_0)^2}{\pi^2 + (\ln e)^2}\right) k_n$$

Normal damping coefficient:

$$\eta_n = \frac{-2 \ln e}{B_2 t_{contact,n}}$$

Tangential damping coefficient:

$$\eta_t = \frac{-2 \ln \beta_0}{B_1 t_{contact,t}}$$

Normal contact time:

$$t_{contact,n} = \sqrt{\frac{\pi^2 + (\ln e)^2}{B_2 k_n}}$$

Tangential contact time:

$$t_{contact,t} = \sqrt{\frac{\pi^2 + (\ln \beta_0)^2}{B_1 k_t}}$$

Collision constants:

$$B_1 = \frac{7}{2}\left(\frac{1}{m_a} + \frac{1}{m_b}\right)$$

$$B_2 = \left(\frac{1}{m_a} + \frac{1}{m_b}\right)$$

Table 3.2: Gas-particle drag relations.

Ergun (1952)	$F = \frac{150}{18}\frac{\phi}{(1-\phi)^2} + \frac{1.75}{18}\frac{Re}{(1-\phi)^2}$	$\epsilon < 0.8$
Wen&Yu (1966)	$F = \frac{1}{24}C_D\epsilon^{-3.65}Re$	$\epsilon > 0.8$
	$C_D = \begin{cases} \frac{24}{Re}(1+0.15Re^{0.687}) & Re < 1000 \\ 0.44 & Re > 1000 \end{cases}$	
	$Re = \frac{\epsilon d_p(\vec{u}-\vec{v}_p)\rho_g}{\mu}$	
Koch&Hill (2001)	$F = F_0(\phi) + \frac{1}{4}F_1(\phi)Re^2$	$Re < 40$
	$F = F_0(\phi) + \frac{1}{2}F_3(\phi)Re$	$Re > 40$
	$F_0 = \begin{cases} \frac{(1-\phi)\left(1+\frac{3}{\sqrt{2}}(\phi)^{1/2}+\frac{135}{64}\phi\ln\phi+17.14\phi\right)}{1+0.681\phi-8.48\phi^2+8.16\phi^3} & \phi < 0.4 \\ \frac{10\phi}{(1-\phi)^2} & \phi > 0.4 \end{cases}$	
	$F_1(\phi) = (1-\phi)(0.110 + 5.10\cdot 10^{-4})$	
	$F_3(\phi) = (1-\phi)(0.0673 + 0.212\phi + \frac{0.0232}{(1-\phi)^5})$	
	$Re = \frac{\epsilon d_p(\vec{u}-\vec{v}_p)\rho_g}{\mu}$	
van der Hoef et al. (2005)	$F = F_0(\phi) + F_1(\phi)Re$	
	$F_0(\phi) = 10\frac{\phi}{(1-\phi)^2} + (1-\phi)^2(1+1.5\sqrt{\phi})$	
	$F_1(\phi) = \frac{0.48+1.9\phi}{18(1-\phi)^2}$	
	$Re = \frac{\epsilon d_p(\vec{u}-\vec{v}_p)\rho_g}{\mu}$	

The drag force F_d as used in equation 3.9 is a function of the momentum exchange coefficient following:

$$\vec{F}_d = \frac{V_p \beta}{1-\epsilon}(\vec{u} - \vec{v}_p) \tag{3.10}$$

Drag relations derived from Lattice Boltzmann simulations are often presented as a dimensionless drag force F, which relates to the drag force $\vec{F}_d$ according to the Stokes-Einstein relation, giving:

$$\vec{F}_d = 3\pi\mu d\vec{U}F \tag{3.11}$$

where $\vec{U}$ is the superficial gas velocity, defined as:

$$\vec{U} = \epsilon(\vec{u} - \vec{v}_p) \tag{3.12}$$

Combining equations 3.10 and 3.11 results into the following equation for the momentum exchange coefficient β as a function of the dimensionless drag force F:

$$\beta = 18(1-\epsilon)\epsilon\mu\frac{F}{d^2} \tag{3.13}$$

Koch and Hill (2001) derived two equations for the dimensionless drag force, one equation for *very* small Reynolds numbers and one equation valid for Reynolds numbers up to $\mathcal{O}(10^2)$ (see Table 3.2). A disadvantage of the drag relation proposed by Koch and Hill (2001) is that it is not valid for the intermediate Re regime, which is reflected in the strong discontinuity at Re = 40 (See Figure 3.1).

Recently, van der Hoef et al. (2005) derived a new expression for the dimensionless drag force that is valid over the entire Re range up to $\mathcal{O}(10^3)$ (see Table 3.2). In Figure 3.1 the drag relations by Ergun, Koch and Hill (2001) and van der Hoef et al. (2005) are listed in dimensionless form. When plotting the dimensionless interphase momentum exchange coefficient as a function of $Re/(1-\epsilon)$, following Bird et al. (1960), the Ergun equation can be represented by a single line, contrary to the closures derived from LBM, showing a strongly different functional dependency of the momentum exchange coefficient on the porosity especially at higher $Re/(1-\epsilon)$. Compared to the Ergun relation the correlations by Koch and Hill (2001) and van der Hoef et al. (2005) predict significantly lower momentum exchange coefficients for higher values of $Re/(1-\epsilon)$. Since

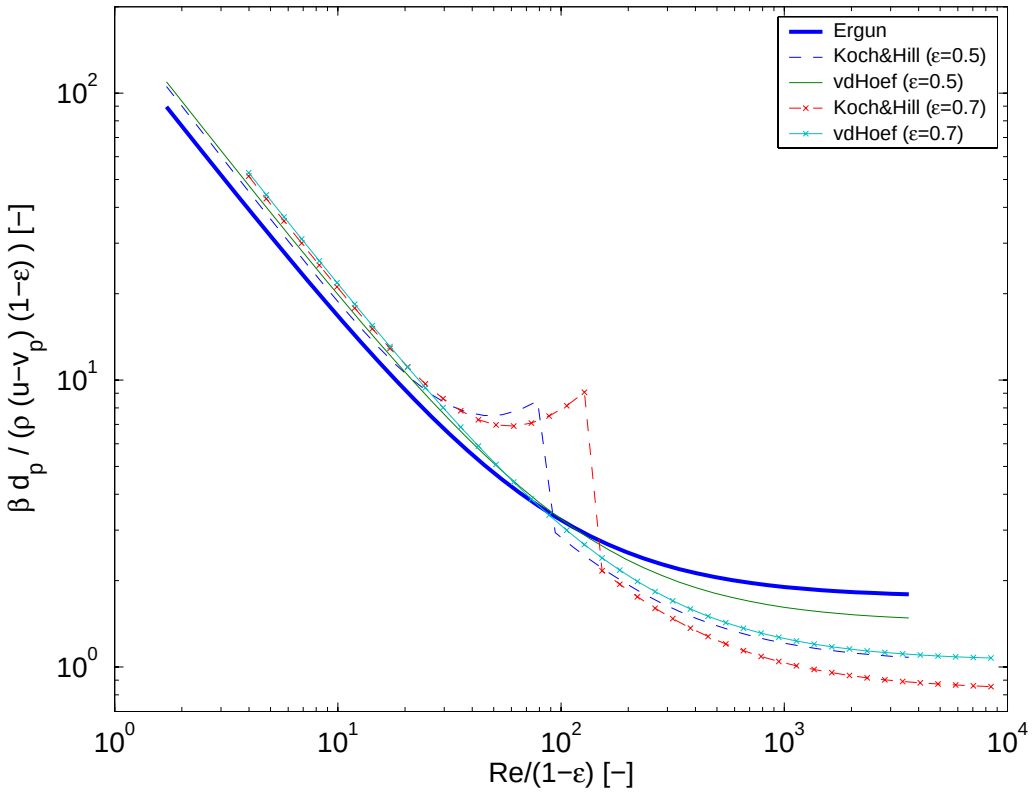

Figure 3.1: Dimensionless momentum exchange coefficient as a function of $Re/(1-\epsilon)$ for different porosities to compare the Ergun drag relation with the ones derived from Lattice-Boltzmann simulations by Koch and Hill (2001) and van der Hoef et al. (2005).

the Re numbers encountered in this study will lie in the range 10-100, the correlation proposed by van der Hoef et al. (2005) has been used in this work.

3.3 Two Fluid Model

The Two-Fluid continuum model describes both the gas phase and the solids phase as fully interpenetrating continua using a generalised form of the Navier-Stokes equations for interacting fluida (see Table 3.3). To describe the particle-particle interactions the Kinetic Theory of Granular Flow is used, which expresses the isotropic and deviatoric parts of the solids stress tensor (i.e. the solids pressure and solids shear rate) as a function of the granular temperature, defined as:

$$\theta = \frac{1}{3} < \vec{C} \cdot \vec{C} > \tag{3.14}$$

Table 3.3: Two Fluid Model, governing equations.

Continuity equations:

$$\frac{\partial}{\partial t}(\epsilon_g \rho_g) + \nabla \cdot (\epsilon_g \rho_g \vec{u}_g) = 0$$

$$\frac{\partial}{\partial t}(\epsilon_s \rho_s) + \nabla \cdot (\epsilon_s \rho_s \vec{u}_s) = 0$$

Momentum equations:

$$\frac{\partial}{\partial t}(\epsilon_g \rho_g \vec{u}_g) + \nabla \cdot (\epsilon_g \rho_g \vec{u}_g \vec{u}_g) = -\epsilon_g \nabla P_g - \nabla \cdot (\epsilon_g \overline{\overline{\tau}}_g) - \beta(\vec{u}_g - \vec{u}_s) + \epsilon_g \rho_g \vec{g}$$

$$\frac{\partial}{\partial t}(\epsilon_s \rho_s \vec{u}_s) + \nabla \cdot (\epsilon_s \rho_s \vec{u}_s \vec{u}_s) = -\epsilon_s \nabla P_g - \nabla \cdot (\epsilon_s \overline{\overline{\tau}}_s) - \nabla P_s + \beta(\vec{u}_g - \vec{u}_s) + \epsilon_s \rho_s \vec{g}$$

Granular temperature equation:

$$\frac{3}{2}\left[\frac{\partial}{\partial t}(\epsilon_s \rho_s \theta) + \nabla \cdot (\epsilon_s \rho_s \theta \vec{u}_s)\right] = -(P_s \overline{\overline{I}} + \epsilon_s \overline{\overline{\tau}}_s) : \nabla \vec{u}_s - \nabla \cdot (\epsilon_s q_s) - 3\beta\theta - \gamma$$

where $\vec{C}$ represents the particle fluctuation velocity. The constitutive equations of the TFM, derived by Nieuwland et al. (1996), are listed in Table 3.4. The gas-particle drag in the TFM is modelled with the same equations as discussed before (see section 3.2.2).

3.3.1 Frictional viscosity

At high particle volume fractions, the momentum transfer in the particulate phase becomes dominated by long-term and multiple particle contacts, which are not accounted for in the KTGF. To be able to model these dense regions with continuum models, an additional term is often added to the shear viscosity, the so-called frictional viscosity. Laux (1998) tested several models from the field of soil mechanics and the frictional viscosity term that gave the best results, is given by:

$$\mu_{s,fric} = \frac{6 \sin \phi_I}{9 - \sin^2 \phi_I} \frac{3\sqrt{2}}{2\sqrt{3}} \frac{|(\lambda_s \nabla \cdot \vec{u}_s - \frac{P_s}{\epsilon_s})|}{\sqrt{\overline{\overline{D}}_{ij} : \overline{\overline{D}}_{ij}}} \tag{3.15}$$

Table 3.4: Two Fluid Model, constitutive equations.

Particle pressure:

$$P_s = [1 + 2(1 + e_n)\epsilon_s g_0]\epsilon_s \rho_s \theta$$

Newtonian stress-tensor:

$$\overline{\overline{\tau}}_s = -\left[\left(\lambda_s - \frac{2}{3}\mu_s\right)(\nabla \cdot \vec{u}_s)\overline{\overline{I}} + \mu_s\left((\nabla \vec{u}_s) + (\nabla \vec{u}_s)^T\right)\right]$$

Bulk viscosity:

$$\lambda_s = \frac{4}{3}\epsilon_s \rho_s d_p g_0 (1 + e_n)\sqrt{\frac{\theta}{\pi}}$$

Shear viscosity:

$$\mu_s = 1.01600\frac{5}{96}\pi\rho_s d_p\sqrt{\frac{\theta}{\pi}}\frac{(1 + \frac{8}{5}\frac{(1+e_n)}{2}\epsilon_s g_0)(1 + \frac{8}{5}\epsilon_s g_0)}{\epsilon_s g_0} + \frac{4}{5}\epsilon_s \rho_s d_p g_0 (1 + e_n)\sqrt{\frac{\theta}{\pi}}$$

Pseudo-Fourier fluctuating kinetic energy flux:

$$\vec{q}_s = -\kappa_s \nabla\theta$$

Pseudo-thermal conductivity:

$$\kappa_s = 1.02513\frac{75}{384}\pi\rho_s d_p\sqrt{\frac{\theta}{\pi}}\frac{(1 + \frac{12}{5}\frac{(1+e_n)}{2}\epsilon_s g_0)(1 + \frac{12}{5}\epsilon_s g_0)}{\epsilon_s g_0} + 2\epsilon_s \rho_s d_p g_0 (1 + e_n)\sqrt{\frac{\theta}{\pi}}$$

Dissipation of granular energy due to inelastic particle-particle collisions:

$$\gamma = 3(1 - e_n^2)\epsilon_s^2 \rho_s g_0 \theta\left[\frac{4}{d_p}\sqrt{\frac{\theta}{\pi}} - (\nabla \cdot \vec{u}_s)\right]$$

where ϕ_I is the internal angle of friction and the rate of strain tensor $\overline{\overline{D}}_{ij}$ is given by:

$$\overline{\overline{D}}_{ij} = \frac{1}{2}\left((\nabla \vec{u}_s) + (\nabla \vec{u}_s)^T\right) - \frac{1}{3}\nabla \cdot \vec{u}_s \overline{\overline{I}} \tag{3.16}$$

Recently, Srivastava and Sundaresan (2003) presented a frictional viscosity model that is given by:

$$\mu_{s,fric} = \frac{p_c(\epsilon_s)\sqrt{2}\sin\phi_I}{2\epsilon_s\sqrt{(\overline{\overline{D}}_{ij} : \overline{\overline{D}}_{ij} + \psi\theta_s/d_p^2)}} \tag{3.17}$$

$$p_c(\epsilon_s) = \begin{cases} F\dfrac{(\epsilon_s - \epsilon_{s,min})^r}{(\epsilon_{s,max} - \epsilon_s)^s} & \epsilon_s > \epsilon_{s,min} \\ \\ 0 & \epsilon_s < \epsilon_{s,min} \end{cases} \tag{3.18}$$

where F, r, s and ψ are constants, with the values $F = 0.05N/m^2$, $r = 2$, $s = 5$ and ψ=1. The main difference between these frictional viscosity models is the additional term ($\psi\theta_s/d_p^2$) in the denominator of the viscosity model proposed by Srivastava and Sundaresan (2003) to account for strain rate fluctuations. Furthermore, Srivastava and Sundaresan (2003) use the critical state pressure (p_c) instead of the solids pressure (P_s) obtained from the KTGF in the calculation of the frictional viscosity and this critical state pressure is also added to the solids pressure when calculating the solids pressure gradient in the solids phase momentum equation.

3.4 Numerical solution strategy

In the DPM the gas phase hydrodynamics are computed with the volume-averaged Navier-Stokes equations, employing a staggered grid to improve numerical stability. The equations are numerically solved following the SIMPLE algorithm by Patankar (1980). The convective fluxes in the conservation equations are calculated using the second order accurate Barton scheme (Centrella and Wilson, 1984; Goldschmidt, 2001) to reduce numerical diffusion and a standard second order discretisation scheme is used for the dispersive terms. In the TFM the same solution strategy has been applied to solve the continuous phases. The only difference, however, is that in the TFM an extra step is implemented to solve the particle volume fraction taking the compressibility

of the particulate phase directly into account. For a more detailed description of this new algorithm the interested reader is referred to Goldschmidt (2001) or Section 4.3 in this thesis.

The motion of the particles in the DPM are resolved in full 3D by integrating Newton's second law of motion, using a first order (Euler) time integration (Hoomans et al., 1996). The collisions between the particles and between the particles and the system walls are computed with a detailed soft-sphere collision model taking into account the non-ideality of the particles.

In the DPM a prescribed inflow boundary condition is applied for the gas phase at the bottom of the bed, no-slip boundary conditions are applied at the side walls and a prescribed pressure condition is applied at the top of the bed. In the TFM the same boundary conditions are applied for the gas phase and a free slip boundary condition is applied for the solids phase.

3.4.1 Verification of the CFD models

In the soft-sphere DPM a value for the normal spring stiffness (k_n) has to be selected. In the limit of an infinitly high value for the spring stiffness the soft-sphere model results coincide with the hard-sphere model results (Hoomans, 1999). However, an infinitly high value of the spring stiffness would require an infinitly small time step to compute the contact forces. To demonstrate the effect of the spring stiffness, three DPM simulations with different values for the spring stiffness have been carried out, simulating a single bubble injected into a mono-disperse fluidised bed at minimum fluidisation conditions. In Figure 3.2 snapshots of the particles are depicted and no differences can be discerned between the simulation results, so that it can be concluded that with a spring stiffness above 5000 sufficiently accurate results are obtained for the system under investigation.

To determine the minimum required grid size, again simulations of a single bubble injected into a mono-disperse fluidised bed has been simulated with the TFM, but with different grid sizes. It can be concluded from Figure 3.3 that with a grid size of 30x90 (5 mm squared) sufficiently accurate results are obtained. Further refinement of the

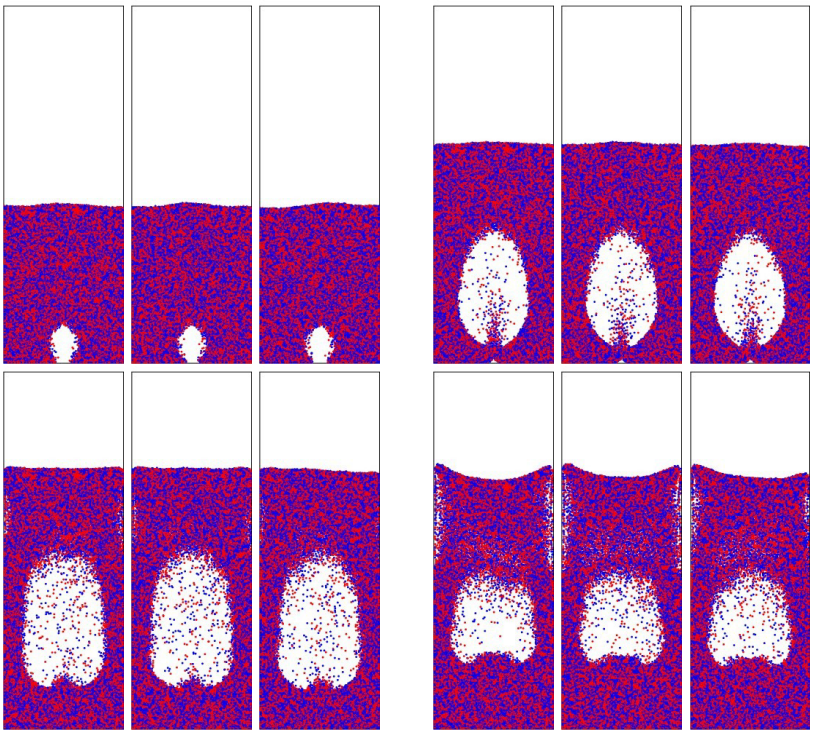

Figure 3.2: Effect of the spring stiffness on a single bubble soft-sphere DPM simulation. Left: k_n = 5000; Middle: k_n = 15000; Right: k_n = 100000.

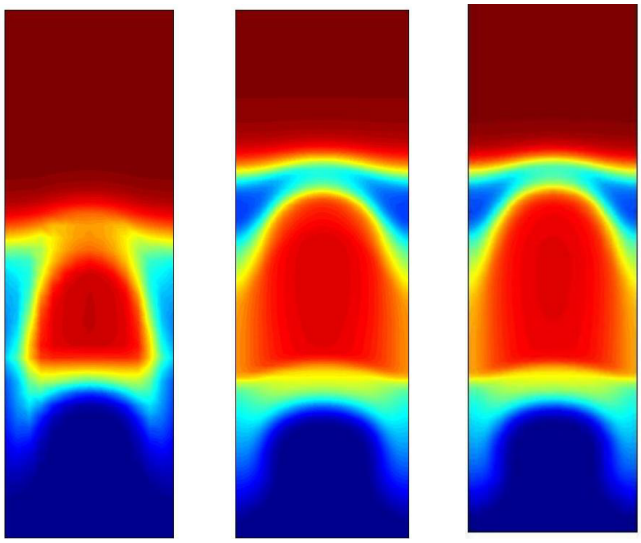

(a) (b) (c)

Figure 3.3: Effect of grid size on TFM results; (a) 15x45; (b) 30x90; (c) 45x90.

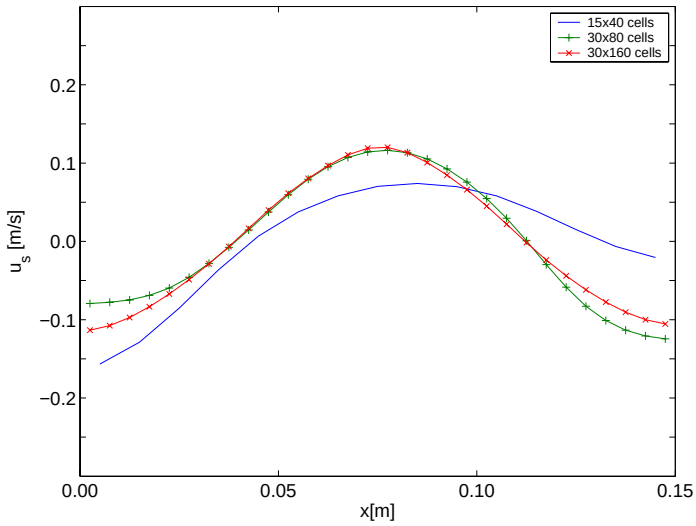

Figure 3.4: Effect of grid size on the time-averaged solids velocity profile in a freely bubbling fluidised bed filled with particles of 2.5 mm computed with the TFM.

grid in the radial direction did not affect the simulation results. In Figure 3.4 the time averaged (between 5 and 10 s) solids velocity profile is shown calculated for a freely bubbling fluidised bed with the TFM using different grid sizes. Also from these simulations it can be concluded that a grid of 30x80 is required to warrant sufficient accuracy.

3.5 Settings of the experiments and the CFD models

Experiments have been carried out in two flat fluidised beds with a bed width of 0.15 and 0.30 m, initially kept at incipient fluidisation conditions using a porous plate for homogeneous background fluidisation and equipped with a central jet for bubble injection. Spherical glass beads of 1.5 and 2.5 mm diameter were used separately of which the normal and tangential coefficients of restitution and the coefficients of friction were determined experimentally (Kharaz et al., 1999). Steam was added to keep the humidity of the inlet air at 60% to avoid build-up of static electricity. The bed was illuminated with four halogen lamps, two on each side to provide uniform lighting. Pictures of the bed where the bubble was injected were taken with a high speed camera. Further details of the experimental setup are listed in Table 3.5 and a schematic overview of the set-up is shown in Figure 3.5 (see also Chapter 2).

Table 3.5: Details of the PIV experimental set-up.

Bed:	*small*	*large*
width	0.15 m	0.30 m
depth	0.015 m	0.015 m
height	1.0 m	1.0 m
initial bed height	0.18 m	0.22 m
front plate	glass	glass
back plate	polycarbonate (''Lexan'')	glass
left and right wall	aluminium	aluminium
porous plate average pore size	10 μm	10 μm
porous plate thickness	1.5 mm	1.5 mm
jet width	0.01 m	0.015 m
Particle properties:	*small*	*large*
material	glass	glass
diameter	1.5 mm	2.5 mm
density	2526 kg/m^3	2526 kg/m^3
minimum fluidisation velocity (experimentally)	0.87 m/s	1.31 m/s
Collision parameters:	*particle-particle collisions*	*particle-wall collisions*
normal restitution	0.97$\pm$0.01	0.97$\pm$0.01
friction	0.10$\pm$0.01	0.09$\pm$0.01
tangential restitution	0.33$\pm$0.05	0.33$\pm$0.05
Camera:		
camera	LaVision ImagerPro HS	
frame rate	625 Hz	
exposure time	0.5 ms	
resolution	1280Hx1024V	

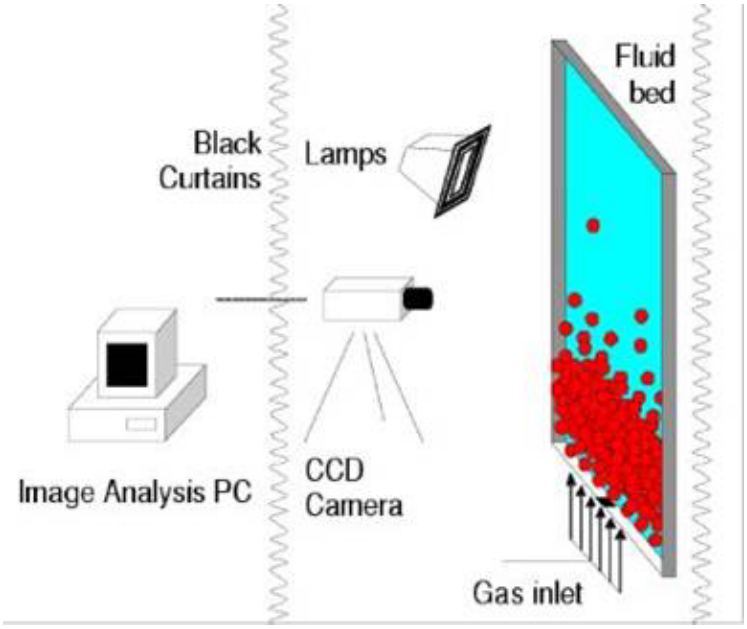

Figure 3.5: Schematic picture of the PIV experimental set-up.

In the DPM the particles are initially placed in a structured array. The first second of simulation the particles are mixed well at a high fluidisation velocity, whereafter the background velocity is set at minimum fluidisation velocity to settle the particles. After 1.5 s of simulation the jet is operated and the bubble is injected. In the TFM the injection of the bubble is started after 0.1 s of simulation since the continuous approach of the particulate phase does not require initial mixing of the particles. The simulation settings are summarised in Table 3.6.

3.6 Bubble size and induced particle drift

Bubbles play a dominant role in the hydrodynamic behaviour of fluidised beds. To eventually model the hydrodynamics of fluidised beds and to be able to determine particle mixing rates quantitatively with the DPM and the TFM, the first step is to study the behaviour of a single bubble injected into a pseudo-2D fluidised bed at incipient fluidisation conditions. First, the shape and size of the injected bubble in a mono-disperse fluidised bed predicted by the DPM and TFM are compared with experiments. Subsequently, the extent of mixing of a coloured under-layer of particles is studied with

Table 3.6: Settings for the DPM and the TFM calculations for the case where a single bubble is injected into a mono-disperse fluidised bed at incipient fluidisation conditions.

DPM:	*small bed*	*large bed*
width	0.15 m	0.30 m
depth	0.015 m	0.015 m
height	0.45 m	0.60 m
initial bed height	0.18 m	0.22 m
grid cells x-direction	15	40
grid cells y-direction	1	1
grid cells z-direction	45	80
TFM:		
width	0.15 m	0.30 m
depth	-	-
height	0.45 m	0.60 m
initial bed height	0.18 m	0.22 m
grid cells x-direction	30	40
grid cells y-direction	-	-
grid cells z-direction	90	120
	small particles	*large particles*
background velocity	0.85 m/s	1.25 m/s
jet pulse velocity	15 m/s	20 m/s
jet pulse duration	150 ms	150 ms
particle density	2526 kg/m^3	2526 kg/m^3
particle diameter	1.5 mm	2.5 mm
flow solver time step	$1.0 \cdot 10^{-4}$ s	$1.0 \cdot 10^{-5}$ s

the DPM and TFM and compared with experiments.

3.6.1 Bubble shape and size

In Figures 3.6-3.9 snapshots and the corresponding particle velocity profiles are depicted of the experiment, the DPM and the TFM, where a single bubble is injected via a central jet into a mono-disperse fluidised bed of 15 cm wide at minimum fluidisation conditions filled with 2.5 mm and 1.5 mm particles respectively. The snapshots are taken 0.1, 0.2 and 0.4 s after injection of the bubble. The bubble shape predicted by both the DPM and the TFM resembles the bubble shape in the experiments very well. Comparison of the bubble size predicted by the DPM and the TFM using the Ergun/Wen&Yu drag model with the experiments for the 2.5 mm glass beads (Figures 3.6 and 3.7) shows that both models predict a somewhat larger bubble compared to the experiment. This may be explained by the fact that the Ergun/Wen&Yu drag relations overpredict the drag force for higher Reynolds numbers (Re $>$ 50), as was recently discovered by Lattice-Boltzmann simulations (see section 3.2.2). In Figure 3.1 this difference between the drag relations is clearly demonstrated. Therefore, the drag model by van der Hoef et al. (2005) has been implemented in the DPM and in the TFM. In Figure 3.6 the results with this new drag model are also depicted and it is shown that with the drag model by van der Hoef et al. (2005) the bubble size is in better agreement with the experiments. In the results for the 1.5 mm particles (see Figure 3.8) the difference between the results obtained with the Ergun/Wen&Yu relations and the drag closure by van der Hoef et al. (2005) is much less pronounced. This can be explained by the fact that the particle Reynolds number is smaller for these particles (see Figure 3.10). From Figure 3.1 it can be concluded that when the value of $Re/(1-\epsilon)$ decreases, the discrepancies between the drag curves of Ergun/Wen&Yu and van der Hoef et al. (2005) decrease.

A striking resemblance between the DPM and the experiment is the interaction of the jet with the particles, which can especially be observed in the snapshots at 0.2 s after injection in Figure 3.6 and 3.8. Due to the high jet velocity, particles present in the wake of the bubble are tossed upwards into the bubble. In the TFM this jet interaction is less

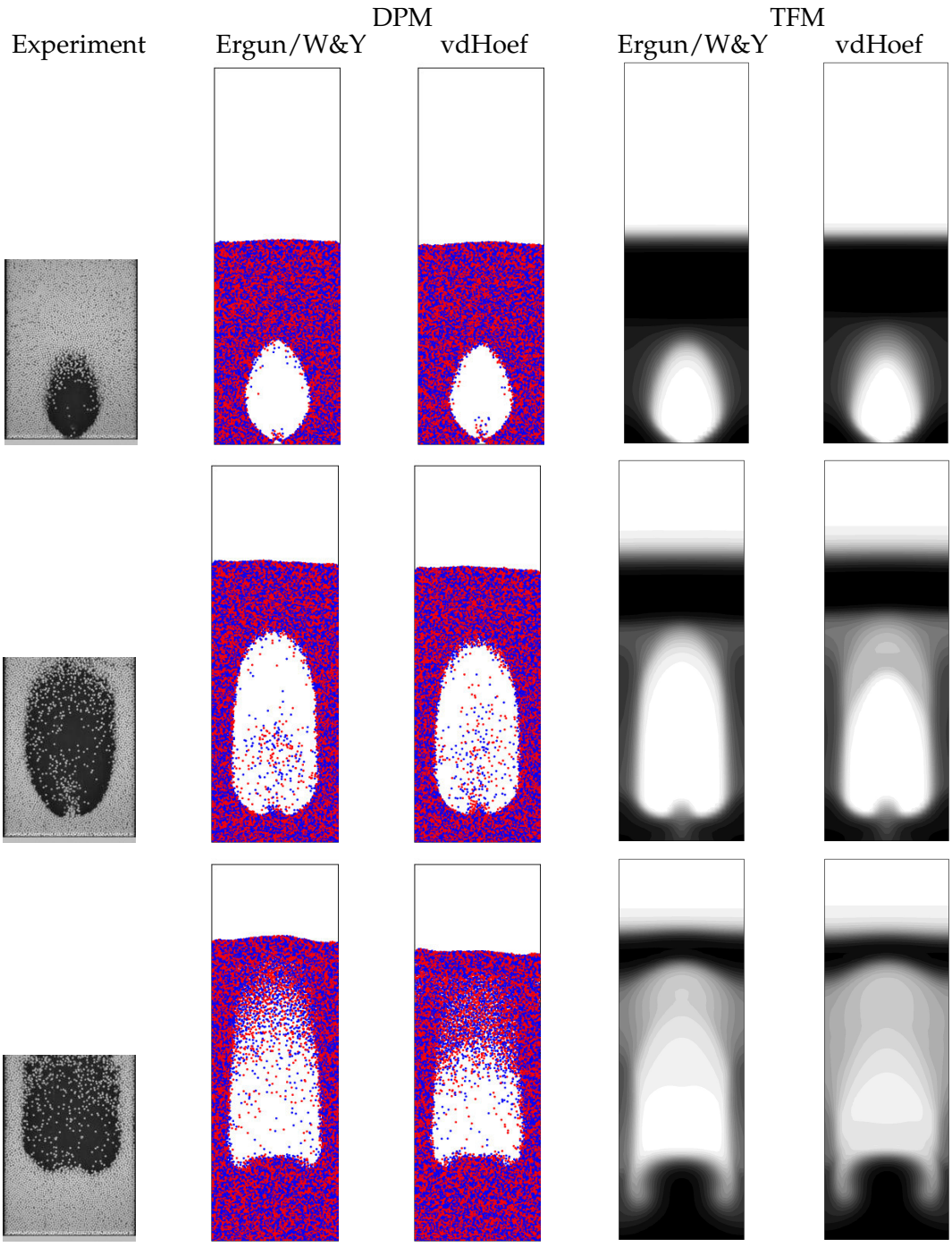

Figure 3.6: Injection of a single bubble into a mono-disperse fluidised bed at incipient fluidisation conditions (bed width: 15 cm, $d_p = 2.5$ mm, $u_{jet} = 20$ m/s). Snapshots are shown of the bubble at 0.1, 0.2 and 0.4 s after injection. Comparison between experiments, DPM and TFM with drag relations by Ergun/Wen&Yu and van der Hoef et al. (2005) (see Table 3.2).

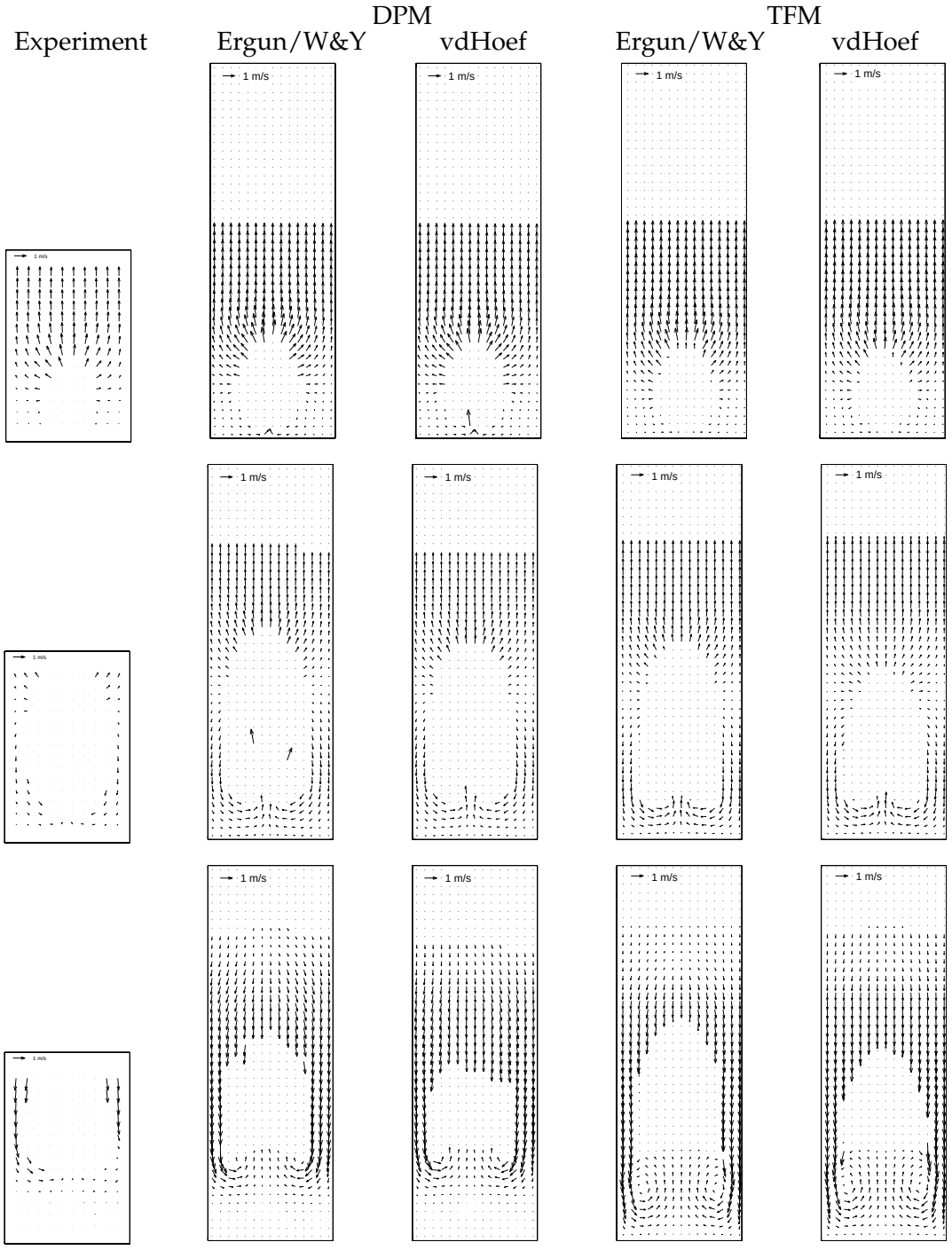

Figure 3.7: Injection of a single bubble into a mono-disperse fluidised bed at incipient fluidisation conditions (bed width: 15 cm, $d_p = 2.5$ mm, $u_{jet} = 20$ m/s). Snapshots are shown of the particle velocity profiles at 0.1, 0.2 and 0.4 s after injection. Comparison between experiments, DPM and TFM with drag relations by Ergun/Wen&Yu and van der Hoef et al. (2005) (see Table 3.2).

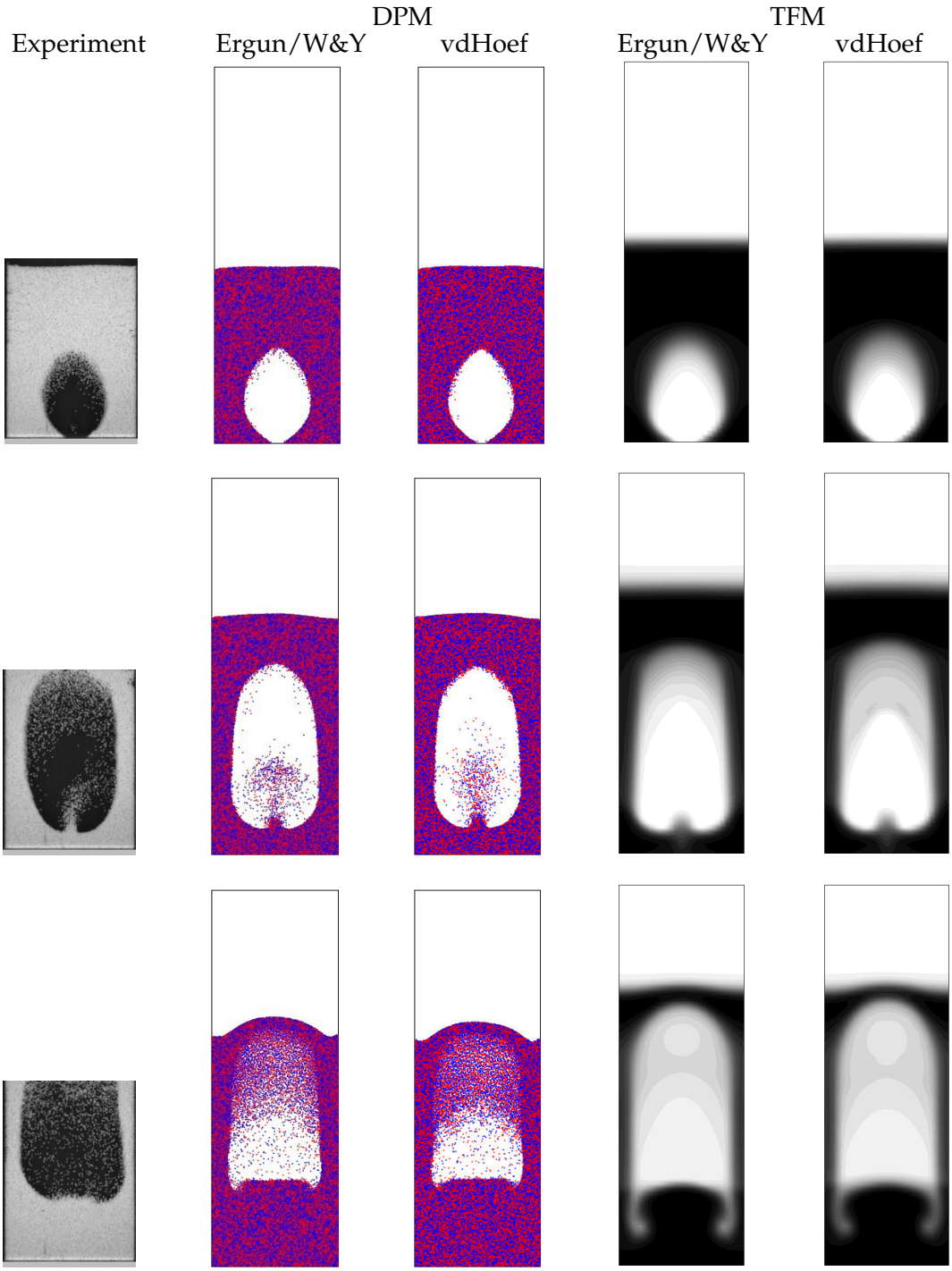

Figure 3.8: Injection of a single bubble into a mono-disperse fluidised bed at incipient fluidisation conditions (bed width: 15 cm, $d_p = 1.5$ mm, $u_{jet} = 15$ m/s). Snapshots are shown of the bubble at 0.1, 0.2 and 0.4 s after injection. Comparison between experiments, DPM and TFM with drag relations by Ergun/Wen&Yu and van der Hoef et al. (2005) (see Table 3.2).

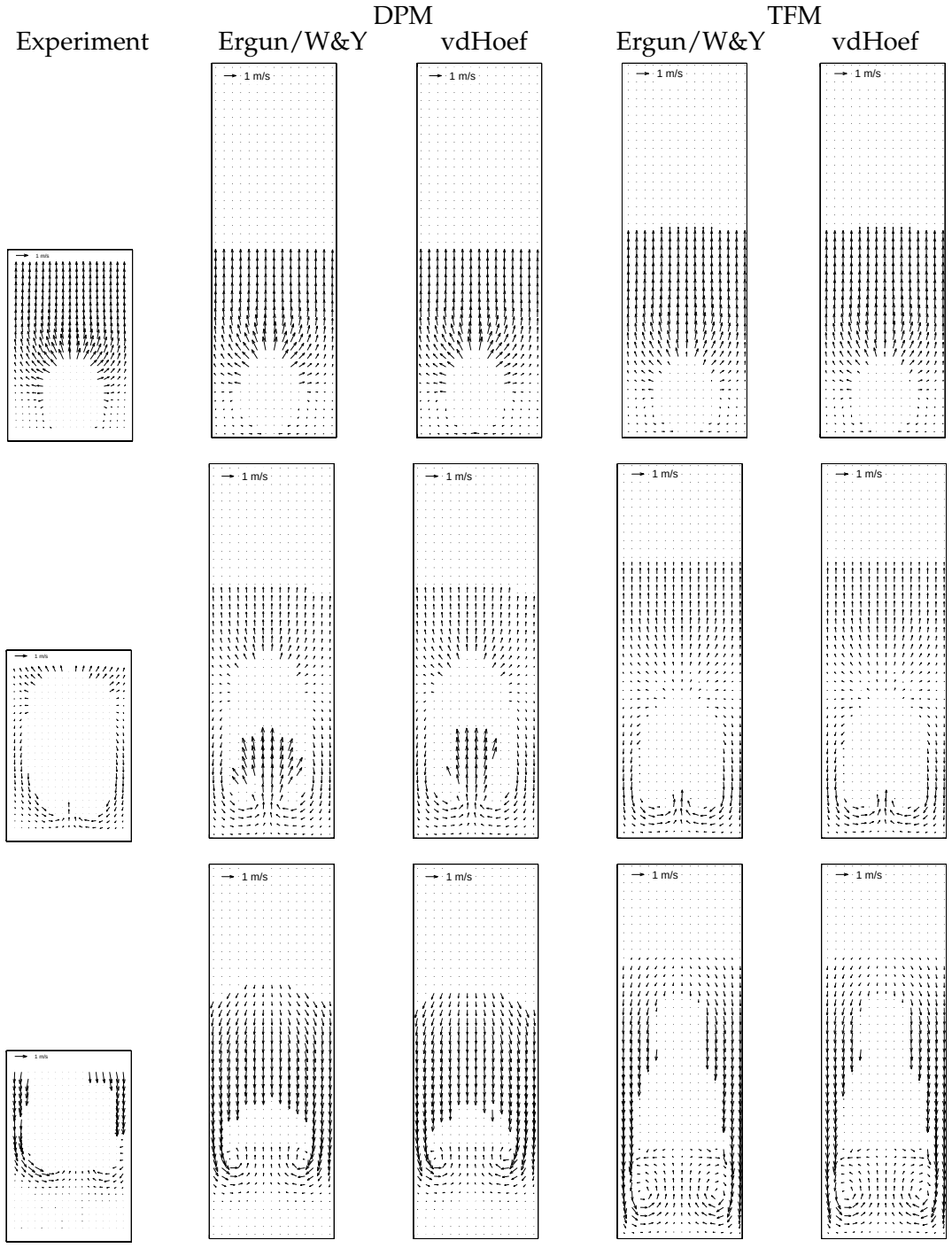

Figure 3.9: Injection of a single bubble into a mono-disperse fluidised bed at incipient fluidisation conditions (bed width: 15 cm, $d_p = 1.5$ mm, $u_{jet} = 15$ m/s). Snapshots are shown of the particle velocity profiles at 0.1, 0.2 and 0.4 s after injection. Comparison between experiments, DPM and TFM with drag relations by Ergun/Wen&Yu and van der Hoef et al. (2005) (see Table 3.2).

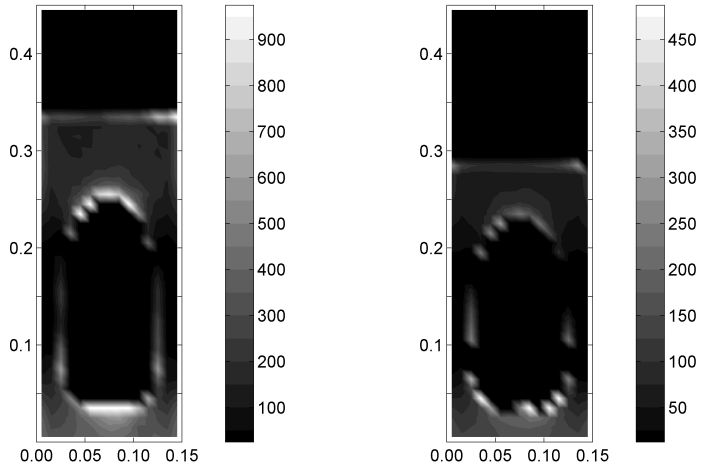

(a) (b)

Figure 3.10: DPM simulation of a single bubble injected in a mono-disperse fluidised bed with the drag relation by Ergun/Wen&Yu. Contour plot of the variable $Re/(1-\epsilon)$ with (a) 2.5 mm particles and (b) 1.5 mm particles (for color figures see Figure A.11).

pronounced because of the continuum approach of the particulate phase.
As the bubble rises in the fluidised bed more particles fall through the roof of the bubble which is termed 'raining' of the particles. In the DPM the raining of particles is also predicted especially in the snapshot at 0.4 s after injection of the bubble. In the TFM the raining is manifested by a diffuse area between the bubble and the particle phase. The TFM with the drag relation by van der Hoef et al. (2005) predicts the raining of particles somewhat better.

As can be seen in Figures 3.6 and 3.8 the bubble injected in the fluidised bed with a width of 15 cm grows to a size that is close to the width of the bed resulting in a considerable influence of the wall on the bubble shape. Therefore, similar experiments have been carried out in a fluidised bed with a width of 30 cm (central jet width of 1.5 cm). In Figures 3.11 and 3.13 snapshots of the experiments, the DPM and the TFM are shown where a single bubble is injected into a mono-disperse fluidised bed at incipient

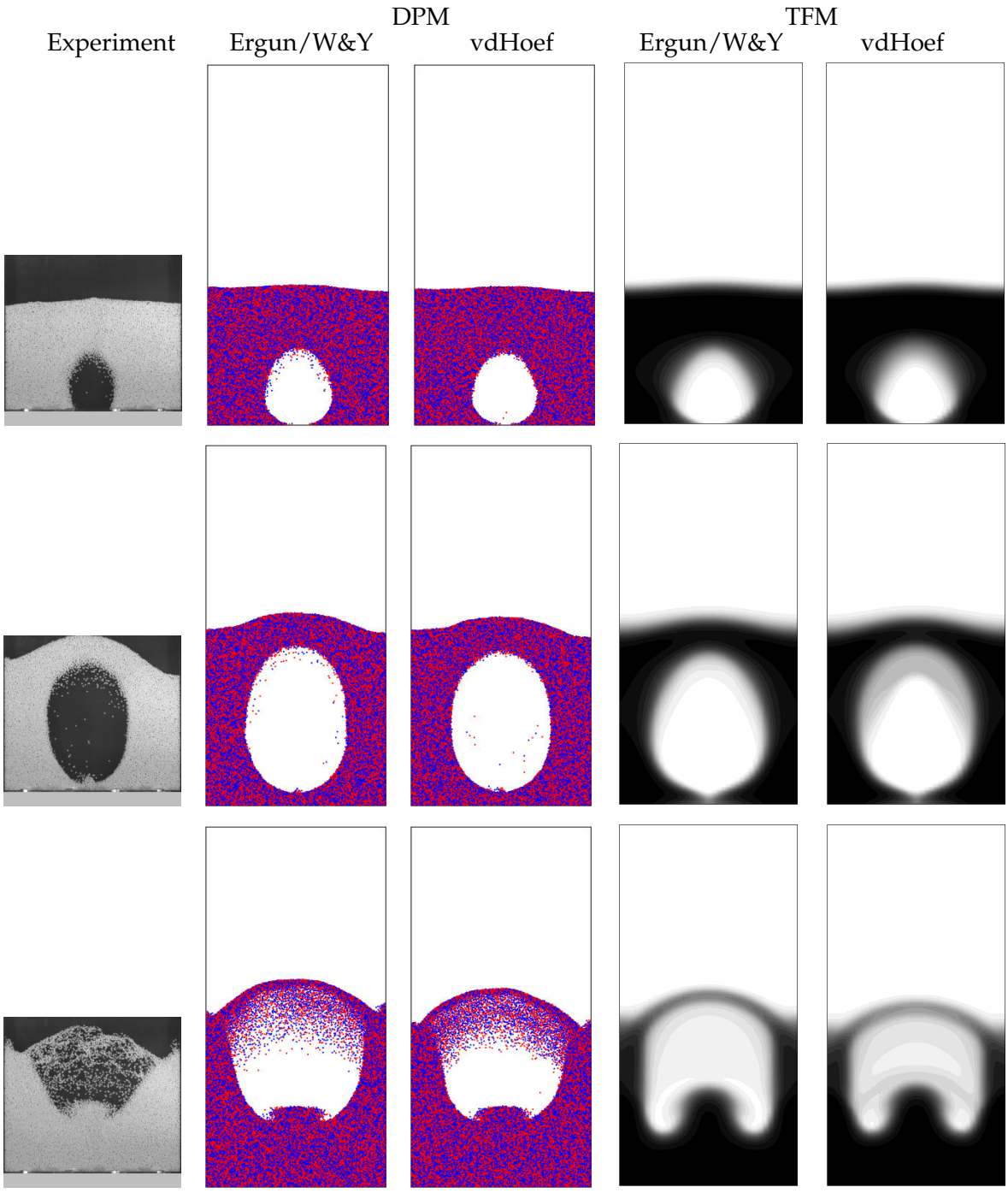

Figure 3.11: Injection of a single bubble into a mono-disperse fluidised bed at incipient fluidisation conditions (bed width: 30 cm, $d_p = 2.5$ mm, $u_{jet} = 20$ m/s). Snapshots are shown of the bubble at 0.1, 0.2 and 0.4 s after injection. Comparison between experiments, DPM and TFM with drag relations by Ergun/Wen&Yu and van der Hoef et al. (2005) (see Table 3.2).

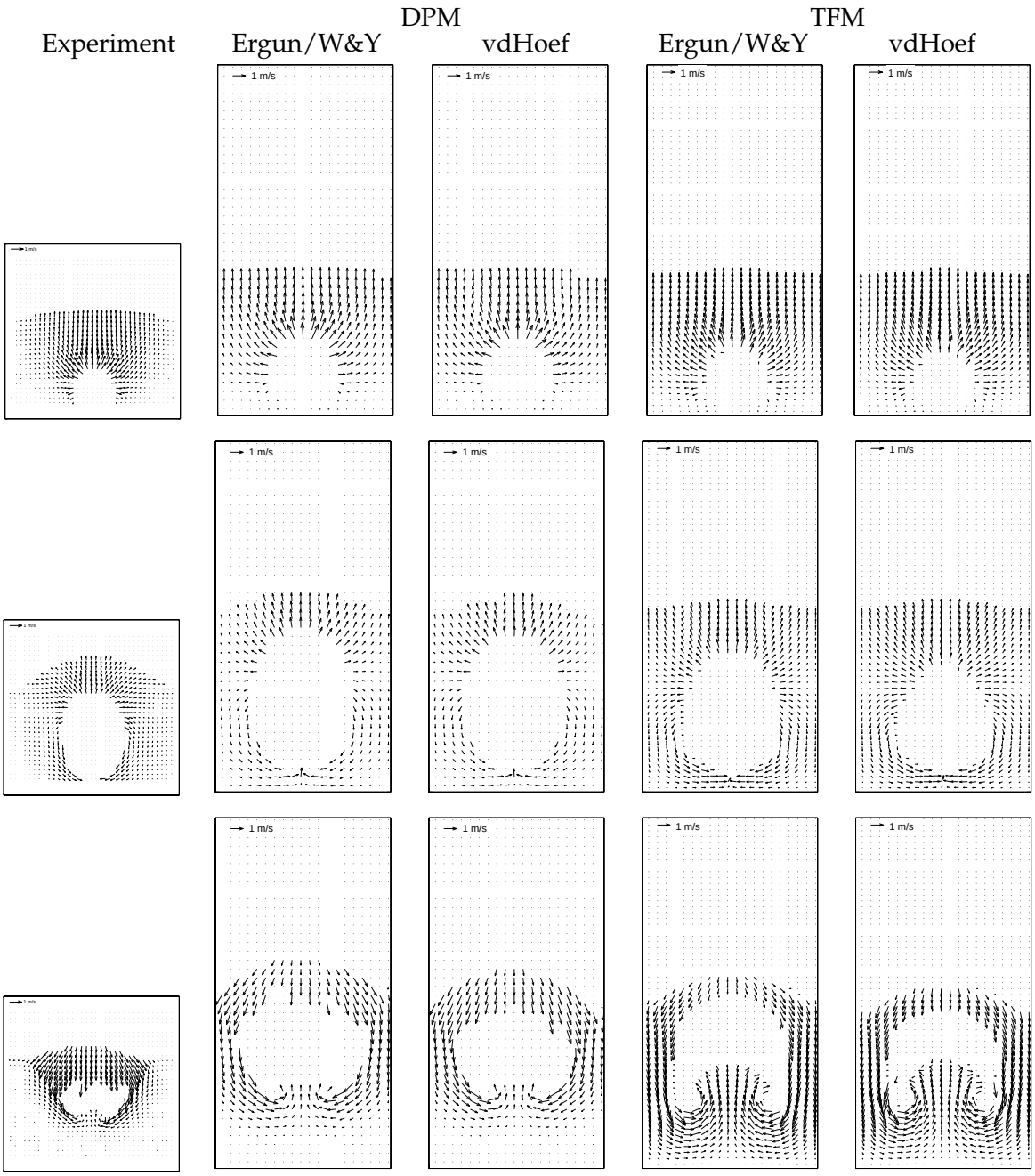

Figure 3.12: Injection of a single bubble into a mono-disperse fluidised bed at incipient fluidisation conditions (bed width: 30 cm, $d_p = 2.5$ mm, $u_{jet} = 20$ m/s). Snapshots are shown of the particle velocity profiles at 0.1, 0.2 and 0.4 s after injection. Comparison between experiments, DPM and TFM with drag relations by Ergun/Wen&Yu and van der Hoef et al. (2005) (see Table 3.2).

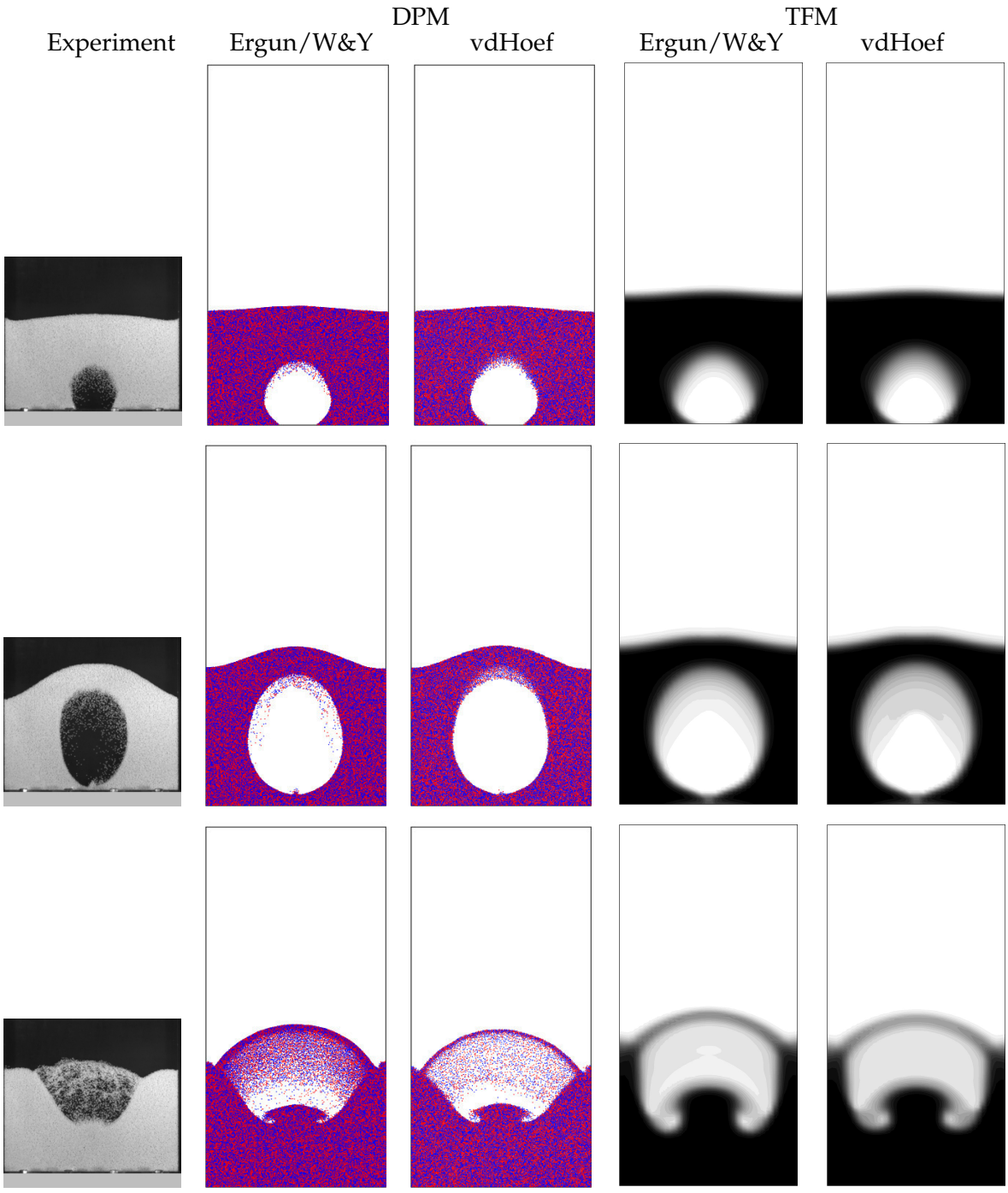

Figure 3.13: Injection of a single bubble into a mono-disperse fluidised bed at incipient fluidisation conditions (bed width: 30 cm, $d_p = 1.5$ mm, $u_{jet} = 13.33$ m/s). Snapshots are shown of the bubble at 0.1, 0.2 and 0.4 s after injection. Comparison between experiments, DPM and TFM with drag relations by Ergun/Wen&Yu and van der Hoef et al. (2005) (see Table 3.2).

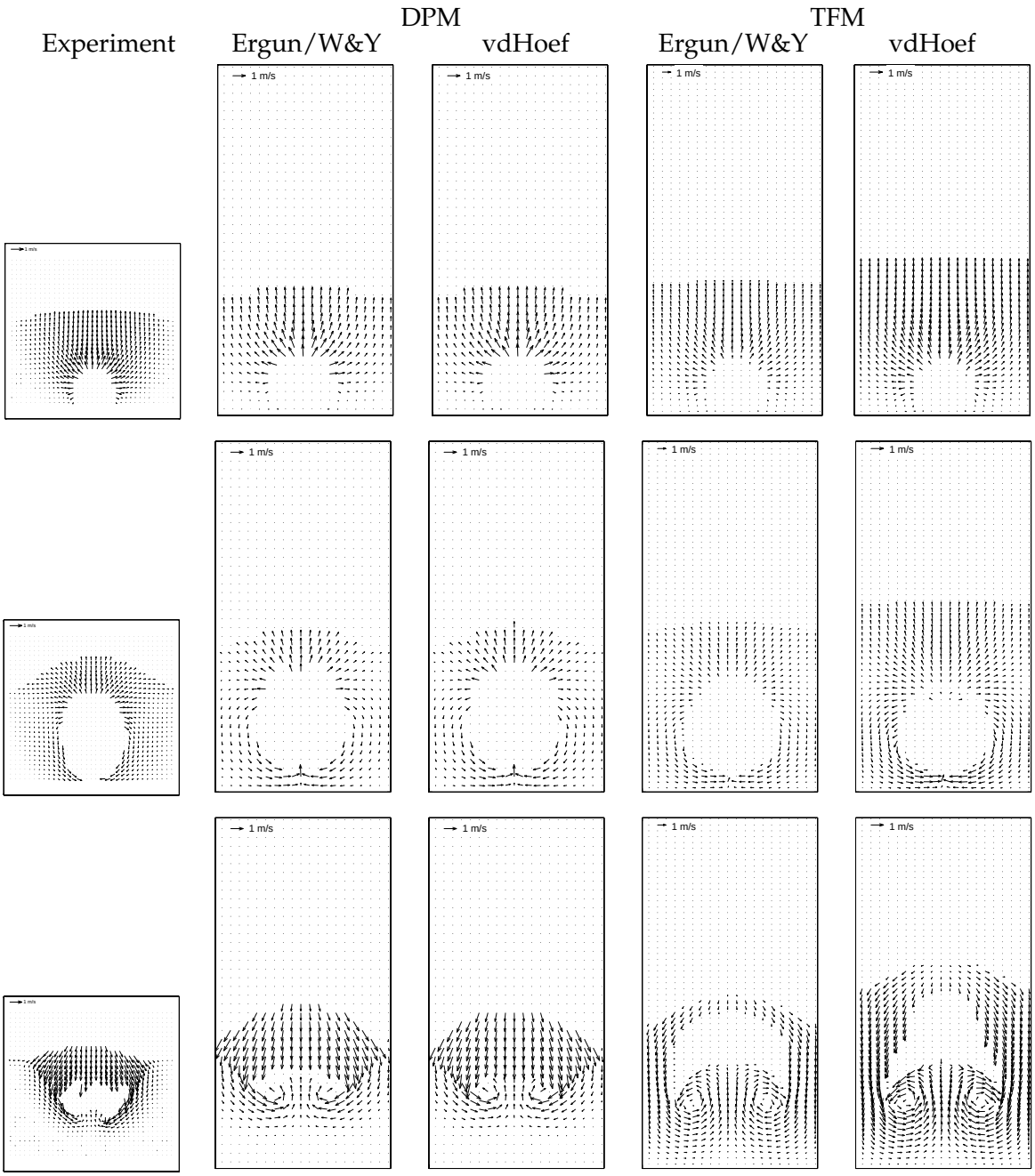

Figure 3.14: Injection of a single bubble into a mono-disperse fluidised bed at incipient fluidisation conditions (bed width: 30 cm, $d_p = 1.5$ mm, $u_{jet} = 13.33$ m/s). Snapshots are shown of particle velocity profiles at 0.1, 0.2 and 0.4 s after injection. Comparison between experiments, DPM and TFM with drag relations by Ergun/Wen&Yu and van der Hoef et al. (2005) (see Table 3.2).

fluidisation conditions with particles of 2.5 mm and 1.5 mm respectively and the corresponding velocity plots are given in Figures 3.12 and 3.14. Since the bubbles are no longer restricted in the radial direction, a rounder shape of the bubbles is observed in the experiments which is well captured by the models. Again the DPM and the TFM with the drag relation of van der Hoef et al. (2005) predict a slightly smaller bubble size compared to the simulations with the Ergun/Wen&Yu drag closures.
In Figure 3.11 at 0.4 s after the bubble injection the experiment shows an indentation at the base of the bubble, which is in fact a wake of particles resting at the bottom of the bubble sphere. This phenomena is well captured by the DPM simulation, whereas the TFM overpredicts this effect somewhat. An explanation for this overprediction is probably related to an underprediction of the solids viscosity as will be discussed in more detail in the next section. Concluding, the bubble size and shape are reasonably well described, especially when the drag closures derived from Lattice-Boltzmann simulations by van der Hoef et al. (2005) are used.

3.6.2 Particle mixing induced by a single bubble

The extent of particle mixing induced by a single bubble rising through a mono-disperse fluidised bed at incipient fluidisation velocity has been studied with the DPM and TFM and compared with experiments. To visualise the particle mixing in the experiment and the DPM two layers of particles are used, only differing in colour. In the TFM simulations fictitious tracer markers, initially positioned at regular spacings, were used to visualise the induced particle mixing. In Figure 3.15 the results are shown for the extent of particle mixing induced by a single bubble in a 15 cm bed filled with 2.5 mm particles. The DPM and the TFM simulations have been carried out with both the Ergun/Wen&Yu and the van der Hoef et al. (2005) drag relations. The particle drift profile in the centre of the bed observed in the experiment, is captured quite well with the DPM. The DPM simulation with the drag relation by van der Hoef et al. (2005) predicts a slightly smaller peak, because the size of the bubble with this drag model is smaller resulting in a smaller wake effect.
The induced particle drift profile in both a fluidised bed of 15 cm wide filled with 1.5

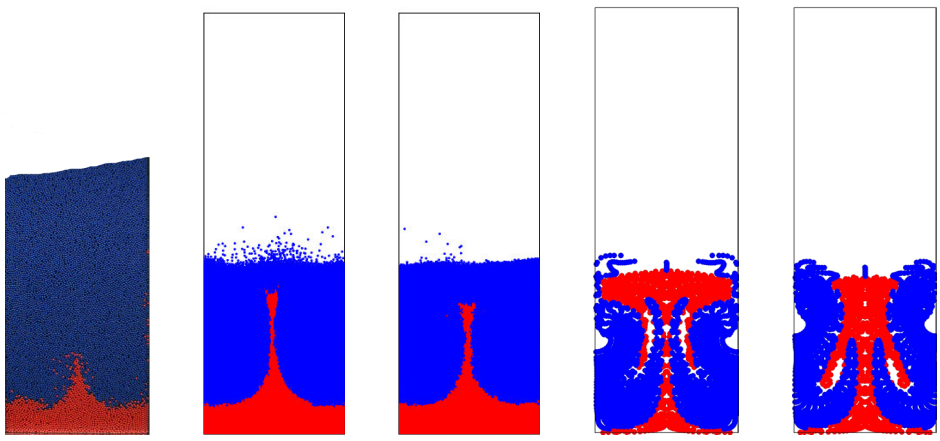

(a) (b) (c) (d) (e)

Figure 3.15: Mixing of a coloured under-layer of particles (d_p = 2.5 mm) induced by a single bubble: (a) Experiment; (b) DPM with Ergun/Wen&Yu; (c) DPM with van der Hoef et al. (2005); (d) TFM with Ergun/Wen&Yu; (e) TFM with van der Hoef et al. (2005)

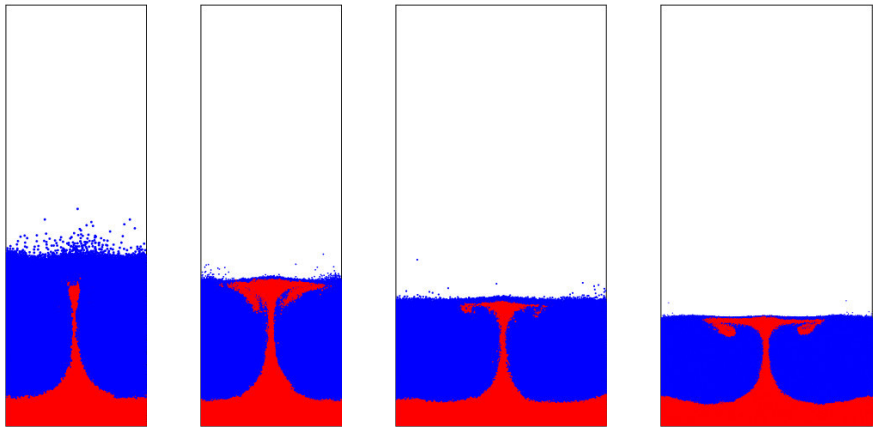

(a) (b) (c) (d)

Figure 3.16: Mixing of a coloured under-layer of particles induced by a single bubble in the DPM: (a) 2.5 mm particles in 15 cm bed; (b) 1.5 mm particles in 15 cm bed; (c) 2.5 mm particles in 30 cm bed; (d) 1.5 mm particles in 30 cm bed.

mm particles and a fluidised bed of 30 cm wide filled with 1.5 or 2.5 mm particles is somewhat different (see Figure 3.16). A single bubble rising in a bed filled with 1.5 mm particles and in a bed of 30 cm wide filled with 2.5 mm particles carries more particles to the top of the bed, as demonstrated by the small triangle at the top of the bed. This characteristic drift pattern was also found experimentally by Rowe (1971). This difference might be caused by the fact that particles with a diameter of 1.5 mm are lighter and can be transported more easily to the top of the bed. Also, the bubble in the 30 cm bed has a rounder shape (see Figure 3.17(c)) with a wider wake that transports more particles to the top of the bed.

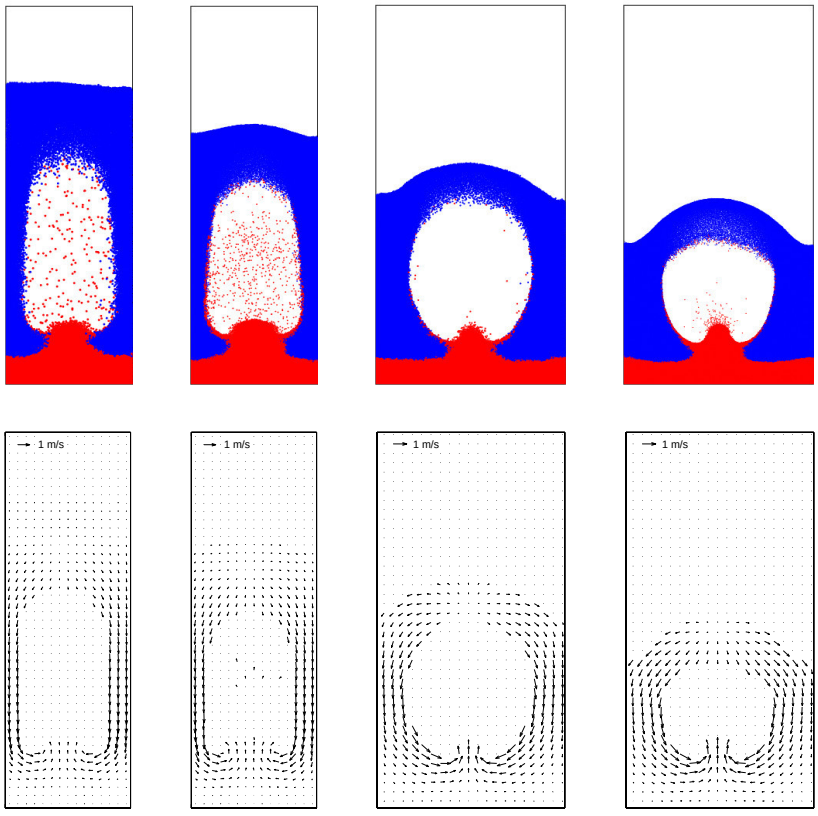

Figure 3.17: Evolution of mixing of a coloured under-layer of particles induced by a single bubble with the DPM with the drag closures by van der Hoef et al. (2005): (a) 2.5 mm particles in 15 cm bed; (b) 1.5 mm particles in 15 cm bed; (c) 2.5 mm particles in 30 cm bed; (d) 1.5 mm particles in 30 cm bed.

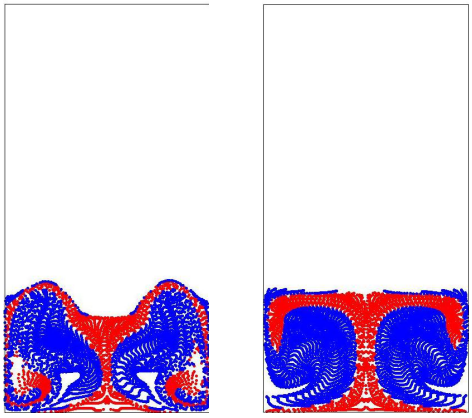

(a) (b)

Figure 3.18: Effect of the solids phase shear viscosity using the CVM: (a) CVM with viscosity of 5 Pa · s; (b) CVM with viscosity of 15 Pa · s.

The TFM, however, largely overpredicts the induced particle mixing as can be seen in Figure 3.15 (d) and (e). This might be explained by the fact that the KTGF only accounts for binary collisions between two particles, where friction between the particles is not included. Omitting friction between the particles and the corresponding additional dissipation of granular energy might result in an under-prediction of the shear viscosity of the solids phase. To show the effect of the shear viscosity on the induced particle mixing, a TFM simulation with a Constant Viscosity Model (CVM) (Patil et al., 2005a,b) instead of the KTGF to describe the solids phase rheology, is shown in Figure 3.18. Increasing the constant viscosity from 5 Pa · s to 15 Pa · s demonstrates that a higher solids viscosity indeed decreases the extent of the particle mixing, however only slightly. The CVM is not able to predict the correct bubble shape when higher shear viscosities are used.

Alternatively, a frictional viscosity model can be used to account for the granular energy dissipation during long-term and multi-particle contacts. The earlier described frictional viscosity models by Laux (1998) and Srivastava and Sundaresan (2003) have both been implemented in the TFM. However, these frictional viscosity models did not improve the TFM simulation results. The model by Laux produced far too high values

for the frictional viscosity, also resulting in a wrong bubble behaviour, and the model by Srivastava and Sundaresan (2003) did not have any effect on the TFM results for the conditions investigated here (Bokkers et al., 2004b). It can be concluded that the frictional viscosity models currently available are not reliable enough to correctly account for the frictional stresses in dense particulate flows, as was also concluded in the work of Huilin et al. (2004) and Goldschmidt (2001).

Effect of coefficient of restitution

An approximate way to account for the additional dissipation of granular energy due to particle-particle friction is via an effective coefficient of restitution. Goldschmidt (2001) showed that the implementation of an effective coefficient of restitution, derived by Jenkins and Zhang (2002), in the dissipation term of the granular temperature equation improved the TFM results significantly. The effective coefficient of restitution can be estimated from:

$$e_{\text{eff}} = e - \frac{\pi}{2}\mu + \frac{9}{2}\mu^2 \tag{3.19}$$

In Figure 3.19 the results are depicted for TFM simulations with and without an effective coefficient of restitution. The extra dissipation of granular energy reduces the mixing of the under-layer of particles slightly, but still the particle mixing is strongly overpredicted.

In Figure 3.20(b) it is shown that a fully developed bubble (at 0.4 s after the bubble injection) simulated with the TFM shows a kind of skirts at the wake of the bubble. This phenomenon is not so pronounced in the DPM results (Figure 3.20(a)). This difference can also be ascribed (partly) to the underprediction of the frictional energy loss with the TFM. Implementation of the effective coefficient of restitution improves the bubble shape to a certain extent, as is depicted in Figure 3.20(c). A closer look at the vector plots in Figures 3.7, 3.9, 3.12 and 3.14 at 0.4 s after injection of the bubble also demonstrates that the emulsion phase velocity predicted by the TFM is too high. The TFM predicts vortices at the wake of the bubble which are not found in the DPM and in the

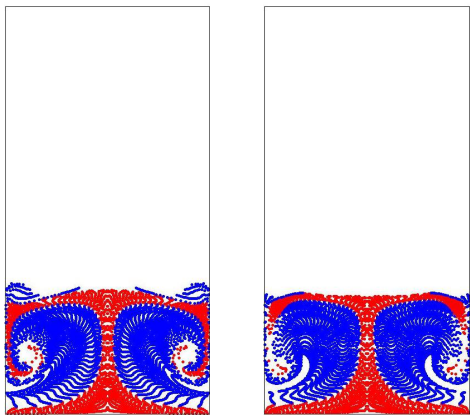

(a) (b)

Figure 3.19: Effect of an effective coefficient of restitution on the induced particle mixing using the TFM with the KTGF: (a) e_{eff}=e=0.97; (b) e_{eff} = 0.86.

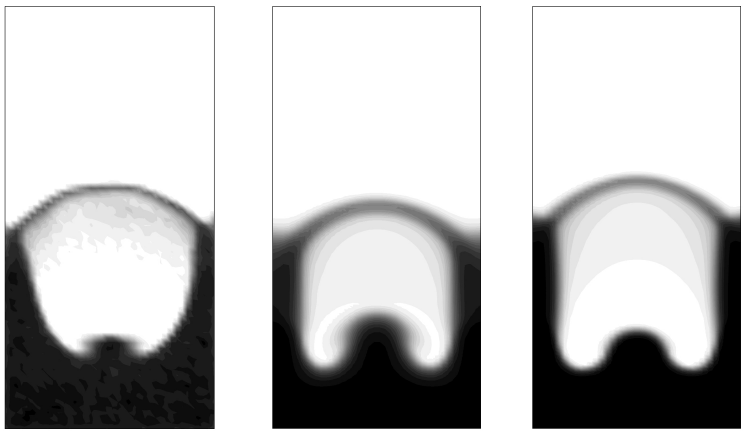

(a) (b) (c)

Figure 3.20: Porosity plots of a single bubble injected in a 30 cm bed filled with 2.5 mm particles: (a) the DPM; (b) the TFM; (c) the TFM with a lower value for the effective coefficient of restitution (e_{eff} = 0.86).

experiment. The amount of energy dissipation in the fluidised bed is directly related to the granular temperature of the particles. The more energy is dissipated the lower the granular temperature will be. In Figures 3.21 and 3.22 a comparison has been made between the granular temperature measured with the extended PIV technique and computed with the DPM and the TFM. The TFM simulation without accounting for friction between the particles predicts a much higher granular temperature in the wake of the bubble compared to the DPM simulation and the experiment. Incorporation of friction via the effective coefficient of restitution results in a lower granular temperature in the wake of the bubble which corresponds much better to the granular temperature predicted by the DPM and the experiment.
From this it can be concluded that accounting for particle-particle friction via an effective coefficient of restitution improves the TFM results significantly, but still is not sufficient to quantitatively predict the extent of particle mixing. It is concluded that, although the friction between the particles is not (fully) incorporated in the TFM resulting in too high solids phase velocities, the level of random fluctuation of the particles (granular temperature) is predicted in the correct order of magnitude by the TFM.

3.7 Conclusions

A comparison has been made between the predictions by a Two Fluid Model based on the Kinetic Theory of Granular Flow and a soft-sphere Discrete Particle Model and experimental results for a pseudo-2D fluidised bed, where a single bubble was injected into a bed of particles at incipient fluidisation conditions. The experiments were carried out in both a small bed (15 cm wide) and in a larger bed (30 cm wide). The particles had a diameter of 1.5 mm and 2.5 mm of which the collision properties were known accurately. Firstly, the behaviour of the bubble injected into a mono-disperse fluidised bed at minimum fluidisation conditions predicted by the TFM and the DPM was compared with the experiments. Subsequently, the extent of mixing of an under-layer of particles was studied with the DPM and the TFM and compared with experiments.

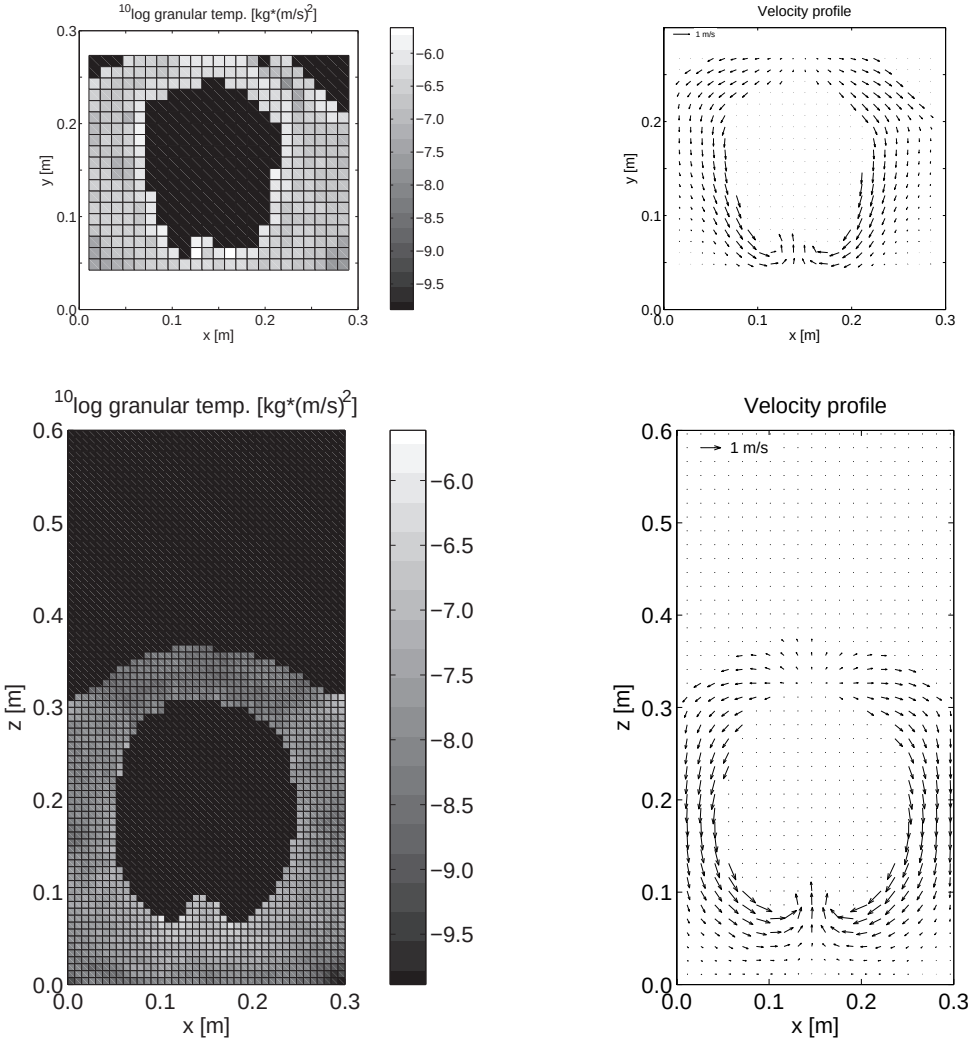

Figure 3.21: Granular temperature and solids velocity profiles around a single bubble injected in a monodisperse fluidised bed of 30 cm wide filled with 2.5 mm particles at 0.3 s after injection; top: Experiment; bottom: DPM (for color figures see Figure A.12).

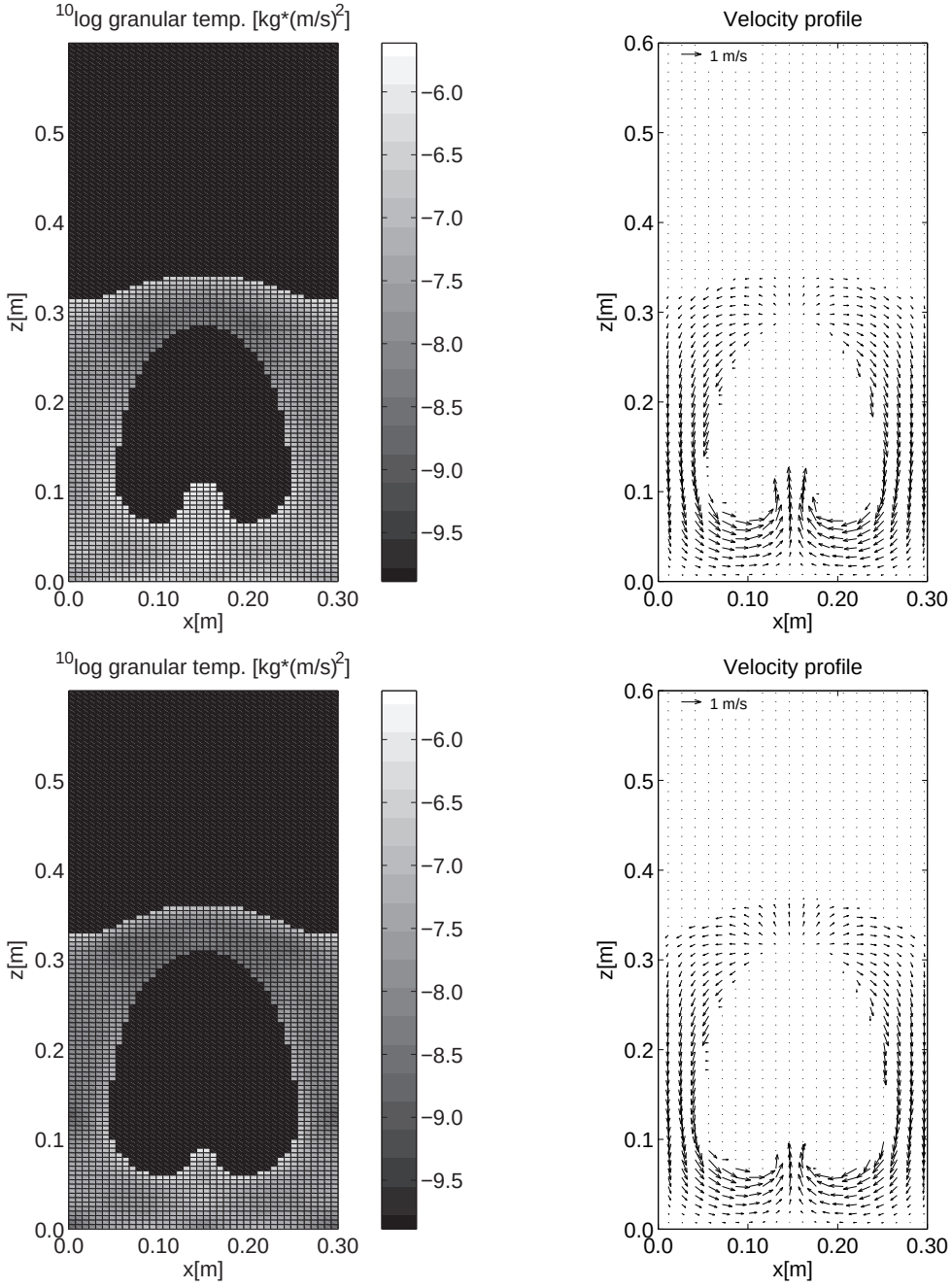

Figure 3.22: Granular temperature and solids velocity profiles around a single bubble injected in a monodisperse fluidised bed of 30 cm wide filled with 2.5 mm particles at 0.3 s after injection; top: TFM; bottom: TFM with e_{eff} = 0.86 (for color figures see Figure A.13).

The TFM and the DPM could well describe the experimentally observed bubble shape, but the bubble size of the injected bubble was somewhat overestimated when using the Ergun/Wen &Yu relations for the gas-particle drag. When using a new drag relation by van der Hoef et al. (2005), based on Lattice-Boltzmann simulations, a slightly better agreement with the experiments was obtained. The bubble injected in the larger fluidised bed had a rounder shape because of the reduced hindrance from the walls, which was well captured by the TFM and the DPM. Also the experimentally observed jet interaction with the particles where particles are tossed upwards into the bubble and the 'raining' of the particles through the roof of the bubbles was reasonably described by the models.

The extent of particle mixing induced by a single bubble injected into the fluidised beds predicted with the DPM corresponded quite well to the experimental findings. The TFM, however, largely overpredicted the particle mixing induced by the bubble. The KTGF does not take into account the friction between two colliding particles resulting in an underprediction of the solids phase (shear) viscosity. Implementation of a frictional viscosity model to account for these long-term and multi-particle contacts did not improve the TFM simulation results. However, using an effective coefficient of restitution to account for the energy dissipation during these long-term, multiple particle contacts, improved the TFM results regarding the granular temperature profile and the shape of the bubble. The amount of particles carried from the under-layer to the top of the bed is however still largely overpredicted. Future research should be focused on the development of reliable frictional viscosity models to be able to further improve the results obtained with continuum models.

Chapter 4

Development of a Multi Fluid Model: derivation and numerical implementation

Abstract

To model the dynamics of mixing and segregation in engineering scale fluidised bed reactors, continuum models have been developed, in which the solids phase rheology is described with the kinetic theory of granular flow. Several authors have derived or used a Multi Fluid Model (MFM) assuming the particle velocities to be (nearly) Maxwellian distributed around different mean velocities and with different granular temperatures for all particle species involved. However, this appears to be inconsistent with the first (equilibrium) approximation obtained from the Chapman-Enskog procedure. Furthermore, it has been shown that segregation rates in binary mixtures of particles predicted with these MFM's are largely overpredicted (Goldschmidt et al., 2001; Huilin et al., 2003a). Therefore, a new set of closure equations for the rheologic properties of multi-component mixtures of slightly inelastic spheres has been derived using the Chapman-Enskog solution procedure of successive approximations. In this theory the particle velocity distribution of all particle species are assumed to be close to Maxwellian distributed around the particle mixture velocity with the particle mixture granular temperature.

A new numerical solution strategy has been devised, referred to the $p - \epsilon_s$ algorithm for multi-component mixtures, which is an extended SIMPLE algorithm that takes the

compressibility of the solids phase directly into account. With this new numerical algorithm much larger time steps can be tolerated (about a factor of 10), especially where regions in the fluidised bed approach the maximum packing density of the particles.

4.1 Introduction

In many fluidised bed applications mixing and segregation phenomena play a very important role. For example, in gas-solid olefin polymerisation reactors the mixing of the polymer particles is essential to avoid hot spots due to the highly exothermic polymerisation reaction. Simultaneously segregation of the larger product particles is effectively used to collect these particles at the bottom of the fluidised bed. Bubbles are known to play an intricate and ambigious role (Rowe and Nienow, 1976). On the one hand, rising bubbles can increase the particle segregation rates by carrying a mixture of particles to the top of the bed disturbing the local packing state of the bed, which might result in segregation of the larger or heavier particles. On the other hand, bubbles induce large scale mixing in the bed equalising the particle size/density distribution. To gain more insight in the rate at which segregation occurs, detailed hydrodynamic models are required that are able to describe the sensitive dynamic equilibrium between particle mixing and segregation, for which a quantitative description of the bubble dynamics is essential.

To study these engineering scale systems with particle size distributions, a continuum approach is required where both the gas and particulate phases are described as continua. Nowadays, the continuum models use the Kinetic Theory of Granular Flow (KTGF) to describe the solids phase rheology, which is derived from the classical kinetic theory of dense gases as described by Chapman and Cowling (1970). To study a system with a particle size distribution or particle density distribution, the KTGF for mono-disperse systems needs to be extended for poly-dispersity. Jenkins and Mancini (1987) proposed a KTGF model for binary mixtures. In their model it was assumed that two species of particles in the mixture have the same granular temperature. However, experiments by Zhang et al. (1996) showed that particles with different diameters possessed unequal turbulence energy in a riser of gas-solid flow. Therefore, Huilin et al. (2000, 2001) derived balance laws and constitutive relations for a binary mixture with *unequal* granular temperatures. In all these Multi Fluid model versions, however,

the particle velocities are assumed to be nearly Maxwellian distributed around *different* mean velocities and *different* granular temperatures for all particle species involved. This assumption appears to be inconsistent with the first (equilibrium) approximation obtained from the Chapman-Enskog procedure, which states that the particle velocity distribution for each species should indeed satisfy a Maxwellian distribution in the equilibrium situation, i.e. in absence of external forces and gradients in porosity, velocity or granular temperature. However, the mean velocity and granular temperature should be *the same* for all the particle species (Jenkins and Mancini, 1989). Furthermore it has been shown in the work of Goldschmidt et al. (2001) and Huilin et al. (2003a) that MFMs using these closure equations largely overpredict the particle segregation rates of binary particle mixtures in freely bubbling fluidised beds. Therefore, a new set of closure relations for the rheologic properties of multi-component mixtures of slightly inelastic spherical particles has been derived using the Chapman-Enskog solution procedure, accurate to the third order Enskog approximation. This derivation is based on the work by López de Haro et al. (1983), Jenkins and Mancini (1989) and Goldschmidt (2001).

Firstly, the derivations of the conservation equations and the closure relations from the kinetic theory of granular flow using the Chapman-Enskog solution procedure are shortly presented. Subsequently, a new solution strategy has been developed that accounts for the compressibility of the solids phase in a direct way. This is necessary to avoid numerical instabilities introduced by the strong non-linear dependency of the radial distribution function close to the maximum packing fraction of the solids.

4.2 Kinetic theory of granular flow of multi-component mixtures

In the Kinetic Theory of Granular Flow (KTGF) particle-particle interactions in a granular medium are modelled following the Chapman-Enskog approach for dense gases (Chapman and Cowling, 1970). However, two important differences should be noted between a dense gas and a mixture of macroscopic bodies. The first difference is that

particles in a granular medium dissipate kinetic fluctuating energy due to inelastic particle-particle collisions. Furthermore, the particles in a granular medium will be subjected to a drag force exerted by the fluidising gas.

4.2.1 Definitions

The kinetic theory of granular flow of multi-component mixtures describes the mean and fluctuating motion of particles of all species (1..NP) based on the assumption that the velocity distribution $f_n(\vec{c}_n, \vec{r}, t)$ of individual particles of species n, among a large number $n_n d\vec{r}$ of particles within an ensemble of volume $d\vec{r}$, can be represented by the distribution of their velocity points $\vec{c}_n$ in the velocity space. The number of particles of species n per unit volume and the ensemble average of a particle quantity ϕ_n are respectively defined by:

$$n_n = \int f_n(\vec{c}_n, \vec{r}, t) d\vec{c}_n \tag{4.1}$$

$$< \phi_n >= \frac{1}{n_n} \int \phi_n f_n(\vec{c}_n, \vec{r}, t) d\vec{c}_n \tag{4.2}$$

Defining the mean velocity $\vec{u}_n$ of particle species n as $< \vec{c}_n >$, the mass average mixture velocity $\vec{u}_s$ is given by:

$$\vec{u}_s = \frac{1}{\epsilon_s \rho_s} \sum_{n=1}^{\mathrm{NP}} \epsilon_n \rho_n \vec{u}_n \tag{4.3}$$

where the particle number density n_s, total solids volume fraction ϵ_s and the mixture density ρ_s are defined as

$$n_s = \sum_{n=1}^{\mathrm{NP}} n_n \tag{4.4}$$

$$\epsilon_s = \sum_{n=1}^{\mathrm{NP}} \epsilon_n \qquad \text{with} \qquad \epsilon_n = n_n \frac{\pi \sigma_n^3}{6} \tag{4.5}$$

$$\rho_s = \frac{1}{\epsilon_s} \sum_{n=1}^{\mathrm{NP}} \epsilon_n \rho_n \qquad \text{with} \qquad \rho_n = m_n \frac{6}{\pi \sigma_n^3} \tag{4.6}$$

The actual particle velocity $\vec{c}_n$ is decomposed in a local mean velocity $\vec{u}_s$ and the random fluctuating velocity $\vec{C}_n$:

$$\vec{c}_n = \vec{u}_s + \vec{C}_n \tag{4.7}$$

To quantify the random fluctuating velocity, Savage and Jeffrey (1981) defined the term granular temperature, given in the following relation:

$$\theta_n = \frac{1}{3} m_n < C_n^2 > \tag{4.8}$$

from which the mixture granular temperature is obtained by

$$\theta_s = \frac{1}{n_s} \sum_{n=1}^{\mathrm{NP}} n_n \theta_n \tag{4.9}$$

The diffusion velocity of species n is defined as:

$$\vec{v}_n =< \vec{C}_n >= \vec{u}_n - \vec{u}_s \tag{4.10}$$

and naturally satisfies

$$\sum_{n=1}^{\mathrm{NP}} \epsilon_n \rho_n \vec{v}_n = 0 \tag{4.11}$$

The KTGF accounts for two transport mechanisms for particulate properties, i.e. mass, momentum and kinetic energy. One way is to transport a property during free flight between the collisions (kinetic transport). On the other hand particle properties can be transported during collisions. To model these transport mechanisms the generalised Boltzmann equation for particulate mixtures is employed, describing the rate of change of the velocity distribution f_n of species n, moving under influence of an external force $\vec{F}_n$ and colliding with particles of all species present in the particle mixture:

$$\frac{\partial f_n}{\partial t} + \vec{c}_n \cdot \frac{\partial f_n}{\partial \vec{r}} + \frac{\partial}{\partial \vec{c}_n} \cdot \left(\frac{\vec{F}_n}{m_n} f_n \right) =$$

$$\sum_p \iint_{(\vec{c}_{12_{np}} \cdot \vec{k}) \geq 0} \left\{ f_{np}^{(2)}(\vec{c}\,'_{1_n}, \vec{r}, \vec{c}\,'_{2_p}, \vec{r} - \sigma_{np}\vec{k}, t) - f_{np}^{(2)}(\vec{c}_{1_n}, \vec{r}, \vec{c}_{2_p}, \vec{r} + \sigma_{np}\vec{k}, t) \right\} \sigma_{np}^2 (\vec{c}_{12_{np}} \cdot \vec{k}) d\vec{k} d\vec{c}_{2_p} \tag{4.12}$$

where $f(\vec{c}, \vec{r}, t) d\vec{r} d\vec{c}$ represents the probable number of particles present at time t in a volume $d\vec{r}$ at position $\vec{r}$ possessing a velocity between $\vec{c}$ and $\vec{c} + d\vec{c}$. The pair distribution function $f_{np}^{(2)}$ is defined in such a way that $f_{np}^{(2)}(\vec{c}_{1_n}, \vec{r}_1; \vec{c}_{2_p}, \vec{r}_2; t) d\vec{r}_1 d\vec{r}_2 d\vec{c}_{1_n} d\vec{c}_{2_p}$ represents the probability of finding a pair of particles in the volume $d\vec{r}_1 d\vec{r}_2$ centred on points

$\vec{r}_1, \vec{r}_2$ and having velocities within the ranges $\vec{c}_{1_n}$ and $\vec{c}_{1_n} + d\vec{c}_{1_n}$ and $\vec{c}_{2_p}$ and $\vec{c}_{2_p} + d\vec{c}_{2_p}$. In this equation $\sigma_{np} = (\sigma_n + \sigma_p)/2$ is the inter-particle distance, $\vec{c}_{12_{np}} = \vec{c}_{1_n} - c_{2_p}$ the relative velocity of particle 1 of species n to particle 2 of species p and $\vec{k}$ the unit vector directed from the center of particle 1 to the centre of particle 2. The particle velocities after collision, $\vec{c}\,'_{1_n}$ and $\vec{c}\,'_{2_p}$, can be related to the velocities prior to collision according to:

$$\vec{c}\,'_{1_n} = \vec{c}_{1_n} - \frac{m_p}{m_n + m_p}(1 + e_{np})(\vec{c}_{12_{np}} \cdot \vec{k})\vec{k} \tag{4.13}$$

$$\vec{c}\,'_{2_p} = \vec{c}_{2_p} + \frac{m_n}{m_n + m_p}(1 + e_{np})(\vec{c}_{12_{np}} \cdot \vec{k})\vec{k} \tag{4.14}$$

where e_{np} represents the coefficient of normal restitution for collisions between particles of species n and p, defined by the following relation for the relative velocity prior and after collision:

$$\vec{c}\,'_{12_{np}} \cdot \vec{k} = -e_{np}(\vec{c}_{12_{np}} \cdot \vec{k}) \tag{4.15}$$

4.2.2 Conservation equations

The Boltzmann equation as shown in equation 4.12 can be transformed to the ensemble average transport equation for particle property ϕ_n by multiplying with $\phi_n d\vec{c}_n$ and integrating over the entire velocity space, yielding:

$$\int \phi_n \frac{\partial f_n}{\partial t} d\vec{c}_n + \int \phi_n \vec{c}_n \cdot \frac{\partial f_n}{\partial \vec{r}} d\vec{c}_n + \int \phi_n \frac{\partial}{\partial \vec{c}_n} \cdot \left(\frac{\vec{F}_n}{m_n} f_n \right) d\vec{c}_n = \sum_{p=1}^{\mathrm{NP}} n_n \Delta_p \phi_n \tag{4.16}$$

in which the term on the right hand side represents the rate of change of property ϕ_n due to collisions with particles of species p, which is decomposed in a collisional source $\chi_{np}(\phi_n)$ and a collisional flux $\theta_{np}(\phi_n)$ according to:

$$n_n \Delta_p \phi_n = \chi_{np}(\phi_n) - \frac{\partial}{\partial \vec{r}} \cdot \theta_{np}(\phi_n) \tag{4.17}$$

Applying the chain rule to the kinetic transport terms on the left hand side of equation 4.18 and expanding $n_n \Delta_p \phi_n$ into Taylor series, the Maxwell transport equation is

obtained:

$$\frac{\partial < n_n \phi_n >}{\partial t} + \frac{\partial}{\partial \vec{r}} \cdot < n_n \phi_n \vec{c}_n > =$$
$$n_n < \frac{\partial \phi_n}{\partial t} > + < n_n \vec{c}_n \cdot \frac{\partial \phi_n}{\partial \vec{r}} > + < \frac{n_n \vec{F}_n}{m_n} \cdot \frac{\partial \phi_n}{\partial \vec{c}_n} > + \sum_{p=1}^{\mathrm{NP}} \left[\chi_{np}(\phi_n) - \frac{\partial}{\partial \vec{r}} \cdot \theta_{np}(\phi_n) \right] \tag{4.18}$$

with

$$\chi_{np}(\phi_n) = \sigma_{np}^2 \iiint_{\vec{c}_{12_{np}} \cdot \vec{k} > 0} (\phi'_{1_n} - \phi_{1_n}) \left[1 + \sum_{m=1}^{\infty} \frac{1}{(2m)!} \left(\frac{1}{2} \sigma_{np} \vec{k} \cdot \frac{\partial}{\partial r} \right)^{2m} \right] \tag{4.19}$$
$$f_{np}^{(2)}(\vec{c}_{1_n}, \vec{r} - \frac{1}{2}\sigma_{np}\vec{k}, \vec{c}_{2_p}, \vec{r} + \frac{1}{2}\sigma_{np}\vec{k})(\vec{c}_{12_{np}} \cdot \vec{k}) d\vec{k} d\vec{c}_{1_n} d\vec{c}_{2_p}$$

$$\vec{\theta}_{np}(\phi_n) = -\frac{1}{2}\sigma_{np}^3 \cdot \iiint_{\vec{c}_{12_{np}} \cdot \vec{k} > 0} (\phi'_{1_n} - \phi_{1_n}) \left[1 + \sum_{m=1}^{\infty} \frac{1}{(2m+1)!} \left(\frac{1}{2} \sigma_{np} \vec{k} \cdot \frac{\partial}{\partial r} \right)^{2m} \right] \tag{4.20}$$
$$f_{np}^{(2)}(\vec{c}_{1_n}, \vec{r} - \frac{1}{2}\sigma_{np}\vec{k}, \vec{c}_{2_p}, \vec{r} + \frac{1}{2}\sigma_{np}\vec{k})(\vec{c}_{12_{np}} \cdot \vec{k}) \vec{k} d\vec{k} d\vec{c}_{1_n} d\vec{c}_{2_p}$$

The conservation equations for mass, momentum and fluctuating kinetic energy for each species n can be obtained from the Maxwell transport equation (see equation 4.18) by substituting the particle property $\phi_n = m_n$, $m_n \vec{c}_n$ and $\frac{1}{2} m_n c_n^2$ respectively. In Table 4.1 the mixture conservation equations are listed which are obtained by summing the conservation equations for all species. The definitions used in these balances are listed as well. The external forces that have been taken into account in the momentum equation are gravity, buoyancy and drag exerted by the gas phase:

$$\frac{\vec{F}_n}{m_n} = \vec{g} - \frac{1}{\rho_n} \nabla P_g + \frac{\beta_{ng}}{n_n m_n} (\vec{c}_g - \vec{c}_n) \tag{4.21}$$

The momentum source term $\vec{\beta}_{np}$ vanishes upon summation of the individual momentum balances. For evaluation of the defined transport coefficients explicit functions for the particle velocity distribution function f_n and the pair distribution function $f_{np}^{(2)}$ are required.

Table 4.1: Conservation equations obtained from the Maxwell transport equation.

Species continuity equation:

$$\frac{\partial}{\partial t}(\epsilon_n \rho_n) + \nabla \cdot \left[\vec{J}_n + \epsilon_n \rho_n \vec{u}_s\right] = 0$$

where $\vec{J}_n = \epsilon_n \rho_n < \vec{C}_n >$

Mixture continuity equation:

$$\frac{\partial}{\partial t}(\epsilon_s \rho_s) + \nabla \cdot (\epsilon_s \rho_s \vec{u}_s) = 0$$

Mixture momentum equation:

$$\frac{\partial}{\partial t}(\epsilon_s \rho_s \vec{u}_s) + \nabla \cdot (\epsilon_s \rho_s \vec{u}_s \vec{u}_s) = -\epsilon_s \nabla P_g - \nabla \cdot \overline{\overline{\tau}}_s - \nabla P_s + \sum_{n=1}^{\mathrm{NP}} \beta_{ng}(\vec{u}_g - \vec{u}_n) + \epsilon_s \rho_s \vec{g}$$

where $P_s^s \overline{\overline{I}} + \overline{\overline{\tau}}_s = \sum_{n=1}^{\mathrm{NP}} \left(n_n m_n < \vec{C}_n \vec{C}_n > + \sum_{p=1}^{\mathrm{NP}} \theta_{np}(m_n \vec{c}_n) \right)$

Mixture granular temperature equation:

$$\frac{3}{2}\left[\frac{\partial(n_s \theta_s)}{\partial t} + \nabla \cdot (n_s \theta_s \vec{u}_s)\right] = -(P_s^s \overline{\overline{I}} + \overline{\overline{\tau}}_s) : \nabla \vec{u}_s - \nabla \cdot q_s - \sum_{n=1}^{\mathrm{NP}} 3\frac{\beta_{ng}}{m_n}\theta_n - \gamma_s$$

where $\vec{q}_s = \sum_{n=1}^{\mathrm{NP}} \left(\frac{1}{2} n_n m_n < C_n^2 \vec{C}_n > + \sum_{p=1}^{\mathrm{NP}} \theta_{np}(\frac{1}{2} m_n C_n^2) \right)$

and $\gamma_s = -\sum_{n=1}^{\mathrm{NP}} \sum_{p=1}^{\mathrm{NP}} \chi_{np}(\frac{1}{2} m_n c_n^2)$

4.2.3 Velocity distribution and pair distribution function

The pair distribution function at contact $f_{np}^{(2)}(\vec{c}_{1_n}, \vec{r} - \frac{1}{2}\sigma_{np}\vec{k}, \vec{c}_{2_p}, \vec{r} + \frac{1}{2}\sigma_{np}\vec{k}, t)$ can be approximated by the product of two single-particle velocity distribution functions and the radial distribution function $g_{np}(\vec{r} - \frac{1}{2}\sigma_{np}\vec{k}, \vec{r} + \frac{1}{2}\sigma_{np}\vec{k}, t)$. Following Enskog (Chapman and Cowling, 1970), assuming binary interactions and 'molecular' chaos, i.e. information on the particle velocity of a certain particle is lost after only a few collisions, this

approximation yields:

$$f_{np}^{(2)}(\vec{c}_{1_n}, \vec{r} - \frac{1}{2}\sigma_{np}\vec{k}, \vec{c}_{2_p}, \vec{r} + \frac{1}{2}\sigma_{np}\vec{k}, t) = \\ g_{np}(\vec{r} - \frac{1}{2}\sigma_{np}\vec{k}, \vec{r} + \frac{1}{2}\sigma_{np}\vec{k}, t) f_n(\vec{c}_{1_n}, \vec{r} - \frac{1}{2}\sigma_{np}\vec{k}, t) f_p(\vec{c}_{2_p}, \vec{r} + \frac{1}{2}\sigma_{np}\vec{k}, t) \tag{4.22}$$

where the radial distribution function g_{np} corrects the probability of a collision for the effect of the volume occupied by the particles.

In order to avoid conflicts with irreversible thermodynamics that arise for multi-size particle mixtures when the radial distribution function is evaluated at a specific point on the line joining the midpoints of the two colliding particles at contact, van Beijeren and Ernst (1973) proposed the so-called Revised Enskog Theory (RET). According to this theory a non-local functional of the particle density field is taken for the radial distribution function, which give rise to gradients of the chemical potential of all species n present in the particle mixture instead of the gradient of the radial distribution function that appears in the standard Enskog theory. The detailed expressions for the particle velocity distribution functions for multi-component mixtures of inelastic spheres derived in this work are based on the work by López de Haro et al. (1983) and Jenkins and Mancini (1987) who also employed the RET.

The particle velocity distribution function of species n can now be obtained by solving the generalised Boltzmann equation as presented in equation 4.12. This equation is solved using the Chapman-Enskog solution method of successive approximation (Chapman and Cowling, 1970):

$$f_n = f_n^{(0)} + f_n^{(1)} + f_n^{(2)} + \dots \tag{4.23}$$

Here the terms up to the second approximation are taken into account. The first approximation of the velocity distribution function $f_n^{(0)}$ satisfies the well-known Maxwell distribution function:

$$f_n^{(0)} = n_n \left(\frac{m_n}{2\pi\theta_s}\right)^{\frac{3}{2}} e^{-\frac{m_n(\vec{c}_n - \vec{u}_s)^2}{2\theta_s}} \tag{4.24}$$

In the derivation of the first approximation it is assumed that the system is in steady state, the particles are not subjected to external forces, the particles are uniformly sus-

pended and that no kinetic energy is dissipated in collisions ($e_{np} = 1$). In the second approximation the effects of spatial gradients and energy dissipation are taken into account and the velocity distribution function is written as a function of the perturbation on the Maxwell distribution function, according to the Chapman-Enskog solution procedure:

$$f_n = f_n^{(0)} + f_n^{(1)} = f_n^{(0)}(1 + \Phi_n^{(1)}) \tag{4.25}$$

Substitution of equation 4.25 in the generalised Boltzmann equation (equation 4.12) results in the following partial differential-integral equation for $\Phi_n^{(1)}$:

$$\begin{aligned}\sum_{p=1}^{\mathrm{NP}} n_n n_p g_{np} I_{np}(\Phi_n^{(1)} + \Phi_p^{(1)}) = - f_n^{(0)} \Bigg\{ & \left(1 + \frac{8\pi}{5} \sum_{p=1}^{\mathrm{NP}} n_p \sigma_{np}^3 \frac{m_n m_p}{(m_n + m_p)^2} g_{np}\right) \\ & \left(\mathbb{C}_{1_n}^2 - \frac{5}{2}\right) \vec{C}_{1_n} \cdot \nabla \ln \theta_s \\ & + \left(1 + \frac{8\pi}{15} \sum_{p=1}^{\mathrm{NP}} n_p \sigma_{np}^3 \frac{m_p}{m_n + m_p} g_{np}\right) 2\vec{\mathbb{C}}_{1_n}{}^{0} \vec{\mathbb{C}}_{1_n} : \nabla \vec{u}_s \\ & + \frac{2}{3} \left(1 + \frac{4\pi}{3} \sum_{p=1}^{\mathrm{NP}} n_p \sigma_{np}^3 \frac{m_p}{m_n + m_p} g_{np} - \frac{P_s^{s(0)}}{n_s \theta_s}\right) \\ & \left(\mathbb{C}_{1_n}^2 - \frac{3}{2}\right) \nabla \cdot \vec{u}_s + \frac{n_s}{n_n} \vec{C}_{1_n} \cdot \vec{d}_n \Bigg\}\end{aligned} \tag{4.26}$$

The collisional integral in this equation is defined as:

$$I_{np}(F) = \frac{1}{n_n n_p} \iint\limits_{(\vec{c}_{12_{np}} \cdot \vec{k}) \geq 0} f_{1_n}^{(0)} f_{2_p}^{(0)} (F - F') \sigma_{np}^2 (\vec{c}_{12_{np}} \cdot \vec{k}) d\vec{k} d\vec{c}_{2_p} \tag{4.27}$$

and the dimensionless peculiar velocity is given by:

$$\vec{\mathbb{C}}_n = \sqrt{\frac{m_n}{2\theta_s}} \vec{C}_n \tag{4.28}$$

The diffusion force $\vec{d}_n$ is obtained by applying the revised Enskog theory and is defined

as:

$$\begin{aligned}\vec{d}_n = &-\frac{\epsilon_n\rho_n}{\epsilon_s\rho_s n_s\theta_s}\left[\nabla P_s^{(0)} + \sum_{p=1}^{\mathrm{NP}}\left(\epsilon_n\rho_n\frac{\vec{F}_{\vec{u},n}}{m_n} - \epsilon_p\rho_p\frac{\vec{F}_{\vec{u},p}}{m_n}\right)\right] \\ &+ \frac{n_n}{n_s}\sum_{p=1}^{\mathrm{NP}}\left[\delta_{np} + \frac{4\pi}{3}\frac{m_n}{m_n+m_p}n_p\sigma_{np}^3 g_{np}\right]\nabla\ln\theta_s + \frac{n_n}{n_s\theta_s}\sum_{p=1}^{\mathrm{NP}}\left(\frac{\partial\mu_n}{\partial n_p}\right)_{\theta_s,n_{k\neq p}}\nabla n_p\end{aligned} \tag{4.29}$$

which satisfies the following relation:

$$\sum_{n=1}^{\mathrm{NP}}\vec{d}_n = 0 \tag{4.30}$$

For the external forces exerted upon the species n gravity, buoyancy and gas-particle drag are taken into account:

$$\frac{\vec{F}_{\vec{u},n}}{m_n} = \vec{g} - \frac{1}{\rho_n}\nabla P_g + \frac{\beta_{ng}}{n_n m_n}(\vec{u}_g - \vec{u}_n) \tag{4.31}$$

and the first order approximation for the particulate phase pressure reads:

$$P_s^{(0)} = \theta_s\left(n_s + \frac{2\pi}{3}\sum_{n=1}^{\mathrm{NP}}\sum_{p=1}^{\mathrm{NP}} n_n n_p\sigma_{np}^3 g_{np}\right) \tag{4.32}$$

Since the left-hand side of equation 4.26 is linear in $\Phi_n^{(1)}$ and the right-hand side linear in gradients of macroscopic quantities of different tensorial character, $\Phi_n^{(1)}$ can be written as (see López de Haro et al. (1983)):

$$\begin{aligned}\Phi_n^{(1)} = &-\frac{1}{n_s}A_n(\mathbb{C}_n)\vec{C}_n\cdot\nabla\ln\theta_s - \frac{1}{n_s}B_n(\mathbb{C}_n)\vec{\mathbb{C}}_n^{\,0}\vec{\mathbb{C}}_n : \nabla\vec{u}_s \\ &- \frac{1}{n_s}\sum_{i=1}^{\mathrm{NP}}D_n^{(i)}(\mathbb{C}_n)\vec{C}_n\cdot\vec{d}_i + \frac{1}{n_s}H_n(\mathbb{C}_n)\nabla\cdot\vec{u}_s\end{aligned} \tag{4.33}$$

In this equation $A_n, B_n, D_n^{(i)}$ and H_n are functions of C_n, which are expanded in a set of orthonormal functions, the Sonine polynomials, to obtain the following definite ex-

pressions:

$$
\begin{aligned}
A_n(\mathbb{C}_n) &= -\frac{m_n}{2\theta_s}\sum_{r=0}^{\mathrm{N}-1} a_r^n S_{3/2}^{(r)}(\mathbb{C}_n^2) \\
B_n(\mathbb{C}_n) &= \frac{m_n}{2\theta_s}\sum_{r=0}^{\mathrm{N}-1} b_r^n S_{5/2}^{(r)}(\mathbb{C}_n^2) \\
H_n(\mathbb{C}_n) &= \sum_{r=0}^{\mathrm{N}-1} h_r^n S_{1/2}^{(r)}(\mathbb{C}_n^2) \\
D_n^{(i)}(\mathbb{C}_n) &= \frac{m_n}{2\theta_s}\sum_{r=0}^{\mathrm{N}-1} d_{n,r}^i S_{3/2}^{(r)}(\mathbb{C}_n^2)
\end{aligned}
\tag{4.34}
$$

The Sonine polynomials have been defined as:

$$
S_m^{(n)}(x) = \sum_{p=0}^{n}(-x)^p \frac{(m+n)_{n-p}}{p!(n-p)!} \tag{4.35}
$$

where r_q denotes the product of the q factors $r, r-1, \ldots, r-q+1$. The coefficients a_r^n, b_r^n, h_r^n and $d_{n,r}^i$ are obtained by solving the sets of equations given in Table 4.2. Explicit expressions for the bracket integrals for hard spheres up to the third order Enskog approximation, appearing in Table 4.2, have been given by Ferziger and Kaper (1972) and López de Haro et al. (1983), and can also be found in Goldschmidt (2001).

It is important to note that in the Enskog solution procedure the first order approximation corresponds to the situation that the particulate suspension is in steady state and at equilibrium, i.e. the particles are not subjected to external forces, the particles are uniformly suspended (no gradients in solids volume fraction and velocity and granular energy) and that no kinetic energy is dissipated in the particle-particle collisions ($e_{np} = 1$). Thus, the first order approximation requires that the particle velocities of all particle species are distributed around *the same mean velocity* (the mixture velocity) with *the same granular temperature* (the mixture temperature). This is in contrast with the equations derived by Manger (1996); Mathiesen (1997); Huilin et al. (2001); Rahaman et al. (2003), who assumed that the first order approximation to the particle velocity distribution is Maxwellian distributed around *different* mean velocities and *different* granular temperatures for all particle species involved. Hence, in this work differences in

Table 4.2: Sonine coefficients.

$$K_n = 1 + \frac{8\pi}{5}\sum_{p=1}^{\mathrm{NP}} n_p\sigma_{np}^3\frac{m_n m_p}{m_0^2}g_{np} \qquad K_n'' = 1 + \frac{4\pi}{3}\sum_{p=1}^{\mathrm{NP}} n_p\sigma_{np}^3\frac{m_p}{m_0}g_{np} - \frac{P_s^{s(0)}}{n_s\theta_s}$$

$$K_n' = 1 + \frac{8\pi}{15}\sum_{p=1}^{\mathrm{NP}} n_p\sigma_{np}^3\frac{m_p}{m_0}g_{np}$$

$$\Lambda_{np}^{qr} = g_{np}\frac{8}{75}\frac{\sqrt{m_n m_p}}{\theta_s}\left\{\delta_{np}\sum_{l=1}^{\mathrm{NP}}\frac{n_n n_l}{n_s^2}\left[S_{3/2}^{(q)}(\mathbb{C}_n^2)\vec{\mathbb{C}}_n, S_{3/2}^{(r)}(\mathbb{C}_n^2)\vec{\mathbb{C}}_n\right]_{nl}' + \frac{n_n n_p}{n_s^2}\left[S_{3/2}^{(q)}(\mathbb{C}_n^2)\vec{\mathbb{C}}_n, S_{3/2}^{(r)}(\mathbb{C}_n^2)\vec{\mathbb{C}}_n\right]_{np}''\right\}$$

$$H_{np}^{qr} = g_{np}\frac{2}{5\theta_s}\left\{\delta_{np}\sum_{l=1}^{\mathrm{NP}}\frac{n_n n_l}{n_s^2}\left[S_{5/2}^{(q)}(\mathbb{C}_n^2)\vec{\mathbb{C}}_n\,{}^{0}\vec{\mathbb{C}}_n, S_{5/2}^{(r)}(\mathbb{C}_n^2)\vec{\mathbb{C}}_n\,{}^{0}\vec{\mathbb{C}}_n\right]_{nl}'\right.$$
$$\left. + \frac{n_n n_p}{n_s^2}\left[S_{5/2}^{(q)}(\mathbb{C}_n^2)\vec{\mathbb{C}}_n\,{}^{0}\vec{\mathbb{C}}_n, S_{5/2}^{(r)}(\mathbb{C}_n^2)\vec{\mathbb{C}}_n\,{}^{0}\vec{\mathbb{C}}_n\right]_{np}''\right\}$$

$$\Gamma_{np}^{qr} = g_{np}\left\{\delta_{np}\sum_{l=1}^{\mathrm{NP}}\frac{n_n n_l}{n_s^2}\left[S_{1/2}^{(q)}(\mathbb{C}_n^2), S_{1/2}^{(r)}(\mathbb{C}_n^2)\right]_{nl}' + \frac{n_n n_p}{n_s^2}\left[S_{1/2}^{(q)}(\mathbb{C}_n^2), S_{1/2}^{(r)}(\mathbb{C}_n^2)\right]_{np}''\right\}$$

$$\Delta_{np}^{qr} = g_{np}\frac{\sqrt{m_n m_p}}{\theta_s}\left\{\delta_{np}\sum_{l=1}^{\mathrm{NP}}\frac{n_n n_l}{n_s^2}\left[S_{3/2}^{(q)}(\mathbb{C}_n^2)\vec{\mathbb{C}}_n, S_{3/2}^{(r)}(\mathbb{C}_n^2)\vec{\mathbb{C}}_n\right]_{nl}' + \frac{n_n n_p}{n_s^2}\left[S_{3/2}^{(q)}(\mathbb{C}_n^2)\vec{\mathbb{C}}_n, S_{3/2}^{(r)}(\mathbb{C}_n^2)\vec{\mathbb{C}}_n\right]_{np}''\right\}$$

Sonine coefficient $a_r^{(n)}$

$$\sum_{p=1}^{\mathrm{NP}}\sum_{r=0}^{\mathrm{N}-1}\Lambda_{np}^{qr}a_r^{(p)} = \frac{4}{5}\frac{n_n}{n_s}K_n\delta_{q1} \qquad (n = 1, 2, \cdots, \mathrm{NP}; q = 0, 1, \cdots, \mathrm{N}-1)$$

$$\sum_{n=1}^{\mathrm{NP}}\frac{\epsilon_n\rho_n}{\epsilon_s\rho_s}a_0^{(n)} = 0 \qquad (n = 1; q = 0)$$

Sonine coefficient $b_r^{(n)}$

$$\sum_{p=1}^{\mathrm{NP}}\sum_{r=0}^{\mathrm{N}-1}H_{np}^{qr}b_r^{(p)} = \frac{2}{\theta_s}\frac{n_n}{n_s}K_n'\delta_{q0} \qquad (n = 1, 2, \cdots, \mathrm{NP}; q = 0, 1, \cdots, \mathrm{N}-1)$$

Sonine coefficient $d_{n,r}^{(l)}$

$$\sum_{p=1}^{\mathrm{NP}}\sum_{r=0}^{\mathrm{N}-1}\Delta_{np}^{qr}d_{p,r}^{(l)} = 3(\delta_{nl} - \frac{\epsilon_n\rho_n}{\epsilon_s\rho_s})\delta_{q0} \quad (l, n = 1, 2, \cdots, \mathrm{NP}; q = 0, 1, \cdots, \mathrm{N}-1)$$

$$\sum_{n=1}^{\mathrm{NP}}\frac{\epsilon_n\rho_n}{\epsilon_s\rho_s}d_{n,0}^{(l)} = 0 \qquad (n = 1; q = 0; l = 1, 2, \cdots, \mathrm{NP})$$

Sonine coefficient $h_r^{(n)}$

$$\sum_{p=1}^{\mathrm{NP}}\sum_{r=1}^{\mathrm{N}-1}\Gamma_{np}^{qr}h_r^{(p)} = \frac{n_n}{n_s}K_n''\delta_{q1} \qquad (n = 1, 2, \cdots, \mathrm{NP}; q = 1, \cdots, \mathrm{N}-1)$$

$$\sum_{n=1}^{\mathrm{NP}}\frac{n_n}{n_s}h_1^{(n)} = 0 \qquad (n = 1; q = 1)$$

the granular temperatures for the different particle species and particle segregation are higher order effects arising from the first order perturbation function.

4.2.4 Radial distribution function and chemical potential

The radial distribution function g_{np} is required to obtain an explicit expression for the pair distribution function according to equation 4.22. In order to fulfill the condition for the diffusion force equation (equation 4.30) it is important that the radial distribution function and the chemical potential both result from the same equation of state. The radial distribution function for a multi-component hard-sphere mixture can be derived from the compressibility of a single-component hard-sphere system (Santos et al., 1999):

$$g_{np} = \frac{1}{1-\epsilon_s} + \left[g_0 - \frac{1}{1-\epsilon_s} \right] \frac{< \sigma^{(2)} > \sigma_n \sigma_p}{< \sigma^{(3)} > \sigma_{np}} \tag{4.36}$$

where

$$< \sigma^{(n)} >= \sum_{i=1}^{\mathrm{NP}} \frac{n_i}{n_s} \sigma_i^n \tag{4.37}$$

The radial distribution function for a mono-disperse hard-sphere fluid is given in its general form by:

$$g_0(\epsilon_s) = \frac{\sum_{n=0}^{8} c_n \epsilon_s^n}{(1-(\epsilon_s/\epsilon_s^{max})^a)^b} \tag{4.38}$$

of which the coefficients given by Song et al. (1988) are listed in Table 4.3.

Table 4.3: Values for the coefficients for the radial distribution function (equation 4.38).

ϵ_s^{max}	0.6435	c_3	$0.01472 \cdot 4^3$
a	1	c_4	$0.0005396 \cdot 4^4$
b	0.76	c_5	$-0.0003574 \cdot 4^5$
c_0	1	c_6	$-0.0005705 \cdot 4^6$
c_1	$0.3298 \cdot 4$	c_7	$-0.0001212 \cdot 4^7$
c_2	$0.08867 \cdot 4^2$	c_8	$-0.0001151 \cdot 4^8$

The general expression for the chemical potential of species n in a hard-sphere system is given by:

$$\mu_n = \theta_s \ln n_n + \theta_s \ln \Lambda_n^3 + \mu_n^{ex} \tag{4.39}$$

in which Λ_n is the equivalent of the De Broglie wavelength for granular materials. The excess chemical potential μ_n^{ex} of component n in a mixture of NP species is given by:

$$\mu_n^{ex} = \theta_s y_n^{(3)} [f^I z^I + f^{II} z^{II}] + g_n^I a^I + g_n^{II} a^{II} \tag{4.40}$$

All the expressions needed to calculate the excess chemical potential are summarised in Table 4.4. For the derivation of the excess chemical potential for a multi-component hard-sphere mixture the interested reader is referred to the work by Goldschmidt (2001).

Table 4.4: Expressions needed to calculate the excess chemical potential.

$$z^I = 4\epsilon_s \frac{\sum_{n=0}^{8} c_n \epsilon_s^n}{(1-(\epsilon_s/\epsilon_s^{max})^a)^b} \qquad z^{II} = \frac{\epsilon_s}{1-\epsilon_s}$$

$$f^I = \frac{1}{2}(m_1 + m_2) \qquad f^{II} = 1 + m_1 - 2m_2$$

$$m_1 = \frac{< \sigma^{(1)} >< \sigma^{(2)} >}{< \sigma^{(3)} >} \qquad m_2 = \frac{< \sigma^{(2)} >^3}{< \sigma^{(3)} >^2}$$

$$< \sigma^{(n)} > = \sum_{i=1}^{\mathrm{NP}} \frac{n_i}{n_s} \sigma_i^n$$

$$a^I = 4\theta_s \epsilon_s^{max} \sum_{n=0}^{8} c_n (\epsilon_s^{max})^n \sum_{m=0}^{n} \frac{(-1)^m}{m-b+1} \binom{n}{m} \left[1 - \left(1 - \frac{\epsilon_s}{\epsilon_s^{max}} \right)^{m-b+1} \right]$$

$$a^{II} = -\theta_s \ln(1-\epsilon_s)$$

$$g_n^I = \frac{1}{2} \left[m_1 (y_n^{(1)} + y_n^{(2)} - y_n^{(3)}) + m_2 (3y_n^{(2)} - 2y_n^{(3)}) \right]$$

$$g_n^{II} = 1 + m_1 (y_n^{(1)} + y_n^{(2)} - y_n^{(3)}) - 2m_2 (3y_n^{(2)} - 2y_n^{(3)})$$

$$y_i^{(n)} = \frac{\sigma_i^n}{< \sigma^{(n)} >}$$

4.2.5 Constitutive equations

With the expressions found for the velocity distribution function and the perturbation function given in equations 4.24, 4.25 and 4.33 the constitutive relations defined in Table 4.1 can be derived up to first order in the gradients. All the required constitutive relations are listed in Table 4.5 and 4.6.

Table 4.5: Constitutive equations of the Multi Fluid Model (1).

Diffusion flux of phase n:

$$\vec{J}_n^{(1)} = -\frac{\epsilon_n \rho_n}{2n_s}\left[\sum_{l=1}^{\mathrm{NP}} d_{n,0}^{(l)} \vec{d}_l - a_0^{(n)} \nabla \log \theta_s\right]$$

Diffusion velocity of phase n:

$$\vec{v}_n = \vec{u}_n - \vec{u}_s = \frac{\vec{J}_n^{(1)}}{\epsilon_n \rho_n}$$

Granular temperature of phase n:

$$\theta_n = \theta_s \left(1 - \frac{h_1^{(n)}}{n_s}(\nabla \cdot \vec{u}_s)\right)$$

Solids phase pressure:

$$P_s^{(1)} = \theta_s \left(n_s + \frac{2\pi}{3}\sum_{n=1}^{\mathrm{NP}}\sum_{p=1}^{\mathrm{NP}} n_n n_p \sigma_{np}^3 \frac{1+e_{np}}{2} g_{np}\right)$$

Solids phase stress tensor:

$$\bar{\bar{\tau}}_s^{(1)} = -\left(\lambda_s^{(1)} - \frac{2}{3}\mu_s^{(1)}\right)(\nabla \cdot \vec{u}_s)\bar{\bar{I}} - \mu_s^{(1)}\left((\nabla \vec{u}_s) + (\nabla \vec{u}_s)^T\right)$$

Solids phase shear viscosity:

$$\mu_s^{(1)} = \frac{\theta_s}{2n_s}\sum_{n=1}^{\mathrm{NP}}\left(1 + \frac{8\pi}{15}\sum_{p=1}^{\mathrm{NP}} n_p \sigma_{np}^3 \frac{m_p}{m_n+m_p}\frac{1+e_{np}}{2} g_{np}\right) n_n b_0^{(n)}$$
$$+ \frac{4}{15}\sqrt{\pi\theta_s}\sum_{n=1}^{\mathrm{NP}}\sum_{p=1}^{\mathrm{NP}} n_n n_p \sigma_{np}^4 \left(\frac{2m_n m_p}{m_n+m_p}\right)^{\frac{1}{2}} \frac{1+e_{np}}{2} g_{np}$$

Table 4.6: Constitutive equations of the Multi Fluid Model (2).

Solids phase bulk viscosity:

$$\lambda_s^{(1)} = \frac{4\pi}{3}\frac{\theta_s}{n_s}\sum_{n=1}^{\mathrm{NP}}\sum_{p=1}^{\mathrm{NP}} n_n n_p \sigma_{np}^3 \frac{m_p}{m_n+m_p}\frac{1+e_{np}}{2} g_{np} h_1^{(n)}$$
$$+ \frac{4}{9}\sqrt{\pi\theta_s}\sum_{n=1}^{\mathrm{NP}}\sum_{p=1}^{\mathrm{NP}} n_n n_p \sigma_{np}^4 \left(\frac{2m_n m_p}{m_n+m_p}\right)^{\frac{1}{2}} \frac{1+e_{np}}{2} g_{np}$$

Granular energy dissipation:

$$\gamma_s^{(1)} = \pi\theta_s \sum_{n=1}^{\mathrm{NP}}\sum_{p=1}^{\mathrm{NP}} n_n n_p \sigma_{np}^3 \frac{m_p}{m_n+m_p}(1-e_{np}^2) g_{np}\left[\frac{4}{\sigma_{np}}\left(\frac{(m_n+m_p)\theta_s}{2\pi m_n m_p}\right)^{\frac{1}{2}} - \nabla\cdot\vec{u}_s\right]$$

Granular energy flux:

$$\vec{q}_s{}^{(1)} = -\frac{5}{4}\frac{\theta_s}{n_s}\sum_{n=1}^{\mathrm{NP}}\left(1+\frac{24\pi}{15}\sum_{p=1}^{\mathrm{NP}} n_p\sigma_{np}^3\frac{m_n m_p}{(m_n+m_p)^2}\frac{1+e_{np}}{2}g_{np}\right) n_n\left(a_1^{(n)}\nabla\ln\theta_s - \sum_{l=1}^{\mathrm{NP}} d_{n,1}^{(l)}\vec{d}_l\right)$$
$$- \frac{4}{3}\theta_s\sum_{n=1}^{\mathrm{NP}}\sum_{p=1}^{\mathrm{NP}}\left(\frac{2\pi m_n m_p\theta_s}{m_n+m_p}\right)^{\frac{1}{2}}\frac{n_n n_p}{m_n+m_p}\sigma_{np}^4\frac{1+e_{np}}{2}g_{np}\nabla\ln\theta_s$$
$$+ \frac{2\pi}{3}\theta_s\sum_{n=1}^{\mathrm{NP}}\sum_{p=1}^{\mathrm{NP}} n_p\sigma_{np}^3\left(\frac{m_n-m_p}{m_n+m_p}\right)\frac{1+e_{np}}{2}g_{np}\frac{\vec{J}_n^{(1)}}{m_n}$$
$$+ \frac{5}{2}\theta_s\sum_{n=1}^{\mathrm{NP}}\left(1+\frac{2\pi}{3}\sum_{p=1}^{\mathrm{NP}} n_p\sigma_{np}^3\frac{1+e_{np}}{2}g_{np}\right)\frac{\vec{J}_n^{(1)}}{m_n}$$

Pseudo-thermal conductivity:

$$\kappa_s^{(1)} = \frac{5}{4}\frac{1}{n_s}\sum_{n=1}^{\mathrm{NP}}\left(1+\frac{24\pi}{15}\sum_{p=1}^{\mathrm{NP}} n_p\sigma_{np}^3\frac{m_n m_p}{(m_n+m_p)^2}\frac{1+e_{np}}{2}g_{np}\right) n_n a_1^{(n)}$$
$$+ \frac{4}{3}\sum_{n=1}^{\mathrm{NP}}\sum_{p=1}^{\mathrm{NP}}\left(\frac{2\pi m_n m_p\theta_s}{m_n+m_p}\right)^{\frac{1}{2}}\frac{n_n n_p}{m_n+m_p}\sigma_{np}^4\frac{1+e_{np}}{2}g_{np}$$

4.3 Numerical solution method

The Multi Fluid Model presented here consists of the total continuity and Navier-Stokes equations for the continuous gas phase and the species and mixture continuity equations, the mixture Navier-Stokes equations and the mixture granular temperature equation for the solids phase. A numerically advantageous feature of this MFM is that only the mixture Navier-Stokes equations and mixture granular temperature equation need to be solved, since explicit expressions have been derived for all the transport properties of the particulate phases in terms of the mixture velocity and the mixture granular temperature. This is in strong contrast to other Multi Fluid models presented in the literature (Manger, 1996; Mathiesen, 1997; Huilin et al., 2001; Rahaman et al., 2003), where a Navier-Stokes equation and a granular temperature equation has to be solved for every particle species present in the solids mixture.

The MFM governing equations are solved with a finite difference technique on a staggered grid using an extended version of the SIMPLE algorithm (Patankar, 1980). A detailed description of the SIMPLE algorithm applied to constant viscosity Two-Fluid models has been presented by Kuipers et al. (1993). In principle this method can also be applied to the MFM equations. However, for lower values of the coefficient of normal restitution the numerical stability of this algorithm strongly deteriorates due to the strong non-linear dependence of the particle pressure on the solids fraction, resulting in unacceptably small time steps required to solve the model equations ($10^{-5} - 10^{-6}$ s). Therefore Goldschmidt (2001) presented a new numerical algorithm for the Two-Fluid model equations, referred to as the $p - \epsilon_s$ algorithm. In this algorithm an additional Poisson equation is solved (sequentially) for the total solids volume fraction field, taking into account the compressibility of the solids phase. This algorithm is here extended to the Multi-Fluid Model. Due to the enhanced numerical stability larger time steps can be handled ($10^{-4} - 10^{-5}$ s) with this method, even for strongly dissipative systems.

In the following sections the governing equations are presented in their discretised

form and the solution procedure of the finite difference equations is given. Finally, the numerical implementation of the diffusion force equation is addressed.

4.3.1 Discretisation of the governing equations

All the conservation equations, i.e. the mass balance, momentum balance and the granular temperature equation, are discretised following a standard finite difference technique. The gas phase continuity equation is discretised using first order time differencing and the convective terms are treated fully implicitly:

$$\begin{aligned}(\epsilon_g\rho_g)^{n+1}_{i,j,k} - (\epsilon_g\rho_g)^{n}_{i,j,k} + \frac{\delta t}{\delta x}\left\{\langle\epsilon_g\rho_g u_{g,x}\rangle^{n+1}_{i+\frac{1}{2},j,k} - \langle\epsilon_g\rho_g u_{g,x}\rangle^{n+1}_{i-\frac{1}{2},j,k}\right\} \\ + \frac{\delta t}{\delta y}\left\{\langle\epsilon_g\rho_g u_{g,y}\rangle^{n+1}_{i,j+\frac{1}{2},k} - \langle\epsilon_g\rho_g u_{g,y}\rangle^{n+1}_{i,j-\frac{1}{2},k}\right\} \\ + \frac{\delta t}{\delta z}\left\{\langle\epsilon_g\rho_g u_{g,z}\rangle^{n+1}_{i,j,k+\frac{1}{2}} - \langle\epsilon_g\rho_g u_{g,z}\rangle^{n+1}_{i,j,k-\frac{1}{2}}\right\} = 0\end{aligned} \tag{4.41}$$

where $n+1$ and n refer to the new and old time level respectively. The convective mass fluxes, but also the momentum and granular energy fluxes are computed following the second order accurate Barton scheme (Centrella and Wilson, 1984). The solids phase continuity equation is computed with exactly the same equation with the subscript g replaced with s.

The x-momentum equation for the solids phase is discretised according to the following equation:

$$(\epsilon_s\rho_s\vec{u}_s)^{*}_{i+\frac{1}{2},j,k} = (A)^{n}_{i+\frac{1}{2},j,k} + \delta t\left[-\nabla P^s_s - \epsilon_s\nabla P_g + \sum_{n=1}^{NP}\beta_{ng}(\vec{u}_g - \vec{u}_s)\right]^{*}_{i+\frac{1}{2},j,k} \tag{4.42}$$

in which the gas phase pressure gradient, the solids pressure gradient and the source term for gas-particle interaction are taken fully implicitly. It should be noted that the momentum transfer coefficient β_{ng} is linearised. The other terms are treated explicitly and collected in the term $(A)^{n}_{i+\frac{1}{2},j,k}$. The equations for the y- and z-direction are derived in a similar manner. The gas phase momentum equations can be obtained from equation 4.42 by replacing the subscript s with g and leave out the solids pressure gradient term.

The granular energy equation is discretised according to:

$$\left\{\frac{3}{2}(n_s)^*_{i,j,k}+\delta t\left[(\frac{\partial P^s_s}{\partial\theta_s})^n_{i,j,k}\nabla\cdot\vec{u}_s+\sum_{p=1}^{\mathrm{NP}}3\frac{(\beta_{pg})^n_{i,j,k}}{m_p}(1-(\frac{h_1^{(p)}}{n_s})^n_{i,j,k}(\nabla\cdot\vec{u}_s))+(\frac{\partial\gamma_s}{\partial\theta_s})^n_{i,j,k}\right]\right\}(\theta_s)^{n+1}_{i,j,k}$$

$$+\delta t\begin{bmatrix}\frac{1}{\delta x^2}((\kappa)^*_{i+\frac{1}{2},j,k}+(\kappa)^*_{i-\frac{1}{2},j,k})\\+\frac{1}{\delta y^2}((\kappa)^*_{i,j+\frac{1}{2},k}+(\kappa)^*_{i,j-\frac{1}{2},k})\\+\frac{1}{\delta z^2}((\kappa)^*_{i,j,k+\frac{1}{2}}+(\kappa)^*_{i,j,k-\frac{1}{2}})\end{bmatrix}(\theta_s)^{n+1}_{i,j,k}-\delta t\begin{bmatrix}\frac{1}{\delta x^2}((\kappa)^*_{i+\frac{1}{2},j,k}(\theta_s)^{n+1}_{i+1,j,k}+(\kappa)^*_{i-\frac{1}{2},j,k}(\theta_s)^{n+1}_{i-1,j,k})\\+\frac{1}{\delta y^2}((\kappa)^*_{i,j+\frac{1}{2},k}(\theta_s)^{n+1}_{i,j+1,k}+(\kappa)^*_{i,j-\frac{1}{2},k}(\theta_s)^{n+1}_{i,j-1,k})\\+\frac{1}{\delta z^2}((\kappa)^*_{i,j,k+\frac{1}{2}}(\theta_s)^{n+1}_{i,j,k+1}+(\kappa)^*_{i,j,k-\frac{1}{2}}(\theta_s)^{n+1}_{i,j,k-1})\end{bmatrix}$$

$$=\frac{3}{2}(n_s)^n_{i,j,k}(\theta_s)^n_{i,j,k}+\delta t\left\{-\frac{3}{2}(n_s\theta_s\vec{u}_s)^*_{i,j,k}+(\overline{\overline{\tau}}_s:\nabla\vec{u}_s)^*_{i,j,k}-(\nabla\cdot\vec{q}_{s,phys})^*_{i,j,k}-(\gamma_s)^*_{i,j,k}+(\frac{\partial\gamma_s}{\partial\theta_s})^*_{i,j,k}(\theta_s)^*_{i,j,k}\right\} \tag{4.43}$$

where the superscript * indicates that these terms are evaluated with the most recently computed θ_s^* (within the Newton-Raphson iteration). The granular energy dissipation term is treated semi-implicitly.

4.3.2 Solution procedure of the finite difference equations

The solution procedure of the MFM consists of a sequence of computational cycles or time steps with a length of δt. In one cycle all the governing and constitutive equations are solved to obtain the new key variables at time level $n+1$. The computational cycle consists of two parts. Firstly, in the explicit part, the sonine coefficients are computed from the sets of equations given in Table 4.2. Furthermore, the diffusion fluxes and velocities are computed from the diffusion force equation (equation 4.29) and the explicit terms A^n, B^n and C^n in the momentum equations are determined. Thereafter, the Newton-Raphson iteration is started, where the pressure and void fractions are calculated for the entire computational domain. The iteration loop consists of several steps and will stop when the mass deficits for the gas and the solids phase are below a specified accuracy. Firstly, the mass residuals $(D_g)_{i,j,k}$ and $(D_s)_{i,j,k}$ are determined from the continuity equations:

$$\begin{aligned}(D_g)_{i,j,k}&=(\epsilon_g\rho_g)^{n+1}_{i,j,k}-(\epsilon_g\rho_g)^n_{i,j,k}+\frac{\delta t}{\delta x}\left\{\langle\epsilon_g\rho_g u_{g,x}\rangle^{n+1}_{i+\frac{1}{2},j,k}-\langle\epsilon_g\rho_g u_{g,x}\rangle^{n+1}_{i-\frac{1}{2},j,k}\right\}\\&+\frac{\delta t}{\delta y}\left\{\langle\epsilon_g\rho_g u_{g,y}\rangle^{n+1}_{i,j+\frac{1}{2},k}-\langle\epsilon_g\rho_g u_{g,y}\rangle^{n+1}_{i,j-\frac{1}{2},k}\right\}+\frac{\delta t}{\delta z}\left\{\langle\epsilon_g\rho_g u_{g,z}\rangle^{n+1}_{i,j,k+\frac{1}{2}}-\langle\epsilon_g\rho_g u_{g,z}\rangle^{n+1}_{i,j,k-\frac{1}{2}}\right\}\end{aligned} \tag{4.44}$$

$$
\begin{aligned}
(D_s)_{i,j,k} &= (\epsilon_s\rho_s)^{n+1}_{i,j,k} - (\epsilon_s\rho_s)^{n}_{i,j,k} + \frac{\delta t}{\delta x}\left\{\langle\epsilon_s\rho_s u_{s,x}\rangle^{n+1}_{i+\frac{1}{2},j,k} - \langle\epsilon_s\rho_s u_{s,x}\rangle^{n+1}_{i-\frac{1}{2},j,k}\right\} \\
&+ \frac{\delta t}{\delta y}\left\{\langle\epsilon_s\rho_s u_{s,y}\rangle^{n+1}_{i,j+\frac{1}{2},k} - \langle\epsilon_s\rho_s u_{s,y}\rangle^{n+1}_{i,j-\frac{1}{2},k}\right\} + \frac{\delta t}{\delta z}\left\{\langle\epsilon_s\rho_s u_{s,z}\rangle^{n+1}_{i,j,k+\frac{1}{2}} - \langle\epsilon_s\rho_s u_{s,z}\rangle^{n+1}_{i,j,k-\frac{1}{2}}\right\}
\end{aligned}
\tag{4.45}
$$

When the convergence criteria are not satisfied a whole field pressure correction is computed following the next equation:

$$
\begin{aligned}
(J_g)^n_{i-1,j,k}\delta(P_g)^*_{i-1,j,k} + (J_g)^n_{i+1,j,k}\delta(P_g)^*_{i+1,j,k} + (J_g)^n_{i,j-1,k}\delta(P_g)^*_{i,j-1,k} + (J_g)^n_{i,j+1,k}\delta(P_g)^*_{i,j+1,k} \\
+ (J_g)^n_{i,j,k-1}\delta(P_g)^*_{i,j,k-1} + (J_g)^n_{i,j,k+1}\delta(P_g)^*_{i,j,k+1} = -(D_g)^*_{i,j,k}
\end{aligned}
\tag{4.46}
$$

where $(J_g)^n$ is the Jacobi matrix for the gas phase. The Jacobi matrix can be obtained by taking the derivative of the mass residual D_g to the gas phase pressure. The matrix element $(J_g)^n_{i+1,j,k}$ for example has the following form:

$$
(J_g)^n_{i+1,j,k} = -\left(\frac{\delta t}{\delta x}\right)^2 (\epsilon_g)^n_{i+\frac{1}{2},j,k} - \left(\frac{\delta t}{\delta x}\right)\left(\frac{\partial(u_{g,x})^n_{i+\frac{1}{2},j,k}}{\partial(P_g)_{i+1,j,k}} - \frac{\partial(u_{s,x})^n_{i+\frac{1}{2},j,k}}{\partial(P_g)_{i+1,j,k}}\right)\delta t \sum_{p=1}^{NP}\beta^n_{gp,i+\frac{1}{2},j,k} \tag{4.47}
$$

where the derivatives of the velocities to the pressure can easily be obtained from:

$$
\begin{bmatrix}
(\epsilon_g\rho_g)^n_{i+\frac{1}{2},j,k} + \delta t\sum_{p=1}^{NP}\beta^n_{gp,i+\frac{1}{2},j,k} & -\delta t\sum_{p=1}^{NP}\beta^n_{gp,i+\frac{1}{2},j,k} \\
-\delta t\sum_{p=1}^{NP}\beta^n_{gp,i+\frac{1}{2},j,k} & (\epsilon_s\rho_s)^n_{i+\frac{1}{2},j,k} + \delta t\sum_{p=1}^{NP}\beta^n_{gp,i+\frac{1}{2},j,k}
\end{bmatrix}
\begin{bmatrix}
\dfrac{\partial(u_{g,x})^n_{i+\frac{1}{2},j,k}}{\partial(P_g)_{i+1,j,k}} \\
\dfrac{\partial(u_{s,x})^n_{i+\frac{1}{2},j,k}}{\partial(P_g)_{i+1,j,k}}
\end{bmatrix} =
$$

$$
\begin{bmatrix}
-\epsilon^n_{g,i+\frac{1}{2},j,k}\dfrac{\delta t}{\delta x} \\
-\epsilon^n_{s,i+\frac{1}{2},j,k}\dfrac{\delta t}{\delta x}
\end{bmatrix}
\tag{4.48}
$$

The same procedure can be followed to determine the other elements of the Jacobi matrix. Equation 4.46 is solved using a robust ICCG sparse matrix solver. When the new pressure field is computed, the gas phase densities can be updated.
In the next step a whole field solids volume fraction correction is computed following the same procedure as the pressure field correction and is solved with the following

equation:

$$\begin{aligned}(J_s)^n_{i-1,j,k}\delta(\epsilon_s)^*_{i-1,j,k} + (J_s)^n_{i+1,j,k}\delta(\epsilon_s)^*_{i+1,j,k} + (J_s)^n_{i,j-1,k}\delta(\epsilon_s)^*_{i,j-1,k} + (J_s)^n_{i,j+1,k}\delta(\epsilon_s)^*_{i,j+1,k} \\ + (J_s)^n_{i,j,k-1}\delta(\epsilon_s)^*_{i,j,k-1} + (J_s)^n_{i,j,k+1}\delta(\epsilon_s)^*_{i,j,k+1} = -(D_s)^*_{i,j,k}\end{aligned} \tag{4.49}$$

where $(J_s)^n$ is the solids phase Jacobi matrix which can be obtained by taking the derivative of the solids phase mass deficit D_s to the volume fraction of the particle phase. The matrix element $(J_s)^n_{i+1,j,k}$ for example yields:

$$\begin{aligned}(J_s)^n_{i+1,j,k} = &-\frac{1}{2}\left(\frac{\delta t}{\delta x}\right)^2\left((P_g)^n_{i+1,j,k} - (P_g)^n_{i,j,k}\right) - \left(\frac{\delta t}{\delta x}\right)^2\left(\frac{\partial P_s}{\partial \epsilon_s}\right)^n_{i+1,j,k} \\ &+ \left(\frac{\delta t}{\delta x}\right)\left(\frac{\partial (u_{g,x})^n_{i+\frac{1}{2},j,k}}{\partial(\epsilon_s)_{i+1,j,k}} - \frac{\partial (u_{s,x})^n_{i+\frac{1}{2},j,k}}{\partial(\epsilon_s)_{i+1,j,k}}\right)\delta t\sum_{p=1}^{NP}\beta^n_{gp,i+\frac{1}{2},j,k}\end{aligned} \tag{4.50}$$

in which the derivatives of the velocities to the solids volume fraction can easily be obtained from:

$$\begin{bmatrix} (\epsilon_g\rho_g)^n_{i+\frac{1}{2},j,k} + \delta t\sum_{p=1}^{NP}\beta^n_{gp,i+\frac{1}{2},j,k} & -\delta t\sum_{p=1}^{NP}\beta^n_{gp,i+\frac{1}{2},j,k} \\ -\delta t\sum_{p=1}^{NP}\beta^n_{gp,i+\frac{1}{2},j,k} & (\epsilon_s\rho_s)^n_{i+\frac{1}{2},j,k} + \delta t\sum_{p=1}^{NP}\beta^n_{gp,i+\frac{1}{2},j,k} \end{bmatrix}\begin{bmatrix} \dfrac{\partial (u_{g,x})^n_{i+\frac{1}{2},j,k}}{\partial(\epsilon_s)_{i+1,j,k}} \\ \dfrac{\partial (u_{s,x})^n_{i+\frac{1}{2},j,k}}{\partial(\epsilon_s)_{i+1,j,k}} \end{bmatrix} =$$

$$\begin{bmatrix} \dfrac{1}{2}\dfrac{\delta t}{\delta x}\left((P_g)^n_{i+1,j,k} - (P_g)^n_{i,j,k}\right) + \dfrac{1}{2}(\rho_g)^n_{i+1,j,k}(u_{g,x})^n_{i+\frac{1}{2},j,k} \\ -\dfrac{1}{2}\dfrac{\delta t}{\delta x}\left((P_g)^n_{i+1,j,k} - (P_g)^n_{i,j,k}\right) - \dfrac{\delta t}{\delta x}\left(\dfrac{\partial P_s}{\partial \epsilon_s}\right)^n_{i+1,j,k} - \dfrac{1}{2}(\rho_s)^n_{i+1,j,k}(u_{s,x})^n_{i+\frac{1}{2},j,k} \end{bmatrix} \tag{4.51}$$

In equation 4.50 it is clearly shown that the compressibility of the solids phase is incorporated in the Jacobi matrix of the solids phase. This will result in a numerically much more stable algorithm for fluidised bed systems with fractions close to the maximum packing fraction. When the new volume fractions are obtained, the new macroscopic densities for both the gas and the solids phase are calculated. Subsequently the new species fractions are computed from the individual species mass balances using the

following equations:

$$(\epsilon_n\rho_n)^{n+1}_{i,j,k} = (\epsilon_n\rho_n)^{n}_{i,j,k} - \frac{\delta t}{\delta x}\left\{\langle\epsilon_n\rho_n u_{n,x}\rangle^{n+1}_{i+\frac{1}{2},j,k} - \langle\epsilon_n\rho_n u_{n,x}\rangle^{n+1}_{i-\frac{1}{2},j,k}\right\} - \frac{\delta t}{\delta y}\left\{\langle\epsilon_n\rho_n u_{n,y}\rangle^{n+1}_{i,j+\frac{1}{2},k} - \langle\epsilon_n\rho_n u_{n,y}\rangle^{n+1}_{i,j-\frac{1}{2},k}\right\} - \frac{\delta t}{\delta z}\left\{\langle\epsilon_n\rho_n u_{n,z}\rangle^{n+1}_{i,j,k+\frac{1}{2}} - \langle\epsilon_n\rho_n u_{n,z}\rangle^{n+1}_{i,j,k-\frac{1}{2}}\right\} + (x^*_n D_s)_{i,j,k} \tag{4.52}$$

$$(\epsilon_n)^{n+1}_{i,j,k} = (\epsilon_n\rho_n)^{n+1}_{i,j,k}/\rho_n \tag{4.53}$$

The species velocity u_n used in the convective flux terms is the sum of the diffusion velocity of species n calculated explicitly in the beginning of the cycle and the solids mixture velocity calculated from the solids momentum equation. The last term in the right hand side of equation 4.52 is needed to make sure that the sum of the individual species fractions equals the total solids mixture volume fraction. From the updated species volume fractions the new species fractions x_n are calculated:

$$(x_n)^{n+1}_{i,j,k} = (\epsilon_n)^{n+1}_{i,j,k}/(\epsilon_s)^{n+1}_{i,j,k} \tag{4.54}$$

In the end of the iteration loop the new solids pressure is computed and the new gas and solids phase velocities are obtained from the coupled momentum equations. Finally, the new mass deficits are computed again and the convergence criteria are checked.

The granular temperature equation (equation 4.43) is solved sequentially at the end of the cycle in a separate (Newton-Raphson) iteration loop. The numerical solution procedure is schematically depicted in Figure 4.1.

4.3.3 Diffusion force equation

The implementation of the diffusion force equation in the MFM needs some further attention. As was mentioned before the diffusion force equation has to satisfy the following rule:

$$\sum_{n=1}^{\mathrm{NP}} \vec{d}_n = 0 \tag{4.55}$$

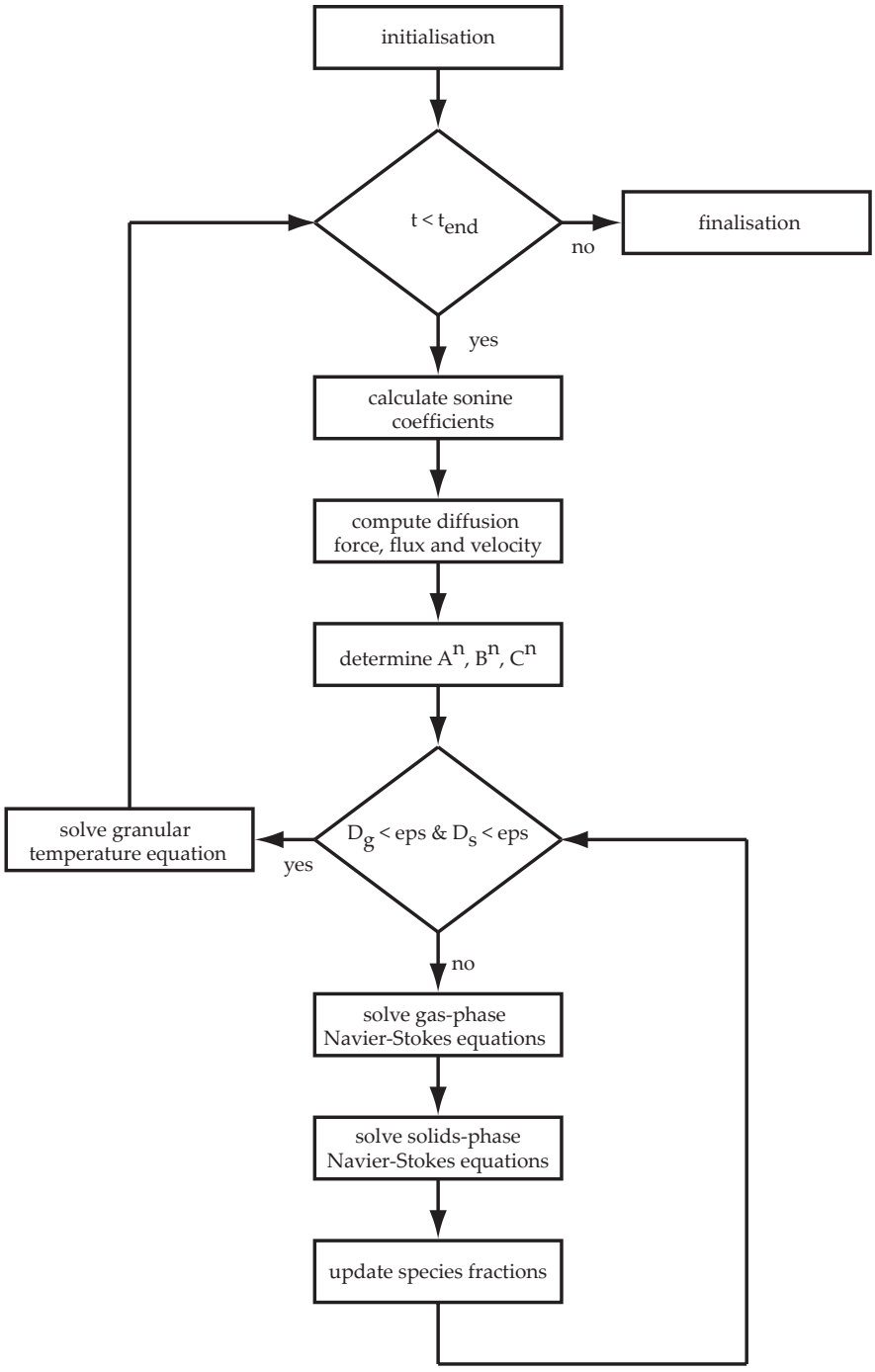

Figure 4.1: Computational flow diagram of the Multi Fluid Model.

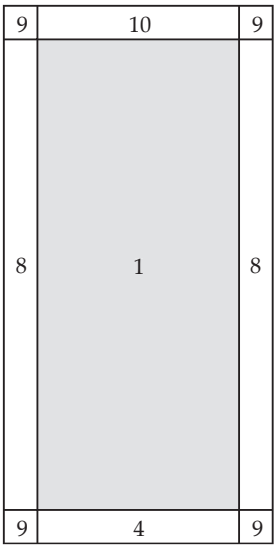

Figure 4.2: Flag matrix used in the flow solver.

Table 4.7: Cell flags and their corresponding boundary conditions.

Flag	Boundary conditions
1	Interior cell, no boundary condition
4	Prescribed influx for gas
8	no-slip for gas and free-slip for particles
9	Corner cell, no boundary condition
10	Prescribed pressure for gas and impermeable no slip for particles

Since the rate of segregation computed with the MFM is determined by the diffusion velocity of the species, which are directly computed from the diffusion forces, it is of primary importance that the sum of the diffusion forces in the MFM equals exactly zero. In order to satisfy this in the MFM, the diffusion force equation should be implemented in the code as a function of the key variables only (i.e. $\epsilon_s, n_s, \theta_s$). Therefore the gradient of the solids pressure and the derivative of the chemical potential to n_p need to be derived analytically in order to ensure that all the terms in the diffusion force equation (equation 4.29) cancel exactly against each other upon summation over all species. In Appendix A.1 a derivation is shown how to obtain an analytical expression for the gradient of the particle pressure. The derivative of the chemical potential can easily be obtained by differentiating all the expressions given in Table 4.4 with respect to n_p.

4.3.4 Boundary conditions

The hydrodynamic boundary conditions used in the flow solver of the MFM are listed in Table 4.7. In Figure 4.2 a schematic picture is shown of the flag matrix (see also Kuipers et al., 1993). The gas flows into the computational domain via a prescribed in-

flux cell and at the top of the bed a prescribed pressure boundary is applied. At the side walls a no-slip boundary condition is applied for the gas phase and a free slip boundary for the solids phase. For the granular temperature a zero-gradient boundary condition is applied, since particle-wall interactions play a minor role in dense gas-solid fluidised beds. For dilute multi-disperse systems the boundary conditions proposed by Sinclair and Jackson (1989) could be extended.

4.4 Conclusions

A new Multi Fluid Model based on the kinetic theory of granular flow for multi-component systems was presented using the Chapman-Enskog solution method of successive approximations for the description of multi-disperse gas-solid fluidised beds. In this theory particle segregation and unequal granular temperatures in multi-disperse systems arise from higher order (nonequilibrium) effects described with the first order perturbation function.

Due to the tendency of inelastic particles to contract into high-density clusters and the strong non-linearity of the particle pressure near the maximum packing density, special care is necessary with the numerical implementation of the MFM. A modified SIMPLE algorithm, the so called $p - \epsilon_s$ algorithm, which was applied earlier to Two-Fluid models by Goldschmidt (2001), has been extended to Multi-Fluid Models. With the new numerical algorithm time steps about 10 times as large as within the conventional SIMPLE algorithm for Two-Fluid models can be tolerated, enormously decreasing the required calculation times.

In the next chapter the performance of this new MFM for the description of particle segregation in binary freely bubbling fluidised beds is assessed.

A.1 Diffusion force equation

The diffusion force equation (see equation 4.29) consists of two parts that cannot be computed straightforwardly; the gradient of the particle pressure and the derivative of the chemical potential. The derivative of the chemical potential can be obtained by differentiating equation 4.39 with respect to n_p together with the terms listed in Table 4.4. In this appendix an analytical derivation is given of the gradient of the particle pressure, containing a gradient of the radial distribution function which needs some further attention.

The zeroth order particle pressure equation is given by:

$$P_s^{s(0)} = \sum_{n=1}^{\mathrm{NP}} P_n^{s(0)} = \theta_s \left[n_s + \frac{2\pi}{3} \sum_{n=1}^{\mathrm{NP}} \sum_{p=1}^{\mathrm{NP}} n_n n_p \sigma_{np}^3 g_{np} \right] \tag{A.1}$$

where

$$\sigma_{np} = \frac{\sigma_n + \sigma_p}{2} \tag{A.2}$$

The total derivative yields:

$$\begin{aligned} \nabla P_s^{s(0)} &= \nabla \left[\theta_s \left(n_s + \frac{2\pi}{3} \sum_{n=1}^{\mathrm{NP}} \sum_{p=1}^{\mathrm{NP}} n_n n_p \sigma_{np}^3 g_{np} \right) \right] \\ &= n_s \nabla \theta_s + \theta_s \nabla n_s + \frac{2\pi}{3} \sum_{n=1}^{\mathrm{NP}} \sum_{p=1}^{\mathrm{NP}} n_n n_p \sigma_{np}^3 g_{np} \nabla \theta_s \\ &+ \frac{2\pi}{3} \theta_s \sum_{n=1}^{\mathrm{NP}} \sum_{p=1}^{\mathrm{NP}} \left[\sigma_{np} (n_n n_p \nabla g_{np} + n_n g_{np} \nabla n_p + n_p g_{np} \nabla n_n) \right] \end{aligned} \tag{A.3}$$

The radial distribution function is given by the following equation:

$$g_{np} = \frac{1}{1-\epsilon_s} + \left[g_0 - \frac{1}{1-\epsilon_s} \right] \frac{< \sigma^{(2)} > \sigma_n \sigma_p}{< \sigma^{(3)} > \sigma_{np}} \tag{A.4}$$

where

$$< \sigma^{(n)} > = \sum_{i=1}^{\mathrm{NP}} \frac{n_i}{n_s} \sigma_i^n \tag{A.5}$$

The radial distribution function for a mono-disperse hard-sphere fluid is given in its general form by:

$$g_0(\epsilon_s) = \frac{\sum_{n=0}^{8} c_n \epsilon_s^n}{(1-(\epsilon_s/\epsilon_s^{max})^a)^b} \tag{A.6}$$

In this work the coefficients by Song et al. (1988) will be used (see Table 4.3).

Before taking the derivative of the radial distribution function, it should be written down in the following form:

$$g_{np} = g_{np}(\epsilon_s, n_1, ..., n_{\mathrm{NP}-1}) \tag{A.7}$$

because n_{NP} can be written as:

$$n_{\mathrm{NP}} = n_s - \sum_{i=1}^{\mathrm{NP}-1} n_i \tag{A.8}$$

With this substitution ϵ_s and n_s can be written in the following form:

$$\begin{aligned} \epsilon_s &= \sum_{i=1}^{\mathrm{NP}} n_i \frac{\pi}{6}\sigma_i^3 = \sum_{i=1}^{\mathrm{NP}-1} n_i \frac{\pi}{6}\sigma_i^3 + (n_s - \sum_{i=1}^{\mathrm{NP}-1} n_i)\frac{\pi}{6}\sigma_{\mathrm{NP}}^3 \\ &= \sum_{i=1}^{\mathrm{NP}-1} n_i \frac{\pi}{6}(\sigma_i^3 - \sigma_{\mathrm{NP}}^3) + n_s \frac{\pi}{6}\sigma_{\mathrm{NP}}^3 \end{aligned} \tag{A.9}$$

$$\begin{aligned} n_s &= \frac{6}{\pi\sigma_{\mathrm{NP}}^3}\left[\epsilon_s - \sum_{i=1}^{\mathrm{NP}-1} n_i \frac{\pi}{6}(\sigma_i^3 - \sigma_{\mathrm{NP}}^3)\right] \\ &= \frac{6\epsilon_s}{\pi\sigma_{\mathrm{NP}}^3} + \sum_{i=1}^{\mathrm{NP}-1} n_i (1 - \frac{\sigma_i^3}{\sigma_{\mathrm{NP}}^3}) \end{aligned} \tag{A.10}$$

Substitution of these equations in the summation term $< \sigma^{(n)} >$ gives:

$$\begin{aligned} < \sigma^{(n)} > &= \frac{1}{n_s}\left\{\sum_{i=1}^{\mathrm{NP}-1} n_i \sigma_i^n + (n_s - \sum_{i=1}^{\mathrm{NP}-1} n_i)\sigma_{\mathrm{NP}}^n\right\} \\ &= \frac{1}{n_s}\left\{\sum_{i=1}^{\mathrm{NP}-1} n_i(\sigma_i^n - \sigma_{\mathrm{NP}}^n) + n_s\sigma_{\mathrm{NP}}^n\right\} \\ &= \sigma_{\mathrm{NP}}^n + \frac{\sum_{i=1}^{\mathrm{NP}-1} n_i(\sigma_i^n - \sigma_{\mathrm{NP}}^n)}{\frac{6\epsilon_s}{\pi\sigma_{\mathrm{NP}}^3} + \sum_{i=1}^{\mathrm{NP}-1} n_i(1 - \frac{\sigma_i^3}{\sigma_{\mathrm{NP}}^3})} \end{aligned} \tag{A.11}$$

The derivatives of the summation term $< \sigma^{(n)} >$ with respect to ϵ_s and n_k yield:

$$\begin{aligned}
\frac{\partial < \sigma^{(n)} >}{\partial \epsilon_s} &= \frac{\partial}{\partial \epsilon_s} \left\{ \sigma_{\mathrm{NP}}^n + \frac{\sum_{i=1}^{\mathrm{NP}-1} n_i(\sigma_i^n - \sigma_{\mathrm{NP}}^n)}{\frac{6\epsilon_s}{\pi\sigma_{\mathrm{NP}}^3} + \sum_{i=1}^{\mathrm{NP}-1} n_i(1 - \frac{\sigma_i^3}{\sigma_{\mathrm{NP}}^3})} \right\} \\
&= -\frac{\frac{6}{\pi\sigma_{\mathrm{NP}}^3} \sum_{i=1}^{\mathrm{NP}-1} n_i(\sigma_i^n - \sigma_{\mathrm{NP}}^n)}{\left[\frac{6\epsilon_s}{\pi\sigma_{\mathrm{NP}}^3} + \sum_{i=1}^{\mathrm{NP}-1} n_i(1 - \frac{\sigma_i^3}{\sigma_{\mathrm{NP}}^3}) \right]} \\
&= -\frac{6}{\pi\sigma_{\mathrm{NP}}^3 n_s^2} \left[\sum_{i=1}^{\mathrm{NP}-1} n_i(\sigma_i^n - \sigma_{\mathrm{NP}}^n) \right]
\end{aligned} \tag{A.12}$$

$$\begin{aligned}
\frac{\partial < \sigma^{(n)} >}{\partial n_k} &= \frac{\partial}{\partial n_k} \left\{ \sigma_{\mathrm{NP}}^n + \frac{\sum_{i=1}^{\mathrm{NP}-1} n_i(\sigma_i^n - \sigma_{\mathrm{NP}}^n)}{\frac{6\epsilon_s}{\pi\sigma_{\mathrm{NP}}^3} + \sum_{i=1}^{\mathrm{NP}-1} n_i(1 - \frac{\sigma_i^3}{\sigma_{\mathrm{NP}}^3})} \right\} \\
&= \frac{(\sigma_k^n - \sigma_{\mathrm{NP}}^n)}{\frac{6\epsilon_s}{\pi\sigma_{\mathrm{NP}}^3} + \sum_{i=1}^{\mathrm{NP}-1} n_i(1 - \frac{\sigma_i^3}{\sigma_{\mathrm{NP}}^3})} - \frac{(1 - \frac{\sigma_k^3}{\sigma_{\mathrm{NP}}^3}) \sum_{i=1}^{\mathrm{NP}-1} n_i(\sigma_i^n - \sigma_{\mathrm{NP}}^n)}{\left[\frac{6\epsilon_s}{\pi\sigma_{\mathrm{NP}}^3} + \sum_{i=1}^{\mathrm{NP}-1} n_i(1 - \frac{\sigma_i^3}{\sigma_{\mathrm{NP}}^3}) \right]^2} \\
&= \frac{(\sigma_i^n - \sigma_{\mathrm{NP}}^n)}{n_s} - \frac{(1 - \frac{\sigma_k^3}{\sigma_{\mathrm{NP}}^3}) \sum_{i=1}^{\mathrm{NP}-1} n_i(\sigma_i^n - \sigma_{\mathrm{NP}}^n)}{n_s^2}
\end{aligned} \tag{A.13}$$

These derivatives are needed in the derivation of the gradient of the radial distribution function g_{np}:

$$\nabla g_{np} = \left(\frac{\partial g_{np}}{\partial \epsilon_s} \right) \nabla \epsilon_s + \sum_{i=1}^{\mathrm{NP}-1} \left(\frac{\partial g_{np}}{\partial n_i} \right) \nabla n_i \tag{A.14}$$

where

$$\begin{aligned}
\frac{\partial g_{np}}{\partial \epsilon_s} &= \frac{1}{(1-\epsilon_s)^2} + \left[\frac{\mathrm{d}g_0}{\mathrm{d}\epsilon_s} - \frac{1}{(1-\epsilon_s)^2} \right] \frac{< \sigma^{(2)} > \sigma_n \sigma_p}{< \sigma^{(3)} > \sigma_{np}} \\
&+ \left(g_0 - \frac{1}{1-\epsilon_s} \right) \frac{\sigma_n \sigma_p}{\sigma_{np}} \left\{ \frac{1}{< \sigma^{(3)} >} \left(\frac{\partial < \sigma^{(2)} >}{\partial \epsilon_s} \right) - \frac{< \sigma^{(2)} >}{< \sigma^{(3)} >^2} \left(\frac{\partial < \sigma^{(3)} >}{\partial \epsilon_s} \right) \right\}
\end{aligned} \tag{A.15}$$

$$\frac{\partial g_{np}}{\partial n_i} = \left(g_0 - \frac{1}{1-\epsilon_s} \right) \frac{\sigma_n \sigma_p}{\sigma_{np}} \left\{ \frac{1}{<\sigma^{(3)}>} \left(\frac{\partial <\sigma^{(2)}>}{\partial n_i} \right) - \frac{<\sigma^{(2)}>}{<\sigma^{(3)}>^2} \left(\frac{\partial <\sigma^{(3)}>}{\partial n_i} \right) \right\} \tag{A.16}$$

Chapter 5

Segregation in bi-disperse fluidised beds: comparison of CFD model predictions with experiments

Abstract

In many industrial scale fluidised bed reactors, particle mixing and segregation phenomena play a very important role. To gain more insight in the mechanism and in the rate at which particle mixing and segregation occurs in multi-disperse fluidised bed systems, fundamental hydrodynamic models are required. In this chapter, the particle mixing and segregation rates in a bi-disperse freely bubbling fluidised bed were studied with a new Multi Fluid model based on the kinetic theory of granular flow for multi-component systems and with a Discrete Particle Model (DPM). The MFM and DPM simulation results have been compared with Digital Image Analysis experiments obtained by Goldschmidt et al. (2003) for bi-disperse mixtures of glass beads.

The DPM overestimated the rate of segregation compared to the experimental observations due to an incorrect gas-particle drag description by the drag relation of Ergun/Wen&Yu. Implementation of a poly-disperse drag relation by van der Hoef et al. (2005) in a DPM simulation performed by Beetstra (2005) improved the computed rate of segregation significantly.

In strong contrast to MFMs previously described in the literature, that strongly over-

estimate the segregation rates, the new MFM seems to underestimate the segregation rates at longer times. This underprediction of the segregation rate is probably related to the neglect of frictional stresses associated with long-term multiple-particle contacts resulting in an overestimation of the mobility of the emulsion phase. Nevertheless, the computed granular temperature levels in a segregating system computed with the new MFM compared quite well with the granular temperatures found in the DPM simulation.

5.1 Introduction

Segregation of particles occurs in a fluidised bed with a mixture of solids with different sizes or densities, where the larger/ heavier particles (jetsam) tend to reside at the bottom and the smaller/lighter particles (flotsam) migrate to the top of the bed. It is known that segregation is most significant at superficial gas velocities between the minimum fluidisation velocities of the jetsam and the flotsam. Segregation and also mixing of the particles play a very important role in many fluidised bed applications in industry. In gas-phase olefin polymerisation processes, for example, segregation of the larger product particles is effectively used to collect the product particles at the bottom of the fluidised bed. Bubbles are known to play an intricate and ambigious role (Rowe and Nienow, 1976). On the one hand, bubbles cause segregation when the denser or larger particles tend to fall preferentially through the disturbed region behind the bubble. On the other hand, the rising bubbles produce a mixing action equalising the particle size/density distribution (Wu and Baeyens, 1998). A better understanding and a quantitative description of the mixing and segregation phenomena is required to improve the design, operation and scale-up of gas-fluidised bed processes.

To gain more insight in the mechanisms and the rate at which particle segregation occurs, fundamental and detailed hydrodynamic models need to be developed. These models should be able to describe the sensitive transition between particle mixing and segregation, for which a quantitative description of the bubble dynamics is essential. For larger (engineering scale) fluidised beds continuum models (Euler-Euler) have been developed, where both the gas phase and the solids phase are described as interpenetrating continua. Owing to the continuum description of the solids phase the kinetic theory of granular flow is employed to obtain closure relations for the solids phase rheology. Many researchers studied the particle mixing and segregation behaviour of dense gas-solid fluidised beds (amongst many others Goldschmidt et al., 2001; Huilin et al., 2003a,b). However, these models were not able to give a quantitative description of the mixing and segregation rates in dense gas-solid fluidised beds. Therefore,

a Multi Fluid model with a novel set of closures was derived, extending the classical kinetic theory for dense gas multi-component mixtures. A detailed derivation of this new Multi Fluid model has been presented in Chapter 4 of this thesis.

For smaller fluidised bed systems (typically $< 1.0 \cdot 10^6$ particles) a more detailed Discrete Particle Model (DPM) can be used to describe the dynamic behaviour of a polydisperse mixture of particles. In this Euler-Lagrange model the particles are tracked individually by solving Newton's second law of motion, whereas the gas phase is computed by solving the volume-averaged Navier-Stokes equations. A detailed collision model accounts for the non-ideal particle-particle and particle-wall interactions. In the literature only a few authors have reported simulation results for a binary mixture of particles using a DPM. Hoomans et al. (2000) studied segregation in a binary mixture of particles by a 2D-approach. Limtrakul et al. (2003) reported the bed-averaged mixing and segregation behaviour of a binary mixture of particles of different size and density. Feng et al. (2004) presented a numerical study of segregation and mixing by means of a DPM, where the motion of the particles was 3D and the gas phase was solved in 2D. They found that the two extremes, well mixed and fully segregated, could be well predicted by their DPM and was qualitatively comparable with experimental results. Since particle-particle interactions play a crucial role in the description of segregating gas-solid fluidised beds and the DPM can account for these interactions in a very fundamental and detailed manner, the DPM is very well suited to be used as a research tool to verify the underlying assumptions required for closures for the solids phase rheology in continuum models.

In addition many authors experimentally studied the behaviour of binary mixtures in gas-solid fluidised beds. The rate of segregation was very often measured by the bed freeze and dissection method, where the particles are taken from the fluidised bed layer by layer and sieved separately to measure the concentrations of the different species (Wu and Baeyens, 1998; Marzocchella et al., 2000; Formisani et al., 2001; Gilbertson and Eames, 2001). A disadvantage of this method is that it is very laborious and the

results suffer from significant inaccuracies. To validate detailed hydrodynamic models, however, an experimental technique is required, where the rate of segregation and the bubble dynamics can be measured simultaneously on relatively short time scales. Therefore, Goldschmidt et al. (2003) developed a whole-field, non-intrusive, digital image analysis technique to measure segregation rates in a binary mixture of coloured particles in a pseudo-2D freely bubbling fluidised bed.

In this chapter the mixing and segregation behaviour of a binary mixture of glass beads is studied with the new Multi Fluid model, as presented in Chapter 4 of this thesis, and with a pseudo-3D Discrete Particle Model as described in detail in Chapter 3. The model results are quantitatively compared with experimental data obtained with the digital image analysis technique by Goldschmidt et al. (2003) for a freely bubbling bi-disperse fluidised bed. Before discussing the particle segregation results with the new MFM and the DPM, firstly it is investigated whether the MFM and the DPM predict the same minimum fluidisation velocity. It is essential for the models to predict the minimum fluidisation velocity accurately in order to quantitatively describe the excess velocity, a key parameter determining the segregation rates. The analysis of the particle segregation results is focussed on the role of particle-particle and gas-particle interactions. The chapter is concluded with a discussion on the granular temperatures for the two different particles, as computed by the MFM and the DPM.

5.2 Minimum fluidisation velocity

The rate of segregation of a binary mixture of particles is very sensitive to the superficial gas velocity and is most significant between the minimum fluidisation velocities of the jetsam and the flotsam. Therefore, it has been studied first whether the MFM and the DPM can accurately predict the minimum fluidisation velocity correctly both for mono-disperse systems and binary particle mixtures. Simulations have been carried out with both models, where in the first second of the simulation the particles are fluidised at a high velocity of 1.7 m/s to completely mix the different particle spe-

cies. Thereafter the gas velocity is suddenly dropped to 0 m/s and again subsequently linearly increased to a maximum superficial gas velocity of 2 m/s. In Figure 5.1 the averaged particle height is plotted as a function of the superficial gas velocity for a DPM simulation with 2.5 mm particles, showing that the averaged particle height suddenly increases. The velocity at which the average particle height departs more than 0.05% from the initial height (plateau in Figure 5.1) has been taken as an approximation for the minimum fluidisation velocity.

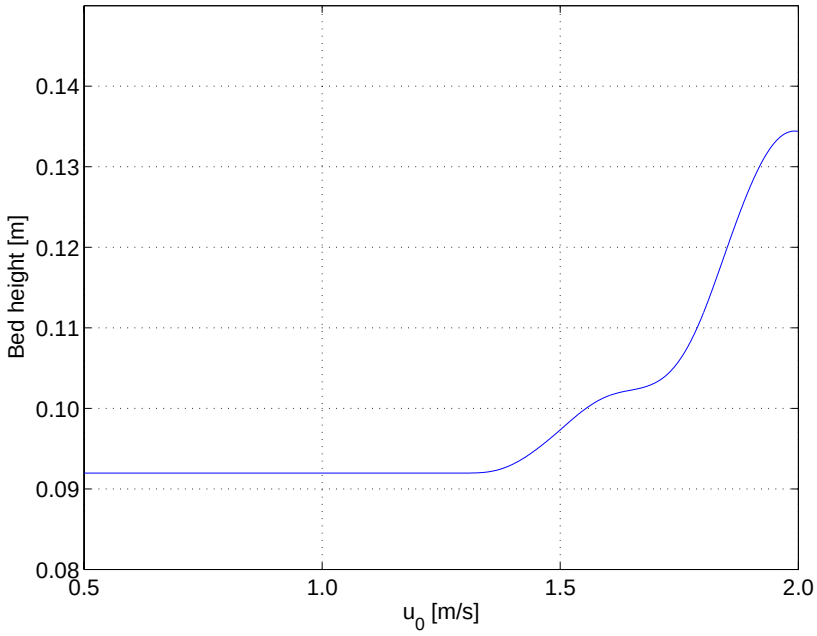

Figure 5.1: Bed height as a function of the superficial gas velocity to determine the minimum fluidisation velocity; computed with the DPM for a bed with particles of 2.5 mm.

Using the DPM, the minimum fluidisation velocities have been determined for 1.5 mm and 2.5 mm particles and for several binary mixtures of these particles. The results are summarised in Table 5.1. It is found that the computed minimum fluidisation velocities for the mono-disperse fluidised beds filled with 2.5 mm particles and 1.5 mm particles agree well with the experimentally determined minimum fluidisation velocities (1.31 m/s and 0.87 m/s respectively). The dependency of the minimum fluidisation velocity on the mass fraction of the small particles is shown in Figure 5.2 and exhibits the same tendency as found in the experiments reported by Goldschmidt et al. (2003).

Table 5.1: The solids volume fractions at minimum fluidisation conditions and the minimum fluidisation velocities for different binary mixtures of particles with diameters of 1.5 mm and 2.5 mm computed with the DPM.

volume ratio 2.5 mm/1.5 mm	$\epsilon_{mf}[-]$	$u_{mf}[m/s]$
100/0	0.400	1.333
75/25	0.390	1.118
50/50	0.383	0.983
25/75	0.390	0.958
0/100	0.398	0.908

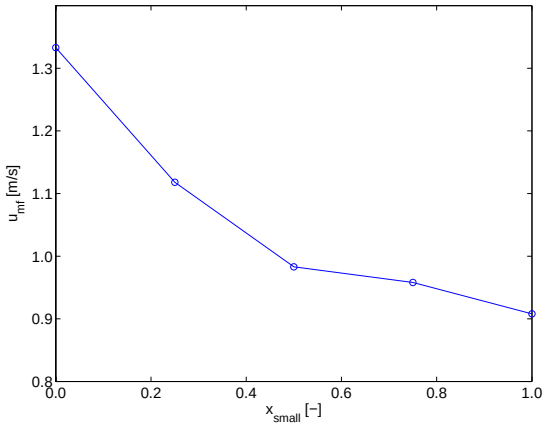

Figure 5.2: Minimum fluidisation velocity (u_{mf}) computed with the DPM as a function of the mass fraction flotsam.

The volume fraction at minimum fluidisation velocity computed with the DPM is also given in Table 5.1. It can be concluded that the volume fraction at minimum fluidisation velocity for both 2.5 mm and 1.5 mm particles is equal to 0.40 and is slightly lower for a binary mixture, since the smaller particles can occupy the free space between the larger particles.

Owing to the continuum description of the particulate phase, in the MFM a maximum solids fraction ϵ_s^{max} has to be specified. In the radial distribution function given by Ma and Ahmadi (1986), which is a commonly used radial distribution function in continuum models, the maximum solids fraction is equal to 0.64356. However, a MFM simulation with a maximum solids fraction of 0.64356 produces a minimum fluidisation velocity that is far below the values found in the experiments and in the DPM, as can be seen in Figure 5.3. Therefore, other MFM simulations have been carried out using higher values for the maximum solids fraction. In Figure 5.3 it is shown that the minimum fluidisation velocity computed with the MFM is a very strong function of the maximum solids fraction. For our MFM simulations a maximum solids fraction of 0.60 has therefore been chosen, which agrees with the solids fraction at minimum

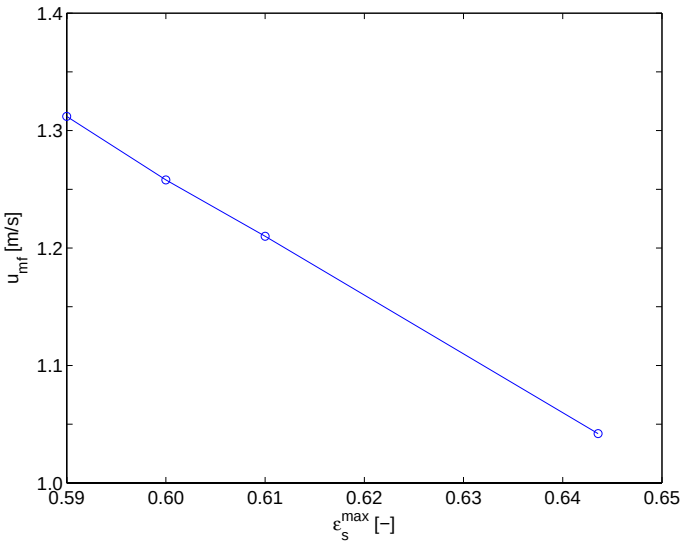

Figure 5.3: Minimum fluidisation velocity (u_{mf}) for 2.5 mm particles as a function of the maximum solids fraction specified in the MFM.

fluidisation conditions obtained from the DPM simulations.

5.3 Particle segregation rates in a freely bubbling bi-disperse fluidised bed

In the following sections the results are presented of particle segregation rates in a freely bubbling bi-disperse fluidised bed, computed with the Multi-Fluid model and the Discrete Particle model and will be compared with the experimental data obtained with digital image analysis technique developed by Goldschmidt et al. (2003). Three different cases have been selected with two different bed compositions and with three different superficial gas velocities as summarised in Table 5.2. Firstly, the settings of the experiments and the CFD models are presented.

5.3.1 Settings of the experiments and the CFD models

The experimental data presented in this chapter were reported by Goldschmidt et al. (2003). For the sake of clarity a short overview of the digital image analysis technique will be given here. The segregation experiments were carried out in a pseudo-2D flu-

Table 5.2: Different cases simulated with the MFM and the DPM.

	x_{small}/x_{large}	u_{bg}	NP_{small}	NP_{large}
base case	0.25/0.75	1.20 m/s	27720	17940
case 1	0.50/0.50	1.10 m/s	55430	11960
case 2	0.50/0.50	1.25 m/s	55430	11960

idised bed with a width of 15 cm, a height of 70 cm and a depth of 1.5 cm. A schematic representation of the digital image analysis set-up is shown in Figure 5.4. Coloured glass beads with two different sizes and equal densities were applied in the segregation experiments. Since this experimental technique was developed for critical validation of fundamental hydrodynamic models, all particle collision properties (i.e. coefficient of normal restitution, coefficient of tangential restitution and coefficient of friction) were accurately determined on basis of separate impact measurements (Kharaz et al., 1999). The bed motion was recorded with a color digital video camera at a frame rate of 25 frames per second. The image analysis software subsequently divided the images in small cells of 1 x 1 cm and determined the particle mixture composition per cell. From the evolution of the mixture composition in time the rate of segregation could be de-

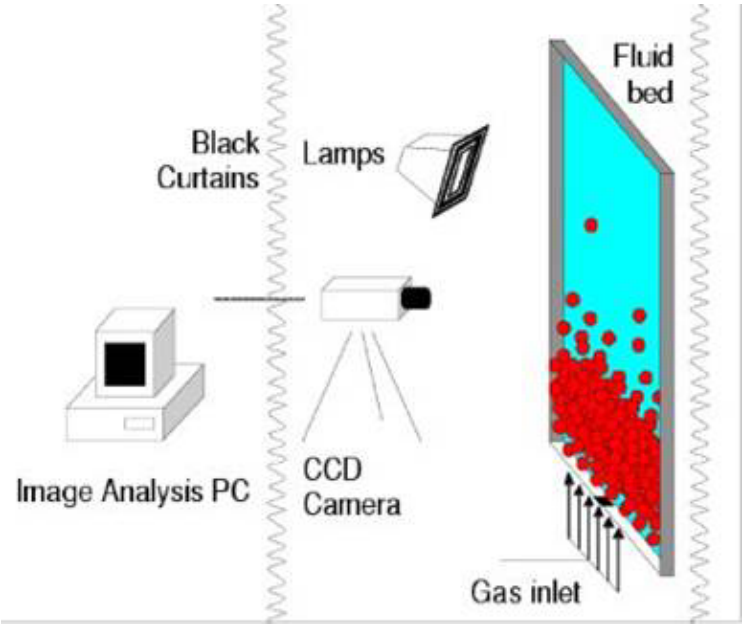

Figure 5.4: Schematic picture of the digital image analysis experimental set-up.

Table 5.3: Settings for the DPM and the MFM calculations for the segregation simulations.

	DPM	**MFM**
width	0.15 m	0.15 m
depth	0.015 m	-
height	1.0 m	0.40 m
grid cells x-direction	45	45
grid cells y-direction	1	-
grid cells z-direction	300	120
flow solver time step	$1.0 \cdot 10^{-4}$ s	$1.0 \cdot 10^{-5}$ s
DEM time step	$2.9 \cdot 10^{-6}$ s	-
drag model	Ergun/Wen&Yu	Ergun/Wen&Yu
	small particles	**large particles**
particle density	2526 kg/m^3	2526 kg/m^3
particle diameter	1.5 mm	2.5 mm
normal restitution	0.97	0.97
friction	0.10	0.10
tangential restitution	0.33	0.33

termined.

In the DPM the particles are initially positioned in a lattice where the small and large particles are randomly distributed. Before the segregation simulation was started, the particles had been mixed well for two seconds of simulation time at a high fluidisation velocity. In the MFM the initial solids fractions were set for a static bed height corresponding to the height used in the experiment and in the DPM. The simulation using the MFM could directly be started, since the continuous description of the particulate phase does not require initial mixing of the particles. To mimic the gas inlet flow conditions prevailing in the experiments, a random fluctuation of 5% has been applied to the gas inlet velocity in both the DPM and MFM simulations. Other relevant simulation settings are listed in Table 5.3.

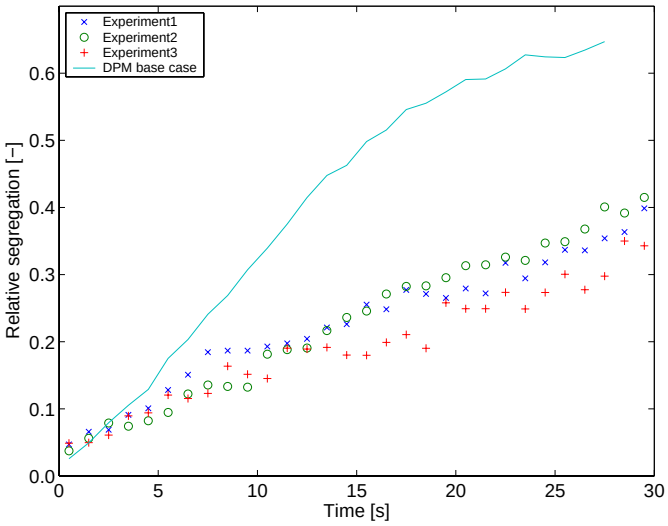

Figure 5.5: Evolution of the relative segregation in time for the base case DPM simulation and the experiments performed by Goldschmidt et al. (2003): u_{bg} = 1.20 m/s, 25% small glass beads ($d_p = 1.5\ mm$), 75% large glass beads ($d_p = 2.5\ mm$).

5.3.2 Segregation rates: comparison of DPM results with experiments

Firstly, the base case DPM simulation results were compared with experimental data reported by Goldschmidt et al. (2003). In Figure 5.6 the snapshots are depicted of the experiments and the base case DPM simulation. In the DPM a small layer of the small (blue) particles was formed at the top of the bed and the thickness of this layer increases as a function of time, which corresponds quite well with the experimental observations. To compare the rate of segregation more quantitatively the evolution in time of the relative segregation is depicted in Figure 5.5. The relative segregation s is defined for a binary mixture as follows:

$$s = \frac{S - 1}{S_{max} - 1} \tag{5.1}$$

where

$$S = \frac{< h_{small} >}{< h_{large} >} \qquad \text{and} \qquad S_{max} = \frac{2 - x_{small}}{1 - x_{small}} \tag{5.2}$$

It is shown that the DPM simulation overpredicts the relative segregation compared to the experimentally observed relative segregation. This difference might be caused

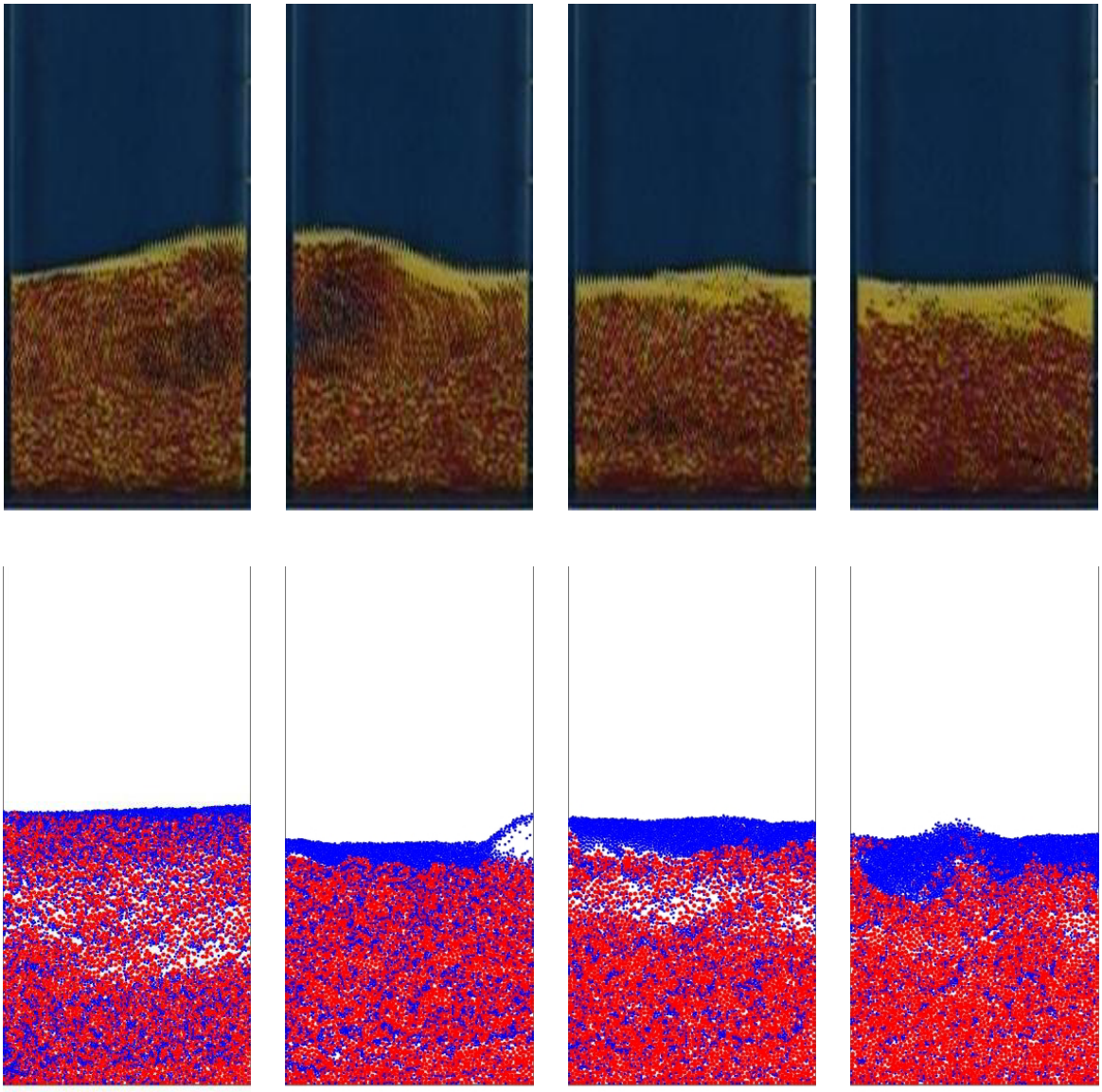

Figure 5.6: Snapshots of the base case DPM simulation and the experiments performed by Goldschmidt et al. (2003): u_{bg} = 1.20 m/s, 25% small glass beads ($d_p = 1.5$ mm), 75% large glass beads ($d_p = 2.5$ mm) (for color figures see Figure A.14).

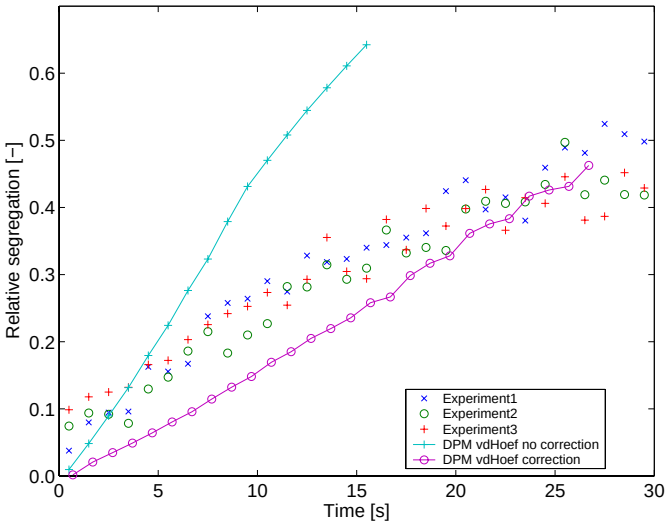

Figure 5.7: Evolution of the relative segregation in time for DPM simulations using a mono-disperse and poly-disperse drag relation (both derived from Lattice Bolzmann simulations), carried out by Beetstra (2005) and the experiments performed by Goldschmidt et al. (2003): u_{bg} = 1.30 m/s, 25% small glass beads ($d_p = 1.5$ mm), 75% large glass beads ($d_p = 2.5$ mm).

by the drag relations used in the DPM, which are the well-known Ergun and Wen&Yu drag closures for respectively lower ($\epsilon_g < 0.8$) and higher ($\epsilon_g > 0.8$) void fractions. In Chapter 3, however, it was found that this drag model slightly overpredicted the experimentally observed bubble size in a fluidised bed containing mono-disperse particles. A new drag relation derived from Lattice-Boltzmann simulations by van der Hoef et al. (2005) for mono-disperse particles gave better results regarding the predicted bubble size. Besides a new drag relation for mono-disperse systems, they also derived a new drag relation for poly-disperse systems. It was found that for binary mixtures of particles with large diameter ratios (1:4), the individual drag force acting on a particle can differ by up to a factor of five compared to for example the drag force obtained from the Ergun and Wen&Yu relations. Therefore, Beetstra (2005) performed two DPM simulations for a freely bubbling fluidised bed filled with 25% of small particles and 75% of large particles with a superficial gas velocity of 1.30 m/s. One simulation was carried out with the mono-disperse drag relation reported by van der Hoef et al. (2005) and the second one with the poly-disperse drag relation including a correction factor

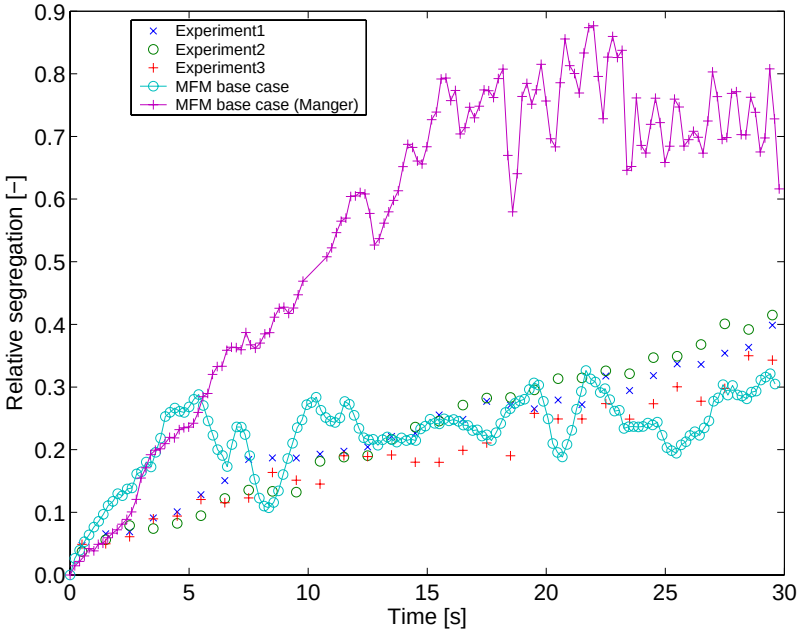

Figure 5.8: Relative segregation computed with base case MFM and with the MFM using the closures obtained by Manger (1996) for case with 25% small glass beads ($d_p = 1.5$ mm), 75% large glass beads ($d_p = 2.5$ mm).

which depends on the composition. The results of these DPM simulations are shown in Figure 5.7 and it can be concluded that the predicted relative segregation by the DPM with the poly-disperse drag relation resembles the experimentally obtained relative segregation much better. In fact, the poly-disperse drag relation increases the drag on the larger particles and decreases the drag on the smaller particles, resulting in a lower rate of segregation. For more details the interested reader is referred to Beetstra (2005).

5.3.3 Segregation rates: comparison of MFM results with experiments

Subsequently, the results for the base case MFM simulation are compared with the digital image analysis experiments performed by Goldschmidt et al. (2003). From Figure 5.8 it can be seen that the new MFM, detailed in Chapter 4, predicts the evolution of the relative segregation in time much better than the MFM using the closures derived by Manger (1996). The MFM with the closures obtained by Manger (1996) predicts almost complete segregation within 15 s, whereas in the experiments only 40% segreg-

ation was observed after 30 s. Also Goldschmidt et al. (2001) and Huilin et al. (2003a,b) reported that MFMs using the closure equations of Manger (1996) significantly over-predicted the particle segregation rates in bi-disperse freely bubbling fluidised beds.
In Figure 5.9 snapshots are shown of the base case MFM simulation where, like in the experiments, a layer of flotsam is formed on top of a mixed bed and a layer of jetsam at the bottom of the fluidised bed. Remarkably, the MFM with the closures by Manger (1996) did not predict the formation of a layer of small particles on top of a mixed bed; this model predicted that the particle segregation proceeds via 'sedimentation' of the heavier particles out of the particle mixture (see Figure 5.10).
Actually, the new MFM seems to even underpredict the rate of segregation compared to the experiments. Especially, after 15 s of simulation the relative segregation remains almost constant. This can most probably be attributed to the fact that frictional stresses associated with long-term multiple-particle contacts are neglected in the current implementation of the MFM. As a consequence, the mobility of the emulsion phase is largely overpredicted, which causes a continuous backmixing of the segregated flotsam and jetsam due to the macro-scale circulation pattern in the fluidised bed induced by the bubbles. This overprediction of the mobility of the emulsion phase was also found in the single bubble simulations with the TFM in Chapter 3.
To account for the additional dissipation of granular energy due to particle-particle friction as an first attempt an effective coefficient of restitution was used in the MFM (see also section 3.6.2). Figure 5.11 shows the rate of segregation computed with the MFM using an effective coefficient of restitution of 0.88. It can be concluded that the rate of segregation is somewhat higher, but apparently the mobility of the emulsion phase is still too high as can also be concluded from the strong fluctuations of the relative segregation which originate from the aforementioned backmixing.

5.3.4 Effect of the superficial gas velocity and the mixture composition

The mixing and segregation behaviour of a bi-disperse freely bubbling fluidised bed is influenced by many variables including the superficial gas velocity and the particle concentration. In this section the DPM and MFM simulation results are presented of

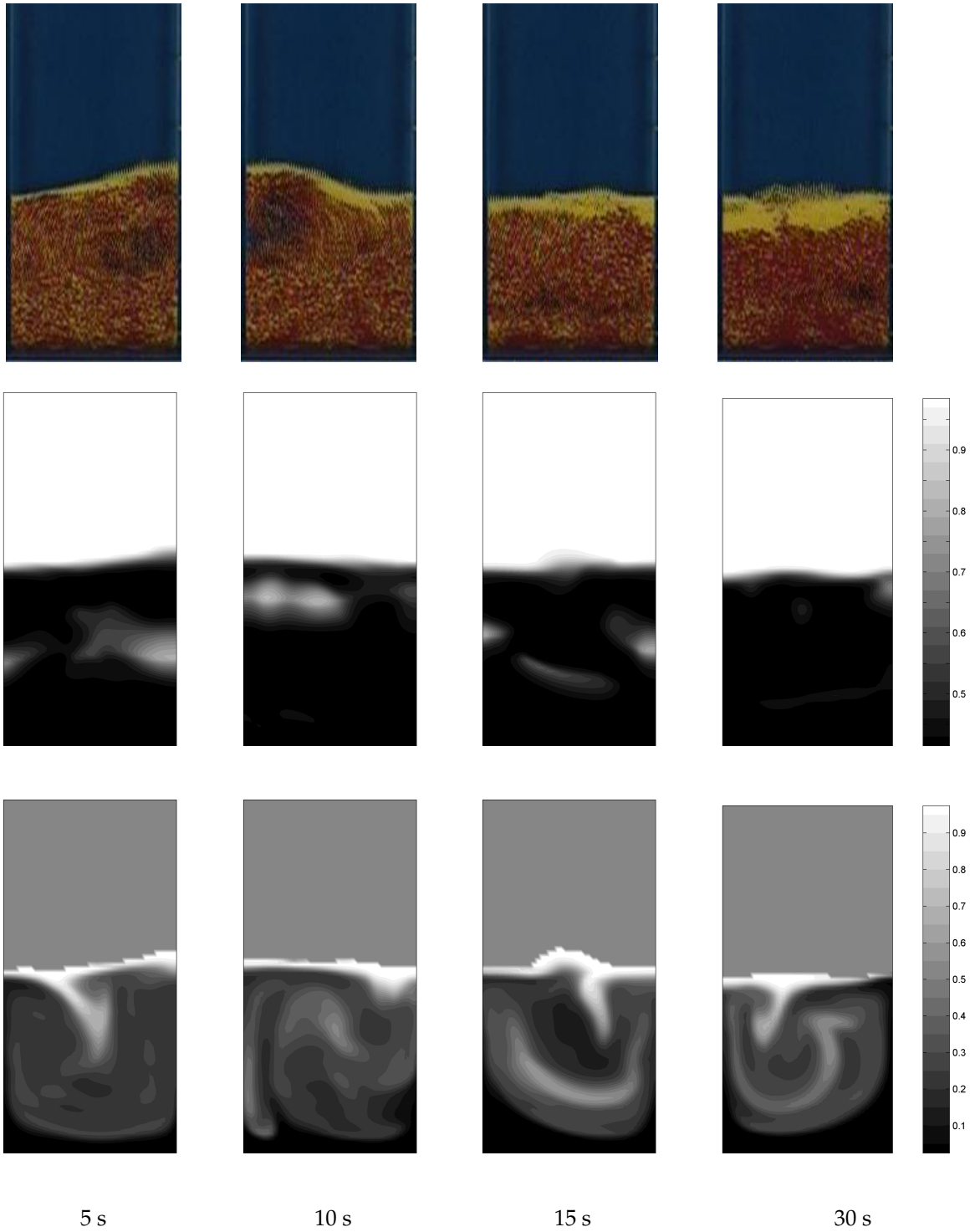

Figure 5.9: Comparison between the new MFM and the experiments performed by Goldschmidt et al. (2003); u_{bg} = 1.20 m/s, 25% small glass beads (d_p = 1.5 mm), 75% large glass beads (d_p = 2.5 mm); top: snapshots of experiments; middle: void fractions; bottom: mass fraction small particles (for color figures see Figure A.15).

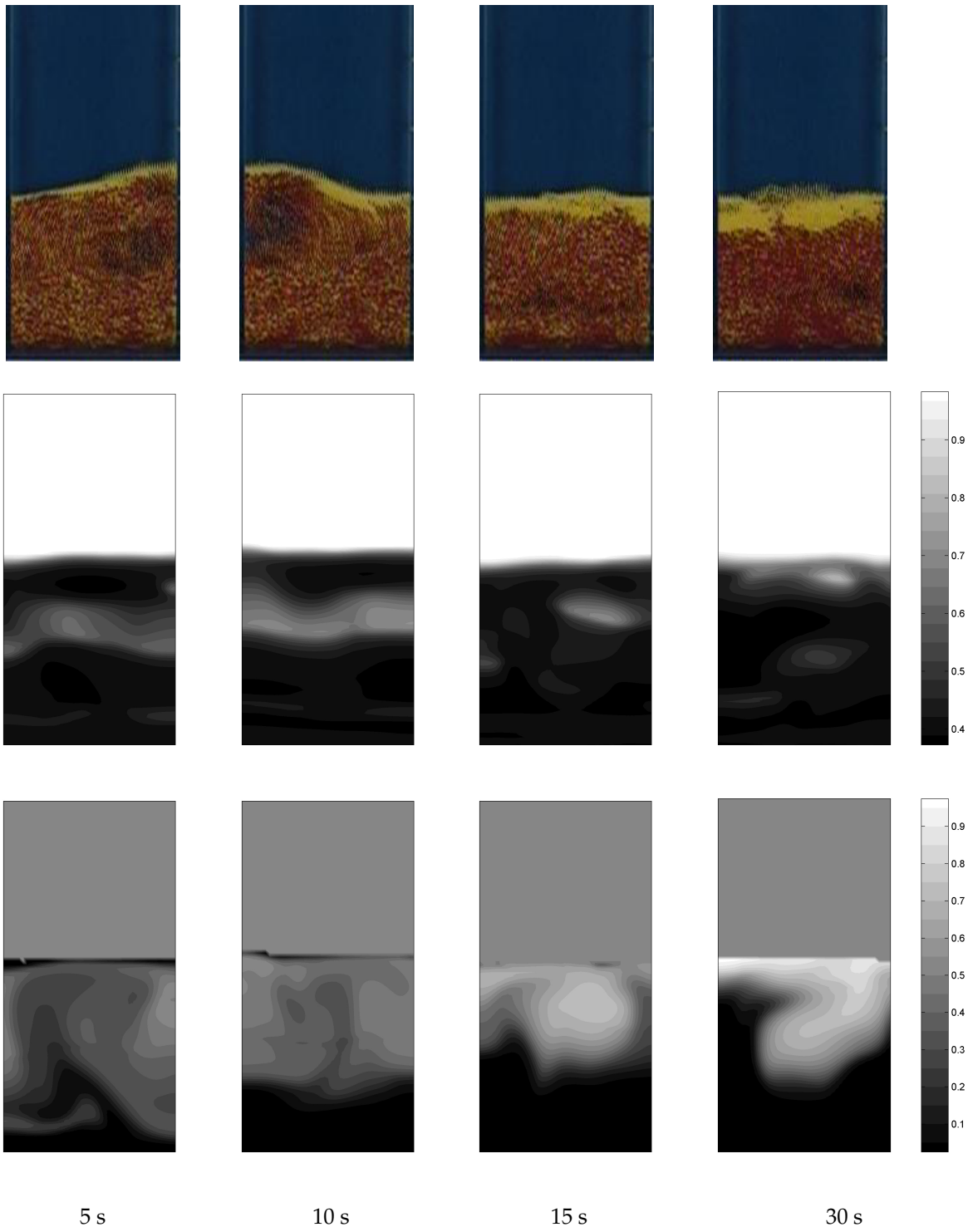

Figure 5.10: Comparison between the MFM with closures by Manger (1996) and the experiments performed by Goldschmidt et al. (2003); u_{bg} = 1.20 m/s, 25% small glass beads ($d_p = 1.5$ mm), 75% large glass beads ($d_p = 2.5$ mm); top: snapshots of experiments; middle: void fractions; bottom: mass fraction small particles (for color figures see Figure A.16).

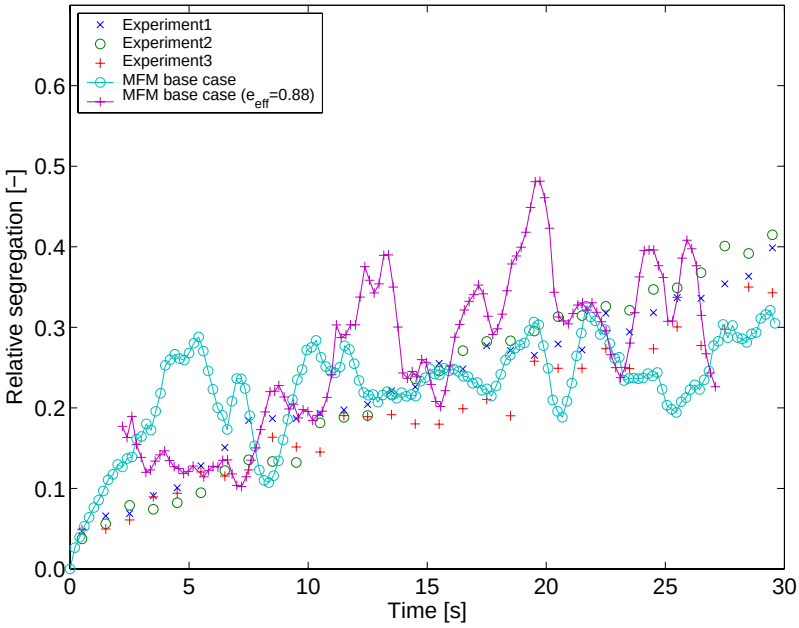

Figure 5.11: Relative segregation computed with base case MFM for case with 25% small glass beads ($d_p = 1.5$ mm), 75% large glass beads ($d_p = 2.5$ mm); effect of e_{eff}.

a segregating freely bubbling fluidised bed consisting of 50% small particles and 50% large particles (case 1) and a mixing freely bubbling fluidised bed with the same bed composition but with a higher superficial gas velocity (case 2). In Figure 5.12 the snapshots are shown of the DPM simulation results for case 1. Also here a top layer of flotsam is formed which becomes larger compared to the base case. Moreover, larger bubbles are formed in the top layer which is rich in small particles. In Figure 5.13 the snapshots of case 2 are depicted. It can clearly be seen that no top layer of flotsam is formed because of the larger bubbles. However, at the bottom a small layer is formed that is rich in jetsam.

The MFM simulation results for case 1 are presented in Figure 5.14. Again, like in the base case MFM simulation, a small layer of flotsam is formed at the top of the bed. However, the thickness of this layer remains much smaller compared to the DPM simulation, because the small particles are dragged downwards by the strong emulsion phase circulation patterns. In Figure 5.15 the snapshots are shown for case 2 computed

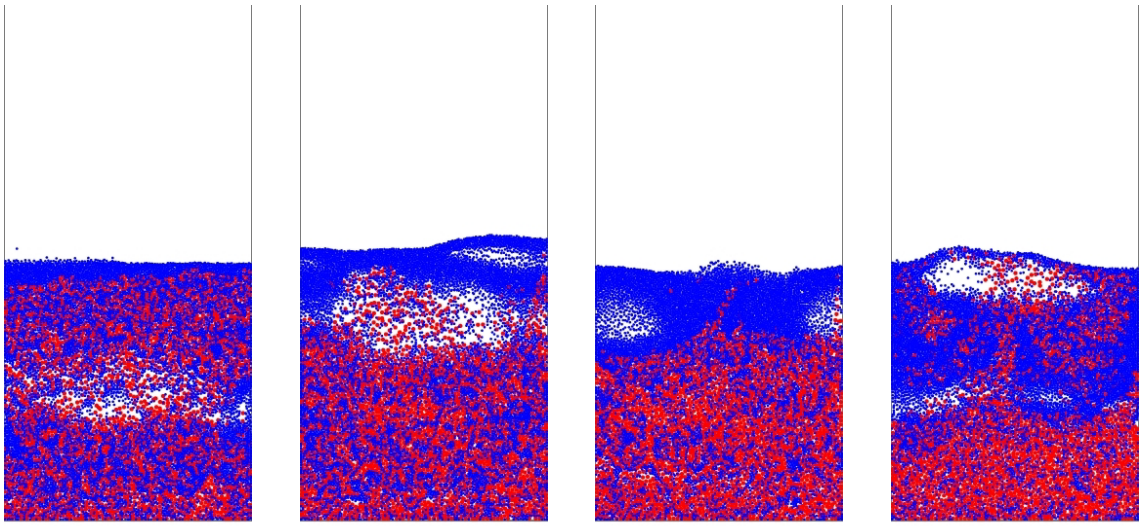

5 s 10 s 15 s 25 s

Figure 5.12: Snapshots of the DPM simulation: u_{bg} = 1.10 m/s, 50% small particles, 50% large particles.

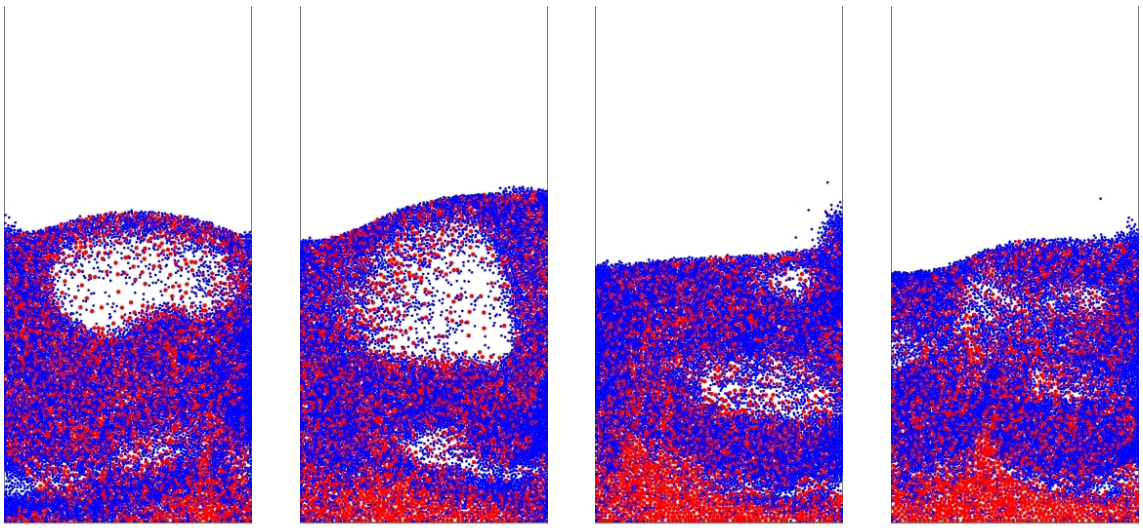

5 s 10 s 15 s 25 s

Figure 5.13: Snapshots of the DPM simulation: u_{bg} = 1.25 m/s, 50% small particles, 50% large particles.

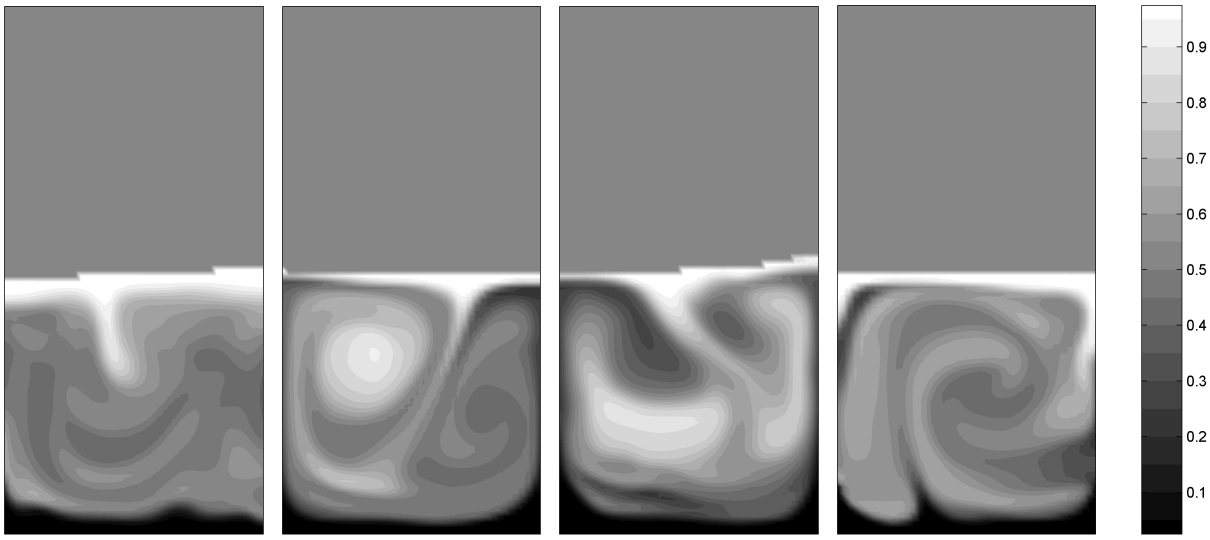

Figure 5.14: Snapshots of the small particle mass fractions computed with the new MFM; u_{bg} = 1.10 m/s, 50% small particles, 50% large particles (for color figures see Figure A.17).

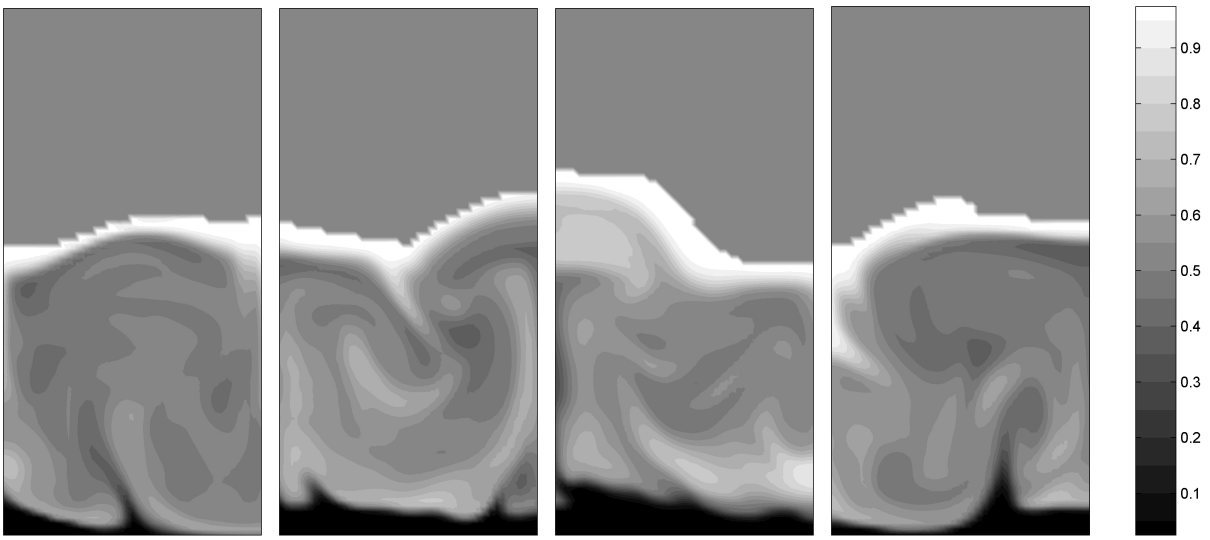

Figure 5.15: Snapshots of the small particle mass fractions computed with the new MFM; u_{bg} = 1.25 m/s, 50% small particles, 50% large particles (for color figures see Figure A.18).

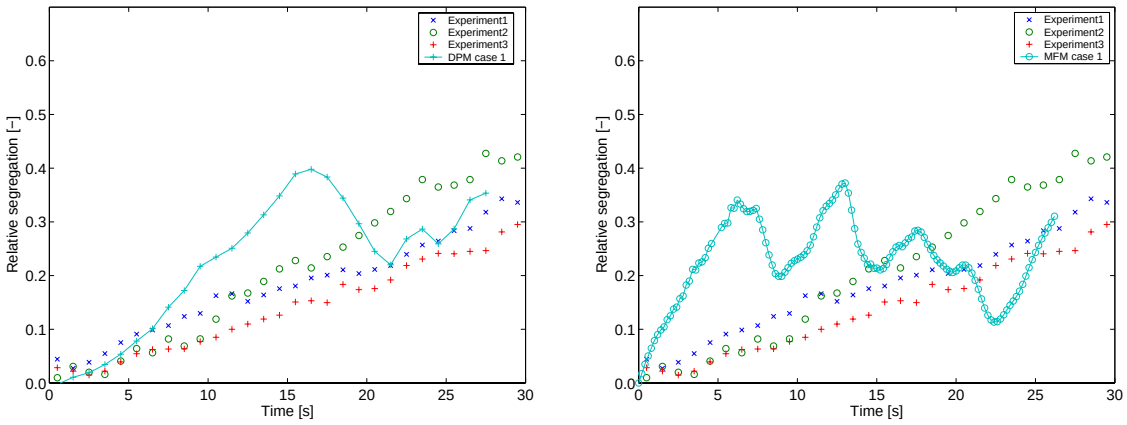

Figure 5.16: Evolution of the relative segregation in time; left: DPM simulation; right: new MFM simulation (case 1).

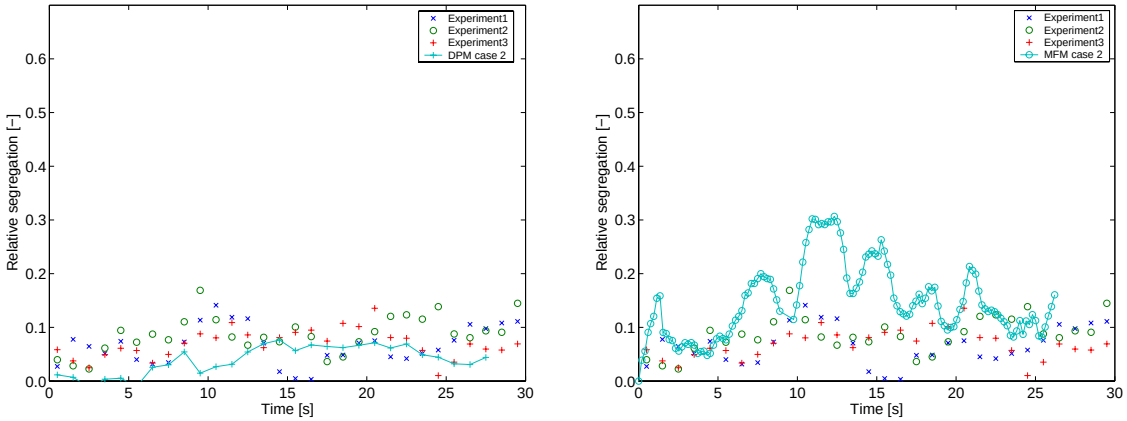

Figure 5.17: Evolution of the relative segregation in time; left: DPM simulation; right: new MFM simulation (case 2).

with the MFM. Also here, a small layer of large particles is found at the bottom of the bed, but also a small layer of small particles remains on top of a mixed bed, which was not observed in the DPM simulation. In Figures 5.16 and 5.17 the evolution of the relative segregation in time for case 1 and case 2 computed with the MFM and the DPM are depicted and compared with the experiments by Goldschmidt et al. (2003). Like in the base case, the DPM overpredicts the rate of segregation in case 1, probably due to the used drag relation by Ergun/Wen&Yu. The DPM simulation result for case 2, however, resembles the experimental results much better. The MFM again overpredicts the mobility of the emulsion phase, resulting in a constant segregation of about 20% for

case 1 and too much fluctuation of the relative segregation in case 2.

5.4 Granular temperature in segregating system

The fluctuating kinetic energy associated with the random particle motion, i.e. the granular temperature, is a key parameter in the MFM. Since experimental data on granular temperature profiles in a binary mixture of particles is not (yet) available, the DPM is used here to validate the granular temperature levels, predicted by the MFM, of the different particle phases in a segregating binary mixture.
In Figure 5.18 the volume fraction weighted bed-averaged granular temperature of every particle species is depicted as a function of time for the base case DPM simulation. It is shown that the granular temperature of the small particles remains almost constant and the granular temperature of the large particles decreases in time. As segregation proceeds the bottom part of the bed becomes rich in jetsam and since the superficial gas velocity is lower than the minimum fluidisation velocity of the larger particles, the bottom part of the bed attains a defluidised state and the average granular temperature of the large particle phase decreases.
The volume fraction weighted bed-averaged granular temperature levels computed with the MFM with the closure equations by Manger (1996) is shown in Figure 5.19. It can be concluded that the granular temperature level of the large particles is much higher than the granular temperature level of the small particles. This difference is not observed in the DPM simulation. The granular temperature level computed with the new MFM, however, resembles the DPM simulation results much better, although the difference between the granular temperatures of the large and small particles is less than in the DPM (see Figure 5.20). In both MFM models the granular temperature level of the large particles is approximately constant, whereas in the DPM the granular temperature of the large particles clearly decreases. In the MFM the bottom part of the fluidised bed will not defluidise, since the frictional stresses in the current implementation of the MFM is neglected.

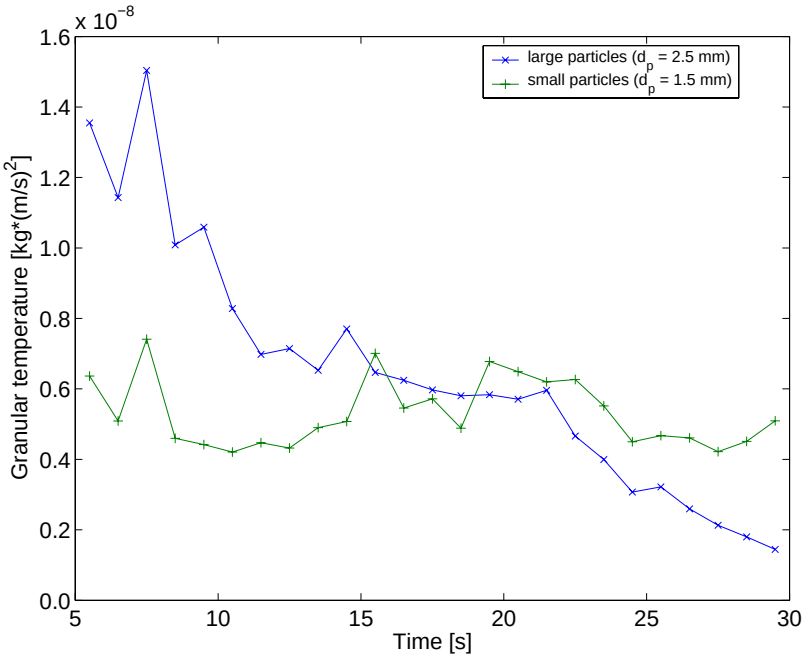

Figure 5.18: Bed averaged granular temperature as a function of time computed with the DPM.

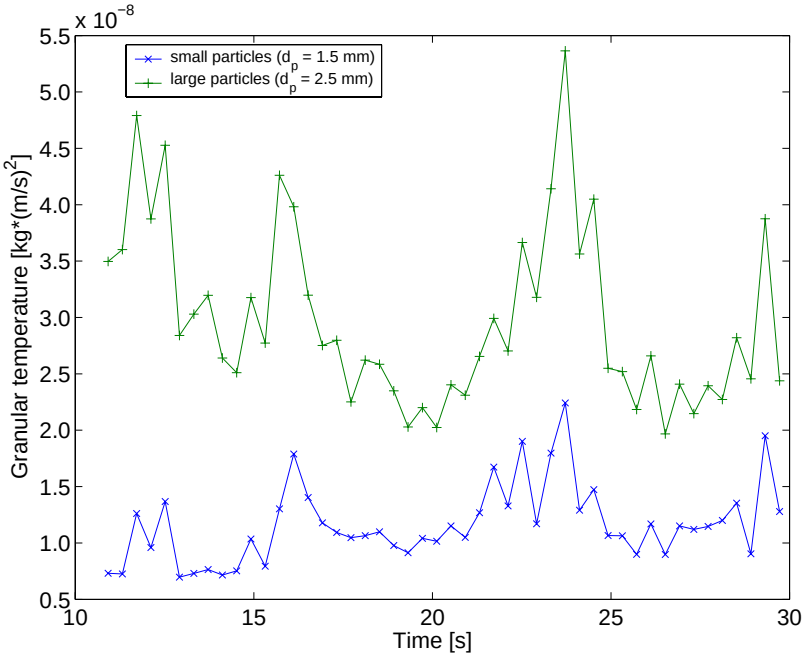

Figure 5.19: Bed averaged granular temperature as a function of time computed with the MFM by Manger (1996).

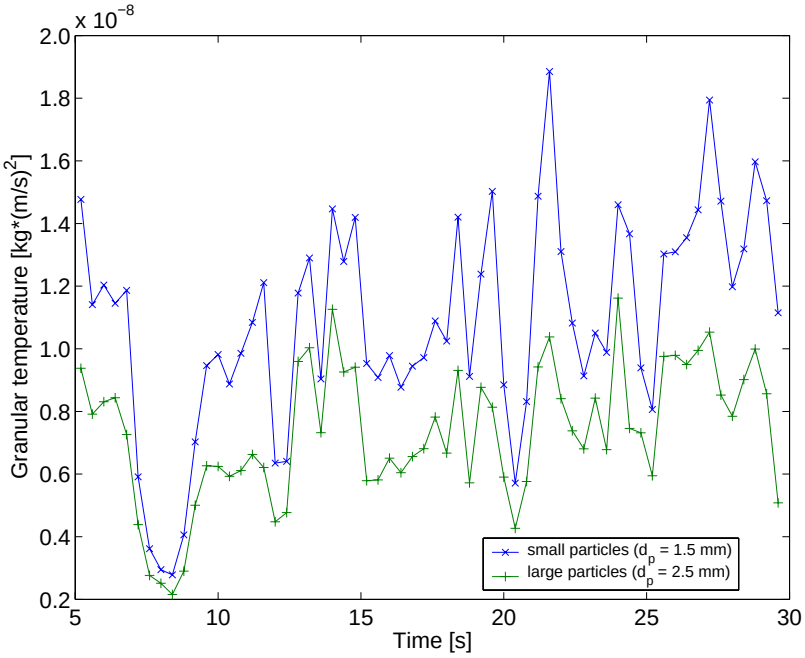

Figure 5.20: Bed averaged granular temperature as a function of time computed with the new MFM.

5.5 Conclusions

In this chapter particle segregation rates in a bi-disperse freely bubbling fluidised bed were computed with a Multi Fluid model based on the kinetic theory of granular flow for multi-component mixtures and with a Discrete Particle Model and were compared with well-defined Digital Image Analysis experiments performed by Goldschmidt et al. (2003). The experiments were carried out in a pseudo-2D fluidised bed of 15 cm wide, filled with different mixtures of 1.5 mm and 2.5 mm particles, of which the particle-particle and particle-wall collision properties were accurately known. Firstly, the minimum fluidisation velocities were determined for mono-disperse and bi-disperse particle systems with the DPM and the MFM. Thereafter, two segregation cases and one mixing case, with different particle fractions and different superficial gas velocities, were computed with both the new MFM and the DPM.

From the minimum fluidisation velocity simulations it could be concluded that the DPM calculated the minimum fluidisation velocities for the 2.5 mm and 1.5 mm particles

correctly. The void fraction at minimum fluidisation conditions was found to be 0.4 for mono-disperse systems and slightly lower for binary mixtures of the particles. Minimum fluidisation calculations with the MFM showed a strong dependency of the specified maximum solids fraction on the computed minimum fluidisation velocity. For the MFM simulations a maximum solids fraction of 0.4 was selected.

In the base case (25% small particles, 75% large particles, $u_{bg} = 1.20$ m/s) DPM simulation with the drag model by Ergun/Wen&Yu, the rate of segregation was overpredicted compared to the experiments. However, a DPM simulation conducted by Beetstra (2005) using a new drag model for poly-disperse particles obtained by van der Hoef et al. (2005) from Lattice Boltzmann simulations, showed that this new drag model improved the prediction of the segregation dynamics significantly. The particle segregation rates computed with the new MFM for the base case compare much better with the experiments and are no longer overestimated, as was the case with MFMs presented before in the literature. Moreover, the formation of a flotsam and jetsam layer at the top and the bottom of the bed was predicted correctly. However, in the MFM the frictional stresses associated with long-term multiple-particle contacts are neglected, resulting in a strong overestimation of the emulsion phase mobility as was also concluded from the single bubble Two-Fluid model calculations reported in chapter 3. Both the new MFM and the DPM predicted the relative segregation for the mixing case (case 2) quite well, but in spite of the higher superficial gas velocity, the emulsion phase mobility is still overpredicted.

The volume fraction weighted bed-averaged granular temperature evolution in time computed with the DPM showed that the granular temperature level of the small particles remains constant, whereas the granular temperature of the large particles decreases, because of the formation of defluidised zones at the bottom of the fluidised bed. The granular temperature level predicted by the new MFM agrees quite well with the values obtained from the DPM simulations, in spite of the large overprediction of the emulsion phase mobility.

To further improve the continuum models for multi-disperse systems, more research is required to correctly describe the frictional stresses in the framework of the kinetic theory of granular flow. Also, future continuum models, but also discrete particle models, can be improved significantly by describing the gas-particle drag with the new poly-disperse drag relations derived from lattice Boltzmann simulations.

Chapter 6

Modelling of large-scale dense gas-solid fluidised beds using the Discrete Bubble Model

Abstract

In this chapter a Discrete Bubble Model (DBM) is developed to model the complex hydrodynamic phenomena prevailing in industrial scale gas-solid fluidised bed reactors, focussing on the macro-scale emulsion phase circulation patterns induced by bubble coalescence. In the DBM, the bubbles are modelled as discrete elements and are tracked individually during their rise through the emulsion phase, which is considered as a continuum. The DBM, originally developed for the description of gas-liquid flows, has been adapted to cope with bubbles with a diameter larger than the size of an Eulerian cell. Moreover, a new drag model for a single bubble rising in a fluidised bed derived from empirical correlations has been implemented, as well as a simple model to account for bubble coalescence and break-up. The strong advantage of the DBM compared to other models previously reported in the literature for the description of large scale fluidised beds is that it fully accounts for the two-way coupling between the bubbles and the emulsion phase, which enables direct computation of the emulsion phase velocity profiles. Comparison of the results of simulations ignoring bubble coalescence and simulations taking bubble coalescence properly into account clearly demonstrated the dominating effect of bubble coalescence on the large-scale circulation patterns prevailing in bubbling fluidised beds. The simulation results for the lateral

profiles of the visible bubble flow rate have been compared qualitatively with experimental results reported by Werther (1974). The effects of the superficial gas velocity and of the bed aspect ratio on the velocity and porosity profiles have been studied. In general, it can be concluded that the DBM is able to capture the salient features of the hydrodynamics of bubbling fluidised beds. However, further research is required to improve the closure equations for the bubble behaviour and bubble coalescence and break-up to enable a quantitative description.

6.1 Introduction

Gas phase polymerisation processes are widely employed nowadays for the polymerisation of ethylene (HDPE and LLDPE) and propylene (Choi and Ray, 1985). In this process highly active and highly selective catalysts are used, which results in an enormous heat production in the reactor. In order to remove the liberated reaction energy to avoid sticking of the produced polymer particles, this process employs a fluidised bed reactor, which is known for its excellent heat transfer characteristics. Because the production capacity of this process is limited by the rate of heat removal, this is a major point of attention in the operation and optimisation of this type of reactors. In today's olefin polymerisation processes there exist two main ways to remove the heat of reaction. One operation mode is the injection of liquid monomer in the bottom of the reactor (condensed mode). Due to the fast evaporation of the liquid monomer part of the produced reaction heat is consumed. The second way of removing the reaction energy is via convection of the emulsion phase in the fluidised bed. It is known that large circulation patterns prevail in industrial scale fluidised bed reactors and the higher the circulation rate, the more heat can be removed from the bottom part of the reactor and the higher the production capacity.

To study these large scale convection patterns detailed hydrodynamic models are required. Earlier work on large scale fluidised bed modelling has been performed by Krishna and van Baten (2001), who modelled large scale air-FCC fluid beds with diameters ranging from 0.1 to 6.0 m in diameter. They developed an Euler-Euler Two-Fluid model, where the emulsion phase was considered as a pseudo liquid and the drag between the bubbles and the dense phase was calculated via the developed Davies-Taylor-Collins relations. In order to account for the influence of the column diameter and the effect of neighbouring bubbles on the rise velocity of the bubbles, a scale factor and an acceleration factor were implemented in the model respectively. Moreover, bubble coalescence and break-up was only implicitly accounted for in their model by using an effective average bubble diameter as a function of the superficial gas velocity and the height in the column, obtained from experimental data.

Another approach to study the global dynamics in gas-fluidised beds was presented by Pannala et al. (2003, 2004), who employed an agent-based bubble model, which allows a direct implementation of bubble coalescence. In their model the bubble trajectory of each individual bubble was computed by integrating the bubble velocity in time, where the bubble velocity was made dependent on the distance to its closest leading neighbour, while taking bubble coalescence into account when two bubbles collide. Although this model has only been used to model fluidised beds with heights smaller than 80 cm, this model should in principle be able to handle large scale fluidised beds. However, in the presented model the dynamics of the emulsion phase was completely ignored, so that their model is incapable of accounting for the important large scale circulation patterns in the emulsion phase. The bubbles rising in a fluidised bed will affect the dynamics of the emulsion phase and, vice versa, the emulsion phase velocity patterns will be dominated by the drag exerted by the bubbles (two-way coupling).
A Discrete Bubble Model (DBM) has been developed to study the hydrodynamics in large-scale fluidised beds that fully accounts for the two-way coupling. The emulsion phase is modelled as a continuum and the bubbles are regarded as discrete elements. The bubble trajectories are computed by integrating the equations of motion (Newton's second law), accounting for bubble coalescence when two bubbles collide, using closures for the forces acting on the individual bubbles. More detailed and fundamental models could be used in addition to experiments to derive the required closures for the bubble behaviour and the emulsion phase rheology. With continuum models (Euler-Euler) using closures from the Kinetic Theory of Granular Flow for the solids phase rheology, or discrete particle models (Euler-Lagrange), where all the individual particles in the fluidised bed are tracked, the bubbles can in principle be completely resolved and the bubble behaviour could be computed. However, for the simulation of the macro-scale circulation patterns prevailing in large, industrial scale fluidised beds with these fundamental models, the required number of grid cells or the required number of particles and the corresponding calculation times would definitely become prohibitive. Therefore, models that are developed to describe the hydrodynamics of very large systems will have to rely on closures for the bubble behaviour. Although the

DBM idealises the bubbles as perfect spheres, its strong advantage is that no a priori assumption is required on the bubble encounter frequency, an important factor determining the bubble coalescence rate.
The DBM, which has been widely used in the field of gas-liquid bubble columns (Lapin and Lübbert, 1994; Sokolichin et al., 1997; Delnoij et al., 1997, 1999), has been somewhat modified to model the hydrodynamics of fluidised beds. Firstly, the DBM together with the closure relations describing the behaviour of bubbles in fluidised beds, including bubble coalescence and splitting, is described. Subsequently, its numerical implementation is shortly presented. After the model verification, simulation results are discussed, focussing on the effect of bubble coalescence and the influence of the gas velocity and aspect ratio on the macro-scale flow structures prevailing in large scale olefin polymerisation reactors.

6.2 Discrete Bubble Model

6.2.1 Model assumptions

The DBM is an Euler-Lagrange type of model, where the dynamics of the continuous emulsion phase is modelled by solving the continuity and volume-averaged Navier-Stokes equations on an Eulerian grid and the bubbles are tracked individually by integrating the equations of motion. A detailed collision model accounts for the bubble-bubble and bubble-wall interactions, including coalescence between bubbles. Constitutive relations are required for the drag force exerted on the bubbles, which are derived from empirical correlations for the terminal rise velocity of a single bubble in fluidised beds, and for the virtual mass force. The emulsion phase density and viscosity are assumed constant (and known from experiments).

6.2.2 Emulsion phase hydrodynamics

The emulsion phase, representing a mixture of particles and gas, is described with the continuity equation and the incompressible volume-averaged Navier-Stokes equa-

tions:

$$\frac{\partial(\epsilon_e \rho_e)}{\partial t} + \nabla \cdot \epsilon_e \rho_e \vec{u} = 0 \tag{6.1}$$

$$\frac{\partial(\epsilon_e \rho_e \vec{u})}{\partial t} + \nabla \cdot \epsilon_e \rho_e \vec{u}\vec{u} = -\epsilon_e \nabla P - \nabla \cdot \epsilon_e \overline{\overline{\tau}}_e + \epsilon_e \rho_e \vec{g} + \vec{S} \tag{6.2}$$

where $\vec{S}$ is the source term that accounts for the momentum transfer between the bubbles and the emulsion phase.

6.2.3 Bubble dynamics

The bubbles in the DBM are considered as discrete elements which are tracked individually according to Newton's second law of motion:

$$m_b \frac{d\vec{v}_b}{dt} = \sum \vec{F} = \vec{F}_g + \vec{F}_p + \vec{F}_d + \vec{F}_{vm} \tag{6.3}$$

where $\vec{F}_g$ is the gravity force, $\vec{F}_p$ the pressure force, $\vec{F}_d$ is the drag force which is the resistance of the moving bubble with the emulsion and $\vec{F}_{vm}$ is the virtual mass force which accounts for the acceleration of the emulsion phase directly surrounding the bubble if a bubble is accelerated. Here, it has been assumed that the bubbles do not exchange gas with the emulsion phase so that the bubbles only grow due to coalescence. Mass transfer between the bubbles and the emulsion phase could in principle be included in the DBM (Darmana et al., 2005a), but has not been implemented yet.
The sum of the pressure and the gravity force, is given in equation 6.4:

$$\vec{F}_g + \vec{F}_p = (\rho_e - \rho_g) V_b \vec{g} \tag{6.4}$$

The drag force on a sphere is computed with the equation by Odar and Hamilton (1964):

$$\vec{F}_d = -\frac{1}{2} C_D \pi R_b^2 \mid \vec{u} - \vec{v} \mid (\vec{u} - \vec{v}) \tag{6.5}$$

where R_b is the radius of the bubble, C_D is the drag coefficient and $\vec{u}$ and $\vec{v}$ are the emulsion and bubble velocity respectively. For the drag coefficient a correlation will be proposed in the next section.

The last force incorporated in the force balance is the virtual mass force, for which the relation derived by Auton (1983) is used:

$$\vec{F}_{vm} = -\left(\frac{D\vec{I}}{Dt} + \vec{I}\cdot\nabla\vec{u}\right) \tag{6.6}$$

$$\vec{I} = C_{vm}\rho_l V_b(\vec{v}-\vec{u}) \tag{6.7}$$

where C_{vm} was assumed to be equal to 0.5.

6.2.4 Number of bubbles

The number of bubbles that enter the fluidised bed in the DBM should correspond with the visible bubble flow rate in the fluidised bed. According to the two-phase theory all the gas in excess to that required for minimum fluidisation flows through the bed as bubbles. However, it was found experimentally that only part of the excess gas flows through the column as visible bubbles. Werther (1992) has measured the fraction of the excess gas visible as bubbles for different particles belonging to different classes according to the Geldart classification (Geldart, 1973; Kunii and Levenspiel, 1991). Using this experimental information and specifying an initial bubble diameter the number of bubbles that enter the bed can be computed. A correlation for the initial bubble diameter for a bubble released from a multihole distributor was given by Chiba and Kobayashi (1972):

$$d_{b0} = 1.71 g^{-0.2} P_t^{0.8} (u-u_{mf})^{0.4} \tag{6.8}$$

where P_t is the orifice pitch.

6.2.5 Bubble coalescence/break-up

Besides the motion of the bubbles calculated with the force balance as described before, the bubbles can meet each other and the system walls. A detailed collision model, originally implemented in the Discrete Particle Model by Hoomans (1999), is employed in the DBM which computes every collision one by one (the so-called hard-sphere approach). To avoid that all the bubbles in the column have to be scanned as a possible

collision partner, the model uses small neighbourlists of possible collision partners. From all the neighbourlists the smallest time to a collision is determined, whereafter this collision is carried out. Of course, bubbles in fluidised beds do not bounce, but will coalesce till a maximum size where the largest bubbles start to break-up, at least for Geldart A/B type particles as encountered in polymerisation reactors. In the DBM this process is simplified in such a way that all the bubbles that meet each other will coalesce till a pre-defined maximum bubble size is reached, whereafter these large bubbles will only collide with other bubbles, approximating a dynamic equilibrium between bubble coalescence and break-up. When the new bubble has accidentally overlap with a third bubble, it has been assumed that this bubble also coalesces with the new bubble. This might result in the formation of a bubble diameter slightly larger than the pre-defined maximum bubble diameter. In the DBM, coalescence is carried out with conservation of mass and momentum. The mass of the new bubble equals the sum of the masses of the two colliding bubbles, the new velocity of the bubble is computed from the total momentum balance and the position of the new bubble is the mass averaged position of the bubbles prior to the collision. A more detailed coalescence model could in principle be easily implemented in the DBM, provided that reliable correlations for bubble coalescence and break-up are available.

6.2.6 Constitutive equation for the drag coefficient

To close the governing equations, the DBM requires a constitutive equation for the drag coefficient of the bubbles, which is derived from an empirical correlation for the steady rise velocity of a single bubble in a fluidised bed.

Bubble rise velocity

Many experimental relations have been derived for the rise velocity of bubbles in a fluidised bed. Main factors influencing the bubble rise velocity are the average diameter of the bubble swarm (d_b), the bed diameter (D_T) and the height of the fluid bed (Krishna and van Baten, 2001). For a single, isolated, bubble with a diameter of d_b the

Table 6.1: parameters for the equation by Werther (1992) (eq. 6.10).

	A	B	D
ψ	0.80	0.65	0.26
α $(D_T < 1)$ m	$3.2D_T^{1/3}$	$2.0D_T^{1/2}$	0.87
α $(D_T > 1)$ m	3.2	2.0	0.87

rise velocity v_b^0 in a quiescent bed of powder is given by Davies and Taylor (1950):

$$v_b^0 = 0.711\sqrt{gd_b} \tag{6.9}$$

In a freely bubbling fluidised bed many bubbles rise together in a swarm and the presence of many neighbouring bubbles affect their rise velocity. Moreover, wall effects may become important in small beds ($D_T < 1$). Werther (1992) formulated a general correlation for the bubble rise velocity in A, B and D powders, where the effect of the bed diameter and swarm effects are incorporated:

$$v_b = \psi(u - u_{mf}) + \alpha v_b^0 \tag{6.10}$$

where ψ is a scale factor accounting for the fraction of visible bubbles and α is a power-law function that incorporates the effect of the column diameter. The different values measured for ψ and α are listed in Table 6.1. More recently, Krishna and van Baten (2001) adapted the Davies-Taylor relation for Geldart A powders by adding two multiplication factors. Firstly, they added a size factor (SF) accounting for the influence of the column diameter on the rise velocity of a single bubble, which was measured by Collins (1967) for gas-liquid systems:

$$SF = \begin{cases} 1 & \dfrac{d_b}{D_T} < 0.125 \\ 1.13e^{-\frac{d_b}{D_T}} & 0.125 < \dfrac{d_b}{D_T} < 0.6 \\ 0.496\sqrt{\frac{D_T}{d_b}} & \dfrac{d_b}{D_T} > 0.6 \end{cases} \tag{6.11}$$

The second factor they added is the wake acceleration factor (AF), since a bubble gets accelerated when it comes into the path of a preceding bubble. The acceleration factor and the averaged bubble diameter were fitted from experimental data, which yielded:

$$AF = 1.64 + 2.7722(u - u_{mf}) \tag{6.12}$$

$$d_b = 0.204(u - u_{mf})^{0.412} \tag{6.13}$$

In these modified correlations by Werther (1992) and Krishna and van Baten (2001) the effect of the emulsion phase velocity patterns is indirectly lumped. In our work the two-way coupling is explicitly accounted for via the momentum transfer rate S. Hence, a drag correlation is derived from the Davies-Taylor correlation for the rise velocity of a single bubble, where the wake acceleration force has been ignored at first.

Drag coefficient

The drag coefficient for a single bubble rising in a quiescent fluid can easily be computed from the steady state force balance and the Davies-Taylor relation (equation 6.9), yielding:

$$m_b \frac{d\vec{v}}{dt} = 0 = \vec{F}_p + \vec{F}_g + \vec{F}_d \tag{6.14}$$

$$(\rho_e - \rho_g)\frac{1}{6}\pi d_b^3 \vec{g} = \frac{1}{2} C_D \frac{1}{4}\pi d_b^2 \rho_e \cdot (0.711)^2 \vec{g} d_b \tag{6.15}$$

This simplifies to the following constant value for the drag coefficient C_D in the usual case that the emulsion phase density largely exceeds the gas density:

$$C_D = \frac{4(\rho_e - \rho_g)}{3\rho_e (0.711)^2} = 2.64 \approx \frac{8}{3} \tag{6.16}$$

This value resembles the drag coefficient given by Darton and Harrison (1974) for high Re_b, who derived the following relation for spherical cap bubbles in fluidised beds:

$$C_D = \frac{16}{Re_b} + \frac{8}{3} \tag{6.17}$$

6.2.7 Boundary conditions

To distinguish internal flow cells from the boundaries, a flag matrix (Kuipers et al., 1993) is used as is schematically depicted in Figure 6.1. The internal cells indicated with number 1 are completely filled with the continuous emulsion phase. That means that no free surface is modelled here, but the emulsion phase can expand through the free in/outflow cells indicated with number 5 when bubbles enter the computational

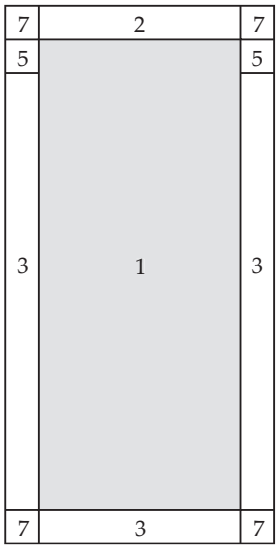

Figure 6.1: Flag matrix used in the flow solver.

Table 6.2: Cell flags and their corresponding boundary conditions.

Flag	Boundary conditions
1	Interior cell, no boundary condition
2	Impermeable wall, free slip boundary
3	Impermeable wall, no slip boundary
5	Prescribed pressure cell, free slip boundary
7	Corner cell, no boundary condition

domain. The other cell flags are explained in Table 6.2.

The bubbles enter the column via nozzles that are equally distributed over the entire area of the bottom plate, as can be seen in Figure 6.2, to mimic a multihole distributor. Each bubble can be displaced randomly in the x and y direction around a nozzle as is depicted in the upperleft corner of Figure 6.2 by the dashed nozzles. Initially, the bubbles start from a randomly determined vertical z-coordinate to avoid that they enter the column simultaneously generating an unwanted pressure wave in the column. Bubbles rise at the plate with a constant velocity indicated as $v_{z,plate}$, corresponding with the specified superficial gas velocity. As soon as the bubble has been released from the plate the movement of the bubble is computed by the force balance as was described before. Bubbles that meet the system walls will bounce fully elastically (no energy dissipation), except collisions with the top of the bed; those bubbles will be removed from the bed.

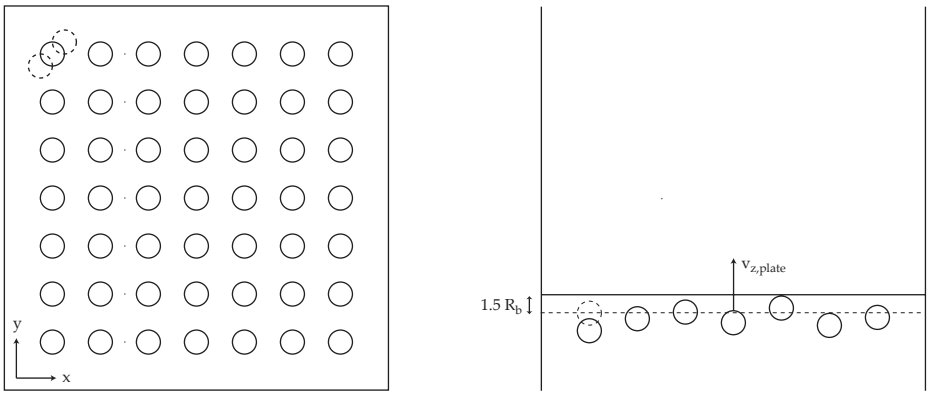

Figure 6.2: Bubble inlet procedure; (a) Configuration of the nozzles and random variation of the x and y positions of the nozzles; (b) Initial vertical bubble positions.

6.2.8 Solution method

The emulsion phase, described by the incompressible Navier-Stokes equations, are discretised on a staggered grid and the SIMPLE algorithm (Patankar, 1980) is employed to obtain the pressure and velocity fields. The incomplete Cholesky conjugate gradient (ICCG) method is used to solve the pressure Poisson equation. The convective terms in the continuity and momentum equations are computed with the second order accurate Barton scheme (Centrella and Wilson, 1984; Goldschmidt, 2001), while the diffusive terms are calculated with standard second order central discretisations.
The force balances for each bubble are integrated with first order explicit time integration, which is sufficient in view of the small time steps used here to move the bubbles (typically $< 1.0 \cdot 10^{-4}$ s). For further details, the interested reader is referred to Delnoij et al. (1997, 1999), van den Hengel (2004) and Darmana et al. (2005a). The issue that needs to be addressed here is the mapping of Lagrangian properties to the Eulerian grid and vice versa, since the bubbles will grow to sizes larger than the Eulerian grid.

Bubble-emulsion interaction

The interaction between the bubbles and the emulsion phase is a two-way coupling mechanism. The bubble phase affects the continuous phase via the void fraction and

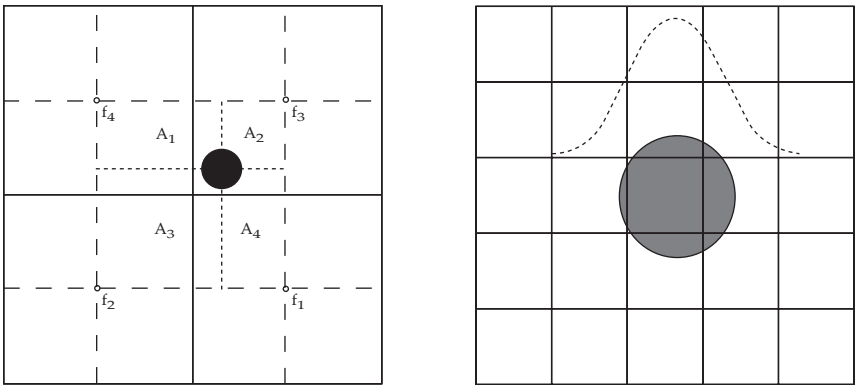

Figure 6.3: Mapping of Lagrangian quantities to the Eulerian grid and vice versa. left: Volume-averaging of bubble properties to the surrounding grid points as applied in the original DBM by Delnoij et al. (1997); right: distribution via a polynomial distribution function (see Darmana et al. (2005b)).

the source term in the Navier-Stokes equation. On the other hand the velocity of the continuous phase influences the force balance of the bubbles via the slip velocity in the drag equation and via the virtual mass force. The source term S in the Navier-Stokes equation is the momentum transfer rate from the bubbles to the emulsion phase per unit volume and is given by:

$$\vec{S} = -\frac{1}{V_{cell}} \sum_{\forall i \in cell} (\vec{F}_{d,i} + \vec{F}_{vm,i}) \tag{6.18}$$

In the conventional DBM developed for gas-liquid flows (Delnoij, 1999), the bubbles were much smaller than the Eulerian grid, which allowed mapping of the bubble quantities to the eight surrounding Eulerian cells via a volume-averaging technique, as is demonstrated in 2D in Figure 6.3. In the DBM for gas-solid fluidised beds, the bubbles coalesce and grow to a size much larger than the grid size required to resolve the emulsion velocity patterns accurately. In this case the volume averaging technique cannot be applied. To map the momentum of bubbles that are larger than a grid cell, a normalised polynomial distribution function is used to distribute the momentum over the surrounding cells and the same function is used to translate Eulerian information

(i.e. emulsion velocities) to the position of the bubble (Deen et al., 2004):

$$D(x_i - x_{i,b}) = \frac{15}{16}\left[\frac{(x_i - x_{i,b})^4}{n^5} - 2\frac{(x_i - x_{i,b})^2}{n^3} + \frac{1}{n}\right] \qquad -n \leq (x_i - x_{i,b}) \leq +n \quad (6.19)$$

The use of a distribution function to map the bubble quantities over the neighbouring Eulerian cells is justified because the averaged larger scale effects of the bubbles on the emulsion phase velocity profiles are of interest and not the detailed velocity profile in the vicinity of a single bubble.

6.3 Model verification

To investigate the effect of the number of nozzles and the initial bubble diameter, simulations have been carried out where only these parameters have been varied while keeping the superficial gas velocity constant (see Figure 6.4). The simulation settings for the base case have been summarised in Table 6.3. In view of the required calculation times the dimensions of the bed were 0.5 x 0.5 x 1.5 m for these test simulations. It can be concluded that the simulations with these different inlet conditions produce the same time-averaged (over 160 s) lateral emulsion velocity profile, indicating that the initial bubble size and number of bubbles do not affect the emulsion phase circulation patterns much.

In order to check whether the time-averaging was carried out over a sufficiently long period, the time-averaged emulsion velocity is depicted in Figure 6.5 averaging over 120, 160 and 200 s for different heights in the fluidised bed. From this figure it can be concluded that an averaging period of 160 s and longer is adequate.

6.4 DBM simulation results

In the base case simulation, the rectangular fluidised bed has a width and depth of 1 m and a height of 3 m. Although a fluidised bed in industry is even larger than the dimensions used here in the simulations, it has been indicated in the literature that a fluidised bed diameter $D > 0.50$ m should already capture qualitatively the main characteristic flow patterns in the fluidised bed. The physical properties of the emulsion

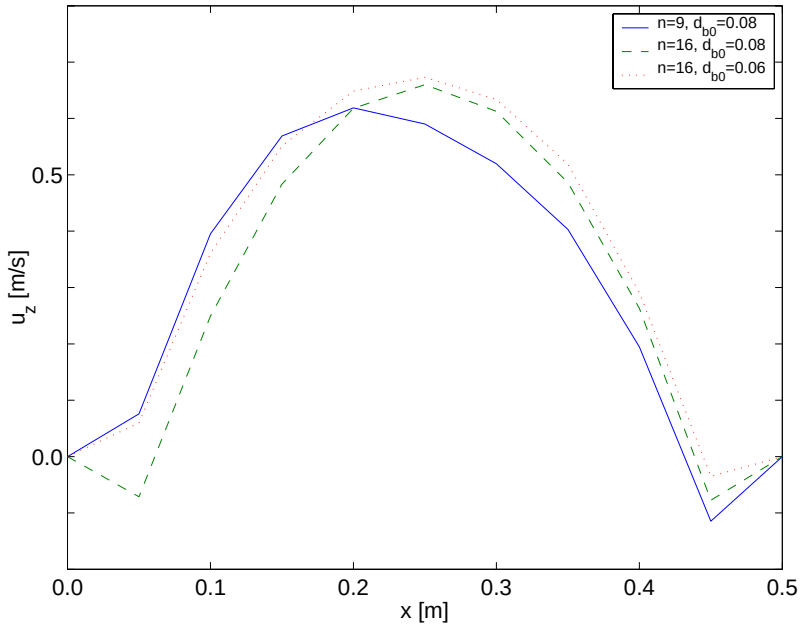

Figure 6.4: Effect of the initial bubble size (d_{b0}) and the number of nozzles (n) on the time-averaged lateral emulsion velocity profile while the superficial gas velocity was kept constant.

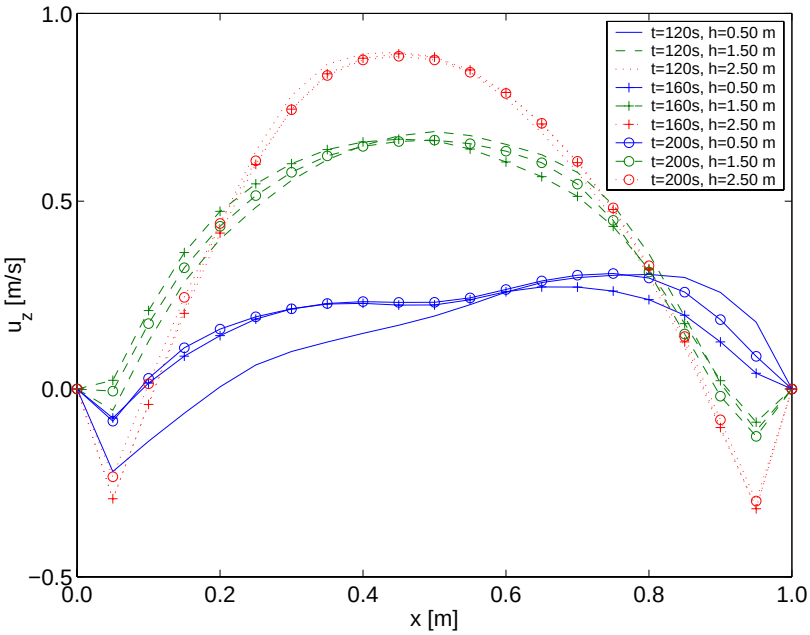

Figure 6.5: Effect of averaging period on the time-averaged lateral emulsion velocity profile at different heights in the bed and a depth of 0.5 m.

Table 6.3: Base case settings used in the DBM.

Variable	Value
emulsion density	$400\,\mathrm{kg/m^3}$
emulsion viscosity	$0.1\,\mathrm{Pa \cdot s}$
gas density	$25\,\mathrm{kg/m^3}$
initial bubble diameter	0.08 m
superficial gas velocity	0.25 m/s
number of nozzles	49
NX	20
NY	20
NZ	60
width	1.0 m
depth	1.0 m
height	3.0 m
time step flowsolver	$5.0 \cdot 10^{-3}$ s
time step bubbles	$5.0 \cdot 10^{-4}$ s
C_{VM}	0.5
C_D	2.67

Table 6.4: Overview of the different simulation cases.

	coalescence	u_0	aspect ratio
base case	yes	0.25 m/s	3
case 1	no	0.25 m/s	3
case 2	yes	0.32 m/s	3
case 3	yes	0.25 m/s	1.5

phase and the bubbles used in the simulations resemble the values that prevail in an industrial scale olefin polymerisation reactor at elevated pressure and are summarised in Table 6.3. The emulsion phase shear viscosity is roughly estimated to be $0.1\,\mathrm{Pa \cdot s}$. Other values used in literature for the emulsion phase viscosity are in the same order of magnitude (Krishna and van Baten, 2001; Kobayashi et al., 2000). The initial bubble diameter is chosen to be 8 cm (estimated with equation 6.8) and the bubbles are allowed to coalesce until a maximum bubble diameter of 20 cm.

Firstly, the effect of bubble coalescence on the time-averaged emulsion phase velocity profile is studied. Thereafter, the lateral profiles of the visible bubble flow computed

with the DBM is compared with an experiment carried out by Werther (1974). Subsequently, the effect of superficial gas velocity and the aspect ratio of the fluidised bed on the emulsion velocity patterns is studied and finally a DBM calculation for a real industrial scale fluidised bed is presented to demonstrate the capabilities of the model. An overview of the simulations is given in Table 6.4.

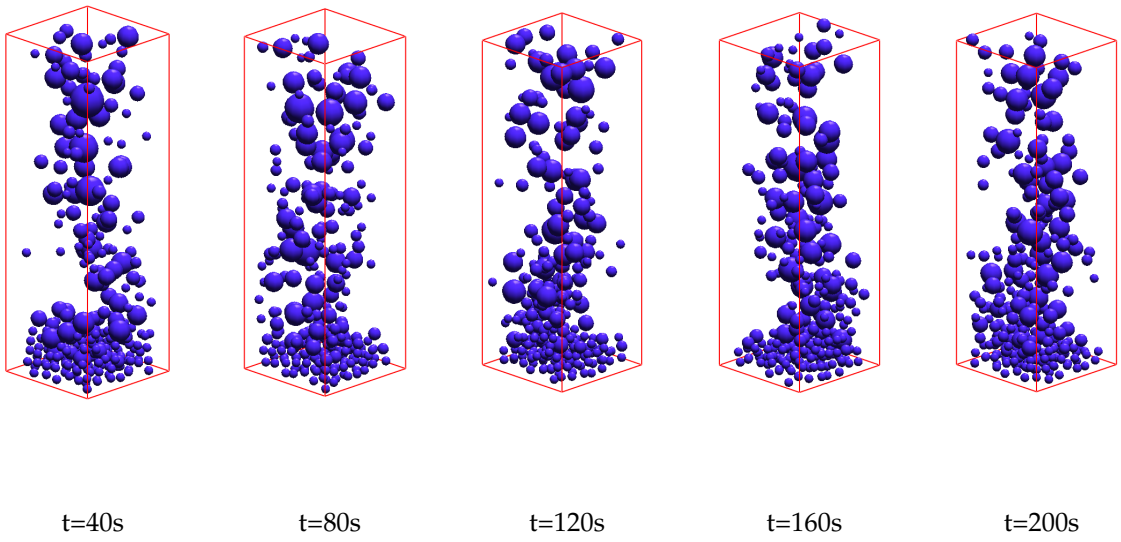

Figure 6.6: Snapshots of the bubbles for the base case simulation at different moments in time.

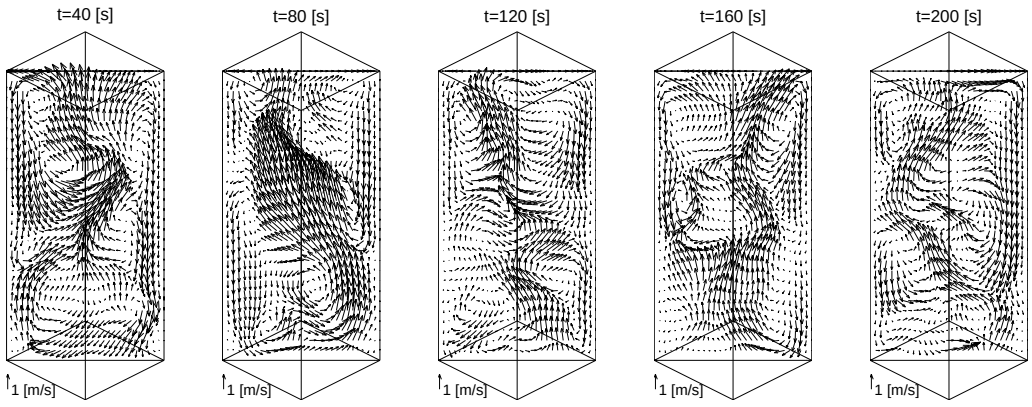

Figure 6.7: Corresponding instantaneous vector plots for the base case simulation.

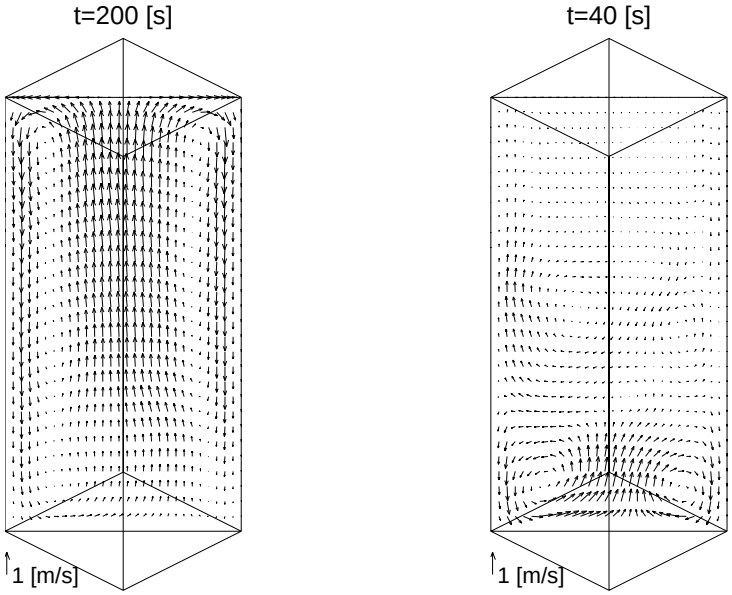

Figure 6.8: Time-averaged velocity profile of the emulsion phase; left: with coalescence; right: without coalescence.

6.4.1 Effect of coalescence

In Figures 6.6 and 6.7 different snapshots and the corresponding emulsion phase velocity fields of the base case simulation are shown. In Kunii and Levenspiel (1991) it is stated that the emulsion flow reflects the rise pattern of the bubbles. The upflow emulsion region should be rich in bubbles and the downflow regions should have few rising bubbles. In Figure 6.6 this pattern can be clearly observed. Time-averaging of the instantaneous emulsion velocity profiles results in a symmetric velocity profile as is shown in Figure 6.8(a). The simulation was time-averaged over 190 s, starting after 10 seconds of simulation to avoid start-up effects. The upwards emulsion velocity in the centre of the bed is low in the bottom part of the bed and increases with height, which can be ascribed to bubble coalescence. Since larger bubbles have higher rise velocities, the emulsion phase velocity will also be higher in the top of the bed due to the bubble-emulsion phase momentum transfer.

In Figure 6.9 the time-averaged lateral profiles of the bubble velocity are shown as a

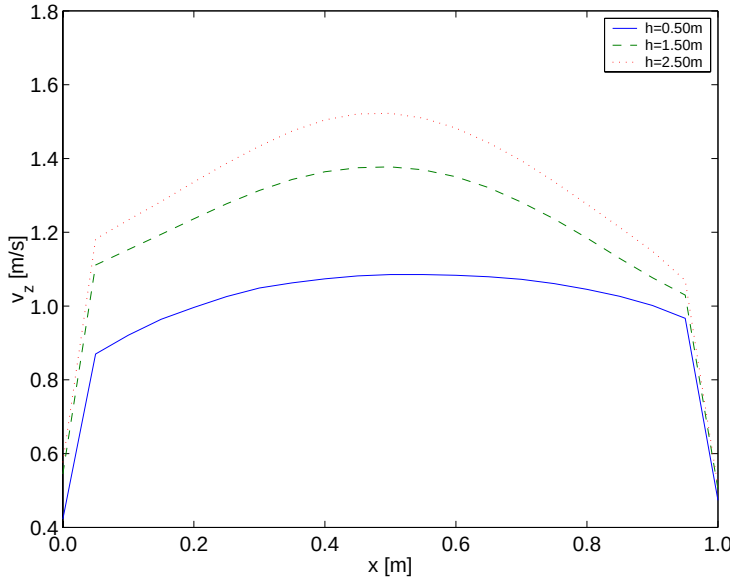

Figure 6.9: Time-averaged lateral bubble velocity profile at different heights in the column and a depth of 0.5 m for the base case.

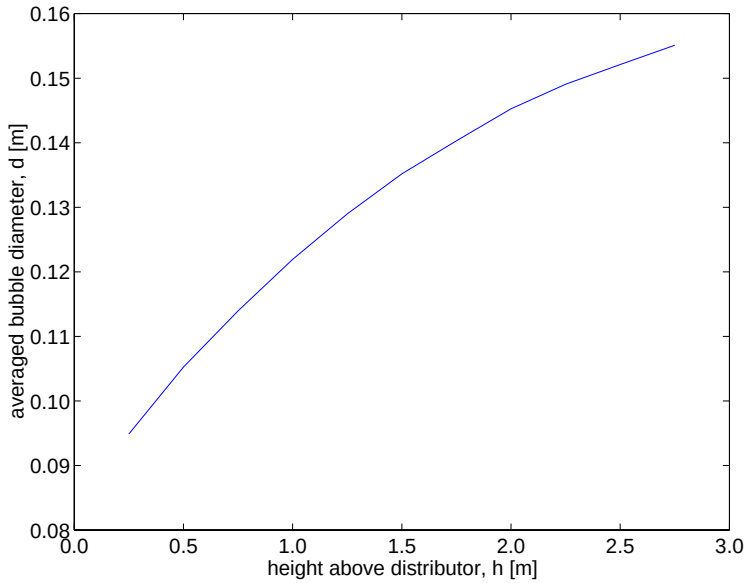

Figure 6.10: Laterally and time-averaged bubble diameter as a function of the height above the distributor for the base case.

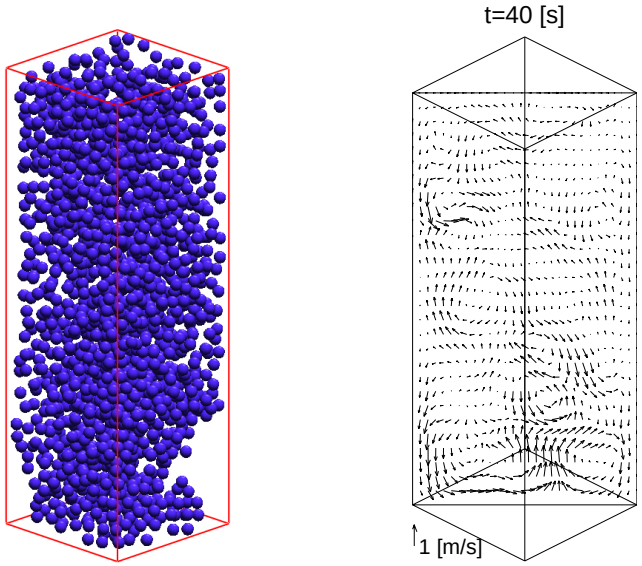

Figure 6.11: Snapshot of the bubbles together with the corresponding instantaneous vector plot of the emulsion phase at 40 s for the base case settings without bubble coalescence (case 1).

function of the height in the fluidised bed and in Figure 6.10 the corresponding averaged bubble diameter as a function of the height above the distributor is depicted. Both figures demonstrate that bubble coalescence occurs till the top of the bed and explains the emulsion velocity profile shown in Figure 6.8(a).

To demonstrate the effect of coalescence on the dynamic behaviour of the fluidised bed, a DBM simulation has been carried out, with the same settings as in the base case simulation, where the bubbles were *not* allowed to coalesce. In Figure 6.11 a snapshot of the fluidised bed without coalescence is depicted together with the corresponding instantaneous emulsion phase velocity field and in Figure 6.8(b) the time-averaged emulsion velocity field is shown. Without bubble coalescence the bed is filled with bubbles that rise in plug flow to the top of the bed. As a consequence of the plug flow behaviour hardly any emulsion phase circulation is induced. In Figure 6.12 the effect of coalescence on the large scale circulation pattern is shown. From this it can be concluded that coalescence is the most important mechanism behind the formation of the strong emulsion upflow in the centre of the bed and the downflow near the walls.

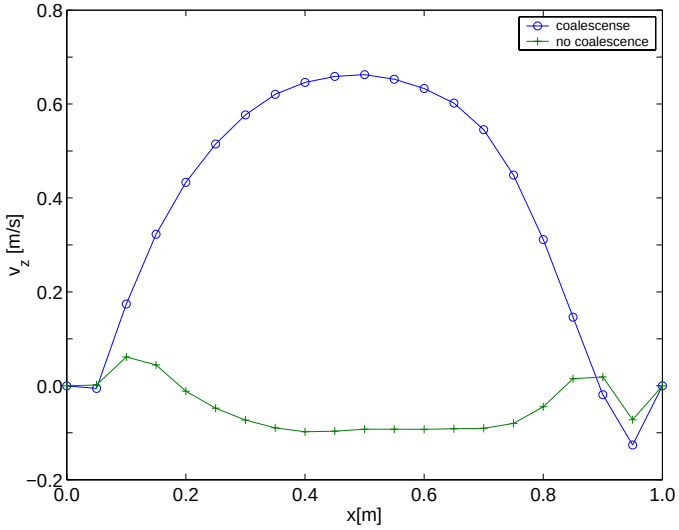

Figure 6.12: Time-averaged velocity profile of the emulsion phase at a height of 1.5 m above the gas distributor and the depth is 0.5 m for the base case settings with and without coalescence (case 1).

6.4.2 Visible bubble flow

The visible bubble flow is defined as the fraction of the total fluidising gas flow that is observable as bubbles. Werther (1974) measured the local bubble gas flow rate with a miniaturised capacitive probe in a cylindrical fluidised bed with a diameter of 20 cm and a height of 50 cm. The bed was filled with quartz sand ($\rho = 2640\,\mathrm{kg/m^3}$) and the minimum fluidisation velocity was 1.8 cm/s. The bed was fluidised with air with a superficial gas velocity of 9.0 cm/s. The results of these measurements are shown in Figure 6.13, showing the lateral profile of the visible bubble flow at different heights in the bed. The zone where most of the bubbles are present is close to the wall for small heights above the distributor and moves towards the centre of the fluidised bed at higher heights above the distributor. The explanation given by Werther (1974) for the fact that the annular zone of increased bubble development moves to the centre of the bed is the rapid increase of the bubble size due to coalescence. It was concluded that this bubble flow pattern is a characteristic property of gas/solid fluidised beds, independent of their diameter.

The same case has been simulated with the DBM, but with a squared fluidised bed in-

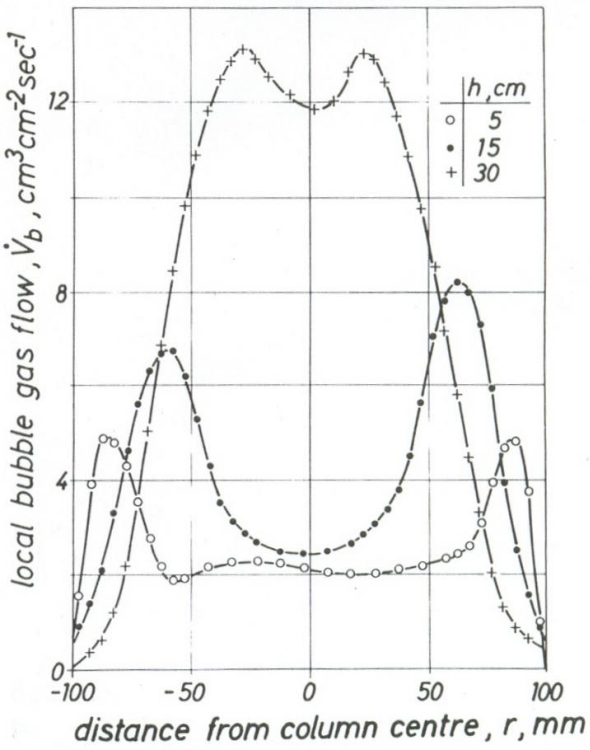

Figure 6.13: The flow pattern of the bubble phase in a fluidised bed of 200 mm diameter (from Werther (1974)).

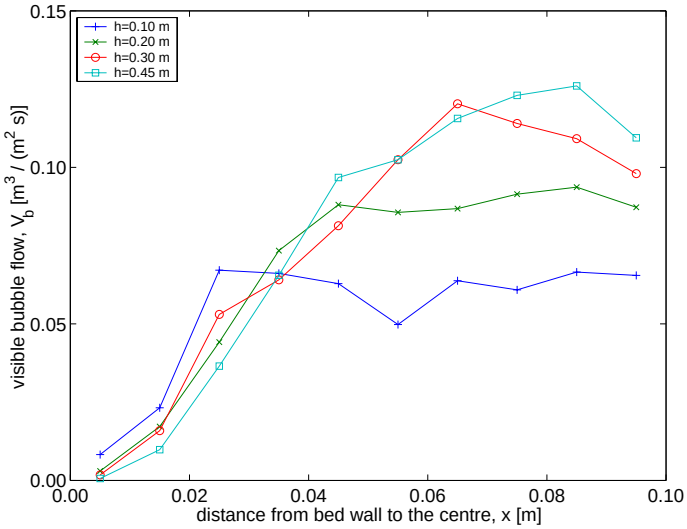

Figure 6.14: Visible bubble flow at different heights and a depth of 0.1 m.

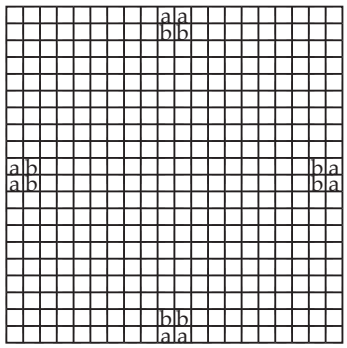

Figure 6.15: Averaging method for constructing visible bubble flow picture. The cells marked with an 'a' are averaged to construct one data point, cells 'b' to make the second point and so forth.

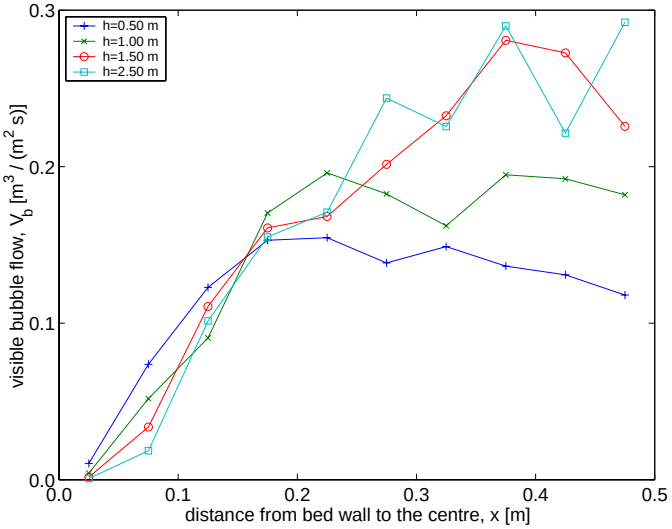

Figure 6.16: Visible bubble flow at different heights and a depth of 0.5 m: Base case simulation.

stead of a cylindrical configuration. The emulsion phase density is set to 1300 kg/m^3 and the emulsion phase viscosity to 0.1 Pa · s. The bubbles enter the bed via 100 nozzles with an initial bubble diameter of 8 mm and the bubbles can coalesce till a maximum diameter of 4 cm. The computed lateral profile of the visible bubble flow with the DBM is depicted in Figure 6.14. During a period of 90 s all the bubbles were counted that passed a cell with their centre of mass in the cross-sectional area of the bed at a certain height. Thereafter, the total volume of bubbles in that cell was divided by the cross-sectional area of that cell and by the averaging time. Here the visible bubble flow pattern is plotted from the bed wall to the centre. All the data points in this figure represent the average of eight values around the centre of the bed as is indicated in Figure 6.15. The visible bubble flow as a function of the bed height predicted by DBM resembles the experimental values by Werther (1974) well. The maximum in the visible bubble flow profile indeed shifts to the column centre, although the maxima computed by the DBM are less pronounced. From this figure it can be concluded that the DBM is able to predict the characteristic bubble flow behaviour in a gas-solid fluidised bed.

The visible bubble flow as computed with the base case DBM simulation is shown in Figure 6.17. This figure shows a top view of the bed at different heights above the dis-

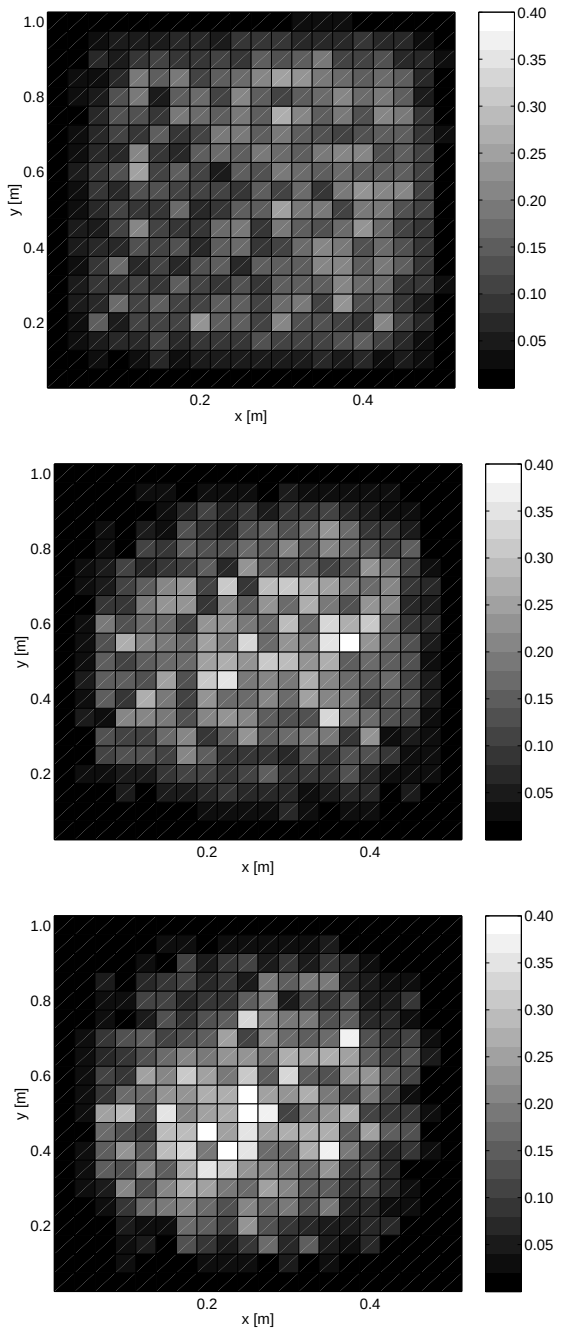

Figure 6.17: Lateral profile of the visible bubble flow (V_b $[m^3/(m^2 s)]$) at different heights computed for the base case; top: 0.5 m; middle: 1.5 m; bottom: 2.5 m.

tributor and the motion of the bubbles towards the centre of the bed is clearly demonstrated. The visible bubble flow as a function of the lateral position is shown in Figure 6.16, showing again the same trend.

6.4.3 Effect of superficial gas velocity

To study the effect of the superficial gas velocity on the hydrodynamics of the fluidised bed a simulation has been carried out with $u_0 = 0.32$ m/s (case 2). In Figures 6.19 and 6.20 snapshots of the bubbles and the time-averaged emulsion phase velocity profiles of the base case and case 2 are depicted. From the snapshots it can be seen that a higher superficial gas velocity results in larger bubbles in the fluidised bed and also less bubbles are observed. Compared to the base case, a higher superficial gas velocity results in a higher upflow velocity of the emulsion phase, especially in the middle part of the bed. In Figure 6.18 the lateral profiles of the emulsion phase velocity is shown for the base case and case 2 at different heights in the bed.

At a higher superficial gas velocity the maximum emulsion velocity is reached in the

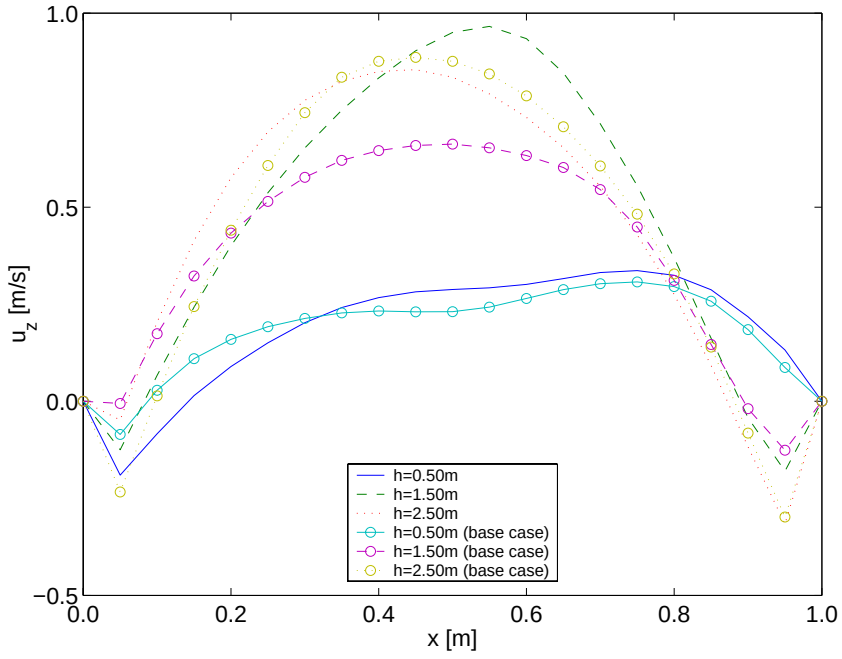

Figure 6.18: Time-averaged lateral emulsion velocity profile at different heights in the bed at a depth of 0.5 m: Effect of superficial gas velocity.

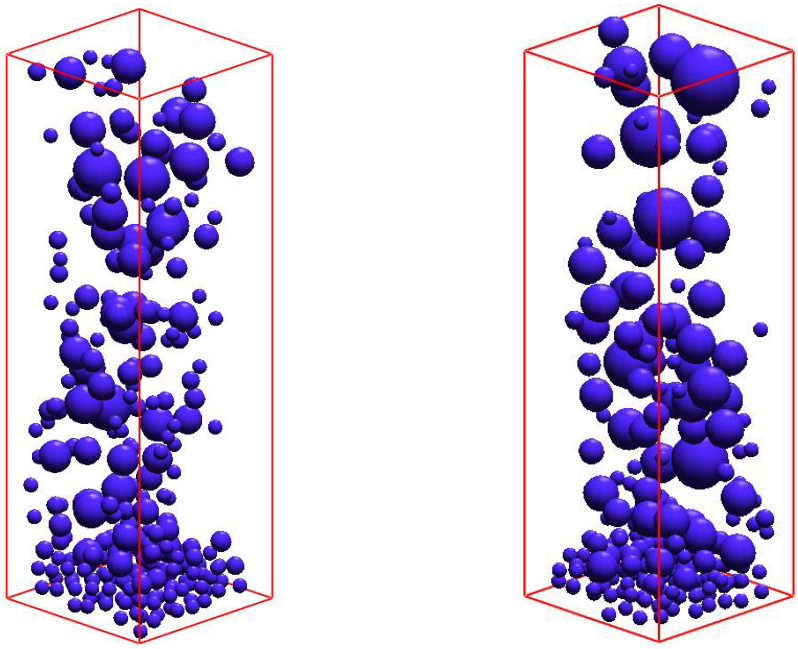

Figure 6.19: Snapshots of the base case (left) and case 2 (right).

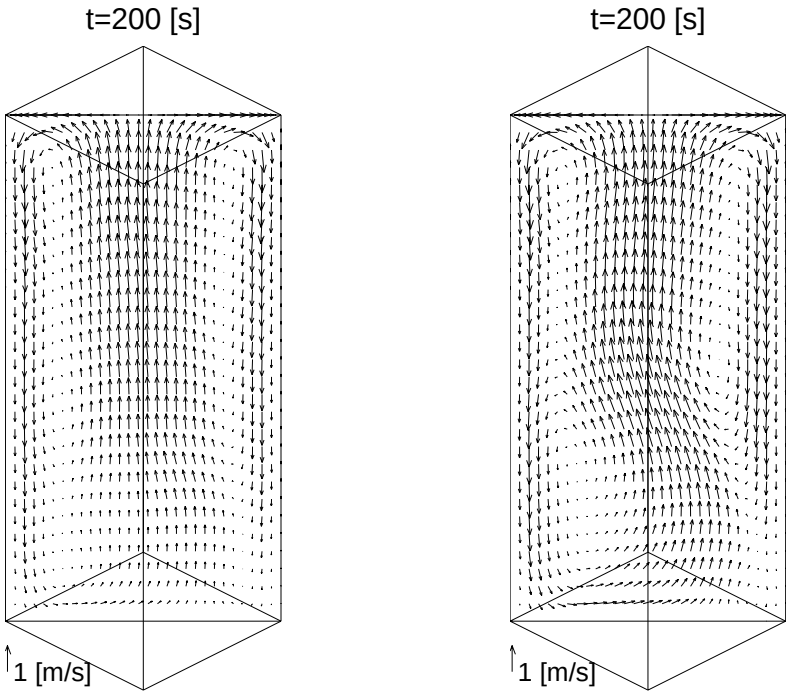

Figure 6.20: Time-averaged vector plots of the base case (left) and case 2 (right).

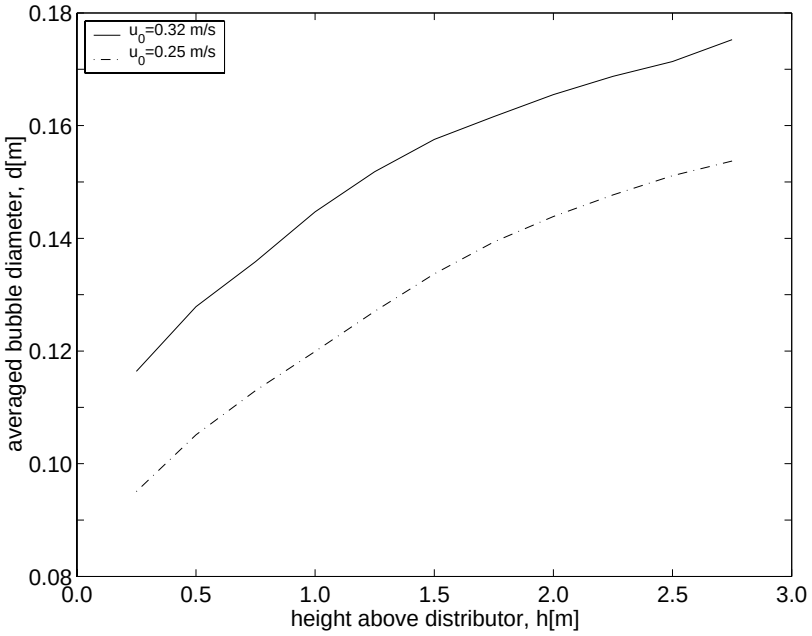

Figure 6.21: Laterally and time-averaged bubble diameter as a function of the height above the distributor: Effect of superficial gas velocity.

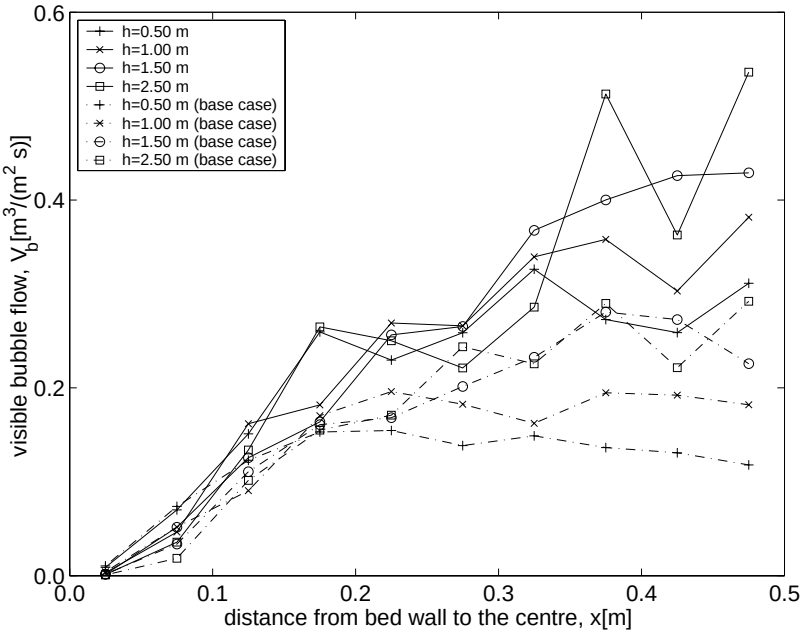

Figure 6.22: Effect of superficial gas velocity on the visible bubble flow pattern.

middle of the bed. This can be explained by the fact that the relative increase in the averaged bubble diameter is smaller at higher bed heights for the case with the higher superficial gas velocity, as is shown in Figure 6.21.
The influence of the height above the distributor on the bubble diameter can be fitted using the generalised Darton's equation:

$$d_b = c(u - u_{mf})^A (h + 4\sqrt{A_0})^B g^{-0.2} \tag{6.20}$$

The value for exponent B fitted from Figure 6.21 is approximately 0.2, which is much lower than the exponent proposed by Darton et al. (1977), 0.8. This difference can be explained by the fact that in the DBM the bubbles grow until a pre-defined maximum bubble size, which is probably smaller than the maximum bubble size encountered in the experiments by Darton et al. (1977).
In Figure 6.22 the effect of the superficial gas velocity on the visible bubble flow is depicted, showing again the same trend for the visible bubble flow pattern. The visible bubble flow is higher for the case with a higher superficial gas velocity, since larger bubbles are formed that rise with a higher rise velocity.

6.4.4 Effect of aspect ratio

In Figures 6.23 and 6.24 snapshots of the bubbles and the corresponding instantaneous emulsion phase velocity profiles are shown of a DBM calculation with a lower aspect ratio (case 3). An important difference with the base case simulation is that the bubbles cannot become as large, which results in a much weaker circulation pattern, as is demonstrated in Figure 6.25. In Figure 6.26 it is shown that the emulsion velocity profile is flatter than in the base case simulation, because the bubbles are still more distributed over the entire cross section of the bed. In the base case simulation much larger bubbles are formed that rise through the centre of the fluidised bed generating a much stronger circulation pattern, which diverts the bubbles towards the bed centre.

The lateral visible bubble flow pattern is shown in Figure 6.27. Except from the lowest part of the bed the characteristic visible bubble flow pattern is rather well pronounced,

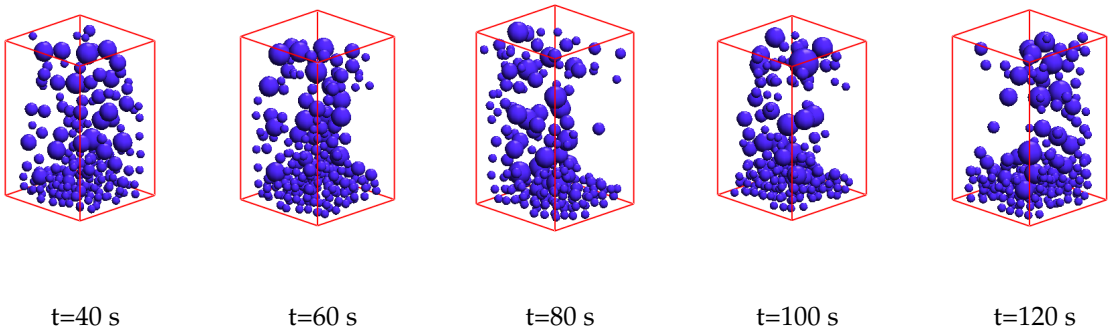

Figure 6.23: Snapshots of the bubbles in the DBM simulation with an aspect ratio of 1.5 (case 3).

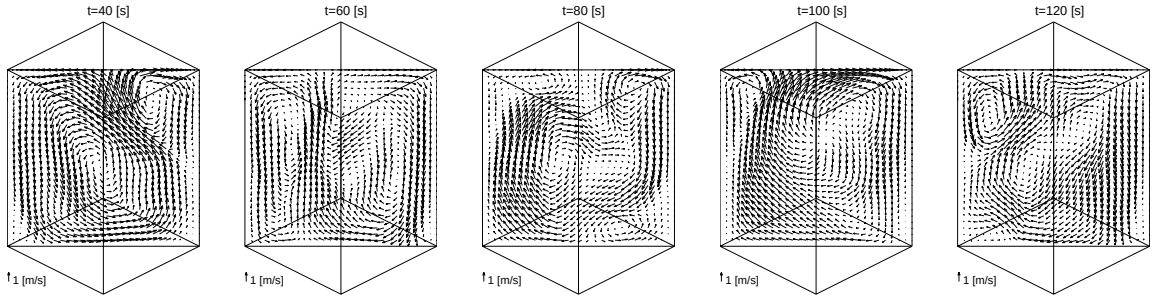

Figure 6.24: Corresponding instantaneous vector plots of the DBM simulation with an aspect ratio of 1.5 (case 3).

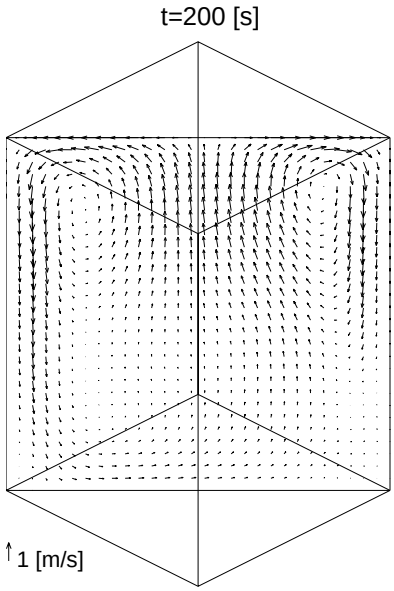

Figure 6.25: Time-averaged vector plot of the simulation with an aspect ratio of 1.5 (case 3).

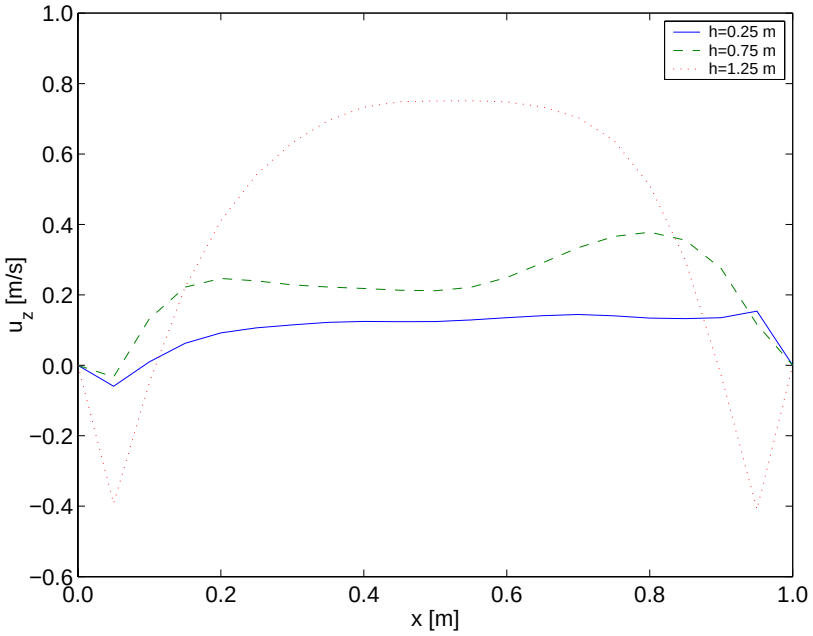

Figure 6.26: Time-averaged emulsion velocity profile at different heights in the column with an aspect ratio of 1.5 (case 3).

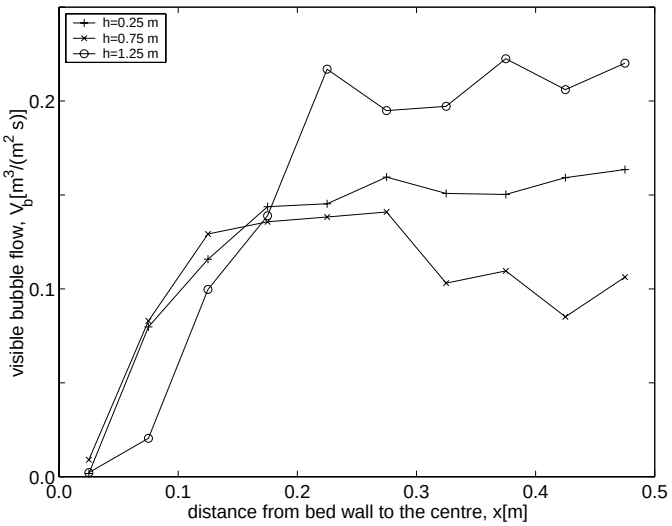

Figure 6.27: Visible bubble flow for different heights in the column (case 3).

much more pronounced than in the base case. The close connection between the flow profile of the bubbles and the movement of the emulsion phase has also been found experimentally by Werther (1974), which is reproduced in Figure 6.28. In this experiment the velocity profile of the bubble phase was measured at a height of 45 cm above the distributor when the total bed height was in one case 50 cm and 100 cm in the other case. A higher bed yields a stronger down-flow of solids near the wall, resulting in a shift in the bubble flow pattern in lower regions of the bed towards the centre of the bed. In the DBM simulations this effect is also observed as is shown in Figure 6.29. The bubble flow pattern of the base case is slightly more directed towards the centre of the bed, compared to the case with a lower aspect ratio.

6.4.5 Industrial scale fluidised bed

In the previous paragraphs, the hydrodynamics have been studied of fluidised beds at an intermediate scale (1 m x 1 m x 3 m). However, an industrial scale fluidised bed reactor used for gas phase olefin polymerisations is even larger. In this paragraph it is demonstrated that the DBM is able to model the hydrodynamics of an industrial scale fluidised bed reactor. In Figure 6.30 a snapshot of the bubbles and the time-averaged emulsion phase velocity field are depicted, for a fluidised bed with a dimension of 4 m x 4 m x 8 m (40x40x40 computational cells). The bubbles entered the fluidised bed via 196 nozzles with an initial bubble diameter of 8 cm. The other simulation settings were kept the same as for the base case simulation. Imagine to model a fluidised bed with this size with a Two Fluid Model approach. To capture the bubble dynamics using a continuum model a minimum grid size of 5 mm is required for sufficient accuracy. This will result in a simulation with 800x800x1600 ($\sim 10^9$!) computational cells to model a fluidised bed at industrial scale. With the computer power currently available this will be an impossible job and will remain impossible in the foreseeable future. Therefore, it can be stated that the DBM is the most suitable model currently available to study the large scale circulation patterns prevailing in industrial scale fluidised bed reactors, provided that an accurate and detailed description of the bubble dynamics and bubble coalescence and splitting is implemented.

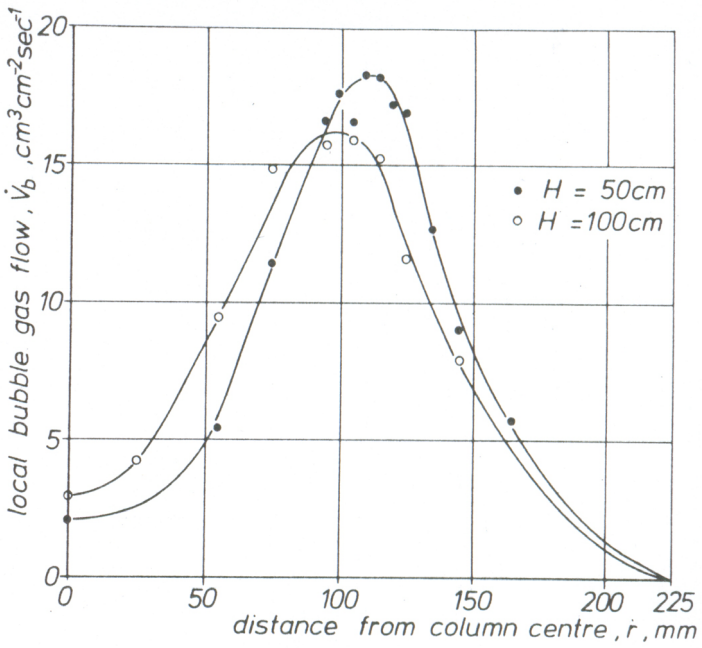

Figure 6.28: Experimentally observed effect of aspect ratio on the bubble flow (from Werther (1974)).

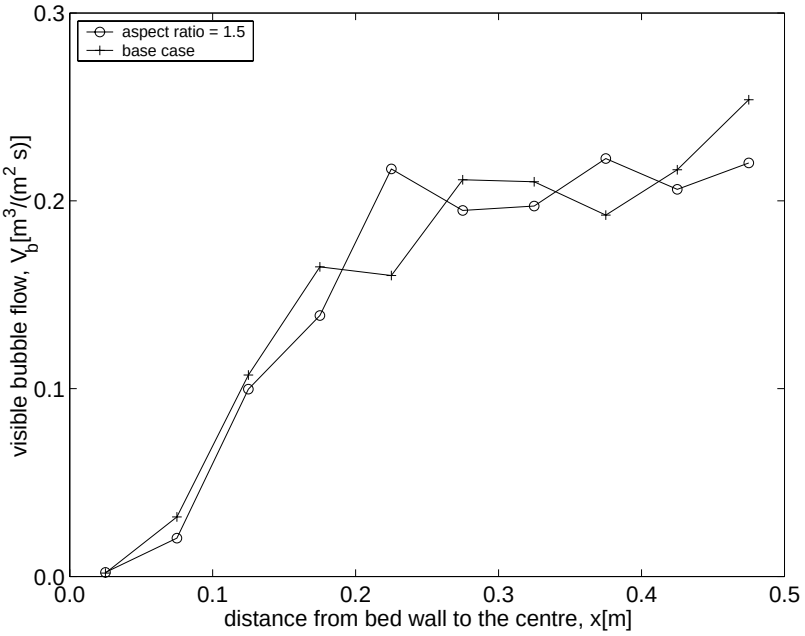

Figure 6.29: Effect of the aspect ratio on the visible bubble flow. Height is 1.25 m and depth is 0.5 m.

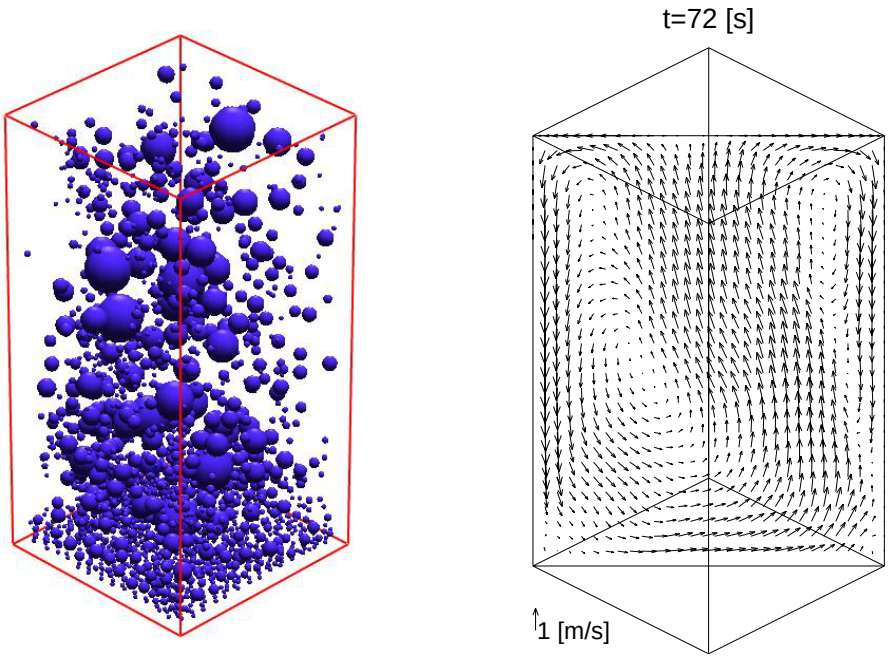

Figure 6.30: Snapshot of the bubbles and the time-averaged emulsion phase velocity field for a DBM simulation for an industrial scale fluidised bed (4 m x 4 m x 8 m).

6.5 Outlook

In this work it is shown that the DBM is able to model characteristic flow patterns prevailing in freely bubbling fluidised beds and that it can be used for further research on industrial scale fluidised beds. However, the wake interaction that exists between the bubbles has not been incorporated yet in the DBM. To get a better prediction of the bubble flow in fluidised beds, this lateral bubble interaction should be implemented in the DBM.

In gas phase olefin polymerisation reactors, the rate of heat removal is the limiting factor in the production process. To gain more insight in the heat transport in these type of reactors, the DBM can relatively straightforward be extended with mass and heat balances, making use of detailed kinetic models available in the literature (e.g. Hatzantonis et al., 2000).

In the DBM the bubbles can coalesce till a pre-defined maximum bubble size, whereas in reality larger bubbles can break-up into smaller ones. The DBM can in principle be

extended with a break-up routine for bubbles in fluidised beds, provided that reliable closures are available.

6.6 Conclusions

In this chapter an Euler-Lagrange model, the Discrete Bubble Model (DBM) has been developed to model the large circulation patterns prevailing in industrial scale fluidised bed reactors. The DBM, originally developed to describe gas-liquid bubble columns, has been modified to simulate gas-solid freely bubbling fluidised beds. The mapping of Lagrangian information to the Eulerian grid and vice versa has been adapted to cope with bubbles larger than an Eulerian grid cell. Moreover, a drag model for a single bubble rising in a fluidised bed was implemented according to the Davies-Taylor relation.

Comparison of a DBM simulation that accounted for bubble coalesce with a simulation without bubble coalescence showed the crucial importance of coalescence for the large scale circulation patterns in the emulsion phase. Without coalescence all the bubbles rise in plug flow to the top of the fluidised bed and hardly any circulation of the emulsion phase is observed. From the simulation results it can be concluded that the large circulation patterns prevailing in industrial scale fluidised beds is a result of bubble coalescence. Since the DBM tracks the bubbles explicitly, bubble coalescence can be accounted for in a direct way.

The DBM results were compared qualitatively with experimental results carried out by Werther (1974), for the characteristic visible bubble flow patterns in freely bubbling fluidised beds. In these experiments a zone of increased bubble development was observed that shifted towards the centre of the bed. The DBM results showed a similar characteristic visible bubble flow pattern, although the zone of preferred bubble flow was somewhat less pronounced.

A higher superficial gas velocity did not change the large emulsion circulation patterns much. A slightly higher time-averaged emulsion velocity was found in the middle of the bed, as a result of the bubble coalescence.
For a lower aspect ratio of the bed a much weaker emulsion phase circulation pattern was found. Due to the lower bed height the bubbles cannot grow as large. The slight shift in the lateral profile for the visible bubble flow towards the bed centre for the case with the lower aspect ratio of the bed, computed by the DBM, corresponds to the experimental results by Werther (1974).

Finally, it was demonstrated that the DBM is able to model the hydrodynamics of industrial scale fluidised bed reactors (4 m x 4 m x 8 m) within acceptable calculation times.
Generally, it can be stated that the DBM is able to capture the characteristic hydrodynamic behaviour of freely bubbling fluidised beds.

Appendix A

Results presented in Chapters 2, 3 and 5

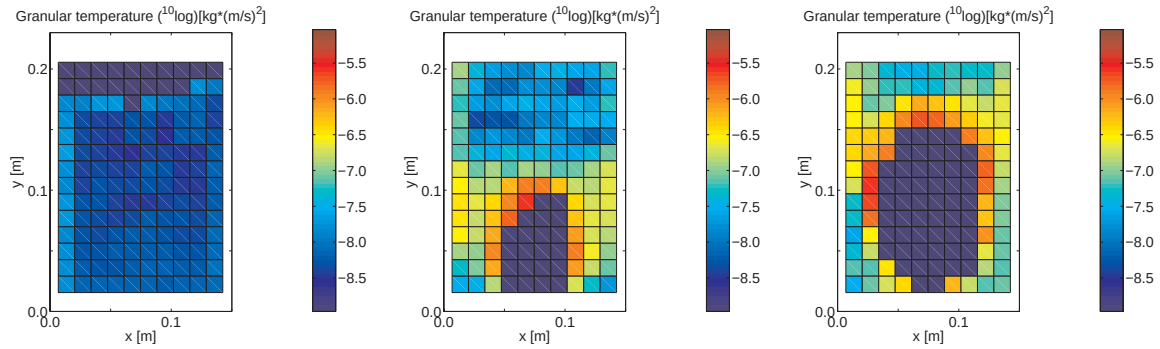

Figure A.1: Single bubble experiment in the 15 cm set-up using 2.5 mm glass beads.

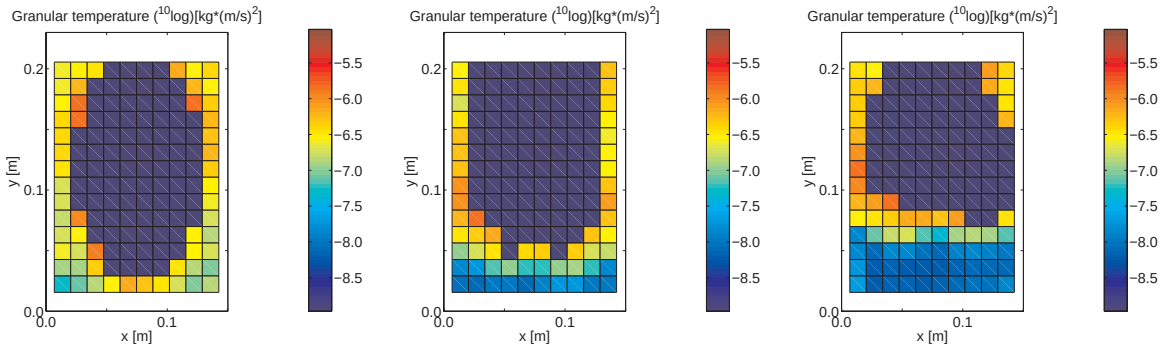

Figure A.2: Single bubble experiment in the 15 cm set-up using 2.5 mm glass beads.

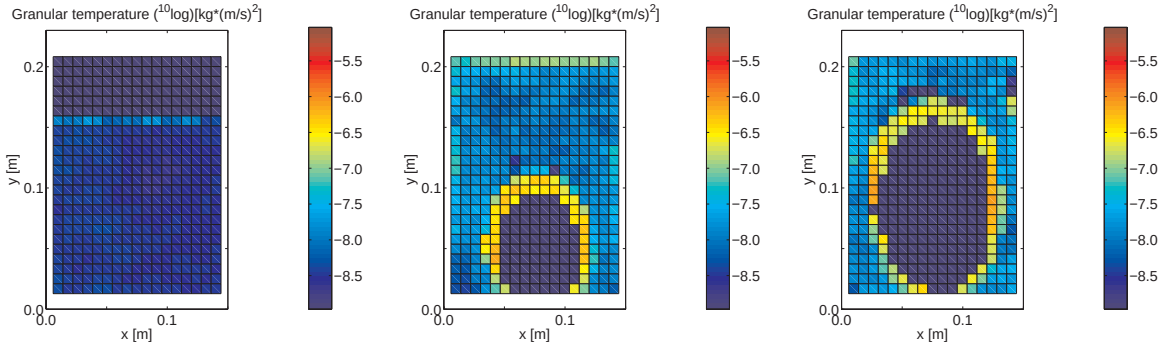

Figure A.3: Single bubble experiment in the 15 cm set-up using 1.5 mm glass beads.

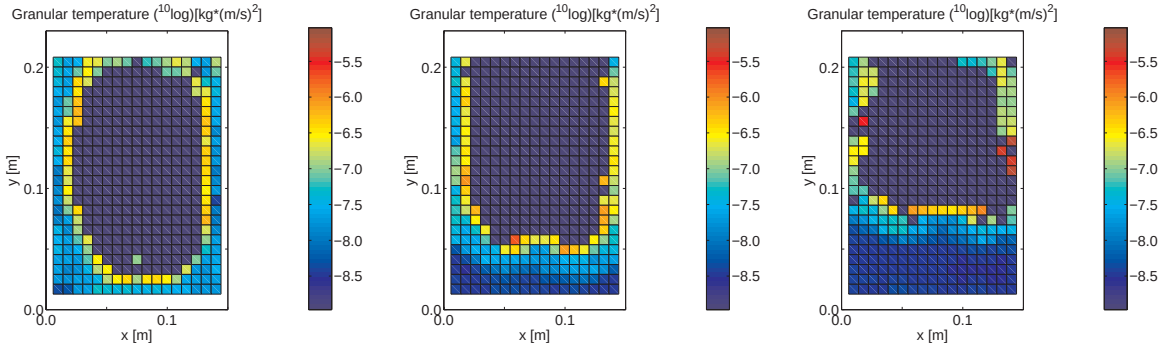

Figure A.4: Single bubble experiment in the 15 cm set-up using 1.5 mm glass beads.

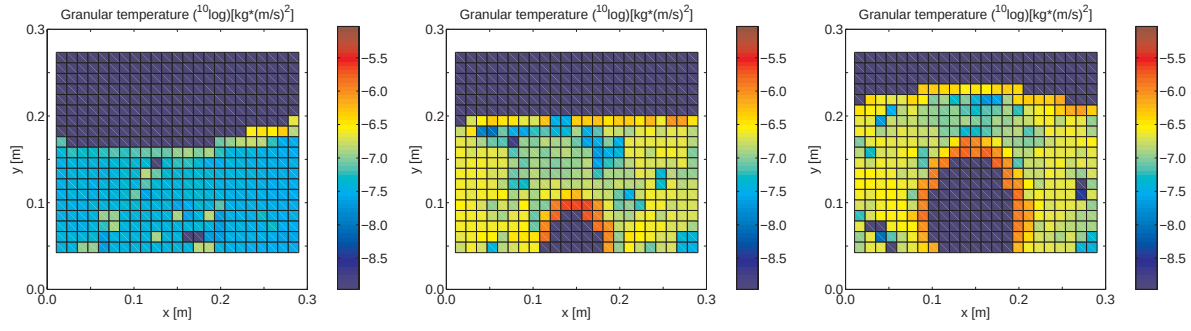

Figure A.5: Single bubble experiment in the 30 cm set-up using 2.5 mm glass beads.

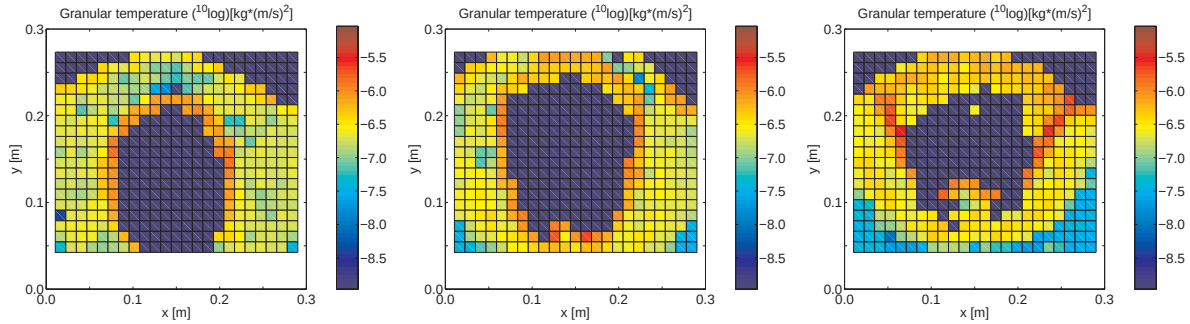

Figure A.6: Single bubble experiment in the 30 cm set-up using 2.5 mm glass beads.

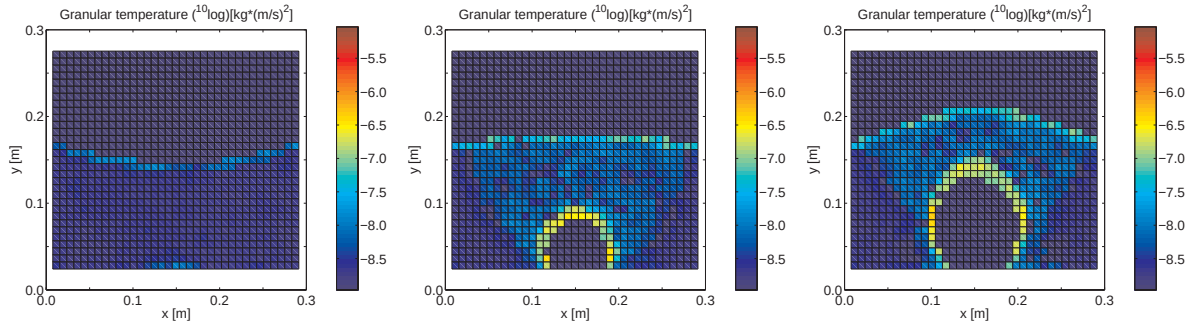

Figure A.7: Single bubble experiment in the 30 cm set-up using 1.5 mm glass beads.

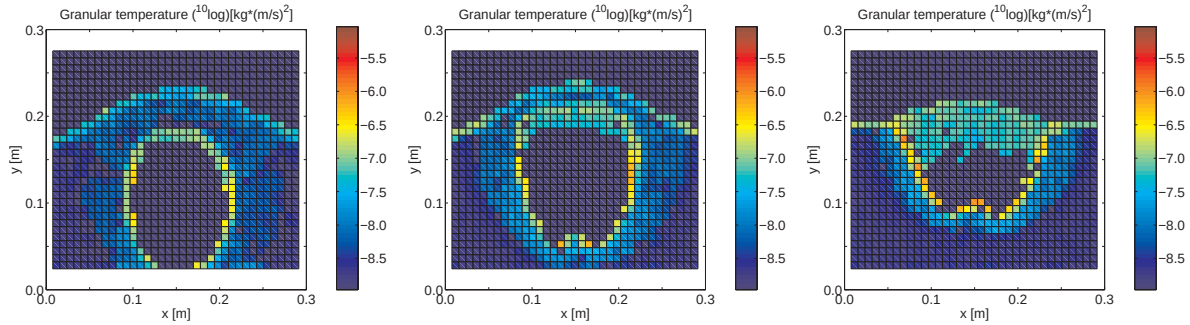

Figure A.8: Single bubble experiment in the 30 cm set-up using 1.5 mm glass beads.

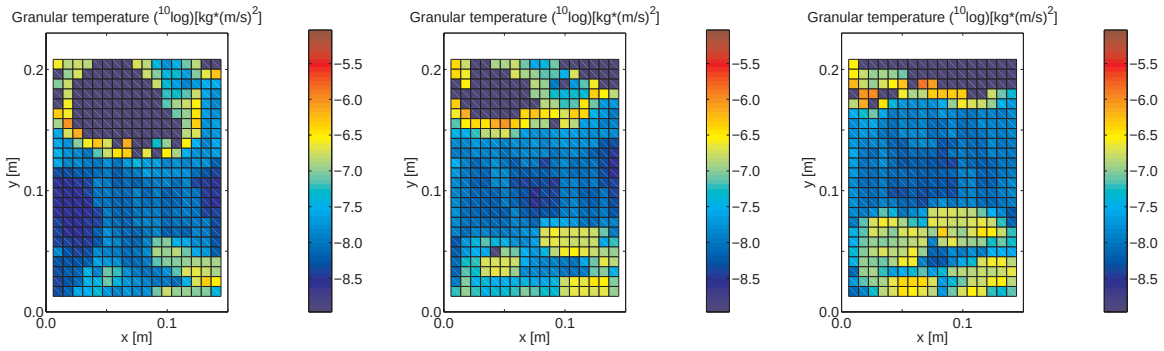

Figure A.9: Freely bubbling experiment in the 15 cm set-up using 1.5 mm glass beads.

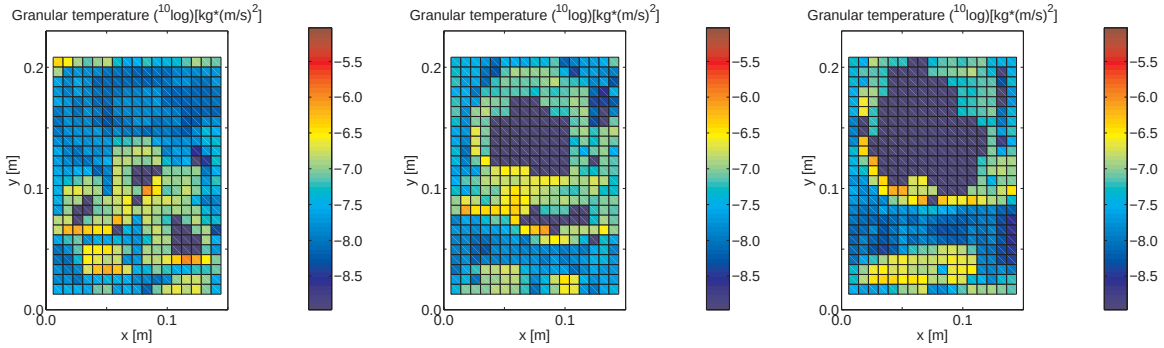

Figure A.10: Freely bubbling experiment in the 15 cm set-up using 1.5 mm glass beads.

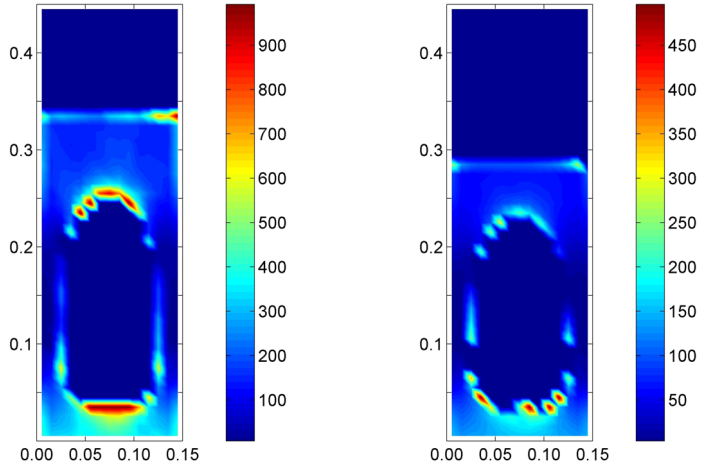

Figure A.11: DPM simulation of a single bubble injected in a mono-disperse fluidised bed with the drag relation by Ergun/Wen&Yu. Contour plot of the variable $Re/(1-\epsilon)$ with (left) 2.5 mm particles and (right) 1.5 mm particles.

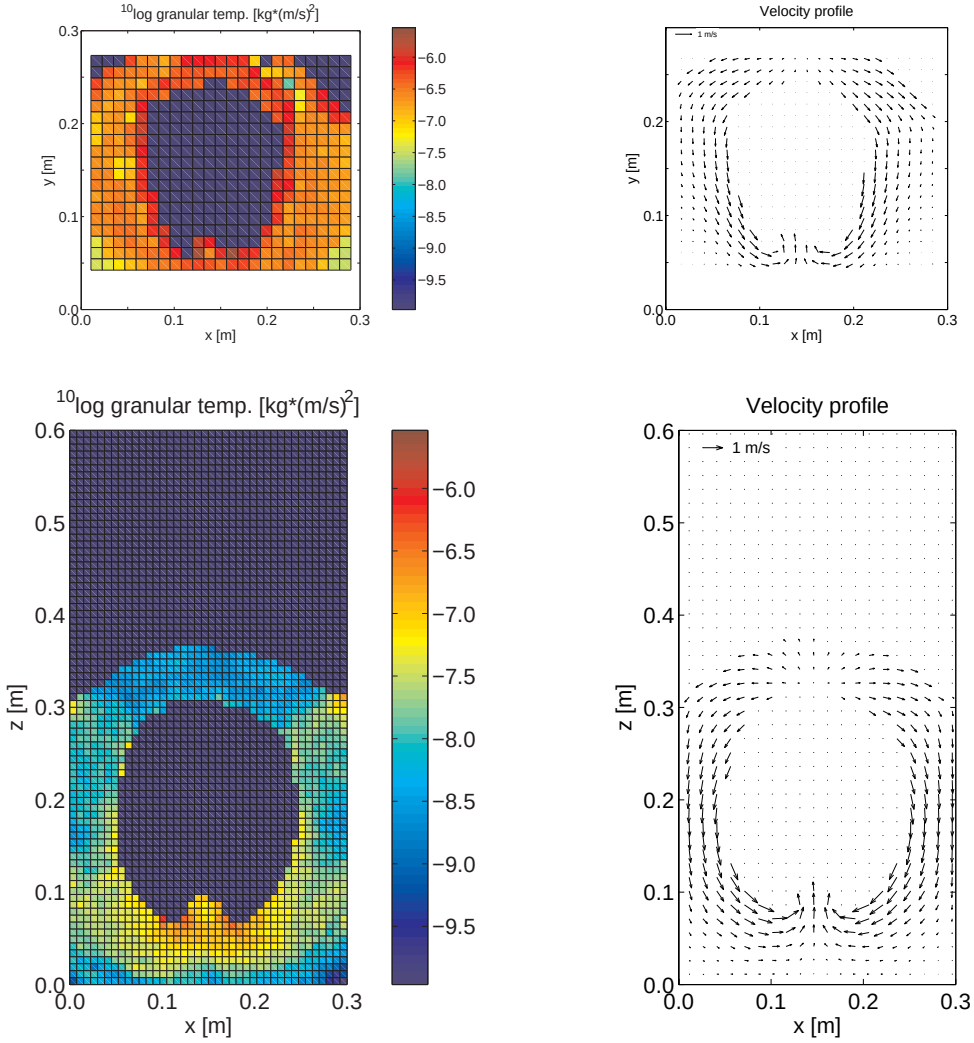

Figure A.12: Granular temperature and solids velocity profiles around a single bubble injected in a monodisperse fluidised bed of 30 cm wide filled with 2.5 mm particles at 0.3 s after injection; top: Experiment; bottom: DPM.

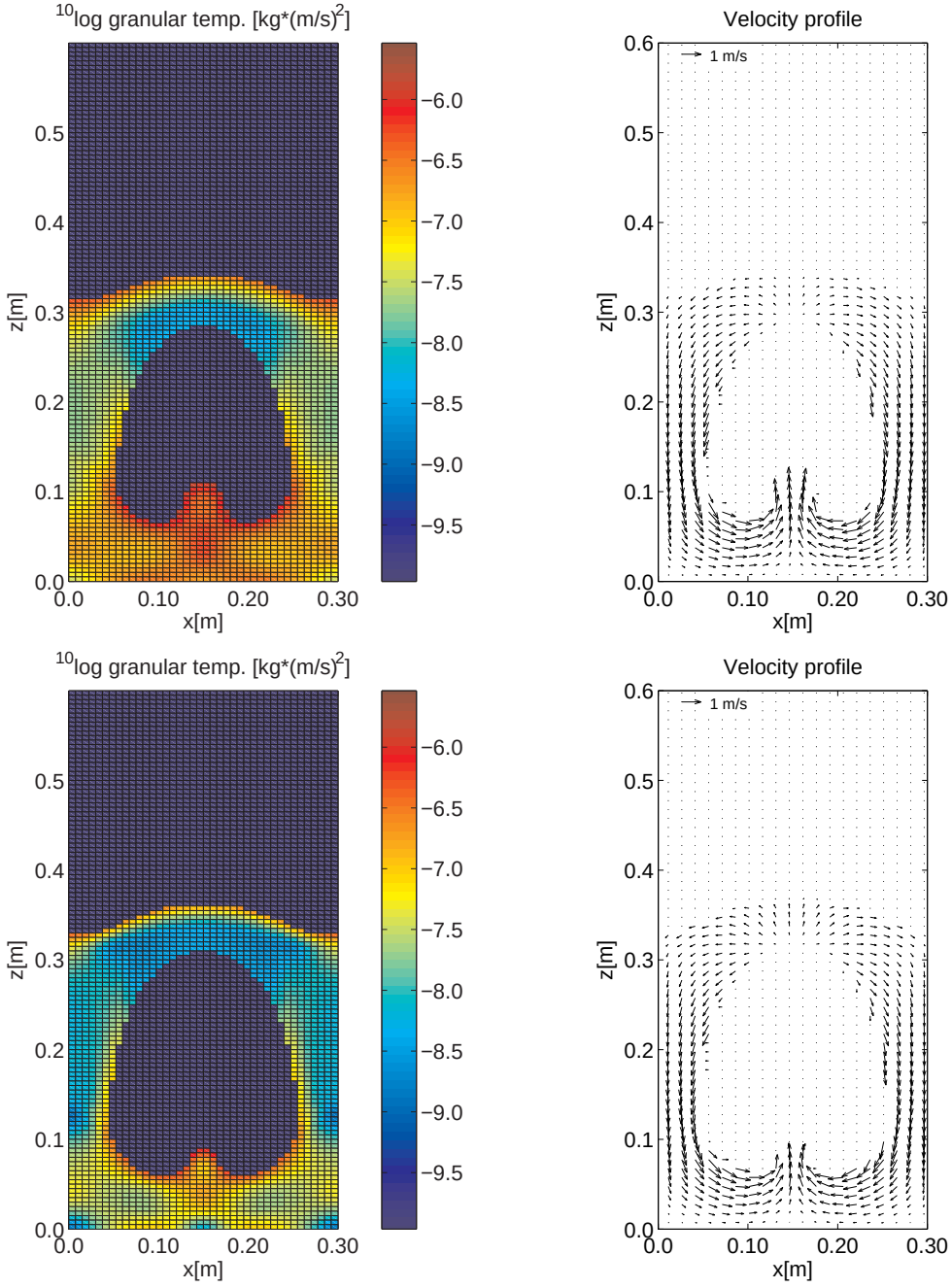

Figure A.13: Granular temperature and solids velocity profiles around a single bubble injected in a monodisperse fluidised bed of 30 cm wide filled with 2.5 mm particles at 0.3 s after injection; top: TFM; bottom: TFM with $e_{\text{eff}} = 0.86$.

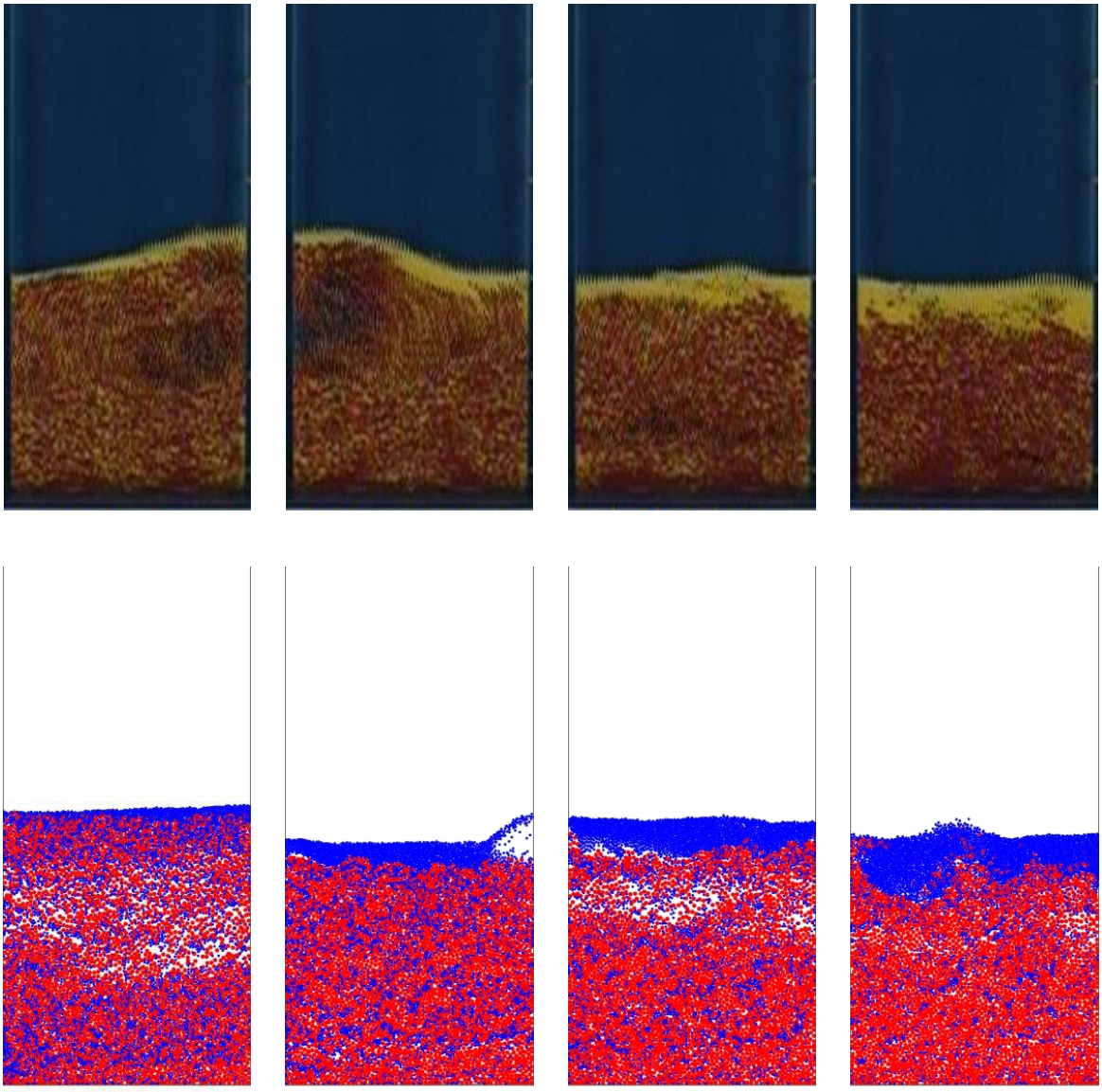

Figure A.14: Snapshots of the base case DPM simulation and the experiments performed by Goldschmidt et al. (2003): u_{bg} = 1.20 m/s, 25% small glass beads ($d_p = 1.5$ mm), 75% large glass beads ($d_p = 2.5$ mm).

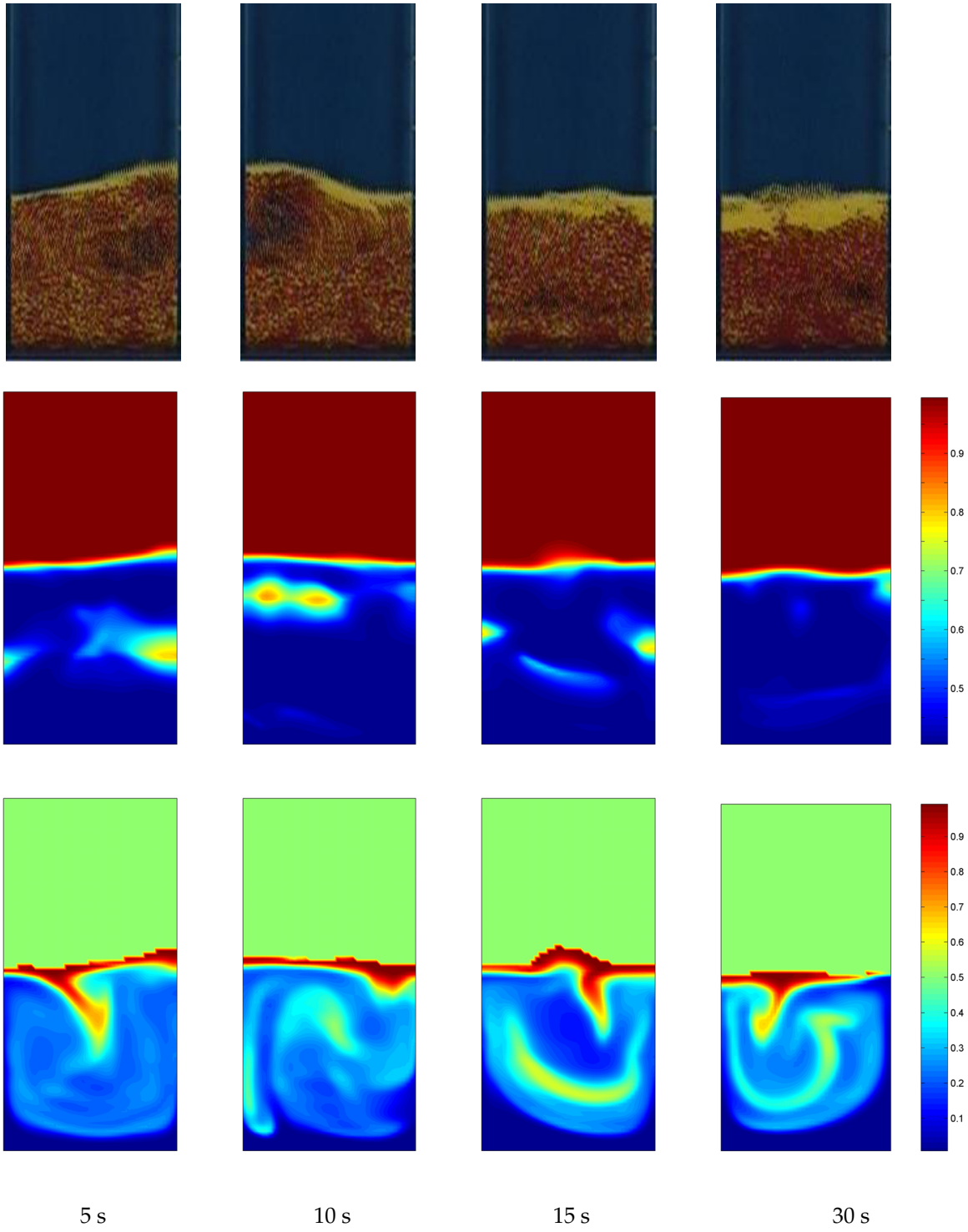

Figure A.15: Comparison between the new MFM and the experiments performed by Goldschmidt et al. (2003); u_{bg} = 1.20 m/s, 25% small glass beads (d_p = 1.5 mm), 75% large glass beads (d_p = 2.5 mm); top: snapshots of experiments; middle: void fractions; bottom: mass fraction small particles.

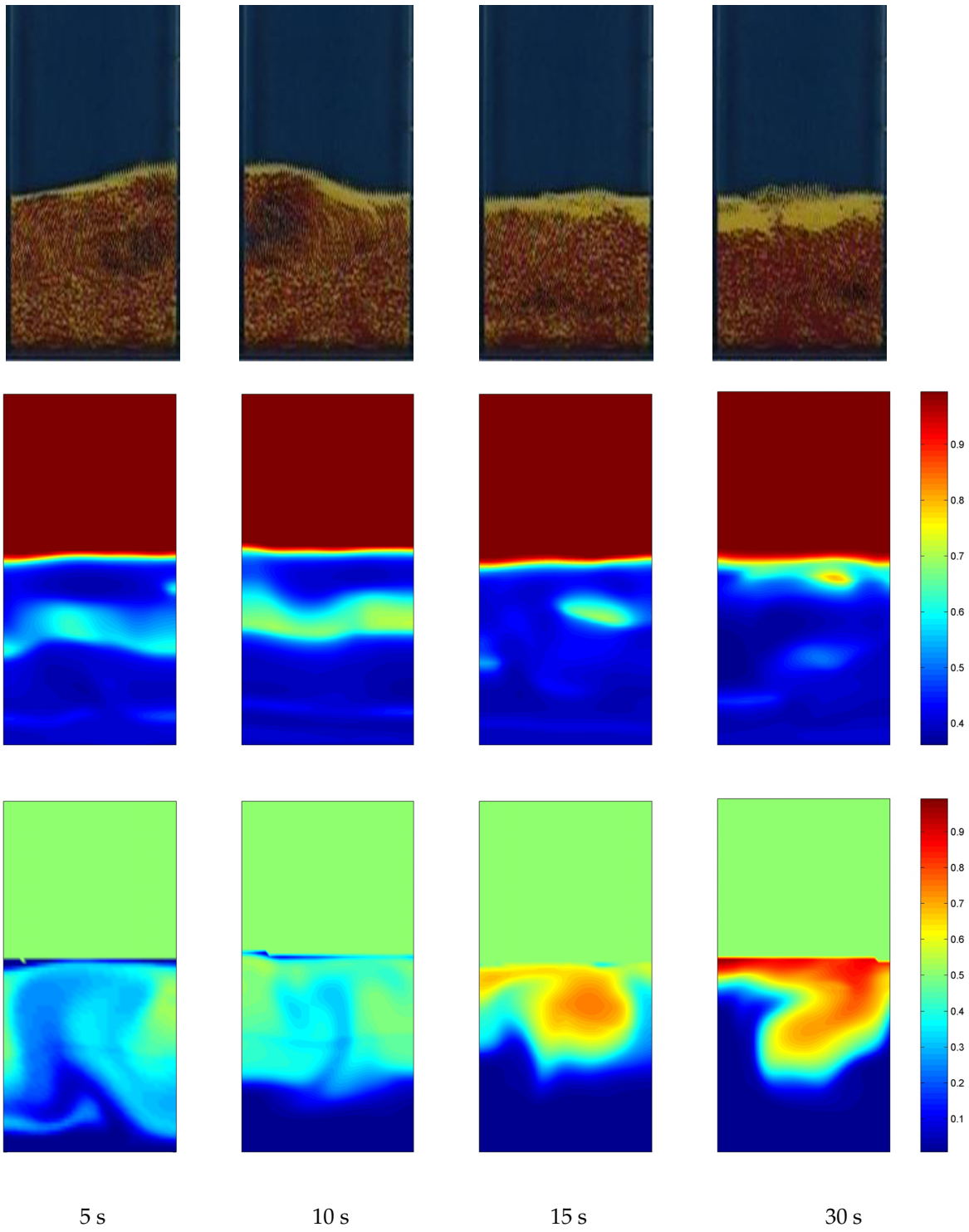

Figure A.16: Comparison between the MFM with closures by Manger (1996) and the experiments performed by Goldschmidt et al. (2003); u_{bg} = 1.20 m/s, 25% small glass beads (d_p = 1.5 mm), 75% large glass beads (d_p = 2.5 mm); top: snapshots of experiments; middle: void fractions; bottom: mass fraction small particles.

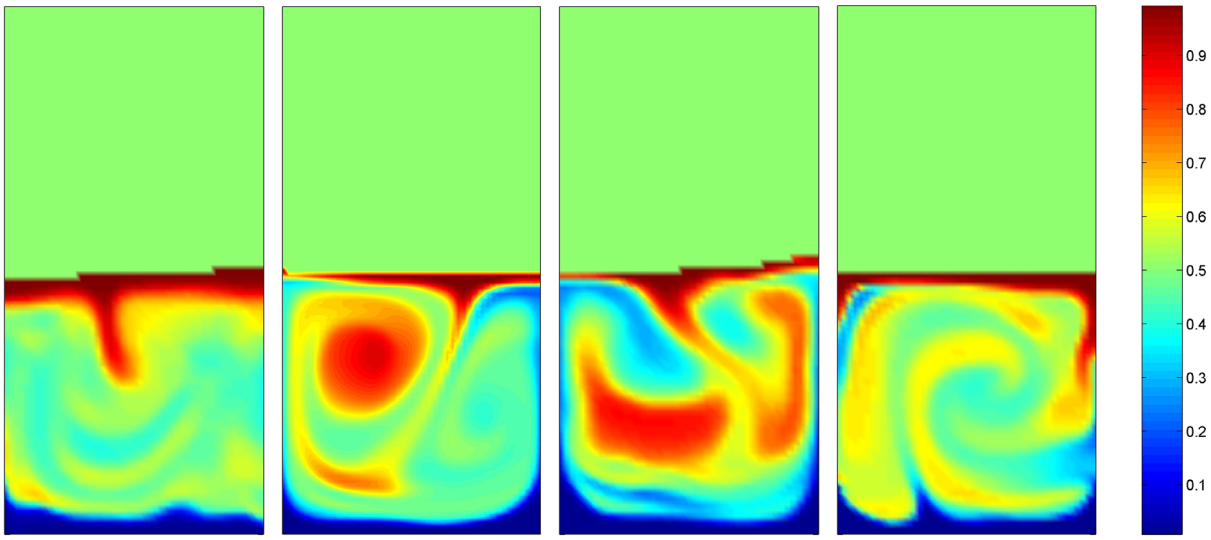

Figure A.17: Snapshots of the small particle mass fractions computed with the new MFM; u_{bg} = 1.10 m/s, 50% small particles, 50% large particles.

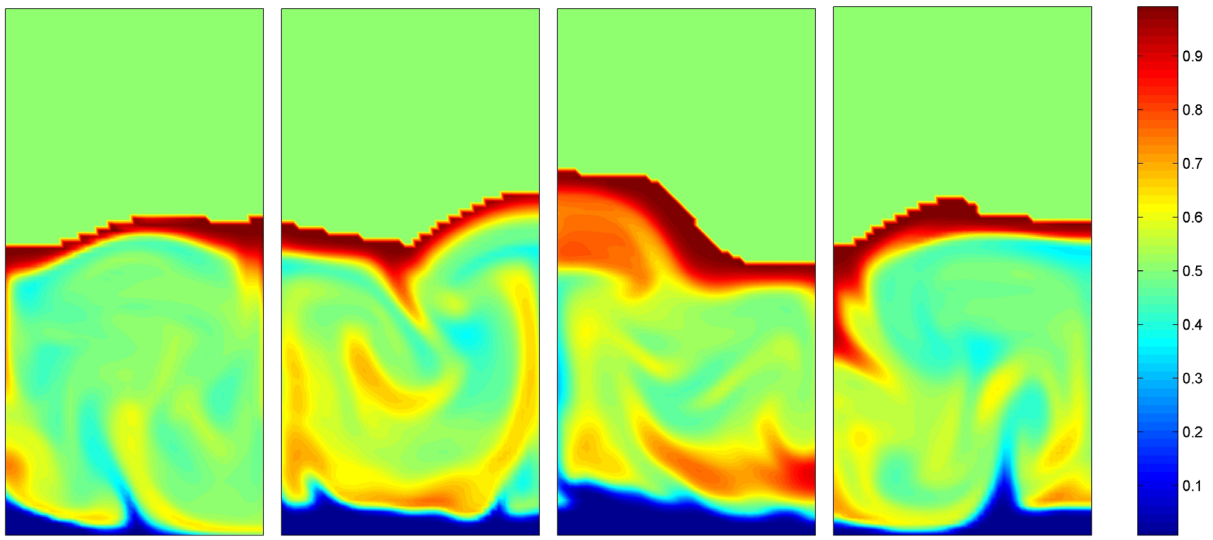

Figure A.18: Snapshots of the small particle mass fractions computed with the new MFM; u_{bg} = 1.25 m/s, 50% small particles, 50% large particles.

Nomenclature

a	sonine coefficient
$A(C)$	function, defined in equation 4.34
A_n	explicit term in the x-momentum equation [kg/(m^{2}s)]
AF	acceleration factor [-]
b	sonine coefficient
$B(C)$	function, defined in equation 4.34
B_n	explicit term in the y-momentum equation [kg/(m^{2}s)]
c	particle velocity [m/s]
c'	particle velocity after collision [m/s]
c_{12}	relative velocity of particle 1 to particle 2 (prior to collision) [m/s]
c'_{12}	relative velocity of particle 1 to particle 2 (after collision) [m/s]
C	spatial cross-covariance [-]
	fluctuating component of the particle velocity [m/s]
$\mathbb{C}$	dimensionless fluctuating component of the particle velocity [-]
C'	random fluctuation in the cross-covariance [-]
C_D	drag coefficient [-]
C_n	explicit term in the z-momentum equation [kg/(m^{2}s)]
C_{vm}	virtual mass coefficient [-]
d	diameter [m]
	sonine coefficient
d_{b0}	initial bubble diameter [m]
d_n	diffusion force [N]
d_t	particle image diameter [px]

D	mass residuals [kg/m^3]
	distribution function to map the momentum of bubbles
$D(C)$	function, defined in equation 4.34
D_T	fluidised bed diameter [m]
e	coefficient of normal restitution [-]
f	particle velocity distribution function [s^3/m^6]
f_{np}	pair distribution function [s^6/m^{12}]
F	force [N]
F_d	drag force [N]
F_g	gravity force [N]
F_I	in-plane particle loss correction factor [-]
F_O	out-of-plane particle loss correction factor [-]
F_p	pressure force [N]
F_T	shape of the correlation peak due to the particle diameter [-]
F_{vm}	virtual mass force [N]
g	gravitational acceleration [m/s^2]
g_0	radial distribution function for mono-disperse system [-]
g_{np}	radial distribution function for mixture [-]
h	sonine coefficient
	height [m]
$H(C)$	function, defined in equation 4.34
I	image intensity [-]
	moment of inertia [kgm^2]
	unit tensor [-]
	collisional integral
J	diffusion flux [kg/(m^{2}s)]
	Jacobi matrix
k	spring stiffness [N/m]

	unit vector along the line of centres at collision [-]
m	mass [kg]
M	camera magnification [m^2/px^2]
n	normal unit vector [-]
	number of particles per unit volume [$1/m^3$]
N	order of Enskog approximation
N_I	number of particles in the interrogation area [-]
NP	number of particles [-]
p_c	critical state pressure [Pa]
P	pressure [Pa]
P_s	particle pressure [Pa]
P_t	orifice pitch [m]
q_s	Pseudo-Fourier fluctuating kinetic energy flux [kg/(m s)]
r	position [m]
R	'true' cross-covariance [-]
	radius [m]
$\hat{R}$	cross-covariance [-]
R_C	background correlation [-]
R_D	displacement correlation peak [-]
R_F	correlation between the mean and fluctuating image intensity [-]
Re	Reynolds number [-]
s	relative segregation [-]
S	drag source term [Pa]
	sonine polynomial
	degree of segregation [-]
SF	size factor [-]
t	time [s]
	tangential unit vector [-]

T	torque [N m]
u	continuum velocity [m/s]
u_0	superficial gas velocity [m/s]
u_s	ensemble average particle velocity [m/s]
U	superficial gas velocity [m/s]
U_{mf}	minimum fluidisation velocity [m/s]
v	velocity [m/s]
v_b^0	terminal rise velocity of bubble [m/s]
v_n	diffusion velocity [m/s]
V	volume [m^3]
V_b	visible bubble flow [$m^3/(m^2 s)$]
x	x-position [m]
	horizontal position in digital image [px]
	species mass fraction
x_c	average horizontal displacement [px]
x_m	horizontal integer location of the cross-correlation peak [px]
y	y-position [m]
	vertical position in digital image [px]
y_c	average vertical displacement [px]
y_m	vertical integer location of the cross-correlation peak [px]
z	z-position [m]

Greek symbols

α	power-law function
β	inter-phase momentum transfer coefficient [$kg/(m^3 s)$]
β_0	coefficient of tangential restitution [-]
γ	dissipation of granular energy due to inelastic particle-particle

	collisions [kg/(ms^3)]
δ_{np}	Kronecker delta
δt	time step [s]
ϵ	volume fraction [-]
$\hat{\epsilon}$	sub-pixel displacement [px]
η	damping coefficient [N s/m]
θ	granular temperature [kgm^2/s^2]
θ_{np}	collisional flux
κ	pseudo-thermal conductivity [kg/(m s)]
λ_s	bulk viscosity [kg/(m s)]
Λ	De Broglie wavelength [m]
μ	friction coefficient [-]
	shear viscosity [kg/(m s)]
	chemical potential [J]
ξ	particle overlap [m]
ρ	shape of the correlation peak due to the velocity distribution [-]
	density [kg/m^3]
σ	standard deviation [px]
	particle diameter [m]
σ_{np}	inter-particle distance [m]
τ	stress tensor [Pa]
ϕ	solids volume fraction [-]
	particle property
ϕ_I	internal angle of friction [rad]
Φ	perturbation function
χ_{np}	collisional source
ψ	scale factor
ω	angular velocity [rad/s]

Subscripts

0	prior to collision
ab	indices of colliding particle pair
ac	auto correlation
b	bubble
bg	background
cc	cross correlation
cell	computational cell
d	displacement
e	emulsion
g	gas
large	2.5 mm particles
mf	minimum fluidisation
n	particle species n
	normal direction
p	particle
s	solid
small	1.5 mm particles
t	tangential direction
x	x-direction (directed from left to right)
y	y-direction (directed from front to back)
z	z-direction (directed from bottom to top)

Superscripts

(0)	first approximation in Chapman Enskog solution procedure
(1)	second approximation in Chapman Enskog solution procedure

^{0}	non-divergent tensor
ex	excess
max	maximum

Abbreviations

CFD	computational fluid dynamics
DBM	discrete bubble model
DEM	discrete element method
DPM	discrete particle model
HDPE	high density polyethylene
ICCG	incomplete Choleski conjugate gradient
KTGF	kinetic theory of granular flow
LBM	lattice Boltzmann model
LDPE	low density polyethylene
LLDPE	linear low density polyethylene
MFC	mass flow controller
MFM	multi fluid model
PE	polyethylene
PIV	particle image velocimetry
PP	polypropylene
RET	revised Enskog theory
SIMPLE	semi-implicit method for pressure linked equations
TFM	two fluid model

Bibliography

T.R. Auton. *The dynamics of bubbles, drops and particles in motion in liquids*. PhD thesis, University of Cambridge, 1983.

R. Beetstra. PhD thesis, University of Twente, Enschede, The Netherlands, 2005.

R.B. Bird, W.E. Stewart, and E.N. Lightfoot. *Transport Phenomena*, page 198. Wiley & Sons, New York, United States of America, 1960.

G.A. Bokkers, M. van Sint Annaland, and J.A.M. Kuipers. Mixing and segregation in a bi-disperse gas-solid fluidised bed: A numerical and experimental study. *Powder Technology*, 140:176–186, 2004a.

G.A. Bokkers, M. van Sint Annaland, and J.A.M. Kuipers. Comparison of continuum models using the kinetic theory of granular flow with discrete particle models and experiments: extent of particle mixing induced by bubbles. In *Fluidization XI*, pages 187–194, Naples, Italy, May 9-14 2004b.

I.D. Burdett, R.S. Eisinger, P. Cai, and K.H. Lee. Gas-phase fluidization technology for production of polyolefins. In M. Kwauk, J. Li, and W.C. Yang, editors, *Fluidization X*, pages 39–52, Beijing, People Republic of China, May 20-25 2001.

J. Centrella and J.R. Wilson. Planar numerical cosmology. II. The difference equations and numerical tests. *Astrophysical Journal Supplement Series*, 54:229–249, 1984.

S. Chapman and T.G. Cowling. *The mathematical theory of non-uniform gases*. Cambridge University press, Cambridge, 3rd edition, 1970.

T. Chiba and H. Kobayashi. Behavior of bubbles in gas-solid fluidized beds, initial formation of bubbles. *Chemical Engineering Science*, 27:965–972, 1972.

K.Y. Choi and W.H. Ray. The dynamic behaviour of fluidized bed reactors for solid catalysed gas phase olefin polymerization. *Chemical Engineering Science*, 40:2261–2279, 1985.

G.D. Cody, D.J. Goldfarb, G.V. Storch, Jr, and A.N. Norris. Particle granular temperatures in gas fluidized beds. *Powder Technology*, 87:211–232, 1996.

R. Collins. The effect of a containing cylindrical boundary on the velocity of a large gas bubble in a liquid. *Journal of Fluid Mechanics*, 28:97–112, 1967.

P.A. Cundall and O.D.L. Strack. A discrete numerical model for granular assemblies. *Géotechnique*, 29, 1979.

D. Darmana, N.G. Deen, and J.A.M. Kuipers. Detailed modeling of the hydrodynamics, mass transfer and chemical reactions in a bubble column using a discrete bubble model. *Chemical Engineering Science*, 60:3383–3404, 2005a.

D. Darmana, N.G. Deen, and J.A.M. Kuipers. Parallelization of an euler-lagrange model using mixed domain decomposition and a mirror domain technique: application to disperse gas liquid two phase flow. 2005b. document in preparation.

R.C. Darton and D. Harrison. The rise of single gas bubbles in liquid fluidized beds. *Transaction of Institution Chemical Engineers*, 52:301–306, 1974.

R.C. Darton, R.D. LaNauze, J.F. Davidson, and D. Harrison. Bubble growth due to coalescence in fluidized beds. *Transactions of the Institutions of Chemical Engineers*, 55: 274–280, 1977.

R.M. Davies and G.I. Taylor. The mechanics of large bubbles rising through extended liquids and through liquids in tubes. *Proceedings Royal Society London*, A200:375–390, 1950.

N.G. Deen, M. van Sint Annaland, and J.A.M. Kuipers. Multi-scale modeling of dispersed gas-liquid two-phase flow. *Chemical Engineering Science*, 59:1853–1861, 2004.

E. Delnoij. *Fluid dynamics of gas-liquid bubble columns*. PhD thesis, University of Twente, 1999.

E. Delnoij, J.A.M. Kuipers, and W.P.M. van Swaaij. A three dimensional cfd model for gas-liquid bubble columns. *Chemical Engineering Science*, 54:2217–2226, 1999.

E. Delnoij, F.A. Lammers, J.A.M. Kuipers, and W.P.M. van Swaaij. Dynamic simulation of dispersed gas-liquid two-phase flow using a discrete bubble model. *Chemical Engineering Science*, 52:1429–1458, 1997.

S. Ergun. Fluid flow through packed columns. *Chemical Engineering Progress*, 48:89, 1952.

Y.Q. Feng, B.H. Xu, S.J. Zhang, A.B. Yu, and P. Zulli. Discrete particle simulation of gas fluidization of particle mixtures. *AIChE Journal*, 50:1713–1728, 2004.

J.H. Ferziger and H.G. Kaper. *Mathematical theory of transport processes in gases*. North-Holland, 1972.

B. Formisani, G. de Cristofaro, and R. Girimonte. A fundamental approach to the phenomenology of fluidization of size segregating binary mixtures of solids. *Chemical Engineering Science*, 56:109–119, 2001.

D. Geldart. Types of gas fluidization. *Powder Technology*, 7:285–292, 1973.

D. Gidaspow. *Multiphase flow and fluidization: Continuum and kinetic theory descriptions*. Academic Press, Boston, 1994.

M.A. Gilbertson and I. Eames. Segregation patterns in gas-fluidized systems. *Journal of Fluid Mechanics*, 433:347–356, 2001.

M.J.V. Goldschmidt. *Hydrodynamic Modelling of Fluidised Bed Spray Granulation*. PhD thesis, University of Twente, Enschede, The Netherlands, 2001.

M.J.V. Goldschmidt, J.A.M. Kuipers, and W.P.M. van Swaaij. Segregation in dense gas-fluidised beds: Validation of a multi-fluid continuum model with non-intrusive di-

gital image analysis measurements. In M. Kwauk, J. Li, and W.C. Yang, editors, *Fluidization X*, pages 795–802, Beijing, People Republic of China, May 20-25 2001.

M.J.V. Goldschmidt, J.M. Link, S. Mellema, and J.A.M. Kuipers. Digital image analysis of bed expansion in dense gas-fluidised beds. *Powder Technology*, 138:135–159, 2003.

H. Hatzantonis, A. Goulas, and C. Kiparissides. A comprehensive model for the prediction of particle-size distribution in catalyzed olefin polymerization fluidized-bed reactors. *Chemical Engineering Science*, 53:3251–3267, 1998.

H. Hatzantonis, H. Yiannoulakis, A. Yiagopoulos, and C. Kiparissides. Recent developments in modeling gas-phase catalyzed olefin polymerization fluidized-bed reactors: The effect of bubble size variation on the reactor's performance. *Chemical Engineering Science*, 55:3237–3259, 2000.

B.P.B. Hoomans. *Granular dynamics of gas-solid two-phase flows*. PhD thesis, University of Twente, Enschede, The Netherlands, 1999.

B.P.B. Hoomans, J.A.M. Kuipers, W.J. Briels, and W.P.M. van Swaaij. Discrete particle simulation of bubble and slug formation in two-dimensional gas-fluidised beds: a hard-sphere approach. *Chemical Engineering Science*, 51:99, 1996.

B.P.B. Hoomans, J.A.M. Kuipers, and W.P.M. van Swaaij. Granular dynamics simulation of segregation phenomena in bubbling gas-fluidised beds. *Powder Technology*, 109:41–48, 2000.

L. Huilin, D. Gidaspow, and E. Manger. Kinetic theory of fluidized binary granular mixtures. *Physical Review E*, 64, 2001.

L. Huilin, L. Wenti, B. Rushan, Y. Lidan, and D. Gidaspow. Kinetic theory of fluidized binary granular mixtures with unequal granular temperature. *Physica A*, 284, 2000.

L. Huilin, H. Yurong, and D. Gidaspow. Hydrodynamic modelling of binary mixture in a gas bubbling fluidized bed using the kinetic theory of granular flow. *Chemical Engineering Science*, 58:1197–1205, 2003a.

L. Huilin, H. Yurong, D. Gidaspow, Y. Lidan, and Q. Yukun. Size segregation of binary mixture of solids in bubbling fluidized beds. *Powder Technology*, 134:86–97, 2003b.

L. Huilin, H. Yurong, L. Wentie, J. Ding, D. Gidaspow, and J. Bouillard. Computer simulations of gas-solid flow in spouted beds using kinetic-frictional stress model of granular flow. *Chemical Engineering Science*, 59:865–878, 2004.

J.T. Jenkins and F. Mancini. Balance laws and constitutive relations for plane flows of a dense binary mixture of smooth, nearly elastic circular disks. *Journal of Applied Mechanics*, 54:27–34, 1987.

J.T. Jenkins and F. Mancini. Kinetic theory for binary mixtures of smooth, nearly elastic spheres. *Physics of Fluids A*, 1(12):2050–2057, 1989.

J.T. Jenkins and C. Zhang. Kinetic theory for identical, frictional, nearly elastic spheres. *Physics of Fluids*, 14:1228–1235, 2002.

Y. Kaneko, T. Shiojima, and M. Horio. DEM simulation of fluidized beds for gas-phase olefin polymerization. *Chemical Engineering Science*, 54:5809–5821, 1999.

A.H. Kharaz, D.A. Gorham, and A.D. Salman. Accurate measurement of particle impact parameters. *Measurement Science and Technology*, 10:31–35, 1999.

J.Y. Kim and K.Y. Choi. Polymer particle mixing and segregation in a gas phase olefin polymerization reactor. *AIChE Symposium Series*, 95(321):77–82, 1999.

N. Kobayashi, R. Yamazaki, and S. Mori. A study on the behavior of bubbles and solids in bubbling fluidized beds. *Powder Technology*, 113:327–344, 2000.

D.L. Koch and R.J. Hill. Inertial effects in suspension and porous-media flows. *Annual Review of Fluid Mechanics*, 33:619–647, 2001.

R. Krishna and J.M. van Baten. Using CFD for scaling up gas-solid bubbling fluidised bed reactors with Geldart A powders. *Chemical Engineering Journal*, 82:247–257, 2001.

J.A.M. Kuipers, K.J. van Duin, F.P.H. van Beckum, and W.P.M. van Swaaij. Computer simulation of the hydrodynamics of two-dimensional gas-fluidized bed. *Computers & Chemical Engineering*, 17:839–858, 1993.

J.A.M. Kuipers and W.P.M. van Swaaij. Advances in chemical engineering. 24:227–328, 1998.

D. Kunii and O. Levenspiel. *Fluidization Engineering*. Butterworth-Heinemann, 2nd edition, 1991.

A. Lapin and A. Lübbert. Numerical simulation of the dynamics of two-phase gas-liquid flows in bubble columns. *Chemical Engineering Science*, 49:3661–3674, 1994.

H. Laux. *Modeling of dilute and dense dispersed fluid-particle flow*. PhD thesis, NTNU Trondheim, 1998.

S. Limtrakul, A. Chalermwattanatai, K. Unggurawirote, Y. Tsuji, T. Kawaguchi, and W. Tanthapanichakoon. Discrete particle simulation of solids motion in a gas-solid fluidized bed. *Chemical Engineering Science*, 58:915–921, 2003.

M. López de Haro, E.G.D. Cohen, and J.M. Kincaid. The Enskog theory for multicomponent mixtures. I. Linear transport theory. *Journal of Chemical Physics*, 78(5):2746–2759, 1983.

D. Ma and G. Ahmadi. An equation of state for dense rigid sphere gases. *Journal of Chemical Physics*, 84:3449–3450, 1986.

E. Manger. *Modeling and simulation of gas solid systems in curvilinear coordinates*. PhD thesis, Telemark Institute of Technology, Norway, 1996.

A. Marzocchella, P. Salatino, V. Di Pastena, and L. Lirer. Transient fluidization and segregation of binary mixtures of particles. *AIChE Journal*, 46:2175–2182, 2000.

V. Mathiesen. *An experimental and computational study of multiphase flow behaviour in circulating fluidised beds*. PhD thesis, Telemark Institute of Technology, Porsgrunn, Norway, 1997.

T.F. McKenna, D. Cokljat, and P. Wild. CFD modelling of heat transfer during gas phase olefin polymerisation. *Computers & Chemical Engineering*, 22:S285–S292, 1998.

T.F. McKenna and J.B.P. Soares. Single particle modelling for olefin polymerization on supported catalysts: A review and proposals for future developments. *Chemical Engineering Science*, 56:3931–3949, 2001.

J.J. Nieuwland, M. van Sint Annaland, J.A.M. Kuipers, and W.P.M. van Swaaij. Hydrodynamic modeling of gas/particle flow in riser reactors. *AIChE Journal*, 42:1569–1582, 1996.

F. Odar and W.S. Hamilton. Forces on a sphere accelerating in a viscous liquid. *Journal of Fluid Mechanics*, 18:302–314, 1964.

S. Pannala, C.S. Daw, and J.S. Halow. Simulations of reacting fluidized beds using an agent-based bubble model. *International Journal of Chemical Reactor Engineering*, 1 (A20):1–18, 2003.

S. Pannala, C.S. Daw, and J.S. Halow. Dynamic interacting bubble simulation (DIBS): An agent-based bubble model for reacting fluidized beds. *Chaos*, 14(2):487–498, 2004.

S.V. Patankar. *Numerical heat transfer and fluid flow*. Taylor & Francis, 1980.

D.J. Patil, M. van Sint Annaland, and J.A.M. Kuipers. Critical comparison of hydrodynamic models for gas-solid fluidized beds: Part I - Bubbling gas-solid fluidized beds operated with a jet. *Chemical Engineering Science*, 60:57–72, 2005a.

D.J. Patil, M. van Sint Annaland, and J.A.M. Kuipers. Critical comparison of hydrodynamic models for gas-solid fluidized beds: Part II - Freely bubbling gas-solid fluidized beds. *Chemical Engineering Science*, 60:73–84, 2005b.

W.H. Press and W.T. Vetterling. *Numerical Recipes for C*. Cambridge University Press, 2nd edition, 1992.

M.F. Rahaman, J. Nasar, and P.J. Witt. An unequal granular temperature kinetic theory: description of granular flow with multiple particle classes. *Powder Technology*, 138, 2003.

P.N. Rowe. Experimental properties of bubbles. In J.F. Davidson and D. Harrison, editors, *Fluidization*, pages 121–191. Academic Press, 1971.

P.N. Rowe and A.W. Nienow. Particle mixing and segregation in gas fluidised beds. A review. *Powder Technology*, 15:141–147, 1976.

A. Santos, S.B. Yuste, and M. López de Haro. Preliminary communication: Equation of state of a multicomponent d-dimensional hard-sphere fluid. *Molecular Physics*, 96: 1–5, 1999.

S.B. Savage and D.J. Jeffrey. The stress tensor in a granular flow at high shear rates. *Journal of Fluid Mechanics*, 110:255–272, 1981.

O. Simonin. Modelling turbulent reactive dispersed two-phase flows in industrial equipments. In *Proc. of the third world conference in applied computational fluid dynamics*, Freiburg, Germany, May 19-23 1996. Workshop E, 17.9.

J.L. Sinclair and R. Jackson. Gas-particle flow in a vertical pipe with particle-particle interactions. *AIChE Journal*, 35:1473–1486, 1989.

A. Sokolichin, G. Eigenberger, A. Lapin, and A. Lübbert. Dynamic numerical simulation of gas-liquid two-phase flows Euler/Euler versus Euler/Lagrange. *Chemical Engineering Science*, 52:611–626, 1997.

Y. Song, R.M. Stratt, and E.A. Mason. The equation of state of hard spheres and the approah to random closest packing. *Journal of Chemical Physics*, 88:1126–1133, 1988.

A. Srivastava and S. Sundaresan. Analysis of a frictional-kinetic model for gas-particle flow. *Powder Technology*, 129:72–85, 2003.

Y. Tsuji, T. Kawaguchi, and T. Tanaka. Discrete particle simulation of two-dimensional fluidised bed. *Powder Technology*, 77:79–87, 1993.

H. van Beijeren and M.H. Ernst. The modified Enskog equation. *Physica*, 68:437–456, 1973.

E.I.V. van den Hengel. *Multi-level modelling of gas-liquid two-phase flow in a bubble column*. PhD thesis, University of Twente, Enschede, The Netherlands, 2004.

M.A. van der Hoef, R. Beetstra, and J.A.M. Kuipers. Lattice Boltzmann simulations of low-Reynolds-number flow past mono- and bidisperse arrays of spheres: results for the permeability and drag force. *Journal of Fluid Mechanics*, 528:233–254, 2005.

M.A. van der Hoef, M. van Sint Annaland, and J.A.M. Kuipers. Computational fluid dynamics for dense gas-solid fluidized beds: a multi-scale modeling strategy. *Chemical Engineering Science*, 59(22-23):5157–5165, 2004.

C.Y. Wen and Y.H. Yu. Mechanics of fluidization. *Chemical Engineering Progress Symposium Series*, 62:100–111, 1966.

J. Werther. Influence of the bed diameter on the hydrodynamics of gas fluidized beds. *AIChE Symposium Series*, 70(141):53–62, 1974.

J. Werther. Fluidized-bed reactors. In B. Elvers, S. Hawkins, and G. Schulz, editors, *Principles of Chemical Reaction Engineering and Plant Design*, volume B4 of *Ullmann's Encyclopedia of Industrial Chemistry*. VCH Verlagsgesellschaft mbH, Weinheim, fifth edition, 1992.

J. Westerweel. *Digital Particle Image Velocimetry - Theory and Application*. PhD thesis, Delft University of Technology, Delft, The Netherlands, 1993.

J. Westerweel. Fundamentals of digital particle image velocimetry. *Measurement science and technology*, 8:1379–1392, 1997.

J. Westerweel. Theoretical analysis of the measurement precision in particle image velocimetry. *Experiments in fluids*, pages S3–S12, 2000.

R.D. Wildman. Measurement of the first and second moments of the velocity distribution in two-dimensional vibro-fluidised granular beds. *Powder Technology*, 127: 203–211, 2002.

R.D. Wildman and J.M. Huntley. Novel method for measurement of granular temperature distributions in two-dimensional vibro-fluidised beds. *Powder Technology*, 113: 14–22, 2000.

S.Y. Wu and J. Baeyens. Segregation by size difference in gas fluidized beds. *Powder Technology*, 98:139–150, 1998.

B.H. Xu and A.B. Yu. Numerical simulation of the gas-solid flow in a fluidised bed by combining discrete particle method with computational fluid dynamics. *Chemical Engineering Science*, 52:2785–2809, 1997.

Y. Zhang, Y. Yang, and H. Arastoopour. Electrostatic effect on the flow behavior of a dilute gas/cohesive particle flow system. *AIChE Journal*, 42:1591, 1996.

Dankwoord

Nu het boekje bijna helemaal af is, is het tijd om een aantal mensen de revue te laten passeren. Hoewel mijn naam de enige is die op dit proefschrift staat vermeld, was de totstandkoming ervan zeker niet gelukt zonder de hulp van vele andere mensen.

Allereerst wil ik mijn promotor Hans Kuipers bedanken voor de mogelijkheid die hij mij heeft geboden om een promotieproject te starten in zijn groep. Zijn jarenlange ervaring op het gebied van gas/vast modellering en zijn positieve coaching tijdens de vergaderingen die wij hebben gehad, hebben bijgedragen aan het slagen van dit project. Terugkijkend kan ik zeggen dat ik met veel plezier aan dit project heb gewerkt en er veel van heb geleerd. Daarnaast is Martin van Sint Annaland heel belangrijk geweest in de dagelijkse begeleiding van mijn promotie-onderzoek. Vooral zijn kennis op het gebied van de kinetische theorie voor granulaire stromingen was van grote waarde. Verder zullen mij de vele uren die we samen achter de computer hebben gezeten om het Multi Fluid Model aan de praat te krijgen nog lang heugen. Martin van der Hoef wil ik nog bedanken voor zijn inbreng op het gebied van Lattice Boltzmann simulaties en de daaruit voortvloeiende gas/deeltjes dragrelaties en Niels Deen voor zijn bijdrage op het gebied van Particle Image Velocimetry (PIV).

Het Dutch Polymer Institute (DPI) wil ik bedanken voor de financiële support voor dit onderzoek. In het bijzonder wil ik Geert Bonte, die vanuit DSM en later SABIC bij het project betrokken was, bedanken voor de bijdrage vanuit de industrie en de interesse in de 'numerieke krachtpatserij' met onze modellen, dat wij presenteerden tijdens de projectbijeenkomsten.

Naast het vele rekenwerk met de modellen zijn er ook experimenten uitgevoerd om de modellen te valideren. Voordat experimenten uitgevoerd kunnen worden, moet er eerst een opstelling gebouwd of verbouwd worden en daar komen de technici om de hoek kijken. In de eerste plaats wil ik Gerrit Schorfhaar bedanken voor het bouwen van mijn opstelling. Ik vond het altijd leuk om met jouw samen te werken. Vooral van de verhalen die jij altijd wist te vertellen over hoe het er vroeger op de UT aan toe ging heb ik erg genoten. Ook Wim Leppink, Robert Meijer en in een later stadium Robert Brouwer wil ik bedanken voor de kleinere klusjes die zij voor mij gedaan hebben.

In de afgelopen vier jaar heb ik een aantal afstudeerders en 1 stagiair gehad die veel nuttig werk hebben verricht. Ik wil hierbij Jurriaan Boon, Remko Westra, Ruud Swarts, Timon Stomp en Wouter Dijkhuizen bedanken voor hun inzet. Wouter wil ik nog extra bedanken voor het extra werk dat hij heeft verricht om zijn afstudeerwerk verder te perfectioneren, hetgeen geresulteerd heeft in een mooi hoofdstuk in dit proefschrift.

Naast de afstudeerders heb ik natuurlijk veel samengewerkt met andere collega AIO's. Allereerst Jeroen, waarmee ik de afgelopen vier jaar mijn kantoor heb gedeeld. Ik heb veel met je kunnen discussiëren over balletjes, maar ook over volleybal en vele andere zaken. Jeroen, bedankt voor de gezelligheid in ons kantoortje. I would also like to thank Dadan for all his effort he put in the DBM code and the postprocessing tools that I could use for my project as well. Alle andere AIO's en oud-AIO's wil ik bedanken voor de leuke tijd in de afgelopen vier jaar. Voor administratieve zaken kon ik altijd terecht bij de secretaresse van de vakgroep. Ria Hofs en Nicole Haitjema, bedankt voor jullie hulp.

Buiten werktijd was er ook zeker tijd voor gezelligheid. Regelmatig werden er uitjes georganiseerd voor de groep. Liesbeth Kuipers wil ik bedanken voor de organisatie van de jaarlijkse skivakantie met de vakgroep. Dankzij de FAP skivakanties ben ik helemaal verslaafd geraakt aan het skiën. Verder zal ik al de gezellige borrels en de jaarlijkse zeilweekenden samen met de collega's van OOIP en de TWAIO's niet snel

vergeten. Ook op sportief vlak heb ik mij kunnen uitleven tijdens de volleybal en voetbal vakgroep competities en natuurlijk bij de volleybal vereniging Harambee. Ik wil dan ook mijn teamgenoten van de afgelopen jaren in de teams Koor II, HarambInc en Brievolutions bedanken voor de gezellige tijd.

Tot slot wil ik mijn ouders bedanken voor hun steun en interesse gedurende mijn periode in Enschede. Hoewel het werk wat ik deed allemaal abracadabra was voor jullie, informeerden jullie regelmatig hoe de vlag er bij stond in Enschede. Ook mijn zus en broer, Annette en Henk-Jan, wil ik bedanken voor hun interesse en gezelligheid als ik weer eens in Barneveld was. Als allerlaatste wil ik Margriet bedanken voor haar steun en geduld. Zeker het laatste half jaar is je geduld op de proef gesteld, toen ik bezig was met het afronden van mijn boekje en ik vele avonden achter mijn pc heb gezeten. Na dit dankwoord is het boekje echt helemaal af en gaan we met z'n tweeën weer heel veel leuke dingen doen.

Albert

Levensloop

Albert Bokkers werd geboren op 29 juni 1976 te Putten, waar hij ook de lagere school heeft gevolgd. Van 1988 tot 1990 heeft hij de Meijntscamp te Nijkerk bezocht, waarna hij van 1990 tot 1994 het VWO heeft afgerond op het Johannes Fontanus College te Barneveld.

In september 1994 begon hij met de opleiding Chemische Technologie aan de Universiteit Twente in Enschede. In het kader van deze opleiding liep hij van september tot december 1998 stage bij Dow Chemicals in Terneuzen. In juni 2000 studeerde hij af bij de werkeenheid Fundamentele Aspecten van de Proceskunde (FAP) op het onderwerp 'Theoretische en Experimentele studie naar gas/vloeistof stromingen met behulp van Volume of Fluid en Laser Doppler Anemometry'.

In september 2000 trad hij in dienst bij de werkeenheid Fundamentele Aspecten van de Proceskunde (FAP) om als promovendus (AIO) een promotieonderzoek te verrichten op het gebied van gas/vast meer-fasenstromingen. De resultaten van dit onderzoek vormen de basis voor dit proefschrift.